An electron force field for simulating large scale excited electron dynamics
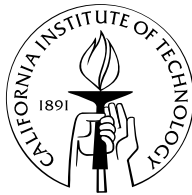
Thesis by
Julius T. Su

In Partial Fulfillment of the Requirements
for the Degree of
Doctor of Philosophy

California Institute of Technology
Pasadena, California

2007

(Defended April 12, 2007)

Acknowledgements

I dedicate this thesis to my parents. I thank them for teaching me early, teaching me well, and indulging and nurturing my curiosity about the world until it became self-sustaining. My brother Jonathan and sisters Judy and Jessica have always been there for me as well, and we have had a good journey together.

It has been a pleasure to work for my advisor, Prof. Bill Goddard, who attacks scientific problems with great enthusiasm, open-mindedness, and a formidable arsenal of ideas and approaches. His way of getting to the root of things and identifying the key experiment that needs to be done is as reflexive for him as breathing.

I appreciate that Bill gave me the freedom to work on many different projects, and his level of expertise and broad range of interests was such that he provided good insights on every one of them. The stimulus behind the electron force field and this thesis was the ideas presented in his *Nature of the Chemical Bond* course – he talked about electrons moving around and "pooching", changing in size and becoming orthogonal to each other, and his level of enthusiasm motivated me to develop a simulation of these events happening.

I also had the privilege to work with Prof. Brian Stoltz for nearly a year on developing the Wolff/Cope reaction. He is a great experimentalist, and I was humbled that he was willing to entrust the initial development of his reaction to a first year graduate student. I appreciated his hands-on guidance and attention to detail. After I joined Bill's group, I continued to do theory on the reaction while Richmond Sarpong took over and made great strides in the experimental work, continued later by Jenny Roizen; it was a very successful division of labor.

Prof. Ahmed Zewail introduced me to computational chemistry as an undergraduate in the context of modeling caging of charge-transfer reactions in clusters. I am indebted to him for his support and encouragement, his scientific and personal insights, and his firm insistence that I learn the theory behind every part of my calculations properly. I appreciate the time he spent with our project, and the interest he took in making sure I developed well as an independent researcher.

An electron force field for simulating large scale excited electron dynamics

by

Julius T. Su

In Partial Fulfillment of the

Requirements for the Degree of

Doctor of Philosophy

Summary

Much interesting chemistry involves the motion of large numbers of excited electrons, yet theory is limited in its ability to simulate such systems. We introduce an electron force field (eFF) that makes simulation of large scale excited electron dynamics possible and practical. The forces acting on thousands of electrons and nuclei can be computed in less than a second on a single modern processor.

Just as conventional force fields parameterize the ground state potential between nuclei, with electrons implicitly included, electron force fields parameterize the potential between nuclei and simplified electrons, with more detailed degrees of freedom implicitly included. The electrons in an electron force field are Gaussian wave packets whose only parameters are its position and its size.

Using a simple version of the electron force field, we compute the dissociation and ionization behavior of dense hydrogen, and obtain equations of state and shock Hugoniot curves that are in agreement with results obtained from vastly more expensive path integral Monte Carlo methods. We also compute the Auger dissociation of hydrocarbons, and observe core hole decays, valence electron ionizations, and nuclear fragmentation patterns consistent with experiment.

Despite the simplicity of the electron representation, with a judicious choice of potentials we are able to describe electrons of different shapes in different environments.

In one chapter, we show we can describe p-like valence electrons using spherical Gaussian functions, enabling us to compute accurate ionization potentials and polarizabilities for first row atoms, and accurate dissociation energies and geometries of atom hydrides and hydrocarbons.

In another chapter, we show that we can describe delocalized electrons in a uniform electron gas using localized eFF orbitals. We reproduce the energy of a uniform electron gas, including correlation effects; and following the historical development of density functional theory, we develop a preliminary eFF that can compute accurate exchange and correlation energies of atoms and simple molecules.

In the following pages, we have highlighted successes of eFF, but have not shied away from analyzing in depth areas where it could be improved. We hope that this combination of promising results and critical analysis stimulates and assists further research in this exciting field.

Contents

List of Figures

List of Tables

Chapter 1

The electron force field, a method for simulating large-scale excited electron dynamics

Simulating excited electron dynamics in condensed matter

From semiconductor etching to molecular memories, from fuel cells to photosynthesis, much essential chemistry is driven by the collective motion of excited electrons (Figure 1.1). Yet computing the dynamics of strongly coupled, nonadiabatic, condensed system electrons on a large scale remains a challenge to theory. We have developed a method called the *electron force field*, which in conjunction with another method called wave packet molecular dynamics, makes simulations of these systems practical.

In wave packet molecular dynamics [5, 16, 3], nuclei are propagated as classical particles, and electrons as localized wave packets described by their average position and size.

In the electron force field (eFF), energies and forces are calculated from an energy expression parameterized as a function of nuclear and electron coordinates, with terms that capture key chemical features like covalent and ionic bonding, core-valence separation, lone pairs, correlation, and the mixing of metallic electrons. Details of the energy expression, as well as an analogy to classical force fields, are given in more depth below.

With our method, we expect simulations of 10^5 excited electrons over 10^3 picoseconds to be practical for a wide range of strongly coupled condensed systems.
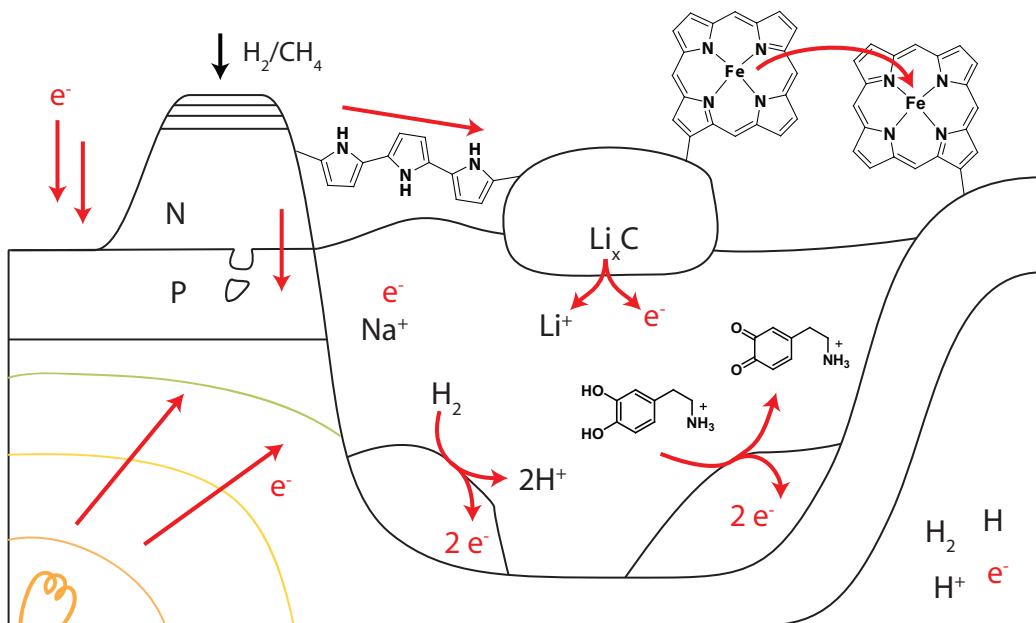
Figure 1.1: Excited condensed state electrons drive essential chemistry.

Electron force field makes large scale simulations possible.

To understand how electron force fields can help us compute approximate excited state dynamics quickly, we make an analogy to traditional force field methods for calculating ground state dynamics (Figure 1.2).

In the ground state, we assume that nuclei are well-localized, so that they can be represented classically; and that since electrons are much lighter than nuclei, the electron wavefunction and energy is a *parameteric* function of the nuclear coordinates (Born-Oppenheimer approximation [4]):

$$\mathcal{H}_{elec}(\mathbf{R})\psi(\mathbf{r}) = E_{elec}(\mathbf{R})\psi(\mathbf{r}) \tag{1.1}$$

$$E_{total}(\mathbf{R}) = \sum_{i<j} \frac{Z_i Z_j}{R_{ij}} + E_{elec}(\mathbf{R}) \tag{1.2}$$

3

Ground state dynamics

Excited state dynamics
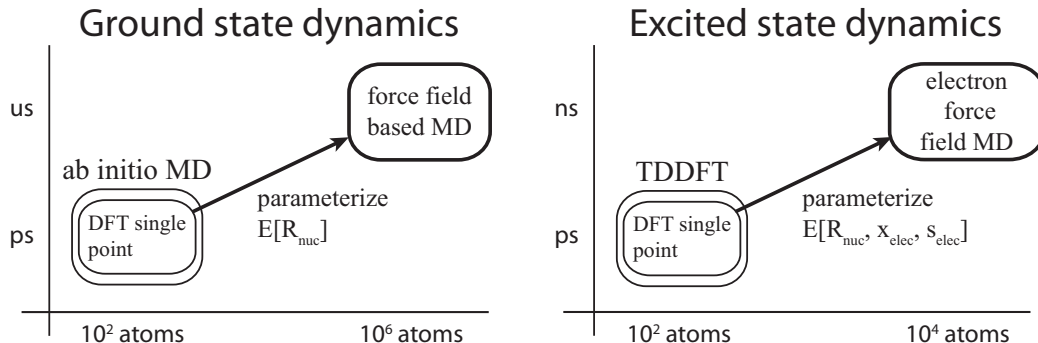
Figure 1.2: Electron force field makes feasible simulations of large scale excited electron dynamics.

where $\mathbf{R}$ are the nuclear coordinates and $\mathbf{r}$ are the electron coordinates.

To compute how the nuclei move over time, we can solve the time-independent electronic Schrodinger equation at each time step, compute forces on the nuclei, get new positions and velocities by integration, and repeat. The forces are calculated using the Hellman-Feynman theorem [5], which states that the force on each nucleus in the presence of a normalized wavefunction ψ is the sum of the electric field from the other electrons and nuclei, as well as a Pulay force [6, 7] that goes to zero if ψ is an eigenfunction of $\mathbf{H}$:

$$
\begin{aligned}
\mathbf{F} &= -\nabla E = -\nabla \langle \psi | \mathcal{H} | \psi \rangle \\
&= \underbrace{- \langle \psi | \nabla \mathcal{H} | \psi \rangle}_{\mathbf{F}_{\mathbf{electrostatic}}} \underbrace{- \langle \nabla \psi | \mathcal{H} | \psi \rangle - \langle \psi | \mathcal{H} | \nabla \psi \rangle}_{\mathbf{F}_{\mathbf{Pulay}}}.
\end{aligned}
\tag{1.3}
$$

However, this method, called Born-Oppenheimer molecular dynamics [8], is slow, because it requires a quantum mechanics calculation at each step. We may speed this up by only partially optimizing the wavefunction at each step, as in the Car-Parinello approach [9], or by using particularly efficient density-functional theory methods [10], but in practice *ab initio* based MD simulations remain limited to hundreds of atoms over picoseconds [3].

Is there any way to get around solving Schrodinger's equation at each step? After all, the Born-Oppenheimer approximation states that the total energy should

be a function of nuclear coordinates alone. In fact, the most common way to perform dynamics on large systems over long times is to use a force field, an approximate energy expression that is a function of nuclear coordinates. A force field typically combines covalent terms between and about bonds with pairwise noncovalent terms between atoms [12, 1, 2]

$$
\begin{aligned}
E_{total}(\mathbf{R}_{nuc}) \;=\; & \sum_{i<j} E_{bond}(R_{ij}) + \sum_{ijk} E_{angle}(\theta_{ijk}) + \sum_{ijkl} E_{dihedral}(\phi_{ijkl}) \\
& + \sum_{i<j} \frac{q_i q_j}{R_{ij}} + \sum_{i<j} E_{vdW}(R_{ij})
\end{aligned}
\tag{1.4}
$$

The ability to parameterize high-accuracy quantum and experimental data into a lower-accuracy nuclear potential is fundamental to being able to simulate systems ranging from homogeneous [15] to hetergeneous [16] catalysts, from amino acids to proteins with solvent effects included [17]. In most force fields, the partitioning of energy terms is physically motivated, and it requires some artistry to determine the functional forms needed to reproduce a broad range of chemical phenomena. The reward for undertaking the laborious procedure of force field development is a function that can be orders of magnitude faster to evaluate than quantum mechanics.

In an electron force field, we consider the situation where electrons are not in the lowest energy state: the bandgap may be small, the temperature may be high, a current may be flowing, light may have excited electrons, or free electrons may be present. In many of these cases, the Born-Oppenheimer approximation no longer holds, and we write the force field energy as a function of both nuclear positions and a reduced set of electron parameters. Which electron parameters to include is a balancing act — too few, and our description will be inadequate to explain chemistry; too many, and the resulting function will be as expensive to evaluate as quantum mechanics.

Following a systematic investigation into the terms needed to capture a broad range of chemical phenomena, we have developed a force-field expression that is a function of nuclear positions $\mathbf{R_i}$, average electron positions $\mathbf{x_i}$, and average electron

sizes s_i:

$$E_{total}(\mathbf{R}, \mathbf{x}, \mathbf{s}) = \sum_{i \in elec} E_{kinetic}(s_i)$$

$$+ \sum_{i,j \in nuc} \frac{Z_i Z_j}{R_{ij}} + \sum_{\substack{i \in elec \\ j \in nuc}} V_{elec-nuc}(R_{ij}, s_i, Z_j) + \sum_{i,j \in elec} V_{elec-elec}(x_{ij}, s_i, s_j)$$

$$+ \sum_{i,j \in \uparrow\uparrow elec} E_{\text{exch}}(x_{ij}, s_i, s_j) + \sum_{\substack{i,j \in \uparrow\uparrow elec \\ k \in nuc}} E_{\text{exch}}^{\text{p-like}}(x_{ik}, x_{jk}, \theta_{ikj}, s_i, s_j, Z_k)$$

$$+ \sum_{i,j \in \uparrow\downarrow elec} E_{\text{corr}}(x_{ij}, s_i, s_j) \tag{1.5}$$

where all pairs are counted once, and the nuclei have charge Z. The energy is a sum of electronic kinetic energies (larger for small electrons); screened electrostatic interactions between all pairs of nuclei, electrons, and electrons and nuclei; repulsive Pauli exchanges between same spin electrons; attractive Pauli exchanges between same spin electrons near the same nucleus; and attractive correlations between opposite spin electrons.

We emphasize similarities and differences between eFF and traditional force fields. Our electron force field is like traditional force fields in that it is fast, and all the methods used to speed up evaluation of traditional force fields, such as neighbor lists [18], multigrid Poisson solvers [19], particle mesh Ewald [20], and so on, can be used to make the electron force field faster as well. In that respect it advances our goal of making large-scale excited electron dynamics simulation practical.

However, the electron force field is different from traditional force fields in that properties such as bonding, hybridization, lone pairs, bond geometry preferences, steric effects, transition state energies, charge distributions, number of electrons in valence shells, spin multiplicity effects, and ionization potentials all appear as emergent properties of the interactions between nuclei and electrons. It is our hope that features of our force field may be incorporated into traditional force fields, so that they can be made more general while requiring fewer parameters.

We note finally that force field development serves a pedagogical as well as a

practical purpose. Force fields break interaction energies into components that are both convenient to calculate and easy to understand in an physical way: terms like bond stretching, van der Waals interactions, electrostatics, and so on. The price paid for the accuracy of high-level theory is often a loss in our ability to analyze results; force fields are a way to recapture this understanding [21].

Wave packet molecular dynamics

In wave packet molecular dynamics, we represent nuclei as classical particles, and electrons as spherical Gaussian wave packets whose positions $\mathbf{x}$ and extents s vary over time:

$$\Psi \propto \prod_j \exp\left[-\left(\frac{1}{s^2} - \frac{2p_s}{s}i\right)(\mathbf{r} - \mathbf{x})^2\right] \cdot \exp[i\mathbf{p_x} \cdot \mathbf{x}]. \tag{1.6}$$

In a harmonic potential, Gaussian wave packets stay Gaussian over time, and it is meaningful to talk about the evolution of the coordinates x, s, and momenta p_x and p_s. Substituting the wave packet into the time-dependent Schrodinger equation gives the Hamilton equations of motion (Appendix A)

$$\dot{\mathbf{p}}_\mathbf{R} = -\nabla_R V, \ \dot{\mathbf{p}}_\mathbf{x} = -\nabla_x V, \ \dot{p}_s = -\partial V/\partial s$$

$$\mathbf{p_R} = m_{nuc}\mathbf{R}, \ \mathbf{p_x} = m_{elec}\mathbf{x}, \ \mathbf{p_s} = (3m_{elec}/4)s \tag{1.7}$$

assuming a locally harmonic interaction potential. These equations can be viewed as a generalization of Ehrenfest's theorem [22], which states that the average position of a wave packet obeys classical dynamics, with the addition that the size of the wave packet obeys classical dynamics as well. The 3/4 factor in front of the mass multiplying the radial coordinate is related to the dimensionality of the Gaussian packet, and becomes 2/4 for a 2D Gaussian, 1/4 for a 1D Gaussian, and so on.

Heller showed these equations could be applied profitably to anharmonic reaction potentials to describe processes such as collinear $He + H_2$ scattering [5]. Klakow later applied the same procedure to the anharmonic Coulomb potentials

Nuclear temperature	$T_{nuc} = \frac{1}{3k_B} \left\langle \sum_{\text{nuc d.o.f.}} \frac{1}{2} m_i \dot{x}_i{}^2 \right\rangle$
Electron temperature	$T_{elec} = \frac{1}{4k_B} \left\langle \sum_{\text{elec d.o.f.}} \frac{1}{2} m_i \dot{x}_i{}^2 \right\rangle$
Pressure	$P = \frac{2\langle K_{total}\rangle}{V} - \frac{1}{3V} \left\langle \sum_{\text{all d.o.f.}} x_i \frac{\partial E}{\partial x_i} \right\rangle$
Current	$\mathbf{J} = \sum_{i \in nuc} Z_i \dot{\mathbf{R}}_i + \sum_{i \in \text{elec}} (-1) \cdot \dot{\mathbf{R}}_i$
Conductivity	$\sigma = \frac{1}{3Vk_bT} \int \int \mathbf{J}(t) \cdot \mathbf{J}(t+\tau) dt d\tau$
Excitation response function	$\upsilon(\tau) = \int \sum_{i \in elec} \dot{\mathbf{R}}_i(t) \dot{\mathbf{R}}_i(t+\tau) dt$
Excitation spectrum	$A(\omega) = \left| \int \upsilon(t) \cos(\omega t) dt \right|^2$
Electron density	$\rho(\mathbf{x}) = \sum_{i \in elec} |\phi(\mathbf{x} - \mathbf{R}_i; r_i)|^2$
Spin polarization	$\zeta(\mathbf{x}) = (\rho^\uparrow(\mathbf{x}) - \rho^\downarrow(\mathbf{x}))/\rho(\mathbf{x})$

Table 1.1: Quantities that can be calculated from wave packet molecular dynamics.

in hydrogen plasma and lithium metal, and found he was able to reproduce equilibrium pair distribution functions well [16]. He also extracted the conductivity of a hydrogen plasma by using a Green-Kubo expression [23, 24] relating the fluctuation of current — obtained from nucleus and electron positions — to the dissipation of current given an applied potential. Indeed, since electrons are just another particle in these molecular dynamics simulations, we can use relations traditionally applied to nuclear positions and velocities to compute a wide range of electrical properties (Table 1.1).

In our simulations, we usually set $m_{electron} = m_H$, so that we may use a longer time step $t = 0.1 - 0.5 fs$. There are additional reasons that can be given for this choice — for example, anharmonic potentials tend to damp out radial oscillations in the wavefunction (Appendix A); the Landau theory of Fermi liquids uses heavy quasiparticles that obey fermion statistics [25] — but it would be best to rerun our simulations with a smaller electron mass to make sure our choice does not have too large an adverse effect.

We are making an assumption of mean field dynamics [26, 27] by propagating electron dynamics via the time-dependent Schrodinger equation. In our approach, the electron exists as a superposition of stationary states (Ψ_i, E_i), and the nuclei

move in a potential that is a linear combination of those states:

$$E = \sum_i |c_i|^2 E_i. \tag{1.8}$$

There are conditions under which this is not a good assumption. For example, if our system has only a few well-separated states, and is prepared into a stationary state through a monochromatic light pulse, that state will tend to stay on one adiabatic path for a long period of time, and switch to other states via conical intersections. In these cases, a surface hopping stochastic dynamics scheme would be more appropriate, as mean field dynamics would split the difference between adjacent paths. A stochastic scheme is also appropriate for cases where the spacing between states changes rapidly during the course of the simulation, for example in the case of an electron scattering off a surface, where the electron goes from a continuum of states in free space to an insulator-like state on the surface.

Most cases we are interested in, however, contain many excited electrons and many closely-spaced states (Figure 1.3), where the entire dynamics of the system take place in a phase space packed with conical intersections with high Massey parameter [28] (see Appendix B). Here, the system is constantly jumping between adiabatic states, and the mean field trajectory is a good approximation of the nonadiabatic motions of the electrons.
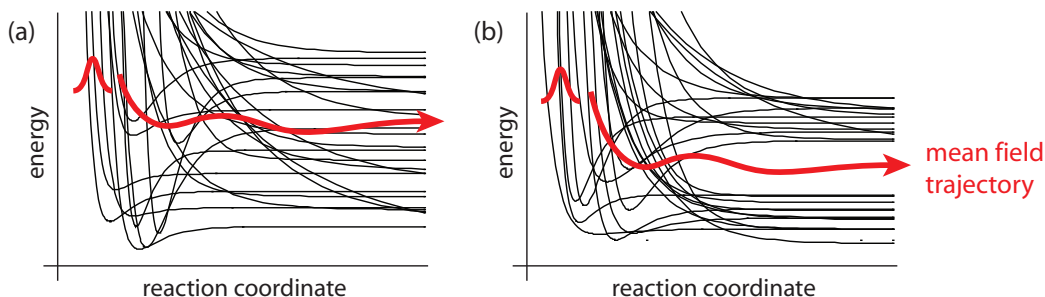
Figure 1.3: (a) Excited condensed system evolves through many curve crossings, and can be approximately described by a mean field trajectory. (b) However, the mean field trajectory may incorrectly bisect well-separated adiabatic states.

Mean field dynamics has seen recent interest lately in combination with time-dependent density functional theory. In time-dependent DFT [29], we solve time-dependent Schrodinger equation

$$i\hbar\frac{d}{dt}\psi_j(\mathbf{r},t) = \left(-\frac{\hbar^2}{2m_e}\nabla^2 + V_s[\rho](r,t)\right)\psi_j(\mathbf{r},t) \qquad (1.9)$$

with a Kohn-Sham potential that is a functional of the time-varying electron density $\rho = \sum_{j=1}^{N}|\psi_j(\mathbf{r},t)|^2$:

$$V_s[\rho] = V_{nuc}(\mathbf{r},t) + \int \frac{\rho(\mathbf{r}',t)}{|\mathbf{r}-\mathbf{r}'|}d\mathbf{r}' + V_{xc}[\rho](\mathbf{r},t). \qquad (1.10)$$

An adiabatic approximation is often applied, where it is assumed that the electron exchange-correlation does not depend on the past history of the electron density:

$$V_{xc}[\rho](\mathbf{r},t) = V_{xc}[\rho](\mathbf{r}). \qquad (1.11)$$

Even the simplest functional, the adibatic local-density approximation (ALDA), gives good excitation spectra [30], Rydberg states [31], and dispersion coefficients [32]. It has been applied to calculate the mean-field dynamics of sodium dimer [33], lithium cyanide ion [33], and ethylene [34] in response to femtosecond laser pulses, and the chemiadsorption of hydrogen on aluminum (111) surfaces [35].

Electron force field wave packet MD simulations are in some sense complementary to TDDFT simulations. Unlike ALDA, eFF has nonlocality in space, due to pairwise interactions of the electron force field, both in exchange and correlation; and nonlocality in time, due to the inertia of the electrons. eFF may serve as a useful method to investigate the significance of the space/time locality assumptions made in TDDFT methods.

Reference methods for ground and excited states

In parameterizing and validating the electron force field, it is necessary to assemble reference data from experiments, and theoretical methods that are appli-

cable to ground states and excited states. Most of the theoretical methods are well known, e.g., Hartree-Fock for computing uncorrelated energies, CCSD(T) for high-accuracy correlated energies. In two cases, though, we have studied systems beyond the scope of those methods: the uniform electron gas and dense hydrogen plasma under high pressure.

For those cases, we have used reference data obtained from stochastic methods, which are very expensive computationally but very accurate and in principle general to any system. Diffusion Monte Carlo [36] is a method for computing high-accuracy energies for ground states. We write the time-independent Schrodinger equation as a diffusion equation in imaginary time:

$$\frac{\partial \Psi}{\partial t} = \frac{1}{2} \nabla^2 \Psi + (E - V(\mathbf{x})) \Psi. \tag{1.12}$$

Then the Green's function for this equation can be approximated for small time steps

$$\Psi(\mathbf{y}) = \int G(\mathbf{y}, \mathbf{x}; \tau) \Psi(\mathbf{x}) d\mathbf{x} \tag{1.13}$$

$$G(\mathbf{y}, \mathbf{x}; \tau) \approx e^{-(\mathbf{y} - \mathbf{x})^2 / 2\tau} \; e^{-(V_{avg}(\mathbf{x}) - E)} \tag{1.14}$$

(which becomes exact as $\tau \to 0$) and applied iteratively to form a probability distribution that converges to the true distribution over time. The energy is exact to within the position of the nodes, which must be specified in advance through a trial wavefunction; this trial wavefunction is also used to sample the distribution preferentially at places where the electron density is highest.

Path integral Monte Carlo [37] is a useful method to compute thermodynamic averages of quantum operators at finite temperature. We write the position density matrix operator as an integral over successive paths:

$$\langle \mathbf{y} | e^{-\mathcal{H}/kT} | \mathbf{x} \rangle = \int \langle \mathbf{x} | e^{-\tau \mathcal{H}} | \mathbf{R_1} \rangle \, \langle \mathbf{R_1} | e^{-\tau \mathcal{H}} | \mathbf{R_2} \rangle \cdots \langle \mathbf{R_{N-1}} | e^{-\tau \mathcal{H}} | \mathbf{y} \rangle \, d\mathbf{R_1} \cdots d\mathbf{R_{N-1}} \tag{1.15}$$

where $\tau = 1/(kTN)$ is the time step. Then each density matrix element can be

evaluated in the short time limit:

$$
\begin{aligned}
\langle \mathbf{R_i}|e^{-\tau(\mathcal{T}+\mathcal{V})}|\mathbf{R_{i+1}}\rangle &\approx \langle \mathbf{R_i}|e^{-\tau\mathcal{T}}\,e^{-\tau\mathcal{V}}|\mathbf{R_{i+1}}\rangle \\
&\propto e^{-(\mathbf{R_i}-\mathbf{R_j})^2/2\tau}\cdot e^{-\tau V(\mathbf{R_i})\delta(\mathbf{R_i}-\mathbf{R_j})}.
\end{aligned}
\tag{1.16}
$$

The path is varied in a Monte Carlo procedure to evaluate the expectation value of the desired operator. The procedure works best for high temperatures; at lower temperatures, the number of path links N must be increased to keep τ small.

History and current progress on the electron force field

The electron force field traces its origins to two lines of inquiry that evolved over the past decades. The first was the development of fermion molecular dynamics methods [17] (FMD) in the late 70s and wave packet molecular dynamics (WPMD) methods [16] in the late 90s, which applied quasiclassical representations of elementary particles to the study of nucleon dynamics [14, 15, 18], hydrogen plasmas [11, 38], ion collisions [19], and so on. In these studies, electrons and nucleons were often represented by Gaussian functions, and effective potentials between these functions were created to reproduce desired static and dynamic properties. The focus was less on describing the details of bonding and electronic structure, and more on obtaining qualitatively correct dynamics; the most advanced effective potentials due to Klakow were limited to describing the interactions of hydrogen, helium, and lithium atoms. Most of these methods employed pairwise potentials between particles, and scaled as N^2, with N being the number of particles.

The second was the development of the floating spherical Gaussian orbital (FSGO) method by Frost [8] in 1964, which combined a single Gaussian function per electron basis with an *ab initio* energy expression which scaled as N^4. This method was able to describe bonding between atoms from hydrogen through argon, with good geometries for molecules containing at most one lone pair, and particularly good geometries for hydrocarbons. The energetics of bonding were described less well however.

Previous work	WPMD, FMD – N^2 scaling, H_2 plasma, nucleons
	FSGO *ab initio* – N^4 scaling, hydrocarbons etc.
First generation, matter at extreme conditions	eFF – N^2 scaling, H_2 plasma and hydrocarbons
Second generation, focus on improved accuracy	eFF/s – H, Li, Be compounds
	eFF/p – first row organics
	eFF/metallic – uniform electron gas
Future work	Universal eFF?

Figure 1.4: Summary of electron force field development.

The electron force field combines the scope of FSGO methods with the speed of WMPD methods, and improves on the accuracy of both methods. We discuss in the next chapter a first-generation eFF which contains kinetic energy, electrostatic energy, and pairwise Pauli repulsion terms, and gives a reasonable description of hydrogen atom reactions and hydrocarbons while scaling as N^2. With this simple force field, we study matter at extreme conditions — the dissociation and ionization of hydrogen at intermediate densities, and the Auger dissociation of hydrocarbons.

In subsequent chapters, we improve the accuracy of eFF by (1) considering the effects of different electron shapes and hybridizations, (2) considering the delocalized electrons in a uniform electron gas, and (3) parameterizing exchange and correlation as separate interactions. In our zeal to determine the optimal eFF for certain interactions, we emerged with with different force fields for different electron types, such as core-like electrons in lithium clusters, valence-like electrons in atom hydrides, and delocalized electrons in metals and the uniform electron gas. This collection of electron force fields constitutes the second generation eFFs.

s-like core electrons   p-like valence electrons   metallic electrons
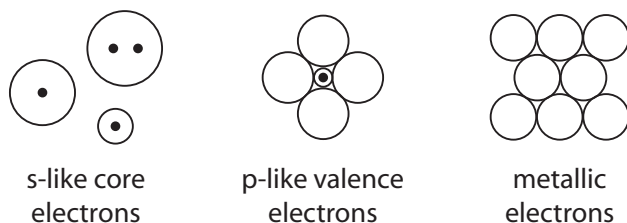
Figure 1.5: Character of electron depends on its proximity to nuclei.

In the future, we will attempt to reunify our many eFFs into a single third-generation eFF that can interpolate between extremes of reactivity and bonding, and act as a universal method for describing large-scale excited electron dynamics.

Appendix A: Wave packet MD equations of motion

The Gaussian wave packets used in our wave packet molecular dynamics contain a radial momentum term that we have only found once in the literature [38]. We give our motivation for this term, and a derivation of the corresponding equation of motion, below.

Consider the wave packet $\Psi = \exp(i\mathbf{p}_x \cdot \mathbf{x}) \cdot \exp(-a(r-x)^2)$. Heller [5] showed that substituting this wavefunction into the time dependent Schrodinger equation gives the Hamilton equations of motion $\mathbf{p_x} = m\,\dot{\mathbf{x}}$ and $\dot{\mathbf{p_x}} = -\nabla V$, consistent with Ehrenfest's theorem, which states that the average position of a wavefunction follows a classical trajectory.

In the above wave packet, x and p_x are real variables that are conjugate to each other. Heller derived an equation of motion for a as well, but only for complex a; substituting $\Psi = \exp(-ax^2)$ into the time-dependent Schrodinger equation with a harmonic potential gives (taking $\hbar = 1$)

$$i\frac{d\Psi}{dt} = -\frac{1}{2m}\frac{\partial^2\Psi}{dx^2} + \frac{1}{2}kx^2\Psi \tag{1.17}$$

$$-i\dot{a}x^2 = -\frac{1}{2m}(4a^2x^2 - 2a) + \frac{1}{2}kx^2 \tag{1.18}$$

$$i\dot{a} = \left(\frac{2}{m}\right)a^2 - \frac{1}{2}k. \tag{1.19}$$

To begin, we examine the time evolution of the wavefunction $\Psi(t = 0) = exp(-ax^2)$ when there is no external potential:

$$i\dot{a} = \frac{2}{m}a^2 \Rightarrow a = \frac{a_0}{1 + (2a0/m)it}. \tag{1.20}$$

Then define

$$\alpha = Re(a) = \frac{a_0}{1 + (4a_0^2/m^2)t^2} \tag{1.21}$$

$$p_\alpha = \frac{m}{4}\dot{\alpha} = -\frac{a_0 m/4}{(1 + (4a_0^2/m^2)t^2)^2} \cdot \frac{8a_0^2}{m^2} \cdot t = \alpha Im(a) \tag{1.22}$$

which gives us

$$\Psi = \exp(-(Re(a) + i\,Im(a))x^2) = \exp(\alpha + i\,p_\alpha/\alpha)$$
$$= \exp\left(-\left(\frac{1}{s^2} - \frac{2p_s}{s}i\right)x^2\right) \tag{1.23}$$

where in the last step we have made the change of variables $\alpha = 1/s^2$.

We substitute $a = 1/s^2 - 2p_s/s$ into equation 1.19 to derive equations of motion for s and p_s:

$$-\frac{2}{s^3}\dot{s}\,i + \frac{2\dot{p}_s}{s} - \frac{2p_s}{s^2}\dot{s} = \frac{2}{m}\left(\frac{1}{s^4} - \frac{4p_s}{s^3}i - \frac{4p_s^2}{s^2}\right) - \frac{1}{2}k. \tag{1.24}$$

Equating imaginary parts:

$$-\frac{2}{s^3}\dot{s}\,i = -\frac{2}{m}\frac{4p_s}{s^3}i \;\Rightarrow\; \boxed{p_s = \frac{m}{4}\dot{s}} \tag{1.25}$$

Equating real parts:

$$\frac{2\dot{p}_s}{s} = \frac{2}{m} - \frac{1}{2}k \;\Rightarrow\; \boxed{\dot{p}_s = -\frac{\partial E}{\partial r}} \text{ where } E = \frac{1}{2}\frac{1}{r^2} + \frac{1}{8}kr^2, \; m = 1 \tag{1.26}$$

which gives us back the Hamilton relations of equation 1.7. In a three-dimensional spherical Gaussian wave packet, there is one radial coordinate but three dimensions affecting its variation. The end effect is that each dimension contributes a mass factor of $1/4$ to equation 1.7. From the equations of motion, it also follows that if we define a kinetic energy T as

$$T = \sum_i \frac{1}{2}m_i v^2 + \frac{1}{2}\left(\frac{3}{4}m_i\right)v_s^2 \tag{1.27}$$

that the total energy $T + V(x, s)$ is a constant of motion. The kinetic energy of motion T is not to be confused with the *electronic* kinetic energy $3/2r_e^{-2}$ which appears in $V(x, s)$.

The wave packet equations of motion are exact for harmonic potentials, but we do not know how well they describe the wave packets in anharmonic potentials. To test our approximation, we propagated wave packets numerically on a 1D line using a discretized version of the time-dependent Schrodinger equation [39], and compared the average position and width of the wave packet to a pure Gaussian wave packet propagated with WPMD. As expected, the expansion of a free electron and the oscillations of a harmonic oscillator matched in both models to within the error of the simulation (Figure 1.6).
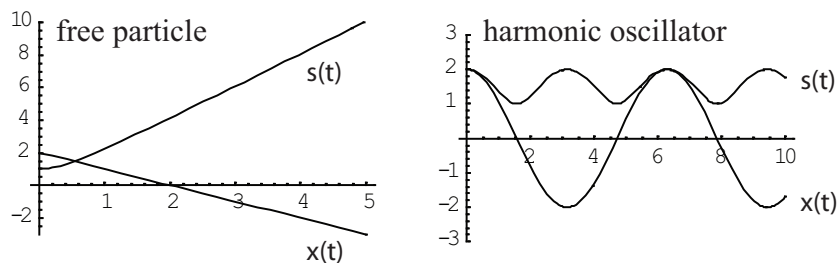
Figure 1.6: Gaussian and exact wave packet dynamics match for free particle and harmonic oscillator potentials.

We then tested the double well potential $V = 1/20x^4 - 1/2x^2$, giving the wave packet enough energy to traverse the center barrier. In the exact simulation, the wave packet bounced back and forth twice, but quickly spread out and delocalized over both wells, so that both the position and size reached a constant value. In contrast, the Gaussian wave packet showed no signs of damping, and had more rapid radial oscillations than in the exact case (Figure 1.7).

Over a short time interval, the two models matched well. We conclude that in systems where electrons are well-localized, wave packet molecular dynamics should describe well how electrons move; but it may overemphasize radial oscillations that in a real system would be damped out by quantum interference. Our practical
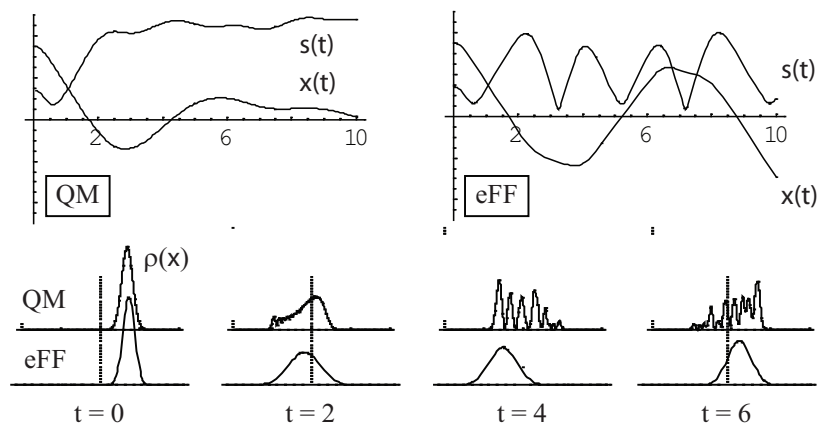
Figure 1.7: Exact and Gaussian wave packet dynamics for a double well potential.

choice of an artificially heavy electron mass may compensate somewhat for this difference.

Appendix B: Adiabatic excited state dynamics

In the previous sections, we discussed the application of the Born-Oppenheimer approximation to ground state dynamics. Under certain circumstances — well-separated electronic states, low nuclear velocities, or excitation into special symmetry states — a similar adiabatic approximation can be made to excited state dynamics as well. We explain below how this can be the case.

Consider the stationary states of a molecule, the solutions of the time-independent Schrodinger equation $\mathcal{H}\Psi_i = E_i\Psi_i$. Usually we solve this equation approximately by varying parameters of a trial function. For the lowest energy or ground state, we have the variational principle

$$E_0 = \langle \Phi_0 | \mathcal{H} | \Phi_0 \rangle \geq E_0(\text{exact}) \tag{1.28}$$

so that we obtain a best estimate for Ψ_0 by varying Φ_0 to minimize E_0.

The most common trial function is an antisymmetrized product of one electron orbitals, called a Slater determinant [40]. Slater determinants are the basis of the Hartree-Fock method, and have well-understood limitations — they do not

properly describe covalent bond breaking, certain atomic symmetries, and instantaneous correlation of electron motions due to Coulomb repulsion. We can account for some of these effects using a density-dependent exchange-correlation functional (DFT) or by adding more determinants corresponding to the excitation of electrons into virtual orbitals (configuration interaction).

For excited states, we can apply a generalized variational principle to obtain an approximate wavefunction solution:

$$E_i = \langle \Phi_i | \mathcal{H} | \Phi_i \rangle \geq E_i(\text{exact}) \text{ if } \langle \Phi_i | \Phi_j \rangle = 0 \text{ for all } j < i. \qquad (1.29)$$

If the excited state has a different symmetry than the ground state, we can write the trial wavefunction as single determinant and simply apply the ground-state optimization procedures to obtain an excited state solution. As long as the trial function is restricted to a symmetry different from the ground state (and the lower excited states), the orthogonality to the ground state is maintained automatically, and the solution is valid [41].

However, if the excited state has the same symmetry as the ground state, the orthogonality needs to be maintained some other way, which poses technical challenges, often overcome through use of a multi-determinant wavefunction [42]. Also, some excited states, such as the open shell $2s^2 2p^2$ carbon atom, require multiple determinants to describe, which is expensive for large systems, and not compatible with default Kohn-Sham density functional theory [43].

Time-dependent methods like TDDFT, described in the earlier sections, can be used to extract excited state energies properties as well, and are gaining popularity because (1) time-dependent functionals can be based on ground-state functionals, (2) an entire excitation spectra can be obtained from one calculation, and (3) we are not restricted to calculating excited states of different symmetry than the ground state. All in all, though, it is not yet possible to find excited stationary states with the same ease, accuracy, or generality as ground states.

Suppose we excite a system to a single stationary state, for instance with a long

duration monochromatic pulse. What happens to a system in such a state? We have prepared a stationary state of the electrons, not necessarily the nuclei, so usually the nuclei move. As this happens, the system begins to include contributions from other stationary states, and a superposition of states evolves [28]:

$$\Psi(\mathbf{R}_{elec}, t) = \sum_j c_j(t) \Psi_j(\mathbf{R}_{elec}; \mathbf{R}_{nuc}(t)) \qquad (1.30)$$

$$i\hbar \dot{c}_k = \sum_j c_j \left(E_k \delta_{kj} - i\hbar \dot{\mathbf{R}}_{nuc} \cdot \mathbf{d}_{jk} \right) \qquad (1.31)$$

where

$$\mathbf{d}_{jk} = \langle \Psi_k | \nabla_{R_{nuc}} \Psi_j \rangle = \frac{\langle \Psi_k | \nabla_{R_{nuc}} \mathcal{H}(\mathbf{R}_{nuc}) | \Psi_j \rangle}{E_j - E_k}. \qquad (1.32)$$

The non-adiabatic coupling vector d_{jk} couples electron and nuclear motions, and is responsible for the mixing of stationary states as they approach each other in energy. The final simplification to write $\mathbf{d}_{jk}$ in terms of the operator $\nabla \mathcal{H}$ comes from $\nabla_{R_{nuc}} \langle \Psi_k | \mathcal{H} | \Psi_j \rangle = \nabla_R E_k \delta_{kj} = 0$.

If d_{kj} is small, the system will evolve adibatically along a single stationary state, and the Born-Oppenheimer approximation applies. For d_{kj} to be large, and the states to mix, certain conditions must hold. First, the states need to be similar in energy. Second, they need to be the same symmetry, so that $\langle \Psi_k | \nabla_{R_{nuc}} \mathcal{H}(\mathbf{R}_{nuc}) | \Psi_j \rangle \neq 0$. And third, even if the states are of similar energy and matching symmetry, when two eigenvalues of an N dimensional Hermitian matrix become the same, the degeneracy spans a N-2 dimensional space called a conical intersection [44] (Figure 1.8). At conical intersections, the Born-Oppenheimer approximation breaks down, since electrons flow from one state to another over a small variation in nuclear position. In the special case of a diatomic molecule, $N = 1$ and the conical intersection becomes an avoided crossing where the curves cannot intersect.

For a two-state avoided crossing, a transition from one adiabatic state to another is probable when the Massey parameter is greater than one [28]:

$$\xi = \left| \frac{\hbar \dot{\mathbf{R}}_{nuc} \cdot \mathbf{d}_{jk}}{E_j - E_k} \right| \geq 1. \qquad (1.33)$$
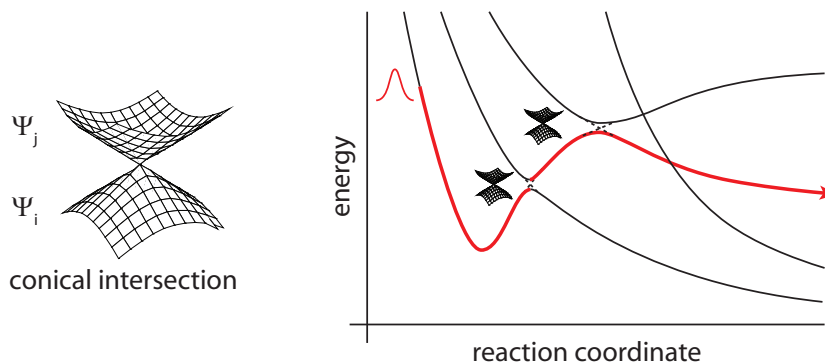
Figure 1.8: In sparse systems, electrons move mostly along adiabatic paths, with crossings limited to conical intersections with reduced dimensionality.

Hence hopping is favorable when the energy gap is small, the nuclear velocities high, and the non-adibatic coupling vector high in magnitude. When electronic states are well-separated and the temperature is low, it is a good approximation to say that the system evolves adiabatically for long periods of time followed by nonadiabatic switches at conical intersections that are restricted to small regions in phase space.

Surface hopping stochastic dynamics [45] makes this approximate picture literal, by propagating the nuclei along single excited state potentials, and switching them randomly to other state potentials with a rate that is a function of $\dot{\mathbf{R}}_{nuc} \cdot \mathbf{d}_{jk}$. Tully's popular minimum switching algorithm [28] executes this switching in an efficient way that preserves fluxes and minimizes the abruptness of switching from one state to another. The excited state potentials can be parameterized from quantum calculations or experiment; or DFT, Car-Parinello, or TDDFT methods can be used to compute them on the fly.

Bibliography

[1] **Heller, E. J.** 1975. Time-dependent approach to semiclassical dynamics. *J. Chem. Phys.* **62(4)**:1544-1555.

[2] **Klakow, D., Toepffer, C., Reinhard, P.-G.** 1994. Semiclassical molecular dynamics for strongly coupled Coulomb systems. *J. Chem. Phys.* **101(12)**:10766-10774.

[3] **Singer, K. and Smith, W.** 1986. Semiclassical many-particle dynamics with gaussian wave packets. *Mol. Phys.* **57(4)**:761-775.

[4] **Born, M. and Oppenheimer, M.** 1927. On the quantum theory of molecules. *Annalen der Physik.* **84**:457-484.

[5] **Feynman, R. P.** 1939. Forces in molecules. *Phys. Rev.* **56**:340-343.

[6] **Pulay, P.** 1969. *Ab initio* calculation of force constants and equlibrium geometries in polyatomic molecules. I. Theory. *Mol. Phys.* **17(2)**:197-204.

[7] **Goddard, W. A. III**. 1968. Improved quantum theory of many-electron systems. IV. Properties of GF wavefunctions. *J. Chem. Phys.* **48(12)**:5337-5347.

[8] **Barnett, R. N. and Landman, U.** 1993. Born-Oppenheimer molecular-dynamics simulations of finite systems: structure and dynamics of $(H_2O)_2$. *Phys. Rev. B* **48(4)**:2081-2097.

[9] **Car, R. and Parrinello, M.** 1985. Unified approach for molecular dynamics and density-functional theory. *Phys. Rev. Lett.* **55(22)**:2471-2474.

[10] **Goedecker, S.** 1999. Linear scaling electronic structure methods. *Rev. Mod. Phys.* **71(4)**:1085-1123.

[11] **Tuckerman, M. E.** 2002. *Ab initio* molecular dynamics: basic concepts, current trends and novel applications. *J. Phys.: Condens. Matter.* **14**:R1297-R1355.

[12] **Allinger, N. L.** 1977. Conformational analysis. 130. MM2. A hydrocarbon force field utilizing V_1 and V_2 torsional terms. *J. Am. Chem. Soc.* **99(25)**:8127-8134.

[13] **Mayo, S. L., Olafson, B. D., Goddard, W. A. III**. 1990. Dreiding: a generic force field for molecular simulations. *J. Phys. Chem.* **94(26)**:8897-8909.

[14] **van Duin, A.C.T., Dasgupta, S., Lorant, F., Goddard, W. A. III**. 2001. ReaxFF: a reactive force field for hydrocarbons. *J. Phys. Chem. A.* **105**:9396-9409.

[15] **Castonguay, L. A. and Rappe, A. K.** 1992. Ziegler-Natta catalysis: A theoretical study of the isotactic polymerization of propylene. *J. Am. Chem. Soc.* **114(14)**:5832-5842.

[16] **Nielson, K. D., van Duin, A. C. T., Oxgaard, J., Deng, W.-Q., Goddard, W. A. III**. 2005. Development of the ReaxFF reactive force field for describing transition metal catalyzed reactions, with application to the initial stages of the catalytic formation of carbon nanotubes. *J. Phys. Chem. A.* **109(3)**:493-499.

[17] **Karplus, M. and Petsko, G. A.** 1990. Molecular dynamics simulations in biology. *Nature.* **347**:631-639.

[18] **Verlet, L.** 1967. Computer "experiments" on classical fluids. I. Thermodynamical properties of Lennard-Jones molecules. *Phys. Review.* **159(1)**:98-103.

[19] **Holst, M. and Saied, F.** 1993. Multigrid solution of the Poisson-Boltzmann equation. *J. Comp. Chem.* **14(1)**:105-113.

[20] **Darden, T., York, D., Pedersen, L.** 1993. Particle mesh Ewald: an $N \log N$ method for Ewald sums in large systems. *J. Chem. Phys.* **12**:10089-10092.

[21] **Mulliken, R. S.** 1965. "... the more accurate the calculations became, the more the concepts tended to vanish into thin air." *J. Chem. Phys.* **43**:S2.

[22] **Liboff, R. L.** *Quantum mechanics* (Holden-Day, San Francisco, 1980).

[23] **Kubo, R.** 1957. Statistical-mechanical theory of irreversible processes. I. General theory and simple applications to magnetic and conduction problems. *J. Phys. Soc. Japan* **12(6)**:570-586.

[24] **Green, M. S.** 1954. Markoff random processes and the statistical mechanics of time-dependent phenomena. II. Irreversible processes in fluids. *J. Chem. Phys.* **22(3)**:398-413.

[25] **Landau, L.** 1957. The theory of a fermi liquid. *Soviet Physics JETP.* **3**:920-925.

[26] **Doltsinis, N. L.** 2002. Nonadiabatic dynamics: mean-field and surface hopping. In *Quantum Simulations of complex many-body systems: from theory to algorithms.* Grotendorst, J., Marx, D., Muramatsu, A. (Eds.) **10**:377-397.

[27] **Tully, J. C.** 1998. Mixed quantum-classical dynamics. *Faraday Discuss.* **110**:407-419.

[28] **Tully, J. C.** 1990. Molecular dynamics with electronic transitions. *J. Chem. Phys.* **93(2)** 1061-1071.

[29] **Burke, K., Werschnik, J., Gross, E. K. U.** 2005. Time-dependent density functional theory: past, present, and future. *J. Chem. Phys.* **123**:062206-1 to 062206-9.

[30] **Petersilka, M., Gossmann, U. J., Gross, E. K. U.** 1995. Excitation energies from time-dependent density functional theory. *Phys. Rev. Lett.* **76**:1212-1215.

[31] **Wassermann, A. and Burke, K.** 2005. Rydberg transition frequencies from the local density approximation. *Phys. Rev. Lett.* **95**:163006-1 to 163006-4.

[32] **Dion, M., Rydberg, H., Schroder, E., Langreth, D. C., Lundqvist, B. I.** 2004. Van der Waals density functional for general geometries. *Phys. Rev. Lett.* **92(24)**:246401-1 to 246401-4.

[33] **Castro, A., Marques, M. A. L., Alonso, J. A., Bertsch, G. F., Rubio, A.** 2004. Excited states dynamics in time-dependent density functional theory. *Eur. Phys. J. D* **28**:211-218.

[34] **Kunert, T., Grossmann, F., Schmidt, R.** 2005. Nonadibatic dynamics of ethylene in femtosecond laser pulses. *Phys. Rev. A.* **72**:023422-1 to 023422-6.

[35] **Lindenblatt, M. and Pehlke, E.** 2006. *Ab initio* simulation of the spin transition during chemisorption: H/Al(111). *Phys. Rev. Lett.* **97**:216101-1 to 216101-4.

[36] **Reynolds, P. J., Ceperley, D. M., Alder, B. J., Lester, W. A., Jr.** 1982. Fixed-node quantum Monte Carlo for molecules. *J. Chem. Phys.* **77(11)**:5593-5603.

[37] **Pollock, E. L. and Ceperley, D. M.** 1984. Simulation of quantum many-body systems by path-integral methods. *Phys. Rev. B.* **30(5)**:2555-2568.

[38] **Knaup, M., Reinhard, P.-G., Toepffer, C.** 2001. Wave packet molecular dynamics simulations of deuterium in the region of laser shock-wave experiments. *Contrib. Plasma. Phys.* **41(2-3)**:159-162.

[39] **Thaller, B.** 2000. *Visual quantum mechanics* (Springer-Verlag).

[40] **Boys, S. F.** 1950. Electronic wave functions. I. A general method of calculation for the stationary states of any molecular system. *Proc. Royal. Soc. London. A.* **200(1063)**:542-554.

[41] **Dreuw, A. and Head-Gordon, M.** 2005. Single-reference *ab initio* methods for the calculation of excited states of large molecules. *Chem. Rev.* **105**:4009-4037.

[42] **Fitzgerald, G. and Schaefer, H. F. III**. 1985. Analytic energy derivative methods for excited singlet states of the same symmetry as the electronic ground state. *J. Chem. Phys.* **83(3)**:1162-1167.

[43] **Ziegler, T., Rauk, A., Baerends, E. J.** 1977. On the calculation of multiplet energies by the Hartree-Fock-Slater method. *Theor. Chem. Acc.* **43(3)**:261-271.

[44] **Laundau, L. and Lifshitz, E. M.** 1977. *Quantum mechanics: volume 3* (Butterworth-Heinemann).

[45] **Worth, G. and Cederbaum, L. S.** 2004. Beyond Born-Oppenheimer: molecular dynamics through a conical intersection. *Annu. Rev. Phys. Chem.* **55**:127-158.

[46] **Hansen, J. P., McDonald, I. R.** 1981. Microscopic simulation of a strongly coupled hydrogen plasma. *Phys. Rev. A.* **23(4)**:2041-2059.

[47] **Boal, D. H., Glosli, J. N.** 1988. Quasiparticle model for nuclear dynamics studies: ground-state properties. *Phys. Rev. C.* **38(4)**:1870-1878.

[48] **Boal, D. H., Glosli, J. N.** 1988. Quasiparticle model for nuclear reaction studies: quasiparticle dynamics. *Phys. Rev. C.* **38(6)**:2621-2629.

[49] **Feldmeier, H., Schnack, J.** 2000. Molecular dynamics for fermions. *Rev. Mod. Phys.* **72(3)**:655-688.

[50] **Maruyama, T., Ohnishi, A., Horiuchi, H.** 1992. Evolution of reaction mechanisms in the light heavy-ion system. *Phys. Rev. C.* **45(5)**:2355-2368.

[51] **Beck, W. A., Wilets, L.** 1997. Semiclassical description of proton stopping by atomic and molecular targets. *Phys. Rev. A.* **55(4)**:2821-2829.

[52] **Frost, A. A.** 1967. Floating spherical gaussian orbital model of molecular structure. I. Computational procedure. LiH as an example. *J. Chem. Phys.* **47**:3707-3713.

Chapter 2

Development of an electron force field. I. Low Z atoms and hydrocarbons, and matter at extreme conditions

Introduction

Many methods exist to compute the large scale dynamics of systems in their electronic ground state, such as conventional [1] and reactive force fields [2], and *ab initio* molecular dynamics [3]. However, we often wish to compute the large scale excited electron dynamics of systems with energies hundreds of electron volts above the ground state, where a multitude of adiabatic states exist, and where condensed materials can coexist with plasmas or highly excited electrons. Few existing methods are fast, accurate, and general enough to satisfy this need.

We introduce an electron force field (eFF) that with only three universal parameters can compute the excited electron dynamics of systems containing hydrogen, helium, lithium, beryllium, boron, and carbon. In our model, nuclei are represented by point charges and electrons by spherical Gaussian wave packets with variable position and extent. Geometries are reproduced well, and energies are calculated with sufficient accuracy so that we can simulate the excited electron dynamics of matter at extreme conditions. We use as examples the temperature dissociation and ionization of high-pressure deuterium, and the Auger fragmentation of hydrocarbons induced by removal of core electrons.

The use of sums of Gaussians to approximate wavefunctions needs no introduction, as Gaussians are prominent in practically every modern *ab initio* method today [4], due to the simplicity of computing integrals of said functions. The use of *single* Gaussian wave packets to represent quantum particles may be less familiar to the reader, and the promise that such a drastic approximation might yield quantitatively accurate quantum dynamics of nuclei, nucleons, or even electrons has motivated research on this topic for the last several decades.

In 1975, Heller [5] demonstrated that the equations of motion for "thawed" Gaussian wave packets in locally harmonic potentials had a particularly simple form, and used them to compute the quantum dynamics of colinear $He + H_2$. He later pioneered use of time-dependent methods to obtain spectroscopic data, for example computing the photodissociation cross-section of methyl iodide [6], and the three-dimensional photodissociation dynamics of ICN [7]. In these cases, the quantum particles were nuclei moving in a parameterized potential where electrons were considered only implicitly.

Computing explicit interactions of indistinguishable fermions such as nucleons or electrons is more difficult than computing interactions between nuclei, because the overall electronic wavefunction must satisfy an antisymmetry principle, which specifies that interchanging any two fermions causes the sign of the wavefunction to change. The simplest function that satisfies this requirement is the antisymmetric sum of N! product wavefunctions; if we assume pairwise electrostatic interactions, evaluating the energy of such a wavefunction requires N^4 operations. In contrast, computing the energy of a Hartree product wavefunction, which does not satisfy the Pauli principle, requires at most N^2 operations (N^2 for electrostatics, and N for kinetic energy).

For practical molecular dynamics, we would like energy evaluation to have better scaling than N^4, which leads to two questions:

1. Given N electrons represented by single Gaussian functions, if we take the wavefunction to be the fully antisymmetrized combination of these functions, with the known N^4 cost for energy evaluation, do we get a reasonably correct

description of molecules?

2. We define the antisymmetrization energy or Pauli energy as the difference in energies of an antisymmetrized wavefunction (which satisfies the Pauli principle) and a product wavefunction (which does not). Can we approximate this energy with an expression that is faster to evaluate than N^4?

The first question was answered by Frost [8] in 1964, with his development of the floating spherical gaussian orbital method (FSGO). In FSGO, the wavefunction is an antisymmetized set of floating Gaussian orbitals $\phi_i = \exp(\alpha_i |r - x_i|^2)$. The energy is simply the combined kinetic and electrostatic energy of this wavefunction; since no adjustable parameters are used, the method is considered fully *ab initio*. Despite the simplicity of the basis functions, Frost found good geometries for molecules like lithium hydride, beryllium dihydride, first and second row hydrides, and hydrocarbons. He concluded that single floating Gaussians have a variational flexibility comparable to larger sums of nuclear-centered fixed-size Gaussians of the sort used in traditional *ab initio* calculations.

The second question was answered in the late 70s and over the next two decades with the development of Pauli potentials by Wilets et al. [9], Kirschbaum and Wilets [10], Hansen and McDonald [11], Dorso et al. [12, 13], Boal and Glosli [14, 15], and Klakow et al. [16], which approximated the antisymmetrization energy with an N^2 pairwise sum between electrons. Typically these potentials exclude some region in position-momentum phase space, so that electrons are well-separated in position and momentum over a wide range of conditions [17]. These potentials have been used to study nuclear collisions and reactions [18], proton stopping by molecular targets [19], as well as hydrogen plasma dissociation and ionization [16, 20].

However, it has been difficult to find a Pauli potential that is accurate enough to keep molecules with larger Z atoms stable, let alone have correct energies and geometries. The most accurate Pauli potential to date, used by Klakow [16] to describe hydrogen plasma, can compute the interaction between electrons of different

sizes — essential for capturing changes in bonding during chemical reactions — yet it causes lithium hydride to be unbound and the valence electrons of alkanes to collapse onto their cores. Kirschbaum's potential [10] has been applied to create stable atoms with Z up to 94 [21] which have a shell structure, but the potential does not describe the structure of valence shells with enough accuracy to form reasonable bonds between atoms.

There is a need for a Pauli potential with improved accuracy for molecular systems. In the current work, we have developed a Pauli potential that scales as N^2 and is applicable to a large range of molecules, including hydrocarbons, which makes it possible to study the excited dynamics interactions of many kinds of bonds — covalent, ionic, multicenter — in many phases of matter — solid, liquid, gas, plasma. In addition to computing the excited state dynamics of high-energy systems, we have validated eFF against a range of simple ground state molecules, with an aim towards highlighting its strengths and particularly its weaknesses, so that it may be improved further in the future.

Although the current eFF contains only one parameterized term — the Pauli potential — we call it a force field because we expect that future improvements will hinge on adding physically motivated terms describing more subtle interactions between electrons and nuclei. Such a force field may open the door to truly practical quantum dynamics on large scale atomic and molecular systems.

The chapter is organized as follows: first we discuss the energy expressions of eFF, show how both hydrogen atom and hydrogen molecule are stable, and give a motivation for our form of the Pauli potential. Then we test how well eFF describes ground state systems, with particular attention to the conformers of hydrocarbons, and the effects of breaking hydrocarbon bonds. We also test systems that include lithium, beryllium, and boron; these contain ionic and/or electron-deficient multicenter bonds, and eFF describes them reasonably well. Having validated eFF against ground state systems, we discuss its application to matter at extreme conditions, using as examples the dissociation and ionization of warm dense hydrogen, and the dynamics of the Auger process in hydrocarbons.

General theory of the eFF

Energy expression

We begin with point nuclei with coordinates $\mathbf{R}$ and momenta $\mathbf{P}$, and electrons defined by spherical Gaussian wave packets with positions $\mathbf{x}$, translational momenta $\mathbf{p_x}$, sizes s, and radial momenta p_s:

$$\Psi \propto \prod_j \exp\left[-\left(\frac{1}{s^2} - \frac{2p_s}{s}i\right)(\mathbf{r} - \mathbf{x})^2\right] \cdot \exp[i\mathbf{p_x} \cdot \mathbf{x}]. \qquad (2.1)$$

Then the overall energy is a sum of the Hartree product kinetic energy, Hartree product electrostatic energy, and antisymmetrization (Pauli) energy:

$$E = E_{ke} + E_{nuc \cdot nuc} + E_{nuc \cdot elec} + E_{elec \cdot elec} + E_{Pauli}$$

which can be broken down further as follows:

$$
\begin{aligned}
E_{ke} &= \frac{1}{2}\sum_i \int |\nabla\psi_i|^2 \, dV = \sum_i \frac{3}{2}\frac{1}{s_i^2} \\
E_{nuc \cdot nuc} &= \sum_{i<j} \frac{Z_i Z_j}{R_{ij}} \\
E_{nuc \cdot elec} &= -\sum_{i,j} Z_i \int \frac{|\psi_j|^2}{R_{ij}} \, dV = -\sum_{i,j} \frac{Z_i}{R_{ij}} \, \mathrm{Erf}\left(\frac{\sqrt{2}\,R_{ij}}{s_i}\right) \\
E_{elec \cdot elec} &= \sum_{i<j} \int \frac{|\psi_i|^2|\psi_j|^2}{x_{ij}} \, dV = \sum_{i<j} \frac{1}{x_{ij}} \, \mathrm{Erf}\left(\frac{\sqrt{2}\,x_{ij}}{\sqrt{s_i^2 + s_j^2}}\right) \\
E_{Pauli} &= \sum_{\sigma_i = \sigma_j} E(\uparrow\uparrow)_{ij} + \sum_{\sigma_i \neq \sigma_j} E(\uparrow\downarrow)_{ij}
\end{aligned}
$$

where $E(\uparrow\uparrow)$ and $E(\uparrow\downarrow)$ are the Pauli potential functions:

$$
\begin{aligned}
E(\uparrow\uparrow)_{ij} &= \left(\frac{S_{ij}^2}{1 - S_{ij}^2} + (1-\rho)\frac{S_{ij}^2}{1 + S_{ij}^2}\right)\Delta T_{ij} \\
E(\uparrow\downarrow)_{ij} &= \frac{\rho S_{ij}^2}{1 + S_{ij}^2}\Delta T_{ij}
\end{aligned}
$$

where ΔT is a measure of the kinetic energy change upon antisymmetrization, and S is the overlap between two wave packets:

$$\Delta T_{ij} = \frac{3}{2}\left(\frac{1}{\bar{s}_1^2} + \frac{1}{\bar{s}_2^2}\right) - \frac{2(3(\bar{s}_1^2 + \bar{s}_2^2) - 2\bar{x}_{12}^2)}{(\bar{s}_1^2 + \bar{s}_2^2)^2}$$

$$S_{ij} = \left(\frac{2}{\bar{s}_i/\bar{s}_j + \bar{s}_j/\bar{s}_i}\right)^{3/2}\exp(-\bar{x}_{ij}^2/(\bar{s}_i^2 + \bar{s}_j^2))$$

where $\rho = -0.2$, $\bar{x}_{ij} = x_{ij} \cdot 1.125$, and $\bar{s}_i = s_i \cdot 0.9$. We will explain the motivation for the Pauli expression, and the consequences of the combined energy terms in more detail below.

Bonding comes from balancing kinetic energy and electrostatics

A Gaussian wave packet automatically satisfies the Heisenbserg uncertainty principle by virtue of its functional form — in fact, it is a minimum uncertainty wave packet. That leaves as a free parameter the size of the wave packet, which is propagated using the equation of motion

$$\frac{3m}{4}\ddot{s}(t) = -\frac{\partial E}{\partial s} = -\frac{\partial}{\partial s}\left(\frac{3}{2}\frac{1}{s^2} + V(s)\right) \tag{2.2}$$

The electron size is optimized when the sum of kinetic and potential energy reaches a minimum with respect to variation in s. We see that even an electron whose size and position is stationary has a kinetic energy that varies inversely as the square of its width. This relation may be seen as a consequence of Heisenberg's principle (better localized electrons have a higher momentum spread, and hence kinetic energy) or of the fact that the kinetic energy is $\int|\nabla\phi|^2 dV \propto (1/s)^2$.

Consider the case of a hydrogen atom, where the potential energy given by the electrostatic interaction of the electron and nucleus varies as $-1/s$. More precisely,

$$E = \frac{3}{2}\frac{1}{s^2} - \sqrt{\frac{8}{\pi}}\frac{1}{s}.$$

The electrostatic potential attempts to squeeze the electron into a point on top

of the nucleus, while the kinetic energy term prevents this collapse. The balance of the two radial forces creates an atom with a stationary size of $s = 1.88$ bohr, and $E = -4/3\pi = -0.424$ hartree. The energy is above the variational limit $E = -0.5$ hartree because the single Gaussian does not have the correct cusp at the nucleus center, or the correct long range drop off; however, it is expected that energy differences in bonding will be more accurately described.

The same logic can be used to explain the stability of the two electron covalent bond. In the eFF description of ground state hydrogen molecule, two electrons lie at the midpoint between two protons. The electrons shrink to interact more strongly with the protons (s = 1.77 bohr versus 1.88 bohr in the atoms), and the decreased potential energy of having each electron interact with two protons drives the formation of the bond (Figure 2.1).
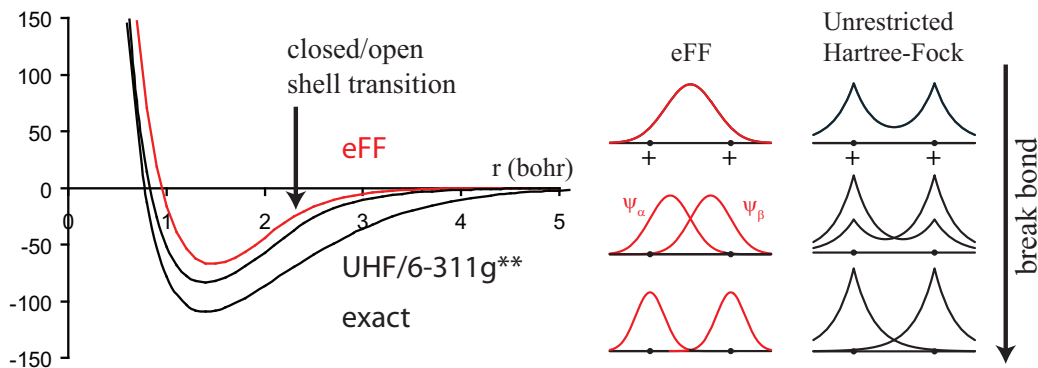
Figure 2.1: H_2 potential energy surface (kcal/mol); eFF properly dissociates H_2, but the simplicity of the basis leads to underbinding.

Pulling the protons apart causes the electrons to interact with the protons less strongly, and the bond weakens. As the bond length is increased past 2.1 bohr, it becomes more favorable for the electrons to become atom-centered. The energy varies smoothly as each electron associates with one proton, and the wavefunction goes from a closed shell to an open shell description. In Hartree-Fock theory, the analogous transition between RHF and UHF occurs at 2.3 bohr. The eFF bond energy is found to be 67 kcal/mol at a bond length of 0.780 bohr (versus 104 kcal/mol exact at 0.741 bohr).

There are some features missing from the eFF picture. First, in the true H_2 molecule, the electron density is a doubly peaked function that reaches a maximum at the sites of the protons. Because the single Gaussian wavefunction cannot become multiply peaked, the bond energy is underestimated. Second, there is a measure of static correlation that is missing; in dissociating H_2, there is a resonance stabilization between having the spin up electron on the right and the spin down electron on the left, and vice versa. This neglect makes the energy fall to zero too quickly. Finally, dynamic correlation is missing; electron-electron repulsion should be diminished when two electrons are placed in the same orbital, as they have a tendency to avoid each other. This correlation effect stabilizes H_2 molecule relative to H atoms, and its neglect contributes to the H_2 underbinding.

Issues of underbinding aside, it remains remarkable that a floating Gaussian description of electrons can give a potential energy curve for hydrogen molecule dissociation that has a plausible inner wall, bonding region, long range tail, and a correct transition between closed and open shell wavefunctions.

Pauli principle causes same spin electrons to repel; a parameterization

Consider localized electrons in a solid. One way to interpret the Pauli principle's effect is to imagine that the electrons have finite extent and are prevented from intersecting each other, like hard spheres. Compressing the solid causes the electrons to squeeze together and shrink, increasing their kinetic energy. This increase in kinetic energy manifests itself in a force resisting compression of the solid. This repulsive force is the dominant interaction between neutral molecules at short range — it is the basis of the steric effect in chemistry, it prevents stars from collapsing, and prevents the reader from falling through the earth.

Electrons do not have finite extent, of course, and even same spin electrons can interpenetrate each other. A more rigorous way to understand the origin of Pauli repulsion, outlined by Wilson and Goddard [22], is to compare the kinetic energy of an antisymmetrized product wavefunction with that of a Hartree product. In a Hartree product, the kinetic energy of the wavefunction is the sum of the orbital

kinetic energies. In an antisymmetrized product, the kinetic energy is the sum of *orthogonalized* orbital kinetic energies; this mathematical simplification is the reason theorists often work in a basis of orthogonal molecular orbitals. Hence we can approximate the Pauli energy as the kinetic energy difference between orthogonalized versus non-orthogonalized orbitals.
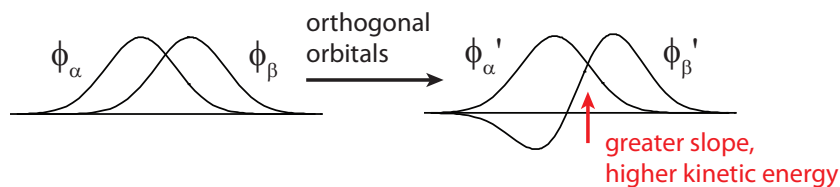
Figure 2.2: Pauli repulsion comes from the kinetic energy increase upon making orbitals orthogonal to each other.

As Figure 2.2 shows, when two same spin electrons intersect in space, their orthogonalized orbitals take on larger slopes to keep their overlap zero. The increase in slope causes an increase in kinetic energy, which causes a large portion of the Pauli repulsion.

In deriving our Pauli potential, we make two assumptions: (1) we can approximate the Pauli energy as a sum over pairs of electrons, and (2) we can assume that the Pauli energy between pairs of electrons is dominated by the kinetic energy change upon forming an antisymmetric wavefunction. This neglects two effects: first, the mutual exclusion of more than two electrons at a time, which may become important when the electron density is high; and second, the fact that electrons, once orthogonalized, may have different electrostatic interactions with each other and with nuclei, which may become important for electrons near nuclei.

Kinetic energy difference-based Pauli potentials have been obtained and used by Boal and Glosli [14], who considered the case of same size nucleons; and by Klakow [16], who considered the more general case of Pauli repulsion between different size electrons. The form of the potentials bear some resemblance to earlier Pauli potentials [9, 12] that decay as e^{-ax^n}, where x is the distance between electron centers and a and n are arbitrary parameters.

Consider the Slater and Hartree wavefunctions for two same spin electrons:

$$
\begin{aligned}
\Psi_{\text{Slater}} &= \frac{1}{\sqrt{2 - 2S^2}}(\phi_1(r_1)\,\phi_2(r_2) - \phi_2(r_1)\phi_1(r_2)) \\
\Psi_{\text{Hartree}} &= \phi_1(r_1)\,\phi_2(r_2)
\end{aligned}
$$

where the factor containing $S = \int \phi_1\phi_j \, dV$ ensures that the wavefunction is normalized. Then we estimate the Pauli energy between wavefunctions ϕ_1 and ϕ_2 as

$$
\begin{aligned}
E_u &= \langle \Psi_{\text{Slater}} | -\frac{1}{2}\nabla^2 | \Psi_{\text{Slater}} \rangle - \langle \Psi_{\text{Hartree}} | -\frac{1}{2}\nabla^2 | \Psi_{\text{Hartree}} \rangle && (2.3) \\
&= \frac{S^2}{1 - S^2}\left(t_{11} + t_{22} - \frac{2t_{12}}{S}\right) && (2.4)
\end{aligned}
$$

where $t_{ij} = \langle \psi_i | -\frac{1}{2}\nabla^2 | \psi_j \rangle$ (detailed derivation given in Appendix A).

Klakow used $E(\uparrow\uparrow) = E_u$ and $E(\uparrow\downarrow) = 0$; to get our expression, we make use of the reference valence-bond wavefunction

$$
\Psi_{\text{VB}} = \frac{1}{\sqrt{2 + 2S^2}}(\phi_1(r_1)\,\phi_2(r_2) + \phi_2(r_1)\phi_1(r_2)). \qquad (2.5)
$$

Then we compute

$$
\begin{aligned}
E_g &= \langle \Psi_{\text{VB}} | -\frac{1}{2}\nabla^2 | \Psi_{\text{VB}} \rangle - \langle \Psi_{\text{Hartree}} | -\frac{1}{2}\nabla^2 | \Psi_{\text{Hartree}} \rangle && (2.6) \\
&= \frac{S^2}{1 + S^2}\left(t_{11} + t_{22} - \frac{2t_{12}}{S}\right) && (2.7)
\end{aligned}
$$

which is a kind of a correlation energy. We mix E_g and E_u together, and scale the orbital exponents and distance between orbitals by a set of fixed and universal parameters: $\alpha = \alpha_{actual}/0.9$, $r = r_{actual} * 1.125$. Finally we calculate the functions:

$$
\begin{aligned}
E(\uparrow\uparrow) &= E_u - (1 - \rho)E_g \\
E(\uparrow\downarrow) &= -\rho E_g.
\end{aligned}
$$

The universal parameter ρ and the scaling factors were adjusted to produce correct

geometries for a range of test structures. Figure 2.3 shows that the effect of the E_g term is to make the Pauli potential between both opposite and same spin electrons more repulsive; this reduces the known tendency for floating orbitals to coalesce into each other and become linearly dependent.
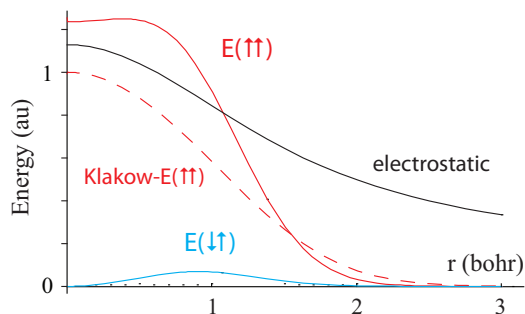
Figure 2.3: Comparison of Pauli repulsion and electrostatic repulsion between two wavefunctions with $s = 1$.

Validation against ground state systems

Tetrahedral carbon forms bonds to other carbons and hydrogen

Optimizing atoms and molecules with eFF, we observe that (1) opposite spin electrons pair, (2) for atoms larger than helium, electrons separate into core electrons that are nucleus centered and valence electrons that are larger than the core electrons, and (3) valence electrons pack like hard spheres, with a maximum of four electron pairs around each core ("octet rule"). It is apparent that the basic rules of Lewis bonding and hybridization arise as a natural result of balancing kinetic energy, electrostatic potential, and Pauli repulsion.

When carbon has a full octet of electrons, they arrange themselves into a tetrahedral sp^3 packing. Methane is stable, and its valence electrons are centered at ~80% of the distance from the core center to the proton, reflecting the greater electronegativity of carbon over hydrogen (Table 2.1, Figure 2.4).

	$d_{CC}(\text{Å})$		$d_{CH}(\text{Å})$		angle (degrees)	
	eFF	exact	eFF	exact	eFF	exact
CH_4			1.143	1.094	109.5	109.5
$CH_3(CH_3)$	1.501	1.536	1.173	1.091	110.8	110.9
$CH_2(CH_2)_2$	1.513	1.526	**1.229**	1.096	107.9	109.5
$CH(CH_3)_3$	1.529	1.525	**1.424**	1.108	**101.8**	109.4
$C(CH_3)_4$	1.573	1.534				

Table 2.1: Geometries of primary, secondary, and tertiary-substituted carbon
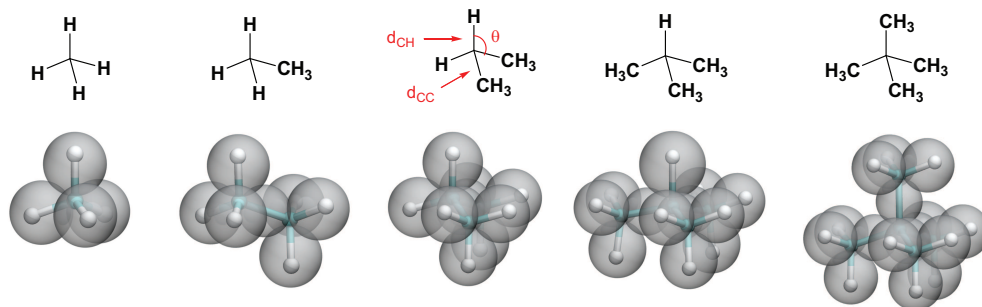
Figure 2.4: eFF geometries of simple substituted hydrocarbons

Ethane is stable as well, with sigma-bond electrons centered at the bond midpoint, as required by symmetry. The C-C bonding electrons do not overlap significantly with the nucleus, unlike the bonding electrons in H_2 This difference is due to the Pauli repulsion between the sigma electrons and the $1s^2$ cores of the carbons in ethane; protons do not have such $1s^2$ cores. Thus carbon-carbon bonds are longer than either carbon-hydrogen or hydrogen-hydrogen bonds. The Pauli function parameters were adjusted so that the carbon-hydrogen and carbon-carbon bond lengths of methane and ethane were close to known values [23].

In eFF, carbon-carbon bonds have slightly smaller electrons than carbon-hydrogen bonds, which causes them to repel each other more strongly than they should. This imbalance causes distortions away from an ideal tetrahedral geometry in secondary and tertiary carbons; for example, isobutane has a too-small HCC angle (101.8º instead of 109.4º exact), and a too-long carbon-hydrogen bond length (1.424 Å vs 1.108 Å).

Carbon-hydrogen bonds have lengths in eFF that are too variable, but we will

see later that their dissociation energies are less variable than their distance varia-
tion would suggest. Also, the carbon-carbon bond lengths are relatively fixed with
respect to different substitution, as they should be. These observations suggest we
would do well to focus on geometries with a core carbon skeleton and outwardly
oriented hydrogens, where too-long C-H bonds would not clash.

Many organic molecules of interest, as well as bulk and surface diamond, fall
into this category. Figure 2.5 shows that eFF can describe a variety of bridged,
fused-cyclic, and strained carbon skeletons, with largely correct carbon-carbon
distances. The worst discrepancies in bond distances involve quaternary carbons
in compounds like ^{t}Bu $-^{t}$ Bu (1.708 Å vs 1.592 Å exact) and diamond (1.681 Å vs
1.545 Å exact).
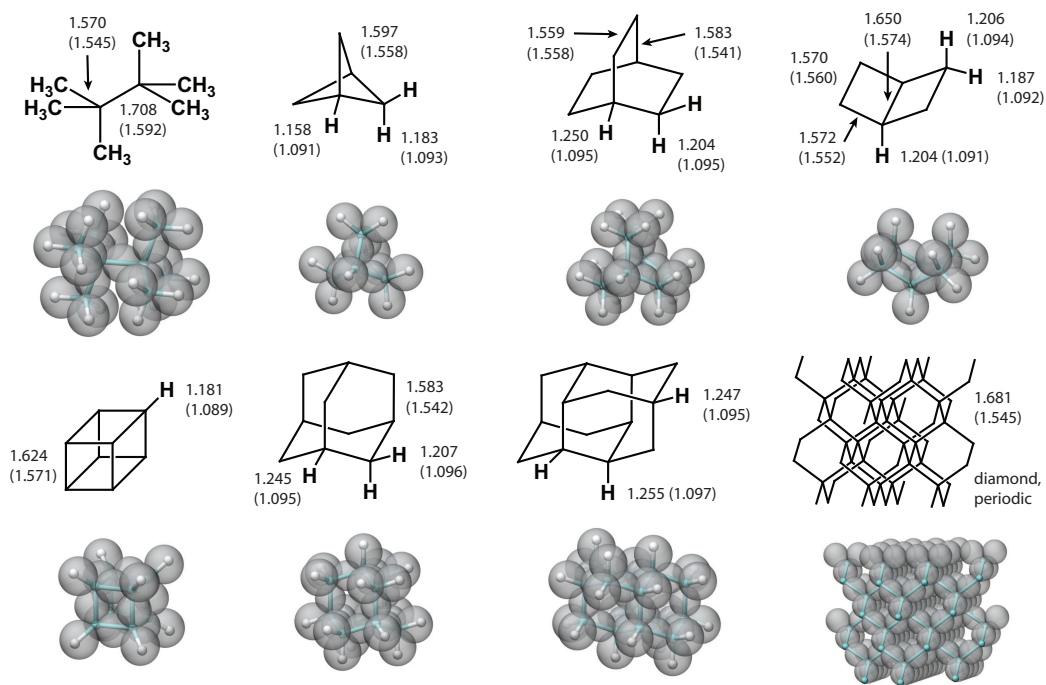
Figure 2.5: eFF geometries of larger hydrocarbons, bond lengths in Angstroms

Carbon forms multiple bonds, with a preference for $\sigma - \pi$ bonding

When two electron pairs are squeezed into the space between the carbon nuclei
of ethylene, they may avoid each other either by moving apart above and below

the plane of the to form "banana bonds"; or by having one electron form a node and become a pi bond that is orthogonal to the other electron pair, which forms a sigma bond. In the Hartree-Fock description, which operates on a basis of orthgonalized orbitals, the two pictures are equivalent, since they can be related to each other by a unitary transformation. Valence bond calculations performed without an orthogonalization constraint show similarly that the two models are nearly identical, with a slight preference toward banana bonding in ethylene (6.5 kcal/mol difference).

It is reasonable to expect that our force field would prefer banana bonding, since no provision has been made for electrons to attain p character. In the FSGO method, this lack of p functions has dire consequences [24]: electrons in multiple bonds coalesce into the same function, which in theory provides a p-like electron in the limit of infinitesimal separation, but in practice causes linear dependency problems, and makes the barrier to rotation of the ethylene pi bond negligible.

We find that contrary to expectation, our force field prefers a $\sigma - \pi$ mode of bonding, but does so in a curious way: a sigma electron pair sits in between the carbons, then the electrons of the other electron pair split, so that an electron of one spin goes above the plane, and an electron of the other spin goes below the plane (Figure 2.6). This spin-polarized bond creates a diffuse effective p function; this mode of sigma-pi bonding is stabilized over equivalent banana bonding in eFF by 160 kcal/mol (Table 2.2).
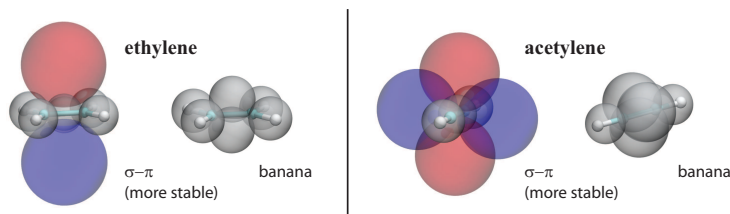
Figure 2.6: Multiple bonds can split $\sigma - \pi$ or form symmetric "banana" pairs.

Triple bonds display a similar preference (183 kcal/mol) for $\sigma - \pi_x - \pi_y$ bonding

		ethylene	acetylene
Banana vs. $\sigma\pi$ energy (kcal/mol) (minus means banana preferred)		-160.5	-183.4
Hydrogenation energy (kcal/mol)	eff-$\sigma\pi$	-141.6	-406.9
	exact	-32.6	-41.7
CC bond length ($\mathring{A}$)	eff-$\sigma\pi$	1.517	1.383
	eff-banana	1.442	1.334
	exact	1.339	1.203
CH bond length ($\mathring{A}$)	eff-$\sigma\pi$	1.089	1.052
	eff-banana	1.125	1.064
	exact	1.086	1.063

Table 2.2: Energetics and geometries of double and triple bonds

over banana bonding where the bonding electron pairs arrange themselves into a triangle normal to the bond.

However, we find that eFF multiple bonds are too long (1.517 Å double bond versus 1.339 Å exact), too unstable (as shown from the hydrogenation energies), and too diffuse in the region above and below the plane, which can cause inappropriate steric clashes with molecular elements lying above and below pi bonds. The weakness of multiple bonds stands in contrast to strength of sigma bonds in eFF, which as we will see in later sections bind overly strongly (163.5 kcal/mol versus 89.7 kcal/mol exact).

It is promising that banana bonds show some stability, as well as a more reasonable length (1.442 Å double bond) within our scheme, and do not coalesce. It may be preferrable in future versions of eFF to construct the potentials so that banana bonds are more stable than $\sigma - \pi$ bonds. It would be elegant if the same Pauli repulsion that separates valence electrons and gives carbon-carbon single bonds the correct length could also separate electrons in multiple bonds and give them the correct length and energy. In the meantime, we limit our applications to those involving saturated hydrocarbons.

Conformational analysis of hydrocarbon geometries

We have demonstrated that eFF obtains correct ground state geometries for the simple hydrocarbons of Figure 2.4 and the constrained hydrocarbons of Figure 2.5. We ask now whether eFF can differentiate between multiple conformers of the same hydrocarbon. This is a tricky task, since we must now (1) have the correct energetics of bending valence electrons away from a tetrahedral arrangement, and (2) accurately describe the magnitude of steric repulsions between electrons on different atoms. In traditional force fields, these interactions are handled via separate angle, dihedral, and noncovalent interaction terms, but in eFF they should arise out of a proper consideration of electrostatics and the Pauli principle.

We start by looking at the cyclic hydrocarbons cyclopropane, cyclobutane, cyclopentane, and cyclohexane (Figure 2.7). The bonding in cyclopropane is known to involve curved bonds, a compromise between the geometrical requirements of the molecule and the hybridization of orbitals on carbon. In eFF, we see that the bonding electrons lie outside the perimeter of a line drawn connecting the carbons, with an angle between bonding electrons of 98°; valence bond calculations [25] show similarly curved bonds with an interorbital angle of 110°. Curved bonds appear naturally in eFF as a consequence of the repulsion between the three carbon-carbon bonding electron pairs.

Continuing on to larger rings, it is known that cyclobutane and cyclopentane attempt to make carbon tetrahedral, but instead of forming curved bonds like cyclopropane, they "pucker" so that the nuclei do not all lie in the same plane. Our force field reproduces this pucker in cyclopentane (dihedral 21.5° versus 33.2° B3LYP/6-311g**), but not in cyclobutane (dihedral 0.3° versus 18.0° B3LYP). In cyclobutane the difference in energy between puckered and planar conformations is known to be small (~1.5 kcal/mol B3LYP), making the electron force field's error reasonable.

In cyclohexane, there are two conformers — chair and twist-boat — with a more significant energy difference of 6.3 kcal/mol (B3LYP, Figure 3.5). We obtain with eFF an energy difference of 4.7 kcal/mol and dihedral angles that compare well
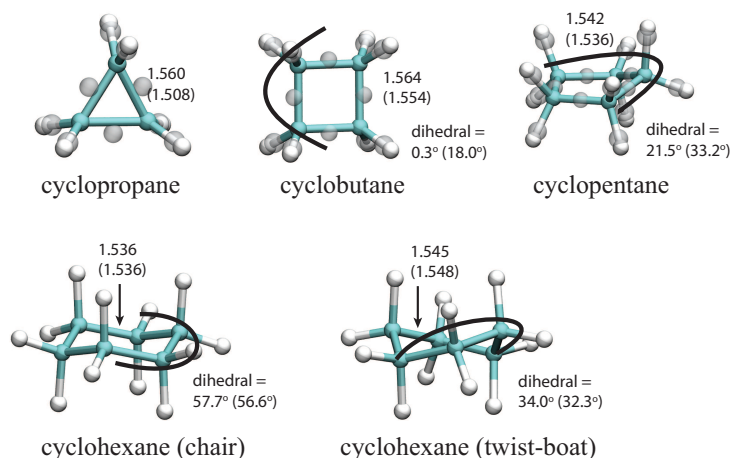
Figure 2.7: eFF reproduces curved bonds of cyclopropane, and pucker of five and six membered rings.

to known values (57.7º versus 56.6º B3LYP for the chair, and 34.0^o versus 32.3^o B3LYP for the twist-boat). The agreement of cyclohexane energies and geometries with B3LYP values is remarkable, considering that it involves a balance between the barrier of twisting about each carbon-carbon bond, and the steric repulsion between axial hydrogens. To test whether it is a fortuitous agreement, or the sum of reliable quantities, we examine the conformational preferences of some simpler systems (Figure 2.8).

system	energy of	relative to	ΔE (kcal/mol)	
			eFF	exact
ethane	eclipsed	staggered	2.1	2.7
butane	gauche	trans	1.6*	0.9
cyclohexane	twist-boat	chair	4.7	6.3
1,3-dimethyl-cyclohexane	ax-ax	eq-eq	5.8	5.9
	ax-eq	eq-eq	2.7	2.1
decalin	cis	trans	12.1	3.2
2-pentene	major	minor	5.5	4.6

Table 2.3: Energy differences between conformers examined. *Gauche butane is not a local minimum, and is constrained at 60º.

In ethane, we find the energy difference between eclipsed and staggered con-
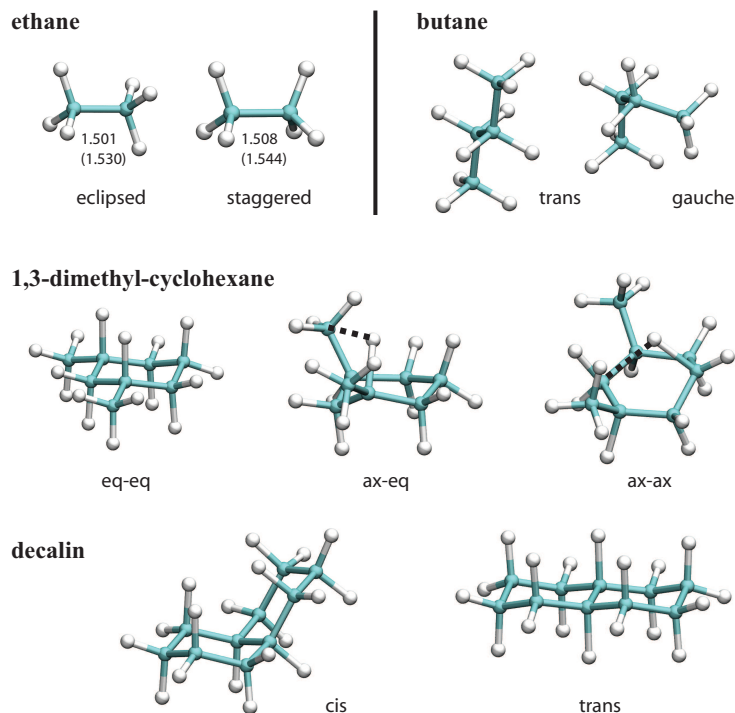
Figure 2.8: eFF reproduces steric repulsions within alkanes

formations — known to be a consequence of Pauli repulsion between C-H bond electrons — to be slightly low (2.1 versus 2.7 kcal/mol B3LYP). In butane, we find the difference between *gauche* and *trans* forms, which arises from the repulsion between methyl groups, to be slightly high (1.6 versus 0.9 kcal/mol B3LYP). This difference is not surprising given our previous observation that carbon-carbon bonds repel carbon-hydrogen bonds more than they should. The combination of high methyl-methyl repulsions and low barriers for hydrogen eclipsing causes *gauche* butane to not be a local minimum structure, but to optimize directly to *trans* butane; the energy difference given is for a fixed dihedral angle of 60°.

In substituted cyclohexanes, axial substituents can become equatorial and vice versa through a chair flip. The stability of a cyclohexane conformer is particularly affected by repulsions between axial substituents, since they are close to each other (2.66 Å B3LYP) and oriented in the same direction. To quantify the magnitude of these 1,3-diaxial interactions, we consider the relative energetics of axial-axial,

axial-equatorial, and equatorial-equatorial 1,3-dimethylcyclohexane. The axial-equatorial dimethyl and axial-axial dimethyl geometries adopt an overly-twisted geometry, a consequence of the overly large repulsion between axial methyl and axial hydrogen. Nonetheless — and this should be viewed as an accident — the energy differences between these conformers closely matches the exact values (5.8 versus 5.9 kcal/mol B3LYP, and 2.7 versus 2.1 kcal/mol B3LYP). To emphasize this point, we examine *cis* versus *trans* decalin, two hydrocarbon conformers that also differ in the number of interactions between axial substituents, but are more rigid and cannot relax so readily. In this case the energy difference is larger than the exact value (12.1 versus 3.2 kcal/mol B3LYP).

When a single bond is connected to a substituted double bond, allylic strain can restrict the rotation about the single bond [26]; this effect is used in designing reagents to perform highly selective diastereoselective enolations [27]. To compute the magnitude of allylic 1,3-strain, we consider two conformers of 2-pentene, noting that the minor form is substantially destabilized by the repulsion between methyl groups (Figure 2.9). eFF estimates the energy difference between conformers to be slightly higher than the exact value (5.5 versus 4.6 kcal/mol B3LYP). In this case, the too-high repulsion between methyl groups in eFF is balanced by the too-long double bond to give a value that agrees well with the known value.
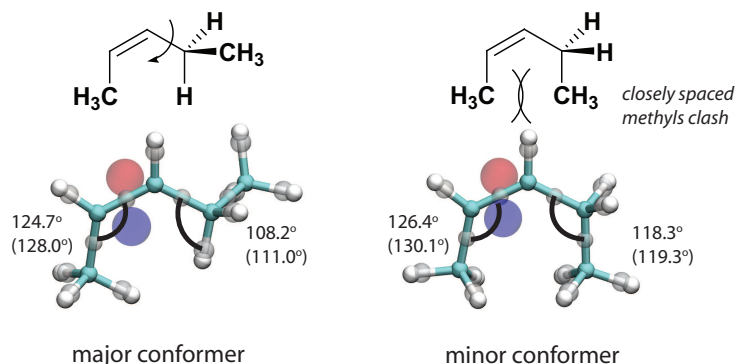
Figure 2.9: eFF reproduces allylic strain interaction

We find that the electron force field gives remarkably good estimations of the energy differences between hydrocarbon conformers. In some cases, this is due

44

to the force field parameters being balanced at a point such known biases of the force field, such as overly repulsive methyl groups, are compensated for by other biases in the force field, such as overly flexible carbon-hydrogen bonds. Overall, it is encouraging that the simple eFF functions can describe subtle conformational preferences of hydrocarbons as well as coarse properties like bond formation and atom hydridization. This is itself noteworthy, considering the number of terms and parameters in a conventional force field [1] devoted solely to the task of computing preferred bond lengths, angles, and torsions within molecules.

Methyl cation, radical, and anion

Although we have focused so far on neutral closed-shell molecules, eFF should in principle be able to optimize cationic and anionic species and radicals as well. To calculate accurate bond dissociation energies, it is especially important to have a well-balanced description of radicals and closed shell species.

Consider the series of molecules CH_3^+, CH_3 radical, and CH_3^-. Both CH_3^+ and CH_3 radical are expected to be planar and have similar bond length. Our force field reproduces bond lengths well (for CH_3^+, 1.095 Å versus 1.087 Å exact; for ·CH_3, 1.091 Å versus 1.079 Å exact).
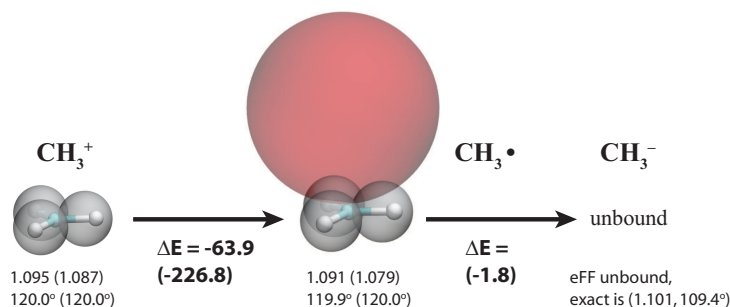
Figure 2.10: In eFF, methyl cation and radical are stable but methyl anion is unbound

eFF makes methyl radical less stable than it should be (adiabatic ionization potential is 64 kcal/mol versus 226.8 kcal/mol exact), as it is not capable of properly describing the radical electron, which should reside in a p orbital. As in the

case of multiple bonds, our force field compensates for its lack of p functions by making the radical electron very diffuse and placing it above the molecular plane.

eFF makes methyl carbanion unbound relative to methyl radical. This is not a surprising result, since in reality methyl carbanion is only marginally more stable than methyl radical (1.8 kcal/mol energy difference [28]); high-level theoretical calculations [29] (1.6 kcal/mol energy difference found) with large basis sets and correlation included are necessary to show that methyl carbanion is a stable species relative to methyl radical.

Homolytic versus heterolytic bond cleavage

We have previously discussed the energetics of breaking hydrogen molecule into hydrogen radicals. Since we have computed the energy of methyl radical and the energy of ethane, we can compute the analogous energetics of breaking ethane into two methyl radicals. We find that while the bond dissociation energy of H_2 is *underestimated* by eFF (67.2 kcal/mol versus 104.2 kcal/mol exact), the bond dissociation energy of the carbon-carbon bond in ethane is *overestimated* (163.5 kcal/mol versus 89.7 kcal/mol exact).

The error in homolytic bond dissociation energies arises from differences in how well the eFF wavefunctions represent the true electron density in the molecule, versus separated fragments. For hydrogen molecule, the true electron density is a doubly peaked atom-centered function, which eFF describes as a singly peaked bond-centered function. Hydrogen atom in contrast is represented well, because in both eFF and in the true case, the electron density has a maximum at the nucleus.

In the ethane carbon-carbon bond, the errors in basis representation take the opposite form. Carbon-carbon sigma bonds have an electron density that is concentrated in the region between the nuclei; hence the eFF bond-centered representation is a good one. In comparison, the methyl radical is poorly represented because, as we have seen in the last section, eFF does not have the proper p functions to describe the radical electron. Hence the relative error is in the opposite direction as in the H_2 case, and we find that H_2 is underbound while ethane is

overbound.

In carbon-hydrogen bonds, the basis representation errors of the molecule versus the dissociated fragments cancel, and the bond dissociation energy is near the correct values (methane 119.9 kcal/mol versus 104.8 kcal/mol exact).

eFF can describe heterolytic bond dissociation as well, where electron pairs split asymmetrically, so that one species is left with two electrons while another is left with none at all. A common example is protonation, and we find that the species HeH^+ has a bond dissociation energy near the exact value (44.1 kcal/mol versus 47.1 kcal/mol exact). This excellent agreement comes about because the electron pair of HeH^+ is mainly centered on the helium, making the singly-peaked eFF density a good approximation to the true electron density (Figure 2.11).

The protonation energy of ammonia is too high (446.0 kcal/mol versus 207.0 kcal/mol), an indicator that eFF does not currently compute the energetics of molecules containing lone pairs correctly.

		ΔE (kcal/mol)	
relative to	energy of	eFF	exact
$H - H$	$2H\cdot$	67.2	104.2
$H_3C - H$	$H_3C + H\cdot$	111.9	104.8
$(CH_3)_3C - H$	$(CH_3)_3C + H\cdot$	108.2	95.2
$H_3C - CH_3$	$2H_3C\cdot$	163.5	89.7
$(CH_3)_3C - CH_3$	$(CH_3)_3C\cdot + \cdot CH_3$	121.4	86.0
HeH^+	$He + H^+$	44.1	47.1
NH_4^+	$NH_3 + H^+$	446.0	207.0

Table 2.4: Hydrocarbon and protonated species bond dissociation energies.

Carbocation rearrangements

Once a carbocation is formed, it can rearrange its pattern of carbon-carbon and carbon-hydrogen bonding through a series of hydride and methyl shifts (Fig-
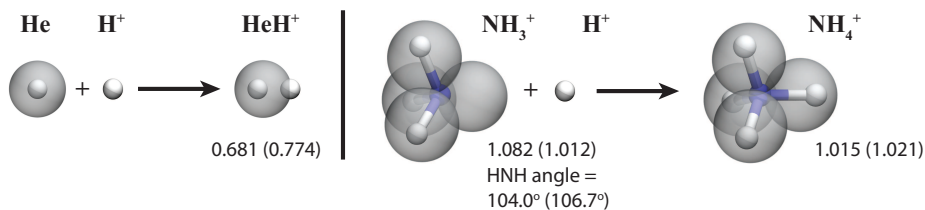
Figure 2.11: Protonation of helium and ammonia

ure 2.12). These shifts proceed via stable "bridged" intermediates that are more stable than the starting carbocation. Consider the ethyl cation $C_2H_5^+$. The bridged intermediate for a [1,2]-hydride shift has a hydride lying above the molecular plane, in between the two carbons of ethyl cation; from this intermediate, a cation can be formed on either carbon. We find that eFF overestimates the extent of the hydride, making the bonds to it too long, and the complex becomes less stable rather than more stable than the carbocation ($\Delta E = 10.1$ kcal/mol vs -8.1 kcal/mol CCSD(T) [30]).

A similar phenomenon is observed for propyl cation, where a methyl carbanion can transfer from one carbon to another in a [1,2] methyl shift. We find that eFF makes the carbanion electrons large and unstable, and the complex is uphill rather than downhill in energy ($\Delta E = 91.0$ kcal/mol vs. -14.0 kcal/mol MP4/6-311g** [31]). In propyl cation, a [1,3] hydride shift is possible as well. The carbon-hydride bond is overestimated by nearly the same amount as in the ethyl case (1.7 Å vs 1.4 Å exact), and the difference between estimated and exact energies are nearly the same as well ($\sim$18 kcal/mol in both cases).

Allowed versus forbidden reactions of hydrogen

We have validated eFF on a variety of ground state minima; now, we examine the energetics of allowed and forbidden reactions, and the transition states that connect different minima. As examples, we compute the potential energy surface of $H + H_2 \rightarrow H_2 + H$, an allowed reaction, and $H_2 + H_2' \rightarrow HH' + HH'$, a forbidden reaction (Figure 2.13).
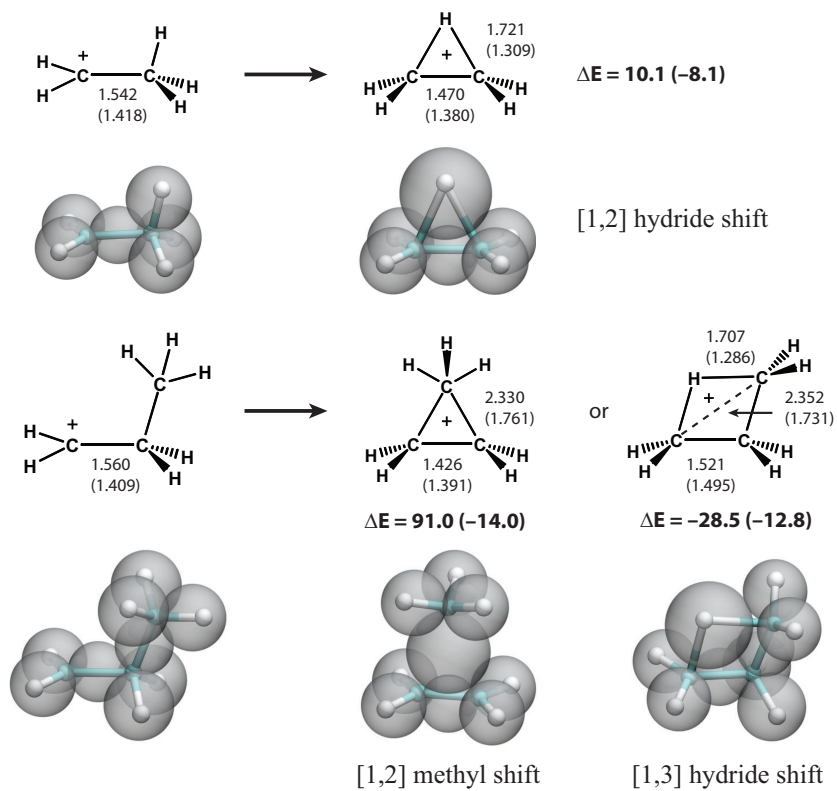
Figure 2.12: Carbocations can rearrange via hydride or methyl shifts.
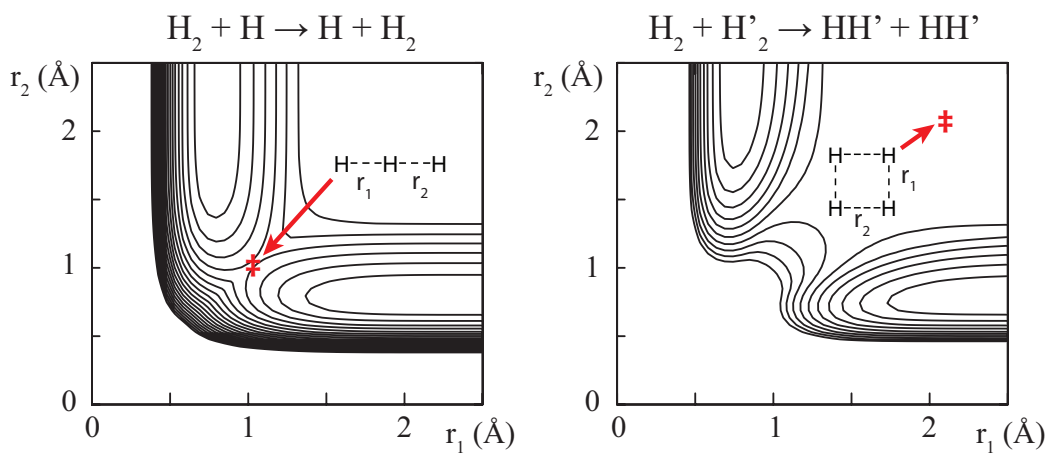
Figure 2.13: eFF distinguishes between allowed and forbidden hydrogen reactions.

For $H + H_2$, we assume that the atoms are colinear, and find a saddle point at the symmetric geometry $r_1 = r_2 = 1.04$ Å with $\Delta E = 42$ kcal/mol relative to separated $H + H_2$. In comparison, quantum Monte Carlo calculations [32] find the transition state to be at $r_1 = r_2 = 0.95$ Å with $\Delta E = 9.7$ kcal/mol. Although the transition state energy is significantly too high, it is still smaller than the H_2 dissociation energy; that together with the shape of the potential energy curve indicates that the reaction is allowed.

For $H_2 + H_2'$, we assume that the atoms are aligned in a square, and we find that there is no low energy path connecting product to reactant — both of the molecules must break simultaneously in order for the reaction to happen. The potential energy surface is rather flat, and there exists a saddle point at $r_1 = r_2 = 2.21$ Å with $\Delta E = 132$ kcal/mol relative to separated $H_2 + H_2$, which makes the reaction forbidden. To compare, we evaluated a potential for H_4 due to Boothroyd [33] derived from MRD-CI calculations over a set of symmetric square geometries, and found a saddle point at $r_1 = r_2 = 1.22$ Å with $\Delta E = 147$ kcal/mol.

Ionic and multicenter bonds

eFF can describe compounds containing the elements hydrogen, helium, and carbon; we now consider the elements that lie in between — lithium, beryllium, and boron. These early elements present us with an opportunity to observe ionic bonding, since they are electronegative, as well as electron deficient multicenter bonding, since they lack enough electrons to complete a full octet. A collection of compounds containing lithium, beryllium, boron, and carbon are shown in Figure 2.14, and their dissociation energies are given in Table 2.5.

Lithium atom adopts a clear $1s^2 2s^1$ configuration, with a valence electron much larger ($s_e = 7.45$ bohr) than the spin-paired core electrons ($s_e = 0.71$ bohr). We can form lithium hydride by combining lithium with a hydrogen atom of opposite spin. The resulting ionic compound has a bond length slightly longer than the
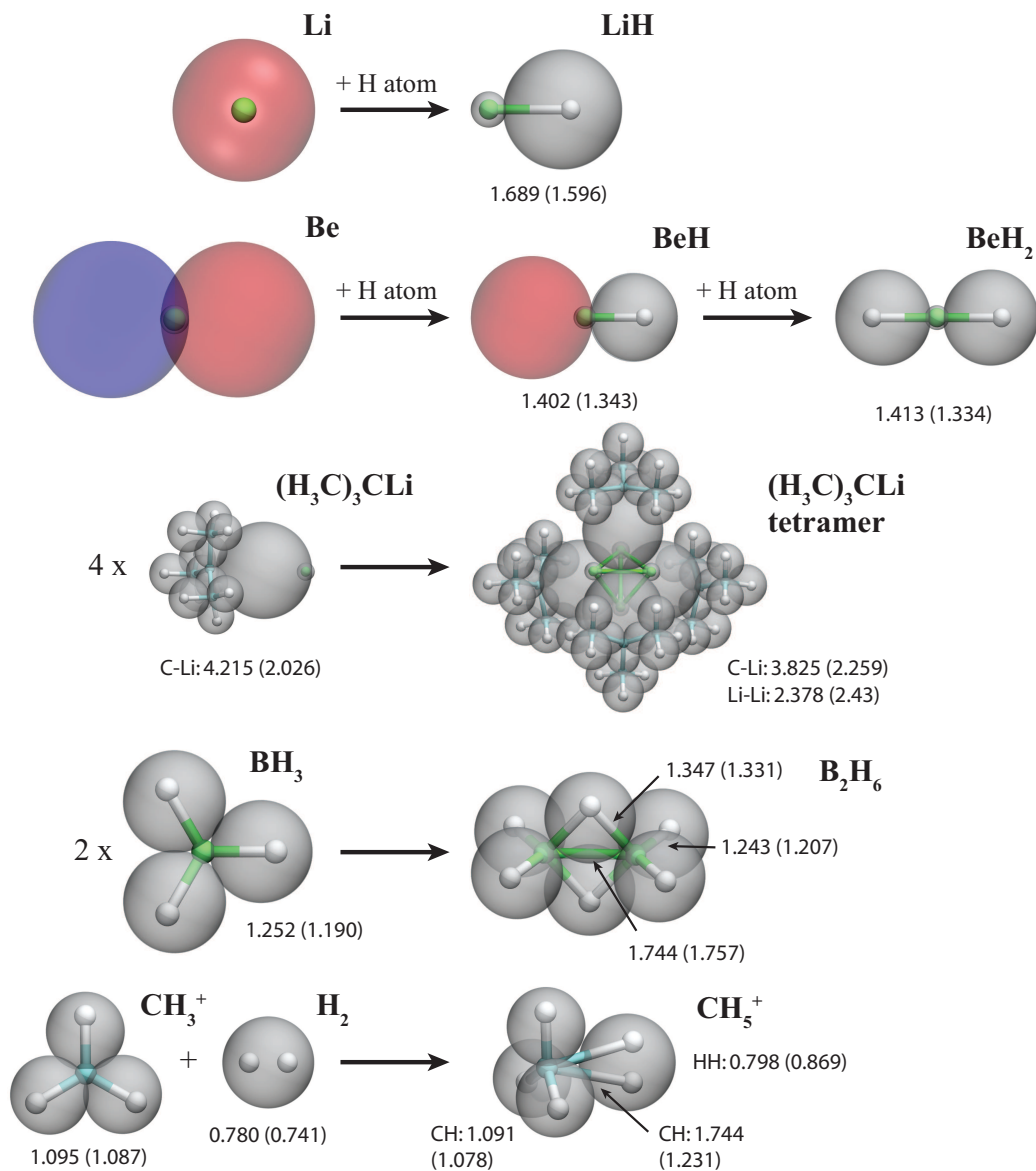
Figure 2.14: eFF can account for ionic and multicenter bonding.

		ΔE (kcal/mol)	
relative to	energy of	eFF	exact
LiH	Li + H	58.1	56.6
BeH$_2$	BeH + H	113.0	98.9
BeH	Be + H	109.6	52.8
B$_2$H$_6$	2 BH$_3$	27.6	41.2
CH$_5^+$	CH$_3^+$ + H$_2$	20.8	45.5

Table 2.5: Dissociation energies.

exact value (1.689 A versus 1.596 A exact), and because of the greater bond length, a slightly higher dipole moment as well (6.51 D versus 5.88 D). The dissociation energy is very near the exact value (58.1 kcal/mol versus 56.6 kcal/mol exact), which is not surprising since the electrons in the species Li, H, and LiH are all well represented by single-peaked functions.

In a similar manner, we form beryllium dihydride by adding two hydrogens to a beryllium atom. The bond length of BeH_2 is shorter than the bond length of LiH, due to the greater nuclear charge of Be; the difference in eFF bond lengths parallels that found in the exact values (-0.29 Å shrinkage versus -0.25 Å exact). The energy of breaking BeH_2 into BeH and H is near the exact value (113.0 kcal/mol versus 98.9 kcal/mol exact); however, the energy of breaking BeH into Be and H atoms is too high (109.6 kcal/mol versus 52.8 kcal/mol exact). This too-high energy is a consequence of a well-known difficulty in describing the valence electrons of beryllium atom as a single configuration wavefunction [34]

In beryllium, the $1s^2 2s^2$ configuration is nearly degenerate to the $1s^2 2p_x^2$, $1s^2 2p_y^2$, $1s^2 2p_z^2$ configurations; hence the wavefunction should be a resonance combination of these configurations. This static correlation is not well-described by Hartree-Fock or other single determinant methods, but the "floating" nature of the eFF electrons can account for these other configurations to some extent by shifting themselves to an average position between configurations. In the case of beryllium, eFF recognizes the $2s-2p$ degeneracy and separates the two valence electrons along an arbitrary axis to relieve electron-electron repulsion. However, it cannot shift electrons along the other two axes simultaneously, hence Be atom cannot gain its full measure of resonance stabilization. Static correlation in less symmetric cases, such as the breaking of a linear bond, should be better handled by eFF.

Ionic compounds can include as participants not only hydrides but carbanions as well. Tert-butyl lithium contains a very polar carbon-lithium bond, and an eFF model shows why this is the case. Imagine the compound $(CH_3)_3CH$, but with the terminal H^+ replaced by Li^+. The Li^+ contains a $1s^2$ core of electrons, and so unlike the proton, moves far away from the center of electron density in what was

formerly the C-H bond. Thus the carbon-lithium bond is polar, and the species acts as a carbanion; the tert-butyl group makes it too hindered to be nucleophilic, but the overall species can act as an active base. eFF makes the carbon-lithium bond too long (4.215 Å versus 2.026 Å B3LYP) because of the previously discussed too-diffuse nature of carbanions in eFF. We can describe as well the agglomeration of ^{t}BuLi into tetramers based upon tetraheral Li_4, where the lithium-lithium bonds optimize to the correct length (2.378 Å versus 2.43 Å Li-Li distance in the crystal structure [35]).

The boron compound BH_3 dimerizes into the borane B_2H_6 via a resonance combination of covalent and donor-acceptor bonds, which can also be viewed as two three-center two-electron bonds [36]. eFF describes nearly all aspects of the BH_3 and B_2H_6 geometries correctly (BH_3 bond length 1.252 Å versus 1.190 Å exact; B_2H_6 B-B 1.347 Å versus 1.331 Å exact; B-H covalent = 1.243 Å versus 1.207 Å exact; B-H bridging = 1.347 Å versus 1.331 Å exact). However, the dimerization energy is too low (27.6 kcal/mol versus 41.2 kcal/mol exact).

Another example of resonance between covalent and donor-acceptor bonds is found in CH_5^+, a fluxional molecule [37] that can be viewed as an interaction between CH_3^+ and H_2 where the hydrogens are similar and rapidly interconvert. However, no such resonance appears in the eFF description, where the hydrogens remain clearly distinguishable — the H atoms that were originally apart of H_2 remain close together (0.798 Å versus 0.869 Å exact [38]) and far away from the carbon (1.744 Å versus 1.231 Å exact). Like borane, the association energy is also too low (20.8 kcal/mol versus 45.5 kcal/mol exact), suggesting a future need for explicit resonance/electron delocalization terms in eFF.

Application to matter at extreme conditions

Dissociation and ionization of warm dense hydrogen

In 1912, Langmuir [39] immersed a hot tungsten wire in a hydrogen atmosphere, and found that above 3000 K, heat was carried away from the wire at a rate

much higher than would be expected by convection alone. The abnormally high conductivity appears because hydrogen molecules dissociate into atoms at that temperature, absorbing heat which is later released when the atoms recombine. At higher temperatures ($\sim$10000 K), hydrogen atoms separate into protons and electrons. Heavier atoms ionize at even higher temperatures, and Saha [40] proposed in 1920 that one could infer the temperature of stars from their relative concentration of ions.

For an equilibrium of ideal gases $C \rightleftharpoons A + B$, we can write the dissociation fraction as a function of the gas temperature and density using the Saha equation (Appendix B, [40]):

$$\frac{f^2}{1-f} = 1.667 \times 10^{-4} \cdot \left(\frac{m_A m_B}{m_C}\right)^{3/2} \frac{Z_A Z_B}{Z_C} \cdot \frac{T^{3/2}}{r_s^3} \exp(-\Delta E_d / kT) \qquad (2.8)$$

where f is the fraction of dissociated species, ΔE_d is the energy of dissociation of C, m are the masses of the species in amu, T is the temperature in Kelvin, and Z are the vibrational-rotational-electronic partition functions. The density is characterized by the parameter r_s, so that each atom takes up a volume $4/3\pi r s^3$. For hydrogen gas at one atmosphere and room temperature, r_s is 86.
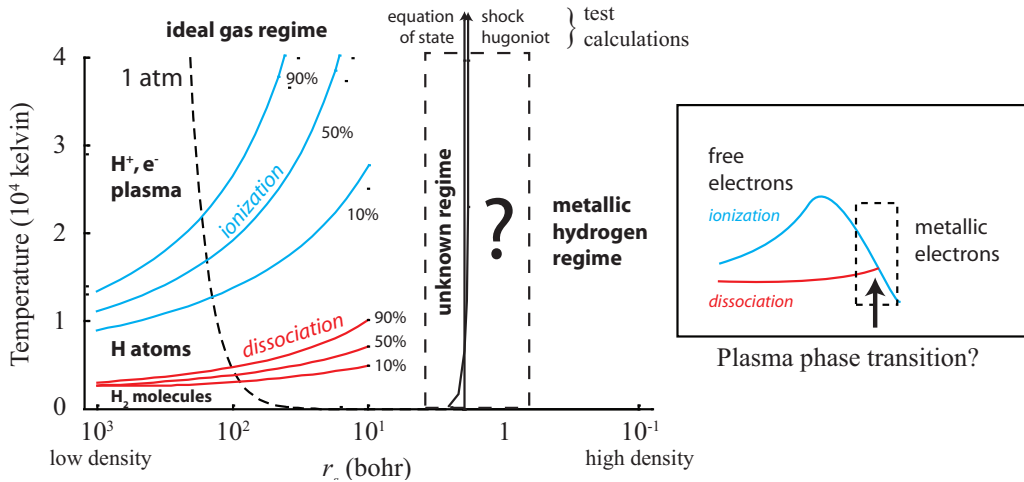
Figure 2.15: Previously proposed plasma phase transition [42, 43] where hydrogen dissociates and ionizes simultaneously

Applying the Saha equation to the reactions $H_2 \rightarrow H + H$ and $H \rightarrow p^+ + e^-$, we find that in dilute gases, dissociation is a gradual process, not an abrupt transition (Figure 2.15). These reactions are entropy driven — the bond dissociation energy of H_2 is ~50,000 K and the ionization potential of H is ~150,000 K, yet dissociation and ionization occur at much lower temperatures, driven by the separation of one particle into two. Two particles take up more space than one, which means that by La Chatlier's principle, compressing a gas shifts the equilibrium toward association. Thus the temperature of dissociation and the temperature of ionization increase with increasing density.

This analysis shows that in dilute gases, dissociation and ionization are two separate events. At higher densities, however, it should become easier to ionize hydrogen, since as atoms are squeezed together, the band gap decreases. At extreme compressions ($r_s = 1$), hydrogen becomes metallic, and the electrons move freely as if in a uniform sea of background positive charge. This pressure ionization occurs even at absolute zero [44]. There has been speculation that at intermediate densities, the temperature needed to ionize hydrogen decreases with temperature, and at some point matches the temperature required to dissociate hydrogen molecules [43]. At such a plasma phase transition, hydrogen would simultaneously dissociate and ionize, and properties like pressure or conductivity could change abruptly with variations in temperature or pressure (depending on the order of the phase transition).

If a plasma phase transition existed, it could lead to the revision of astrophysical models [42] — for example, giant planets like Jupiter have dense hydrogen near their core, and an abrupt phase change would change the way helium partitioned itself between molecular and metallic phases of hydrogen. Recently there has been a renewed interest in studying dense hydrogen, stemming from (1) the development of path-integral Monte Carlo methods to calculate hydrogen equations of state *ab initio* [45, 50, 46, 47, 48, 49] (2) shock hugoniot experiments with gas guns [51], lasers [54, 55], and exploding wires [52, 53] able to access densities and temperatures near the postulated PPT (~15000 K, $r_s \approx 2$ bohr, according to a chemical

model [43]. We demonstrate that the electron force field gives results consistent with the most recent high-level theory [49] and shock Hugoniot experiments [53]

In our simulations, we placed hydrogen molecules (64 nuclei) in a cubic periodic box, set atom velocities randomly from a Boltzmann distribution, then integrated the dynamics equations of motion with fixed volume and energy and a time step of 0.01 fs. We set the electron mass to be the same as the proton mass, making our simulation a plausible model of deuterium. We calculated the instantaneous temperature as the total kinetic energy of nuclei and electrons divided by $3/2kT$; we computed electrostatic energies by the Ewald method; and we averaged thermodynamic data over 1 ps following a 200 fs equilibration period.

Holding density fixed ($r_s = 2$ bohr) and performing simulations at a range of temperatures, we observed a thermal transition from a molecular to an atomic fluid (Figure 2.16). Proton-proton pair distribution functions plotted as a function of temperature (Figure 2.17) show a gradual transition between molecular and atomic fluid extremes, with an intermediate point at $T = 15400$ K, which compares well with the phase transition temperature of 15300 K estimated from a chemical model [43]. The pair distribution curves look similar to ones obtained using path-integral Monte Carlo [46], where an intermediate point (roughly estimated by looking at pair distribution curves by eye) occurs at 10000 K.

| 9100 K | 15400 K | 21100 K |
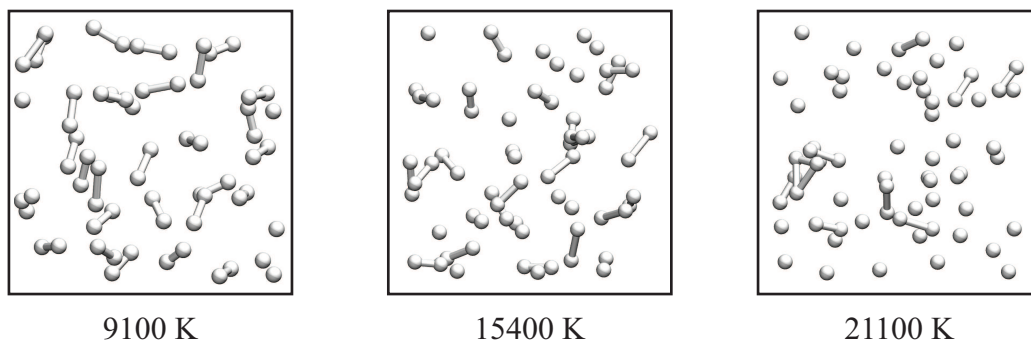
Figure 2.16: Dynamics snapshots showing deuterium dissociation as temperature is raised.
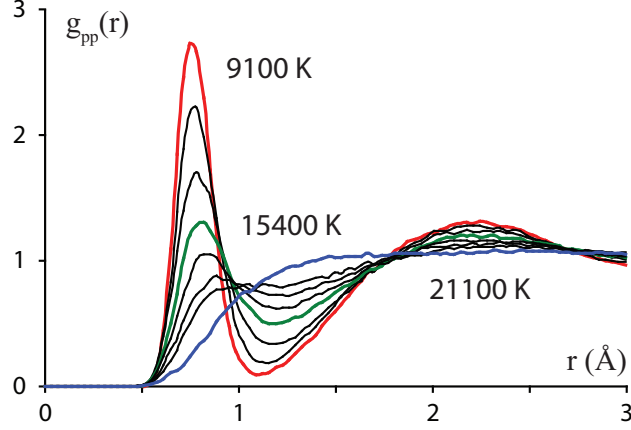
Figure 2.17: Proton-proton pair distribution function shows gradual dissociation.

We can also calculate pressure using the virial expression

$$P = \frac{2 \langle K_{total} \rangle}{V} - \frac{1}{3V} \left\langle \sum_{\text{all d.o.f.}} x_i \frac{\partial E}{\partial x_i} \right\rangle. \tag{2.9}$$

We note that for a purely electrostatic system, we have the simple virial

$$\sum_{i<j} \vec{F}(\vec{r}_{ij}) \cdot \vec{r}_{ij} = \sum_{i<j} -\frac{q_i q_j}{r^2} \hat{r}_{ij} \cdot \vec{r}_{ij} \tag{2.10}$$

$$= -\sum_{i<j} \frac{q_i q_j}{r_{ij}} \tag{2.11}$$

$$= -U. \tag{2.12}$$

However, since our system includes Pauli exclusion forces as well, such a calculation gives the wrong result, whereas ours agrees with numerical differentiation of $-dE/dV$. We hold $r_s = 2$ bohr and plot the equation of state, which we find agrees well with the chemical model at low temperatures and the QMC model at high temperatures, exactly the range of applicability each model is expected to have. We note that early path integral methods [50] predicted a first-order plasma transition with a negative slope dP/dT at $\tilde{1}0000$ K; however, more accurate calculations with a more accurate nodal surface did not show any evidence of this negative slope [49]. Given that our method handles both low and high

temperatures consistently, and we do not see any evidence of a negative dP/dT, we conclude that a first-order PPT does not exist in the temperature and density range considered.
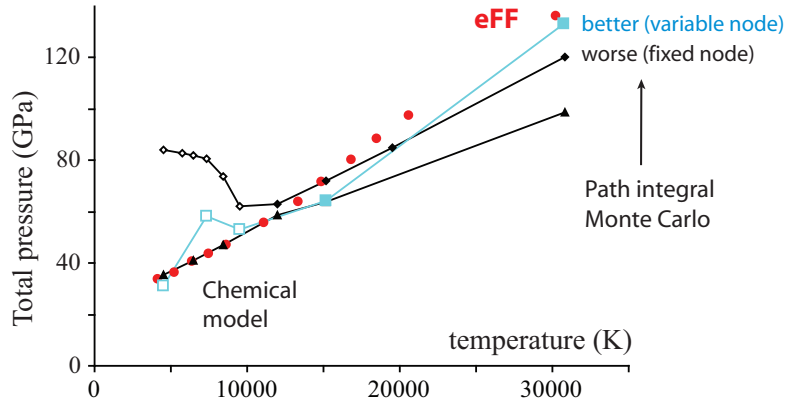
Figure 2.18: Equation of state ($r_s = 2$ bohr) shows good agreement with best available theory.

By looking at the distribution of electron sizes over the course of the simulation, we can estimate how many electrons become ionized. At low temperatures, we observe a Maxwell-Boltzmann-like distribution of electron sizes that broadens with increasing temperatures. At higher temperatures, we find that a small fraction of electrons escape and expand to be larger than the size of our periodic box; at that size, they no longer interact strongly with the rest of the system. Taking electrons with $r_s > 10$ bohr to be ionized, we find that some ionization occurs for $r_s = 2.6$ bohr, $L_{box} = 16.8$ bohr at $\sim$25000 K and for $r_s = 2.2$ bohr, $L_{box} = 14.2$ bohr at $\sim$30000 K but not for $r_s = 2$ bohr, $L_{box} = 12.9$ bohr. The ionization we observe is consistent with thermal ionization of hydrogen atoms in a dilute gas, where the electrons, not having a nucleus to associate with, expand to fill free space; in this regime, it is reasonable to expect the temperature required for ionization to increase with increasing density. However, further work needs to be done to determine whether metallic-like electrons appear at higher density and lower temperature. Metallic electrons in the electron force field would be

characterized not by a large size, but by an increased mobility.
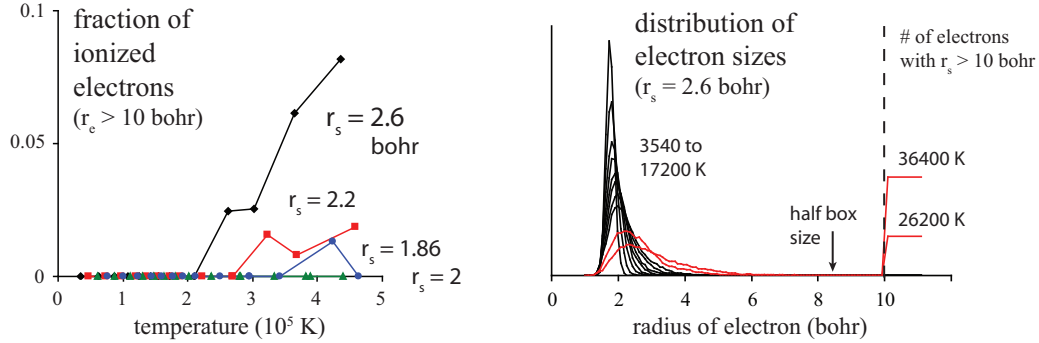
Figure 2.19: High densities suppress ionization that occurs at high temperature.

Experimentally, liquid deuterium can be compressed to near-metallic densities using shock waves generated by explosives, exploding wires, or lasers. In these experiments, the deuterium is compressed with a solid pusher; by measuring the position and acceleration of the pusher over a duration of nanoseconds, we deduce a density-pressure relation called a Hugoniot curve that is a characteristic of the material. From conservation of mass, energy, and momentum over the boundary of a shock wave, we know the internal energy, volume, and pressure must satisfy the Hugoniot relation

$$U - U_0 + \frac{1}{2}(V - V_0)(P + P_0) = 0. \tag{2.13}$$

The Hugoniot curve measures how compressible liquid deuterium is to shock. In the last decade, there has been some controversy over compressibility, with laser driven experiments (Nova [54, 55]) indicating a maximum compressibility of six times, and gas gun experiments indicating a lower compressibility of four times with a stiffer response. More recent experiments done with exploding wires ([52, 53]) support the stiffer response function. We would like to see what kind of Hugoniot our theory, which has only been parameterized to fit bond lengths of simple alkanes, would produce.

To estimate the Hugoniot curve using eFF, we carry out a series of simulations

at fixed volume and different fixed temperatures; measure the pressure; plot the Hugoniot function versus pressure; and find by interpolation the pressure that makes the Hugoniot function zero. As a starting point, we compute a box of liquid hydrogen with $r_s = 3.16$ ($\rho = 0.171 \text{g/cm}^3$), $T = 19.6K$; we find $U_0 = -0.477043$ hartrees/atom and $P = 0$.

r_s (bohr)	ρ (g/cm^3)	P (gPa)	T (K)
2.6	0.31	0.1	375
2.2	0.51	8.1	1768
2	0.68	34.2	6688
1.93	0.75	66.8	12464
1.86	0.84	151.0	23198
1.86	0.84	1216.5	344144

Table 2.6: eFF computed Hugoniot curve.

The eFF Hugoniot curve matches the curves obtained by the gas gun and Z machine, but not the ones obtained by the Nova laser. eFF reproduces the nearly vertical curve upward that path integral Monte Carlo shows; the vertical curve in eFF is the result of a Hugoniot function that was zero at two different pressures. It is believed that the true Hugoniot bends to the left slightly at high temperatures; if this is the case, we should be able to run the simulation at a slightly higher temperature, and have the Hugoniot curve be zero at only one point.

While PIMC shows a maximum density of $\sim$0.73 g/cm^3 (compressibility of 4.3 times), eFF shows a maximum density of $\sim$0.84 g/cm^3 (compressibility of 4.9 times). In contrast, the Nova laser Hugoniot shows a maximum compressibility of 6.0 times. eFF also shows a comparable rise in temperature to PIMC (ours is $\sim$1/3 less) over the course of its Hugoniot.

Another group has performed a WPMD simulation of hydrogen plasma, but used the earlier described Klakow potential, with an additional term added to capture electrostatic energy changes upon antisymmetrization. Their results agreed well with eFF at low temperatures, but deviated significantly at higher temperatures, with a higher compressibility (6.4 times) that better matches the Nova

laser data. The same extra repulsion that prevents electrons from inappropriately coalescing in the eFF model may be serving to give a higher compressibility and better agreement with path-integral Monte Carlo over Pauli potentials based on Klakow's expression.
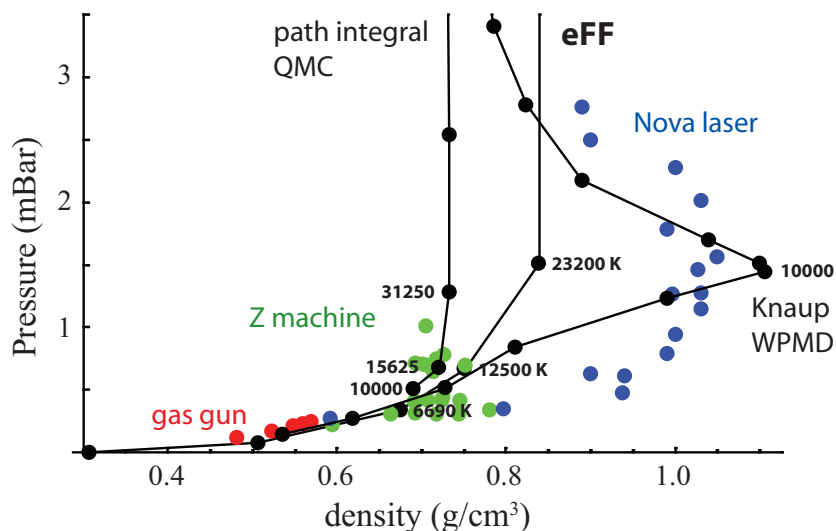
Figure 2.20: Reproduction of the experimental shock Hugoniot curve obtained by gas gun and Z machine; Nova laser remains an outlier.

To summarize, the electron force field shows that at $r_s = 2$ bohr, dissociation from molecular to atomic fluid is gradual, and the equation of state and proton-proton pair distribution functions are consistent with path-integral Monte Carlo calculations. We observed no evidence of a plasma phase transition at this density. The good agreement with Hugoniot curves obtained from gas gun and Z machine experiments, as well as those obtained from PIMC, further confirms that we are describing the thermal transition from molecules to atoms correctly.

We have examined ionization as well, but only by measuring the concentration of free (large) electrons; we find that at low densities, the temperature required to create large electrons in free space increases with increasing density, as we would expect from a Saha model. Pressure ionization creates metallic electrons that are smaller yet highly mobile. It would be interesting to measure electron mobility at higher densities to determine if eFF can model metallic phases of hydrogen

properly, and to better characterize pressure induced transitions from molecular to metallic hydrogen.

Dynamics of the Auger process in hydrocarbons

In Auger electron spectroscopy [56], core electrons in a sample are ionized using x-rays or electron impact. Once the core hole is generated, it is found that within ~10 fs, a valence electron "falls into" the hole [57], and the energy released causes a secondary electron to be ejected (Figure 2.21). If the two-hole state contains bonded atoms, it may relax by breaking bonds or ejecting additional electrons. Core ionized methanol, for example, breaks its OH bond over 100 fs, while core ionized formic acid breaks its OH bond over 50 fs [58].
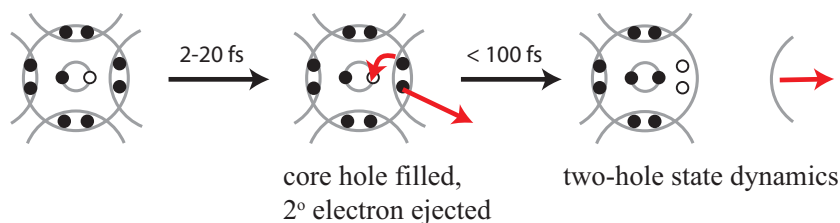
Figure 2.21: Core holes relax via a two stage Auger decay process.

The release of low-energy secondary electrons upon core electron ionization was first observed by Auger in 1923 [59], who bombarded noble gases with x-rays in a cloud chamber, and found that in addition to a long photoelectron track, a short secondary electron track appeared. He found that the energy of the secondary electrons was dependent on the species being ionized, but not on the incident x-ray energy.

Today, Auger spectroscopy is widely used to characterize the elemental composition and chemical bonding of surfaces [60], since secondary Auger electrons can only travel a few nanometers in solids, depending on their energy, without being absorbed. Thus a signal appears only from the top layers of atoms. Furthermore, since the secondary electron energy is independent of the means used to excite the core electron, and since core electron energies are mostly the same in atoms,

regardless of chemical environment, it is possible to use broad spectrum sources for excitation while still getting a clean secondary energy spectra.

Theory has mostly focused on reproducing Auger spectra by looking at the transition probabilities of moving from an initial ionized state to a final two-hole state [61, 62]. Such theory has been broadly successful at reproducing the Auger spectra of atoms, atom hydrides, and substituted hydrocarbons. In those cases, an implicit assumption is that the nuclei are held stationary. Any movement of the nuclei prior to the release of secondary electrons is assumed only to broaden the spectral lines.

In the last decades, it has become apparent Auger chemistry can be used to create and modify surfaces as well as characterize them. In 1978, Knotek and Fiebelman [63] provided evidence that electron-stimulated desorption in ionic solids operating proceeded via core-hole Auger decay; a year later, Knotek, Jones, and Rehn [64] reported photon-stimulated desorption of ions from a surface via a similar mechanism. Since then, it has been proposed that covalent solids [65] may be etched via Auger chemistry as well. To study these processes, which may be key to manufacturing the next generation of semiconductors with smaller and sharper feature sizes [66] ($\sim$20 nm, aspect ratios $\sim$10:1), we would like to simulate how molecules fragment during the Auger process, taking into account excited electron dynamics.

Theory has only recently risen to the challenge of computing extended nuclear dynamics after the initial Auger excitation. *Ab initio* molecular dynamics has been used to study the dissociation of a single water molecule following core-hole excitation [67], as well as the dissociation of a water molecule in an $(H_2O)_5$ cluster [68]. Using the electron force field, we can easily model the Auger dynamics of systems containing hundreds of atoms, with all electrons included; we show below a simulation of $C_{197}H_{112}$ over 100 fs, accomplished in two days real time.

In the previous sections, we have shown that eFF gives a reasonable model of bonding, but to ensure that eFF produces a correct distribution of secondary electrons and molecule fragments, we would like to compare the vertical ionization

energies of electrons to experiment. This comparison is not entirely straightforward, since vertical ionization potentials (IPs) of the sort measured using photoelectron spectroscopy are from delocalized molecular orbitals rather than from localized orbitals of the sort eFF uses. We settle on an indirect procedure, calibrating a Hartree-Fock method against experimental IPs [69], then comparing eFF orbital energies to theoretical Boys localized Hartree-Fock orbital energies, with corrections from the calibration applied (Figure 2.22, Appendix C).

For hydrocarbons methane, ethane, neopentane, and adamantane, we find that carbon-carbon electron are bound by almost exactly the correct amount (on average, eFF 16.8 eV vs 16.7 eV corrected localized HF); but carbon-hydrogen electrons are underbound by $\sim$2 eV (on average, eFF 13.9 eV vs 16.0 eV corrected localized HF). These differences are small in comparison to the energy difference between valence and core electrons ($\sim$270-280 eV), and so we expect energy to be properly distributed among electrons and molecular fragments. However, we also find that eFF underbinds $1s$ core electrons by $\sim$18% (236.0 eV average versus 290.6 eV experimental), due to its lack of a proper nuclear-electron cusp; this reduces the energy available in the Auger decay process.
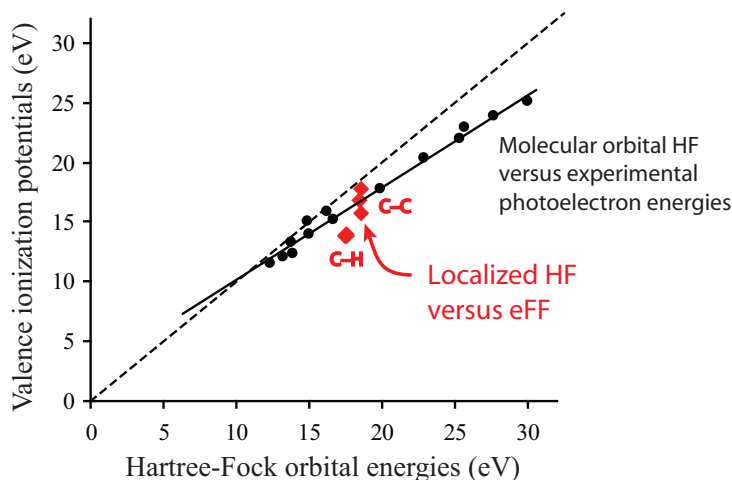
Figure 2.22: Red points compare Boys localized Hartree-Fock orbital energies to eFF orbital energies.

Since the vertical ionization potentials of valence electrons are correct, we start by creating single valence-hole states in ethane and observing how the molecule fragments. In the simulations, we assume instantaneous removal of the initial electron. Dynamics were integrated with a time step of 0.001 fs over 100 fs, and $m_{elec} = m_H$. Some of the core hole relaxation steps involved an abrupt motion of electrons, and an adaptive step size algorithm was used to shorten the time step further during those periods to ensure that energy was conserved to better than 0.0001 hartrees. Following the creation of single hole states, we find selective bond breaking: removal of a carbon-hydrogen bonding electron causes the carbon-hydrogen bond to break, while removal of a carbon-carbon bonding electron causes the carbon-carbon bond to break. In the case of CC bond dissociation, there is an additional complication in that there is no symmetry breaking, so that the remaining CC electron remains at the center of symmetry, effectively creating a two-hole state. We find that this effect disappears in larger, less symmetric molecules. The proper instability of single hole states gives us confidence that we will be able to properly describe the fragmentation of double hole states.
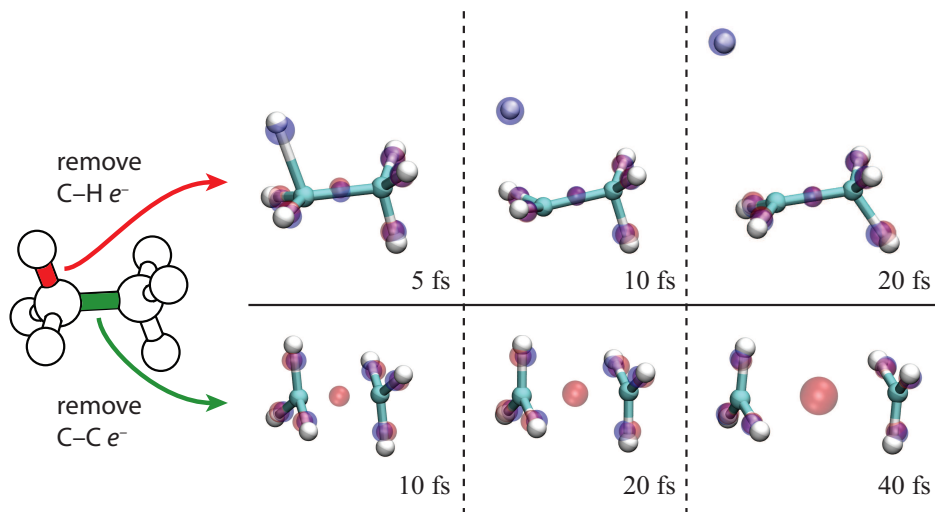
Figure 2.23: Removal of valence electrons from ethane results in selective bond breaking.

We next remove *1s* core electrons from the hydrocarbons methane, ethane,

adamantane, neopentane, and the diamondoid $C_{197}H_{112}$. We track the Auger process by plotting the potential energies of the eFF electrons over time (Figure 2.24); the advantage of having localized electrons becomes apparent here, as it is straightforward to distinguish loosely bound, valence, and core electrons. We find that the key stages of the Auger process are well reproduced: for 2-20 fs, the core-hole is stable, then there is an abrupt transition where a valence electron jumps into the hole and a valence hole is created; then over the next 20-100 fs, secondary electrons are ejected and/or fragmentation occurs. We find however that in many cases the secondary electrons are not usually released simultaneously with the filling of the core hole, but several femtoseconds afterward, as the highly excited valence hole state relaxes.

Core hole lifetimes are measured experimentally as the lifetime broadening of the x-ray photoelectron peak ($\Delta t = \hbar / \Delta E$). With eFF, we estimate the lifetime of the core hole as the moment when what was formerly a valence electron becomes bound by greater than 160 eV, an arbitrary threshold set to distinguish core-like and valence-like electrons. We find a core hole lifetime for methane that is comparable to experiment (9.2 fs versus 7.9 fs expt), and a lifetime for ethane that is lower then experiment (2.0 fs versus 6.7 fs). Neopentane, adamantane, and the large diamondoid particle $C_{197}H_{112}$ all have core hole lifetimes between 2 and 20 fs, in line with the ranges observed experimentally [57]. Aside from primary carbons having a particularly short core hole lifetime (2 fs), we did not observe any particular correlation between the degree of substitution of the carbon and the core hole lifetime (Table 2.7).

With x-ray photoelectron spectroscopy, it is also possible to measure the energy and geometry changes that occur during the initial creation of the core hole, e.g., the difference between vertical and adiabatic ionization potentials [70]. With eFF, we assume a vertical ionization, but we can estimate the magnitude of core-hole induced relaxation by averaging over all geometries from zero time to the core-
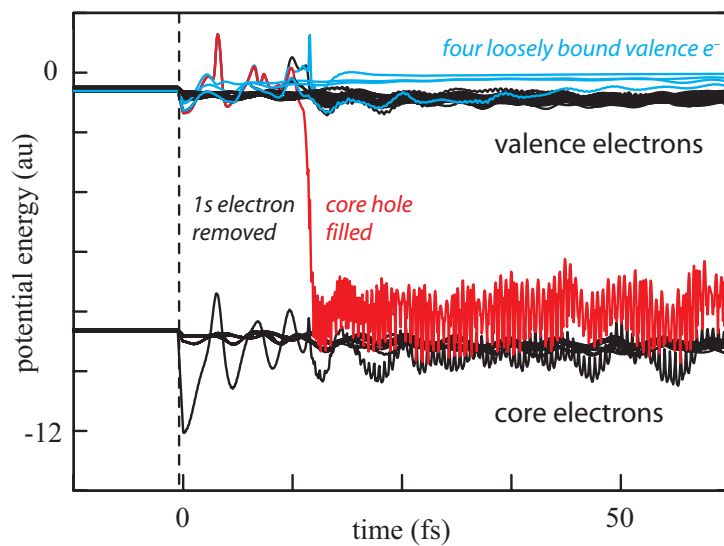
Figure 2.24: Electron energies show Auger process in adamantane in detail.

| | Core-hole lifetime (fs) | |
	eFF	expt
methane	9.2	7.9
ethane	2.0	6.7
neopentane (C)	15.0	
neopentane (CH$_3$)	2.0	
adamantane (CH)	11.7	
admantane (CH$_2$)	6.1	
C$_{197}$H$_{112}$ (C)	4.0	

Table 2.7: Core-hole lifetimes are on the correct time scale.

hole lifetime. This is not a perfect comparison, as it assumes that the period over which the ionization occurs is comparable to the core-hole lifetime; however, such an assumption is made when the core-hole lifetime is estimated from the width of the *1s* photoelectron peak, and so we regard it as justified.

Comparing eFF averaged relaxations to experiment [71, 72], we found that (1) geometry changes for methane were comparable to those observed experimentally, but for ethane the C-H bonds stretched and bent in an opposite manner to what was observed (Table 2.8), and (2) the core hole showed a relaxation energy nearly *eighty times* greater than what was observed experimentally.

The larger-than-observed energy relaxation of the core-hole state suggests that eFF has made an uneasy truce between adiabatic curve hopping abrupt transitions and a mean-field description of electron dynamics. Experiments [70] suggest that the core-hole is filled in an abrupt way: while the methane C *1s* electrons is being ionized, for instance, the CH_4 molecule only lowers its energy by -0.15 eV, but we know that within 8 fs the energy of the molecule drops by 290 eV. In eFF, core-hole filling is abrupt, but the "plateau before the cliff" is slightly steeper, which suggests that a portion of the valence-hole state is mixing in with the core-hole state prior to the electron jump. This larger core-hole prerelaxation may explain why we are able to obtain core-hole lifetimes comparable to experiment, even with massive electrons.

| | | Core-hole relaxation | |
		eFF	expt
methane	ΔE(eV)	**-12.43**	-0.15
	Δd_{CH} (A)	-0.07	-0.05
ethane	ΔE(eV)	**-12.03**	-0.17
	Δd_{CH} (A)	0.03	-0.05
	Δd_{CC} (A)	0.00	0
	Δd_{HCC} (degrees)	0.36	-3.00

Table 2.8: In eFF, core hole shows strong relaxation even before it is filled.

We consider now the nuclear dynamics *after* the core hole has been filled by a valence electron. In the case of methane, we find the following sequence of events (Figure 2.25):

$$
\begin{aligned}
\mathrm{CH_4^+} \;\; &\rightarrow \;\; \mathrm{core - hole\ collapse\ (9\ fs)} \\
&\rightarrow \;\; \mathrm{CH_3^+ + H\ (17\ fs)} \\
&\rightarrow \;\; \mathrm{CH_2^+ + 2H\ (23\ fs)} \\
&\rightarrow \;\; \mathrm{CH_2^{2+} + e^- + 2H\ (25\ fs)} \\
&\rightarrow \;\; \mathrm{CH^{2+} + e^- + 3H\ (49\ fs)} \\
&\rightarrow \;\; \mathrm{C^+ + H^+ + e^- + 3H\ (79\ fs).}
\end{aligned}
$$
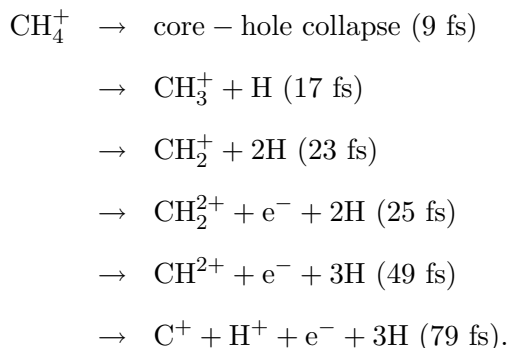
In our simulations, the secondary electron is not ejected from the highly excited $\mathrm{CH_4^+}$ until two hydrogen atoms have already dissociated from it. Experimentally, it is possible to find out which fragments are present when the secondary electron is released through the use of energy-resolved electron-ion coincidence (EREICO). Kukk et al. [73] found that core-ionized deuteromethane produces along with the secondary electron the major fragment $\mathrm{CD_2^+}$, with $\mathrm{CD^+}$ and $\mathrm{C^+}$ also present, and almost no $\mathrm{CD_3^+}$. It may seem curious that $\mathrm{CD_3^+}$ and $\mathrm{CD_4^+}$ do not appear in the spectra, especially given that ionization of the valence electrons have been shown by the same method to produce *only* $\mathrm{CD_3^+}$ and $\mathrm{CD_4^+}$.

Most likely $\mathrm{CH_4^+}$ (or by their finding $\mathrm{CD_4^{2+}}$) is created as a very hot molecule, and it is only by detaching bound hydrogen atoms that it becomes stable enough to detect. This is consistent with our model. It may also be possible that our unusual observation that the secondary electron is only released *after* two hydrogen atoms have dissociated is correct, and the two-hole state is created in a nonconcerted fashion. This would also explain the lack of $\mathrm{CD_3^+}$ and $\mathrm{CD_4^+}$ in the experimental spectra.

In the case of ethane, ionizing a core electron causes a σ_{CC} electron to fill in the core hole. At that point, the carbon-carbon bond breaks, lengthening steadily from 1.48 Å; 12.5 fs after the core hole fills, the carbon-carbon bond is already
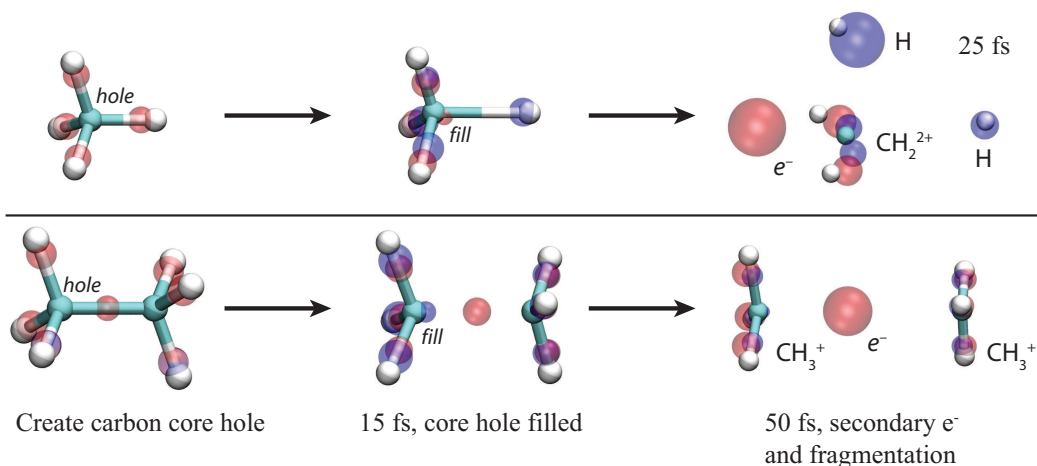
Figure 2.25: Auger dissociation of methane and ethane following creation of a core hole.

2 Å long. During this period, the single remaining σ_{CC} electron remains at the center of the bond to maintain the system's overall symmetry, making it appear as if bond breaking and secondary electron ionization happen at the same time. In contrast to the methane dynamics, and perhaps because the secondary electron is released early, the CH_3^+ fragments are not left with enough energy to break carbon-hydrogen bonds, and no further fragmentation is observed.

We continue to the larger hydrocarbons neopentane and adamantane (Figure 2.26). In the case of neopentane, there are two different carbons whose *1s* electrons we may ionize: the quaternary carbon at the center, or the four primary carbons at the periphery. Ionizing the quaternary carbon causes four surrounding valence electrons with the same spin as the ionized electron to simultaneously move inward to fill the vacancy; symmetry breaks, and after 15 fs only one valence electron fills in to occupy the core. As in ethane, the loss of a σ_{CC} electron causes the neopentane to dissociate into $(CH_3)_3C^+ + CH_3^+$ plus a secondary electron.

Unlike ethane, however, the $(CH_3)_3C^+$ fragment is released highly excited — recall that we had three valence electrons surrounding the central carbon that were drawn inward but did not fall into the core. These valence electrons now transfer their energy to the C-C bonds of $(CH_3)_3C^+$, causing the C-C bond lengths to

increase to ~2.3 Å before collapsing back down to an equilibrium size. Ultimately the $(CH_3)_3C^+$ remains intact and does not dissociate further.

Ionizing a primary carbon in neopentane causes prompt fragmentation (2 fs) into $(CH_3)_3C^+ + CH_3^+ + e^-$, and, as in ethane, the two fragments have minimal excess vibrational energy. It is interesting to note that the bond connecting the excited carbon is *selectively broken*. This is relevant for understanding how photon and electron stimulated diffusion operates; if both holes are localized on the same bond, we can have selective bond breaking dominated by excited state kinetics rather than an overall heating of the molecule and statistical bond breaking. Jennison et al. has noted both experimental and theoretical evidence for localization of two-hole final states in hydrocarbons, including neopentane [74]. We observe such localization, i.e., the electron that falls into the hole stimulates *nearby* electrons to be ionized, in both neopentane and the next molecule to be discussed, adamantane.

Adamantane contains two different types of carbons that may be ionized: four tertiary carbons (CH) and six secondary carbons (CH_2). Removing a *1s* electron from a tertiary carbon causes the following events to occur:

$$
\begin{aligned}
C_{10}H_{16}^+ \quad &\rightarrow \quad C_{10}H_{15}^{2+} + H^- \text{ (6 fs)} \\
&\rightarrow \quad core - hole \ collapse \ (11.7 \ fs) \\
&\rightarrow \quad C_{10}H_{15}^{3+} + e^- + H^- \text{ (13 fs)} \\
&\rightarrow \quad C_9H_{15}^{3+} + C + e^- + H^- \text{ (20 fs)} \\
&\rightarrow \quad C_9H_{15}^{3+} + C^+ + 2e^- + H^- \text{ (48 fs).}
\end{aligned}
$$
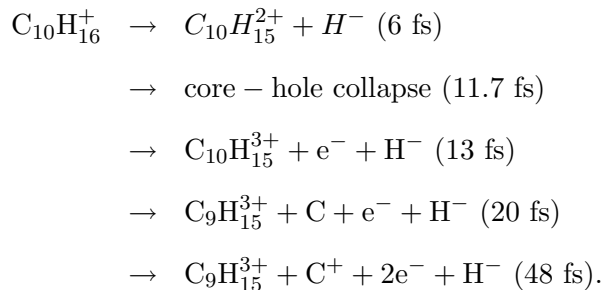
The core-hole relaxation causes a hydride to be dissociated even before the core hole is filled; only 1 fs after the core hole is filled, a secondary electron is ejected, followed by a neutral carbon atom 7 fs later. The carbon that is ejected is the carbon that was initially ionized — more evidence of two hole localization. The system is mostly stable at this point, only stopping to release an electron from the neutral carbon atom after another 28 fs. All these steps take ~48 fs from the

initial formation of the core hole, in line with the typical nuclear relaxation time of first row Auger dissociative processes.

Removing a *1s* electron from a secondary carbon of adamantane causes the following events to occur:

$$
\begin{aligned}
C_{10}H_{16}^+ \quad &\rightarrow \quad \text{core} - \text{hole collapse (6.1 fs)} \\
&\rightarrow \quad C_{10}H_{14}^{2+} + e^- + 2H^- \text{ (8 fs)} \\
&\rightarrow \quad C_9H_{14}^{2+} + C^{2+} + e^- + 2H^- \text{ (15 fs)} \\
&\rightarrow \quad C_9H_{14}^{2+} + CH_2^+ + 2e^- \text{ (40.5 fs)} \\
&\rightarrow \quad C_9H_{14}^{2+} + CH_2^{2+} + 3e^- \text{ (51.5 fs)} \\
&\rightarrow \quad C_9H_{14}^{2+} + CH^+ + H + 2e^- \text{ (80 fs)}
\end{aligned}
$$
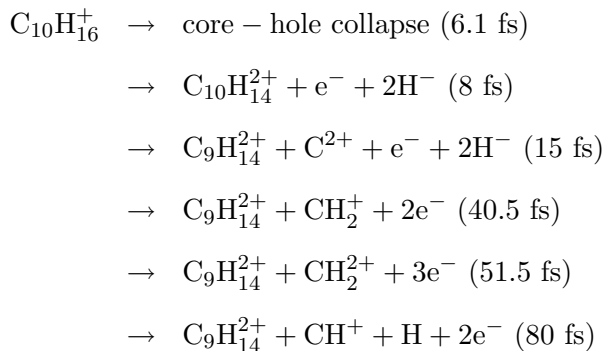
In this case, core-hole relaxation causes the C-H bonds attached to the ionized carbon to stretch out but not break before the hole is filled; after the core hole is filled, two hydrides and one secondary electron are promptly (2 fs) released. The next steps involve release of an ionic carbon, recombination of carbon and hydrides to form a stable CH_2 ion, and the ultimate dissociation of the CH_2^{2+} into $CH^+ + H + e^-$.

In these larger hydrocarbons, we observe (1) significant core-hole relaxations in C-H bonds attached to the ionized carbon, but not attached C-C bonds, (2) a tendency to eject the ionized carbon atom and a secondary electron very soon after the core hole is filled, and (3) fragmentation and electron ion recombination events over the next tens of picoseconds.

In even larger hydrocarbons, we enter a regime where secondary electrons may be produced, but trapped inside a bulk solid and recombined. This effect is the reason Auger spectroscopy can be used to analyze surfaces — secondary electrons can only escape from the top monolayers of a surface. To test whether eFF can simulate this effect, we ionize a *1s* electron from the center of a roughly spherical diamondoid $C_{192}H_{112}$ (Figure 2.27). The diamondoid was constructed by starting with a 3x3x3 diamond lattice taken from a periodic structure, truncating primary
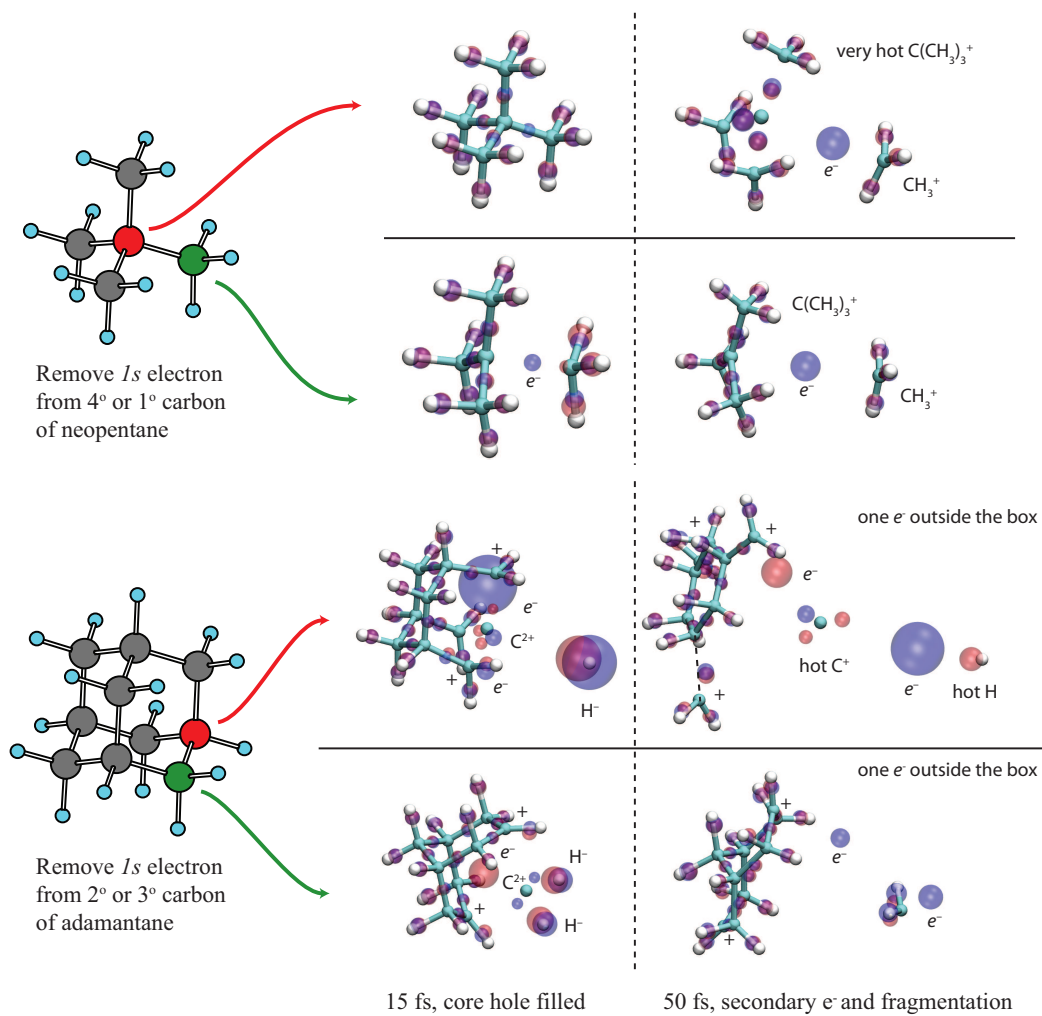
Figure 2.26: Auger dissociation of neopentane and adamantane following creation of a core hole.

carbons, then manually reconstructing (100) faces via dehydrogenation. This process introduces some strain into the particle, and we found smaller diamond lattices tended to relieve this strain by forming sp^2 carbons and sheet-like structures. As we are interested in the case of saturated hydrocarbons, we chose a larger particle to ionize.

As in neopentane, removing a center core electron causes four surrounding valence electrons to move inward. One valence electron fills the core (4 fs), causing the other three valence electrons to make large amplitude motions and move a short distance through the lattice. The carbon lattice expands slightly around the excitation site, then recontracts as the excited valence electrons recombine with the core. Plotting the trajectories of all the electrons around the excited core, we find that after 5 fs the three valence electrons have moved; after 10 fs motion has been transferred to adjacent electrons; and after 50 fs the motion has been dissipated into thermal motion throughout the lattice (Figure 2.28). Plotting the energy distribution of the electrons over time shows the same effect (Figure 2.29).
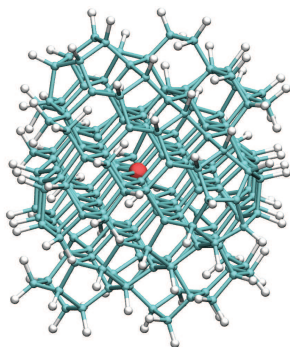
Figure 2.27: We remove a core electron from a central carbon of a diamondoid particle.

In conclusion, we reproduce nearly all the qualitative aspects of the Auger process — abrupt core-hole filling, followed by fragmentation and secondary electron generation; localization of two hole states; and trapping of secondary electrons in a bulk solid. We also remarkably reproduce some key quantitative aspects as well, such as the core-hole lifetime and time scale for fragmentation. The theory
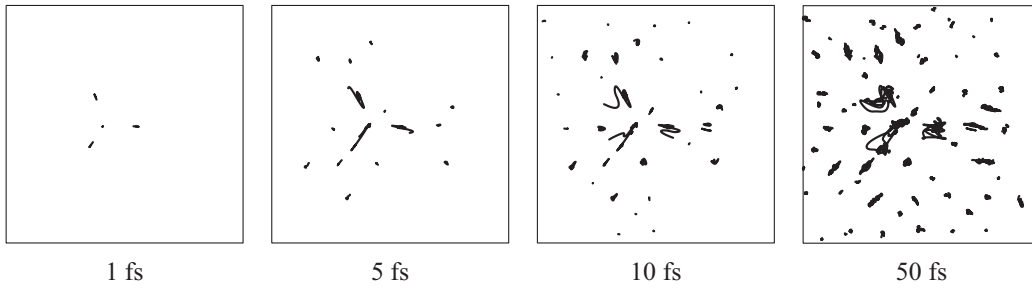
Figure 2.28: Trajectories of electrons after removal of a core electron.
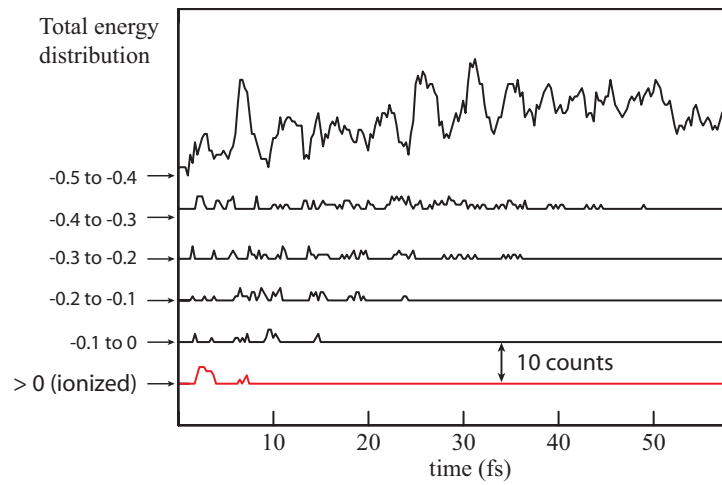
Figure 2.29: Excited electrons dissipate their energy into their surroundings.

suggests that in some cases, secondary electron emission may occur only some time *after* the core hole has been filled, and we speculate that this nonconcerted formation of the two-hole state may explain the lack of CD_3^+ and CD_4^+ ions following core-ionization of CD_4. We hope that the eFF method will lead eventually to simulations of electron and photon stimulated desorption processes on realistic surfaces and bulk solids, and provide correct microscopic mechanisms for observed macroscopic behavior, such as the selectivity in etch rates that make it possible to create small sharp surface features.

Conclusion

With our electron force field, we find that we obtain correct geometries for a wide range of hydrocarbons, particularly ones with a rigid carbon core and outwardly-directed hydrogens. Using a formulation that contains only pairwise interactions between the nuclei and electrons in the system, we are able to describe not only bonds, but reasonable energy differences between different hydrocarbon conformers. Multiple bonds are described as $\sigma - \pi$-like structures, and carbon radicals are properly planar. We are able to describe ionic compounds like LiH and BeH_2 correctly, as well as multicenter compounds like B_2H_6.

Further work is needed though. Lone pairs are poorly described (^-OH and HF and Ne are unstable), and multiple bonds and radicals are too diffuse, causing carbon-carbon bonds to be too strong; this suggests we need a better way of describing p electrons. Electron sizes tend to be too variable, particularly in C-H bonds. eFF also underestimates the strength of covalent atom-centered bonds, i.e., H_2 is underbound while HeH^+ is not. On a larger scope, we would like to add correlation, resonance/delocalization, and proper Fermi-Dirac statistics to eFF.

In simulating warm dense deuterium dynamics, we looked at temperature dissociation and ionization of D_2 in a region where it might be expected to have mixed covalent and metallic character. We obtained an equation of state and shock Hugoniot curve that was in agreement with most experiments [51, 52, 53] and path integral Monte Carlo calculations [46]. We found no evidence for a plasma

phase transition in the temperature and density range considered, contrary to some predictions [43], but consistent with recent path-integral Monte Carlo studies [49].

In simulating the Auger dynamics of small hydrocarbons, we found that after a core electron was removed, a valence electron transferred to reoccupy the core within a few femtoseconds, followed by additional valence electrons ejecting and the molecule fragmenting over tens of femtoseconds. The time scales were on the same scale as those observed experimentally [57]. When core electrons were removed from small hydrocarbons, we observed selective bond breaking and secondary electron ejection; in contrast, core ionization inside a diamondoid particle caused secondary electrons to be released but rapidly recombined with the core, with no bonds broken. That bond cleavage occurs only near the surface and only near excited sites may help to explain the precision of surface etching observed in photon and electron stimulated desorption. Finally, we offer the intriguing possibility that in some systems, such as methane, formation of the two-hole state may be *nonconcerted*, so that the secondary electron leaves significantly after the core hole is filled, when bond breaking may have already occurred.

With eFF, we can compute the energy and forces in systems containing a thousand electrons in less than a second. We have shown that compounds containing atoms from hydrogen through carbon are reasonably well described, and the accuracy is sufficient to make possible the simulation of matter at extreme conditions. Work is in progress to improve the accuracy and scope of eFF, and we hope that the formulation presented here, as well as its progenitors, will enable the simulation of a wide range of interesting excited electron chemistry on realistic systems.

Appendix A: Derivation of Pauli function terms

Wavefunction plus abbreviation, where $S = \langle \phi_1 | \phi_2 \rangle$

$$
\begin{aligned}
\Psi &= \frac{1}{\sqrt{2 \pm 2S^2}} (\phi_1(r_1)\phi_2(r_2) \pm \phi_2(r_1)\phi_1(r_2)) \\
&= \frac{1}{\sqrt{2 \pm 2S^2}} (12 \pm 21).
\end{aligned}
$$

Verification of normalization:

$$
\begin{aligned}
\langle \Psi | \Psi \rangle &= \frac{1}{2 \pm 2S^2} \langle 12 \pm 21 | 12 \pm 21 \rangle \\
&= \frac{1}{2 \pm 2S^2} \left(\langle 12 | 12 \rangle \pm 12 | 21 \rangle \right) \\
&= \frac{1}{2 \pm 2S^2} \left(\langle 1 | 1 \rangle \langle 2 | 2 \rangle \pm \langle 1 | 2 \rangle \langle 2 | 1 \rangle \right) \\
&= 1.
\end{aligned}
$$

Evaluate kinetic energy of these wavefunctions, using operators $t_1 = -\frac{1}{2} \nabla_1^2$ and $t_2 = -\frac{1}{2} \nabla_2^2$:

$$
\begin{aligned}
\mathrm{KE}(12 \pm 21) &= \langle 12 \pm 21 | t_1 + t_2 | 12 \pm 21 \rangle \\
&= \frac{1}{2 + 2S^2} \cdot 2 \cdot \langle 12 \pm 21 | t_1 | 12 \pm 21 \rangle \\
&= \frac{1}{1 + S^2} \left(\langle 12 | t_1 | 12 \rangle + \langle 21 | t_1 | 12 \rangle \pm 2 \langle 21 | t_1 | 21 \rangle \right) \\
&= \frac{1}{1 + S^2} \left(\langle 1 | t_1 | 1 \rangle \langle 2 | 2 \rangle + \langle 2 | t_1 | 2 \rangle \langle 1 | 1 \rangle \pm 2 \langle 1 | t_1 | 2 \rangle \langle 2 | 1 \rangle \right) \\
&= \frac{1}{1 + S^2} \left(t_{11} + t_{22} \pm 2 S t_{12} \right)
\end{aligned}
$$

where

$$
\begin{aligned}
t_{11} &= \langle 1 | -\frac{1}{2} \nabla^2 | 1 \rangle = \frac{3}{2} \frac{1}{s_1^2} \\
t_{22} &= \langle 2 | -\frac{1}{2} \nabla^2 | 2 \rangle = \frac{3}{2} \frac{1}{s_2^2} \\
t_{12} &= \langle 1 | -\frac{1}{2} \nabla^2 | 2 \rangle = S \left(\frac{3(s_1^2 + s_2^2) - 2x_{12}^2}{(s_1^2 + s_2^2)^2} \right) \\
S_{12} &= \langle 1 | 2 \rangle = \left(\frac{2}{s_1/s_2 + s_2/s_1} \right)^{3/2} \exp(-x_{12}^2/(s_1^2 + s_2^2)).
\end{aligned}
$$

Then we have

$$
\begin{aligned}
E_u &= \mathrm{KE}(12-21) - \mathrm{KE}(1) - \mathrm{KE}(2) \\
&= \frac{1}{1-S^2}(t_{11} + t_{22} - 2St_{12}) - \frac{1-S^2}{1-S^2}(t_{11} + t_{22}) \\
&= \frac{S^2}{1-S^2}\left(t_{11} + t_{22} - \frac{2t_{12}}{S}\right)
\end{aligned}
$$

and

$$
\begin{aligned}
E_g &= \mathrm{KE}(12+21) - \mathrm{KE}(1) - \mathrm{KE}(2) \\
&= \frac{1}{1+S^2}(t_{11} + t_{22} - 2St_{12}) - \frac{1+S^2}{1+S^2}(t_{11} + t_{22}) \\
&= -\frac{S^2}{1+S^2}\left(t_{11} + t_{22} - \frac{2t_{12}}{S}\right).
\end{aligned}
$$

Appendix B: Derivation of the Saha equation

This derivation follows the one provided in [41], and is included here for completeness. Consider an equilibrium of ideal gases $C \rightleftharpoons A + B$. We compute the number of particles n_A, n_B, and n_C by maximizing the total number of available states:

$$
\frac{Z_A^{n_A}}{n_A!} \cdot \frac{Z_B^{n_B}}{n_B!} \cdot \frac{Z_C^{n_C}}{n_C!} \tag{2.14}
$$

where Z_A, Z_B, and Z_C are the partition functions of A, B, and C. If we take f to be the fraction of dissociated C, we then have

$$
\begin{aligned}
\frac{f}{1-f} &= \frac{n_A n_B}{n_C} = \frac{Z_A Z_B}{Z_C} \\
&= \frac{(V/\Lambda_A^3)Z_A^{\mathrm{vre}} \cdot (V/\Lambda_B^3)Z_B^{\mathrm{vre}}}{(V/\Lambda_C^3)Z_C^{\mathrm{vre}} \cdot \exp(\Delta E_d/kT)}
\end{aligned}
$$

where we have factored out the translational partition functions explicitly to leave Z^{vre}, the vibrational-rotational-electronic partition functions. We compute the partition functions from the "bottom of the well," which incurs a factor of $\exp(\Delta E_d/kT)$, where E_d is the dissociation energy of C. Substituting the de

Broglie wavelength $\Lambda = (h^2/2\pi mkT)^{1/2}$ and the volume per atom $V = 4\pi r_s^3/3$ we are left with the expression

$$\frac{f}{1-f} = \frac{Z_A^{vre} Z_B^{vre}}{Z_c^{vre}} \frac{3}{4\pi r_s^3} \left(\frac{m_A m_B}{m_C}\right) \left(\frac{2\pi kT}{h^2}\right)^{3/2} \exp(-\Delta E_d/kT). \qquad (2.15)$$

For hydrogen atom, electron, and proton, we take $Z^{vre} = 1$; for hydrogen molecule we use the expression for an ideal diatomic

$$Z^{vre} = \frac{T}{2\Theta_r} \cdot \frac{\exp(-\Theta_v/2T)}{1 - \exp(-\Theta_v/T)} \qquad (2.16)$$

where $\Theta_r = 85.3$ K and $\Theta_v = 6215$ K.

Appendix C: Hartree-Fock orbital energies versus photoelectron energies

We wish to compare vertical ionization energy of core and valence electrons determined experimentally using photoelectron spectroscopy with eFF electron energies. However, photoelectron spectroscopy measures ionization from molecular orbitals, which are delocalized, in contrast to the localized electrons in eFF. To validate eFF, we use Hartree-Fock (6-311g** basis) as an intermediate reference theory. First, we relate Hartree-Fock orbital energies to the experimental ionization potentials:

$$E(IP) = 0.777E(HF) + 2.386eV. \qquad (2.17)$$

Then, we compare eFF electron energies to *localized* Hartree-Fock orbital energies.

	Valence IP (eV)		
	eFF	HF/local*	difference
methane CH	13.98	16.02	-2.04
ethane CH	13.82	15.99	-2.17
neopentane CH	13.83	15.98	-2.15
adamantane CH	13.84	15.99	-2.15
adamantane CH	13.85	15.95	-2.10
average	*13.86*	*15.99*	*-2.12*
ethane CC	17.75	16.76	1.00
neopentane CC	15.77	16.77	-1.00
adamantane CC	16.75	16.68	0.07
average	*16.76*	*16.74*	*0.02*

Table 2.9: eFF computed valence ionization potentials are close to ones estimated by Hartree-Fock (corrected energies, see text).

	Core IP (eV)		
	eFF	expt	difference
methane	239.20	290.84	-51.65
ethane	237.07	290.71	-53.64
neopentane (C)	230.52	290.35	-59.82
neopentane (CH_3)	237.30	290.53	-53.23
adamantane (CH)	233.92		
adamantane (CH_2)	235.98		
average, first four	*236.02*	*290.61*	*-54.59*

Table 2.10: eFF underbinds core electrons, making less energy available for Auger decay.

| | Valence IP (eV) | |
	HF	expt
methane	25.71	22.9
	14.86	15.0
ethane	27.71	23.9
	22.94	20.4
	16.24	15.8
	13.83	13.3
	13.24	12.1
neopentane	30.01	25.1
	25.30	21.9
	19.91	17.8
	16.63	15.2
	15.05	14.0
	13.90	12.4
	12.30	11.5

Table 2.11: Comparison of Hartree-Fock orbital energies with vertical ionization potentials from photoelectron spectroscopy [69].

Bibliography

[1] **Mayo, S. L., Olafson, B. D., Goddard, W. A. III.** 1990. Dreiding: a generic force field for molecular simulations. *J. Phys. Chem.* **94(26)**:8897-8909.

[2] **van Duin, A.C.T., Dasgupta, S., Lorant, F., Goddard, W. A. III.** 2001. ReaxFF: a reactive force field for hydrocarbons. *J. Phys. Chem. A.* **105**:9396-9409.

[3] **Tuckerman, M. E.** 2002. *Ab initio* molecular dynamics: basic concepts, current trends and novel applications. *J. Phys.: Condens. Matter.* **14**:R1297-R1355.

[4] **Hehre, W. J.** 1976. *Ab initio* molecular orbital theory. *Acc. Chem. Res.* **9(11)**:399-406.

[5] **Heller, E. J.** 1975. Time-dependent approach to semiclassical dynamics. *J. Chem. Phys.* **62(4)**:1544-1555.

[6] **Lee, S-Y., Heller, E. J.** 1982. Exact time-dependent wave packet propagation: application to the photodissociation of methyl iodide. *J. Chem. Phys.* **76(6)**:3035-3044.

[7] **Henriksen, N. E., Heller, E. J.** 1989. Quantum dynamics for vibrational and rotational degrees of freedom using Gaussian wave packets: application to the three-dimensional photodissociation dynamics of ICN. *J. Chem. Phys.* **91(8)**:4700-4713.

[8] **Frost, A. A.** 1967. Floating spherical gaussian orbital model of molecular structure. I. Computational procedure. LiH as an example. *J. Chem. Phys.* **47**:3707-3713. Seven other papers in this series available; see also references by **Pakiari A. H.** (fixing water geometry and lone pairs), **Walther, P.** and **Ratner, M.** (pseudopotentials), **Bartlett, R.** (use as correlating orbitals), **Borisov, Y.** (density functional theory), **Sales, K.** (different oribtals for different spins), **Ray, N. K.** (organometallics),

Linnett, J. W. (solving coalesence problem), and **Lu, S.-L.** (use as starting wave-function for quantum Monte Carlo).

[9] **Wilets, L., Henley, E. M., Kraft, M., Mackellar, A. D.** 1977. Classical many-body model for heavy-ion collisions incorporating the Pauli principle. *Nuc. Phys.* **A282**:341-350.

[10] **Kirschbaum, C. L., Wilets, L.** 1980. Classical many-body model for atomic collisions incorporating the Heisenberg and Pauli principles. *Phys. Rev. A.* **21(3)**:834-841.

[11] **Hansen, J. P., McDonald, I. R.** 1981. Microscopic simulation of a strongly coupled hydrogen plasma. *Phys. Rev. A.* **23(4)**:2041-2059.

[12] **Dorso, C., Duarte, S., Randrup, J.** 1987. Classical simulation of the fermi gas. *Phys. Lett. B.* **188(3)**:287-294.

[13] **Dorso, C., Radnrup, J.** 1988. Classical simulation of nuclear systems. *Phys. Lett. B.* **215(4)**:611-616.

[14] **Boal, D. H., Glosli, J. N.** 1988. Quasiparticle model for nuclear dynamics studies: ground-state properties. *Phys. Rev. C.* **38(4)**:1870-1878.

[15] **Boal, D. H., Glosli, J. N.** 1988. Quasiparticle model for nuclear reaction studies: quasiparticle dynamics. *Phys. Rev. C.* **38(6)**:2621-2629.

[16] **Klakow, D., Toepffer, C., Reinhard, P.-G.** 1994. Semiclassical molecular dynamics for strongly coupled Coulomb systems. *J. Chem. Phys.* **101(12)**:10766-10774.

[17] **Feldmeier, H., Schnack, J.** 2000. Molecular dynamics for fermions. *Rev. Mod. Phys.* **72(3)**:655-688.

[18] **Maruyama, T., Ohnishi, A., Horiuchi, H.** 1992. Evolution of reaction mechanisms in the light heavy-ion system. *Phys. Rev. C.* **45(5)**:2355-2368.

[19] **Beck, W. A., Wilets, L.** 1997. Semiclassical description of proton stopping by atomic and molecular targets. *Phys. Rev. A.* **55(4)**:2821-2829.

[20] **Knaup, M., Reinhard, P-G., Toepffer, C., Zwicknagel, G.** 2003. Wave packet molecular dynamics simulations of warm dense hydrogen. *J. Phys. A: Math. Gen.* **36**:6165-6171.

[21] **Cohen, J. S.** 1998. Extension of quasiclassical effective Hamiltonian structure of atoms through Z = 94. *Phys. Rev. A.* **57(6)**:4964-4966.

[22] **Wilson, C. W., Goddard, W. A. III.** 1972. *Ab initio* calculations on the $H_2 + D_2 \rightarrow 2HD$ four-center exchange reaction. II. Orbitals, contragradience, and the reaction surface. *J. Chem. Phys.* **56(12)**:5913-2920.

[23] Unless otherwise indicated, all thermochemistry and geometry data was taken from the NIST Chemistry Webbook: **Linstrom, P. J., Mallard, W. G., Eds** 2005. *NIST Chemistry Webbook*, NIST standard reference database number 69, National Institute of Standards and Technology, Gaithersburg, MD, 20899 (http://webbook.nist.gov).

[24] **Frost, A. A., Rouse, R. A.** 1968. A floating spherical gaussian orbital model of molecular structure. IV. Hydrocarbons. *J. Am. Chem. Soc.* **90**:1965-1969.

[25] **Hamilton, J. G., Palke, W. E.** 1993. Bonding in cylcopropane. *J. Am. Chem. Soc.* **115**:4159-4164.

[26] **Hoffman, R. W.** 1989. Allylic 1,3-strain as a controlling factor in stereoselective transformations. *Chem. Rev.* **89**:1841-1860.

[27] **Gage, J. R., Evans, D. A.** 1990. Diastereoselective aldol condensation using a chiral oxazolidinone auxiliary. *Org. Synth.* **68**:83-91.

[28] **Ellison, G. B., Engelking, P. C., Lineberger, W. C.** 1978. An experimental determination of the geometry and electron affinity of methyl radical. *J. Am. Chem. Soc.* **100**:2556-2558.

[29] **Dixon, D. A., Feller, D., Peterson, K. A.** 1997. Accurate calculations of the electron affinity and ionization potential of the methyl radical. *J. Phys. Chem. A.* **101**:9405-9409.

[30] **Perera, S. A., Bartlett, R. J., Schleyer, P. von R.** 1995. Predicted NMR coupling constants and spectra for ethyl carbocation: a fingerprint for nonclassical hydrogen-bridged structures. *J. Am. Chem. Soc.* **117**:8476-8477.

[31] **Koch, W., Liu, B., Schleyer, P. von R.** 1989. Definitive characterization of the $C_3H_7^+$ potential energy surface. *J. Am. Chem. Soc.* **111**:3479-3480.

[32] **Diedrich, D., Anderson, J. B.** 1994. Exact quantum Monte Carlo calculations of the potential energy surface for the reaction $H + H_2 \rightarrow H_2 + H$ *J. Chem. Phys.* **100(11)**:8089-8095.

[33] **Boothroyd, A. I., Martin, P. G., Keogh, W. J., Peterson, M. J.** 2001. An accurate analytic H_4 potential energy surface. 2001. *J. Chem. Phys.* **116(2)**:666-689.

[34] **Barbosa, A.G.H., Nascimento, M.A.C.** 2004. Ground state of the beryllium atom: reinvestigation based on a proper independent particle model. *Int. J. Quant. Chem.* **99**:317-324.

[35] **Kottke, T., Stalke, D.** 1993. Structures of the classical synthesis reagents $(BuLi)_6$ and $(Me3CLi)_4$ and the metastable $(Me_3CLi.OEt_2)_2$. *Angew. Chem. Int. Ed.* **32(4)**:580-582.

[36] **Dill, J. D., Schleyer, P.v.R., Pople, J. A.** 1975. Molecular orbital theory of the electronic structure of organic compounds. XXIV. Geometries and energies of small boron compounds. Comparisons with carbocations. *J. Am. Chem. Soc.* **97(12**:3402-3409.

[37] **Schreiner, P. R.** 2000. Does CH_5^+ have (a) structure? A tough test for experiment and theory. *Angew. Chem. Int. Ed.* **39(18)**:3239-3241.

[38] **Komornicki, A., Dixon, D.A.** 1987. Structure, vibrational spectrum, and energetics of the CH_5^+ ion. A theoretical investigation. *J. Chem. Phys.* **86(10)**:5625-5634.

[39] **Langmuir, I.** 1912. The dissociation of hydrogen into atoms. *J. Am. Chem. Soc.* **34**:860-877.

[40] **Saha, M. N.** 1920. Ionization in the solar chromosphere. *Phil. Mag.* **40**:72-88.

[41] **Nickel, G. H.** 1980. Elementary derivation of the Saha equation. *Am. J. Phys.* **48(6)**:448-450.

[42] **Van Horn, H. M.** 1991. Dense astrophysical plasmas. *Science.* **252(5004)**:384-389.

[43] **Saumon, D., Chabrier, G.** 1989. Fluid hydrogen at high density: the plasma phase transition. *Phys. Rev. Lett.* **62(20)**:2397-2400.

[44] **Saumon, D., Chabrier, G.** 1992. Fluid hydrogen at high density: pressure ionization. *Phys. Rev. A.* **46**:2084-2100.

[45] **Pierleoni, C., Ceperley, D.M., Bernu, B., Margo, W.R.** 1994. Equation of state of the hydrogen plasma by path integral Monte Carlo simulation. *Phys. Rev. Lett.* **73(16)**:2145-2149.

[46] **Militzer, B., Margo, W., Ceperley, D.** 1999. Characterization of the state of hydrogen at high temperature and density. *Contrib. Plasm. Phys.* **39(1-2)**:151-154.

[47] **Militzer, B., Ceperley, D.M.** 2000. Path integral Monte Carlo calculation of the deuterium hugoniot. *Phys. Rev. Lett.* **85(9)**:1890-1893.

[48] **Militzer, B., Ceperley, D.M.** 2001. Path integral Monte Carlo simulation of the low-density hydrogen plasma. *Phys. Rev. E.* **63**:66404.

[49] **Delaney, K. T., Pierleoni, C., Ceperley, D.M.** 2006. Quantum Monte Carlo Simulation of the high-pressure molecular-atomic crossover in fluid hydrogen. *Phys. Rev. Lett.* **97**:235707.

[50] **Margo, W.R., Ceperley, D.M., Pierleoni, C., Bernu, B.** 1996. Molecular dissociation in hot, dense hydrogen. *Phys. Rev. Lett.* **76(8)**:1240-1243.

[51] **Holmes, N.C., Ross, M., Nellis, W.J.** 1995. Temperature measurements and dissociation of shock-compressed liquid deuterium and hydrogen. *Phys. Rev. B.* **52(22)**:15835-15845.

[52] **Knudson, M.D., Hanson, D.L., Bailey, J.E., Hall, C.A., Asay, J.R., Anderson, W.W.** 2001. Equation of state measurements in liquid deuterium to 70 GPa. *Phys. Rev. Lett.* **87(22)**:225501.

[53] **Knudson, M.D., Hanson, D.L., Bailey, J.E., Hall, C.A., Asay, J.R.** 2003. Use of a wave reverberation technique to infer the density compression of shocked liquid deuterium to 75 GPa. *Phys. Rev. Lett.* **90(3)**:35505.

[54] **Da Silva, L.B., et al.** 1997. Absolute equation of state measurements on shocked liquid deuterium up to 200 GPa (2 Mbar). *Phys. Rev. Lett.* **78(3)**:483-486.

[55] **Collins, G.W., et al.** 1998. Measurements of the equation of state of deuterium at the fluid insulator-metal transition. *Science.* **281**:1178-1181.

[56] **Thompson, M., Baker, M.D., Christie, A., Tyson, J.F.** 1985. *Auger electron spectroscopy.* John Wiley and Sons (ISBN 0-471-04377-X).

[57] **Coville, M., Thomas, T.D.** 1991. Molecular effects on inner-shell lifetimes: possible test of the one-center model of Auger decay. *Phys. Rev. A.* **43(11)**:6053-6056.

[58] **Prince, K. C., Richter, R., de Simone, M., Coreno, M.** 2003. Dynamics of core hole states and ultrafast dissociation of organic molecules. *Elettra research highlights*, http://www.elettra.trieste.it/science/highlights/2003-2004/elettra-hl0304-r03.pdf.

[59] **Auger, P.** 1923. The secondary rays produced in a gas by X-rays. *Compt. Rend.* **177**:169-172.

[60] **Tilinin, I. S., Jablonski, A., Werner, W. S. M.** 1996. Quantitative surface analysis by Auger and x-ray photoelectron spectroscopy. *Prog. Surf. Sci.* **52(4)**:193-335.

[61] **Tarantelli, F., Cederbaum, L. S., Sgamellotti, A.** 1995. The ab initio simulation of Auger spectra. *J. Elec. Spec. and Rel. Phenom.* **76**:47-54.

[62] **Rye, R. R., Jennison, D. R., Houston, J. E.** 1980. Auger spectra of alkanes. *J. Chem. Phys.* **73(10)**:4867-4874.

[63] **Knotek, M. L., Feibelman, P. J.** 1978. Ion desorption by core-hole Auger decay. *Phys. Rev. Lett.* **40(14)**:964-967.

[64] **Knotek, M. L., Jones, V. O., Rehn, V.** 1979. Photon-stimulated desorption of ions. *Phys. Rev. Lett.* **43(4)**:300-303.

[65] **Jennison, D. R., Kelber, J. A., Rye, R. R.** 1982. Localized Auger final states in covalent systems. *Phys. Rev. B.* **25**:1384-1387.

[66] **Gillis, H.P., et al** 1995. Low energy electron-enhanced etching of Si(100) in hydrogen/helium direct-current plasma. *Appl. Phys. Lett.* **66(19)**:2475-2477.

[67] **Takahashi, O., et al** 2006. Auger decay calculations with core-hole excited-state molecular-dynamics simulations of water. *J. Chem. Phys.* **124**:064307.

[68] **Brena, B., et al.** 2004. Ultrafast molecular dissociation of water in ice. *Phys. Rev. Lett.* **93(14)**:148302.

[69] **Bieri, G., Burger, F., Heilbronner, E., Maier, J. P.** 1977. Valence ionization energies of hydrocarbons. *Helv. Chim. Acta.* **60(7)**:2213-2233.

[70] **Myrseth, V., Bozek, J. D., Kukk, E., Saethre, L. J., Thomas, T.D.** 2002. Adiabatic and vertical carbon 1s ionization energies in representative small molecules. *J. Elec. Spec. and Rel. Phen.* **122**:57-63.

[71] **Carroll, T. X., et al.** 1999. Carbon 1s photoelectron spectrum of methane: Vibrational excitation and core-hole lifetime. *Phys. Rev. A.* **59(5)**:3386-3393.

[72] **Karlsen, T., et al.** 2001. Vibrational structure and vibronic coupling in the carbon 1s photoelectron spectra of ethane and deuteroethane. *J. Phys. Chem. A.* **105**:7700-7706.

[73] **Kukk, E., et al/** 2002. Dissociation of deuteromethane following carbon 1s core ionization. *Phys. Rev. A.* **66**:012704.

[74] **Jennison, D. R., Kelber, J. A., Rye, R. R.** 1982. Localized Auger final states in covalent systems. *Phys. Rev. B.* **25(2)**:1384-1387.

Chapter 3

Development of an electron force field. II. New treatment of p-like electrons, resulting in improved accuracy for first-row atoms, atom hydrides, and hydrocarbons

Introduction

Previously we introduced an electron force field which we used to simulate matter at extreme conditions — the dissociation and ionization of hydrogen at intermediate densities, and the Auger dissociation of hydrocarbons. We would like to simulate excited electron dynamics at lower temperatures, investigating processes such as electrolysis, electrochemistry, combustion, unimolecular decomposition, and organic reactions with solvated electrons. For this to be possible, we need to improve the scope and accuracy of the electron force field.

We assumed previously that we could treat the electrons as if they were all the same shape and could be well-represented by spherical Gaussian functions. For hydrogen and saturated hydrocarbons with excess energy, this approximation was a reasonable one. For molecules with lone pairs or multiple bonds, however, the approximation breaks down and in the old eFF (1) atoms with lone pairs were too easily ionized, (2) radical electrons in alkyl radicals were too diffuse, and (3) multiple bond electrons were too diffuse, all indications that we were not properly

describing p electrons.

In this chapter, we describe a way to include the effects of different electron shapes. This results in an improved description of first-row atoms, atom hydrides, and hydrocarbons and, to a lesser extent, hydrogen bonds and molecules containing heteroatoms.

How can we incorporate electrons with different shapes into an electron force field? One approach is to make the electron's shape explicit, by writing each orbital as a sum of higher angular momentum functions. This is the tack taken by most *ab initio* methods today. With the floating spherical gaussian orbital (FSGO) method, water has a too-small bond angle of 89º versus 104º exact [1], but making the lone pairs variationally optimized sums of floating s and p functions makes it possible [2] to raise the bond angle to 104º.

It is difficult however to make this approach general. Adding floating higher angular momentum basis functions to FSGO causes the method to become as complex and expensive as traditional *ab initio* methods, with the added complication that there are additional parameters to optimize, and problems if basis functions move on top of each other and become linearly dependent.

We take a different approach. First, we make electron shape an implicit scalar variable that depends solely on the electron's proximity to the nuclei in the system. This approximation arises from the observation that it is the nuclei and their associated core electrons that most greatly perturb and determine electron shape. Second, we make energy terms such as Pauli repulsion and wavefunction kinetic energy depend on electron shape. Using such an approach, we maintain the simplicity of the spherical Gaussian description while still accounting for the diversity of electron shapes present in excited electron systems.

The chapter is organized as follows. First we discuss the new energy expressions, and give a physical motivation for the terms we have changed and added. Then we study the energies and structures of first row atoms, atom hydrides, carbon-carbon single and multiple bonds, heteroatom single and multiple bonds, and van der Waals dimers. Along the way we point out both how eFF has im-

proved, and what systems it can describe better, and then demonstrate systems that we can newly describe that the old eFF could not describe. We also discuss limitations that remain, and suggest what the causes of those limitations might be.

Methods

Energy expression

As before, the system is composed of point nuclei with coordinates $\mathbf{R}$ and momenta $\mathbf{P}$, and of electrons defined by spherical Gaussian wave packets with positions $\mathbf{x}$, translational momenta $\mathbf{p_x}$, sizes s, and radial momenta p_s:

$$\Psi \propto \prod_j \exp\left[-\left(\frac{1}{s^2} - \frac{2p_s}{s}i\right)(\mathbf{r} - \mathbf{x})^2\right] \cdot \exp[i\mathbf{p_x} \cdot \mathbf{x}]. \qquad (3.1)$$

The overall energy is a sum of the Hartree product kinetic energy, Hartree product electrostatic energy, and antisymmetrization (Pauli) energy:

$$E = E_{ke} + E_{nuc \cdot nuc} + E_{nuc \cdot elec} + E_{elec \cdot elec} + E_{Pauli}.$$

The electrostatic energy expressions are the same as before:

$$
\begin{aligned}
E_{nuc \cdot nuc} &= \sum_{i<j} \frac{Z_i Z_j}{R_{ij}} \\
E_{nuc \cdot elec} &= -\sum_{i,j} \frac{Z_i}{R_{ij}} \operatorname{Erf}\left(\frac{\sqrt{2}\,R_{ij}}{s_i}\right) \\
E_{elec \cdot elec} &= \sum_{i<j} \frac{1}{x_{ij}} \operatorname{Erf}\left(\frac{\sqrt{2}\,x_{ij}}{\sqrt{s_i^2 + s_j^2}}\right).
\end{aligned}
$$

There are two major changes from the old eFF. First, we divide electrons into core and valence electrons, and assume they do not switch categories over the course of the simulation. We assume an electron is a core electron if $s_i < 1.5 \cdot s_{core}$ and

$|x_i - \mathbf{R_{nuc}}| < 0.5 \cdot s_{core}$, where

$$s_{core} = \frac{3\sqrt{\pi}}{2\sqrt{2}Z_{nuc} - 1}$$

is the size of a helium-like ion optimized with eFF.

Second, we make the kinetic and Pauli energies depend on the hybridization of an electron, which can vary during the course of the simulation, and depends on the proximity of the electron to the nuclei present in the system. We have

$$E_{ke} = \sum_i \frac{3}{2} \frac{1}{s_i^2} \cdot f_{ke}$$

$$E_{Pauli} = \sum_{\sigma_i = \sigma_j} \frac{1}{2} \frac{S_{ij}}{1 - S_{ij}^2} \Delta T_{ij} \cdot (f_{repel} + f_{switch})$$

where, as before, ΔT_{ij} is a measure of the kinetic energy change upon antisymmetrization, and S_{ij} is the overlap between two wave packets:

$$\Delta T_{ij} = \frac{3}{2} \left(\frac{1}{s_1^2} + \frac{1}{s_2^2} \right) - \frac{2(3(s_1^2 + s_2^2) - 2x_{12}^2)}{(s_1^2 + s_2^2)^2}$$

$$S_{ij} = \left(\frac{2}{s_i/s_j + s_j/s_i} \right)^{3/2} \exp(-x_{ij}^2/(s_i^2 + s_j^2))$$

and the factors f_{KE}, f_{repel}, and f_{switch} are defined as follows:

$$f_{ke} = c_{s-ke}\chi_{ke} + c_{p-ke}(1 - \chi_{ke})$$

$$f_{repel} = \left[c_{repel} + c_{size} \left(\frac{s_2}{s_1} + \frac{s_1}{s_2} - 2 \right) \right] \cdot \frac{S_{ij}}{1 - S_{ij}^2}$$

$$f_{switch} = [c_{s-Pauli}\chi_{Pauli} + c_{p-Pauli}(1 - \chi_{Pauli})] \cdot (1 - S_{ij})$$

which depend on the hybridization variables χ_{ke} and χ_{Pauli}, which equal one for an electron with s character only, and zero for an electron with p character only. Hybridization is a function of an electron's position relative to the protons and cores (nuclei with core electrons on top of them) in the system. We assume that all nuclei with $Z > 2$ have $1s^2$ core electrons on top of them. The expression for

χ_{ke} is

$$\chi_{ke} \quad = \quad \prod_{protons} \zeta_{proton}\left(\frac{|x_i - R_{proton}|}{s_i}\right) \cdot \left[1 - \prod_{cores} \zeta_{core}\left(\frac{|x_i - R_{core}|}{s_i}\right)\right]$$

if $i, j \in$ valence electrons, 1 otherwise

while the expression for χ_{Pauli} is

$$\chi_{Pauli} \quad = \quad \prod_{protons} \zeta_{proton}\left(\frac{|x_i - R_{proton}|}{s_i}\right) \cdot \zeta_{proton}\left(\frac{|x_j - R_{proton}|}{s_j}\right)$$

$$\cdot \left[1 - \prod_{cores} \zeta_{core}\left(\frac{|x_i - R_{core}|}{s_i}\right) \zeta_{core}\left(\frac{|x_j - R_{core}|}{s_j}\right) \sin^2 \theta_{i-core-j}\right]$$

if $i, j \in$ valence electrons, 1 otherwise.

The parameters c_{repel}, c_{size}, $c_{s-Pauli}$, $c_{p-Pauli}$, c_{s-ke}, c_{p-ke} are shown in Table 3.1.

Parameter	Value	Purpose
c_{repel}	0.5	Prevents electron coalescence
c_{size}	3	Nearby electrons tend to match size
$c_{s-Pauli}$	1	Pauli is repulsive for s-like electrons
$c_{p-Pauli}$	-1	Pauli is attractive for p-like electrons
c_{s-ke}	1	No change in kinetic energy for s-like electrons
c_{p-ke}	1.2	Slightly larger kinetic energy for p-like electrons

Table 3.1: Parameters in the new eFF, in addition to splines in Table 3.2.

The functions ζ_{proton} and ζ_{core} determine how an electron's p versus s character varies with their distance from the protons and cores in the system. They are defined as piecewise quintic splines specified so that the function's value, first, and second derivatives match at the points given:

$$\{x_1, f(x_1), f'(x_1), f''(x_1)\} \ldots \{x_N, f(x_N), f'(x_N), f''(x_N)\}.$$

Written in terms of the boundary conditions and matching points, we have

$$
\zeta_{proton}(r) = \begin{cases} \text{spline} \begin{pmatrix} \{0, & 0.5, & 0.55, & 0\} \\ \{2.5, & 1, & 0, & 0\} \end{pmatrix} & \text{if } r < 2.5 \\[2ex] 1 & \text{if } r \geq 2.5 \end{cases}
$$

$$
\zeta_{core}(r) = \begin{cases} \text{spline} \begin{pmatrix} \{0, & 0, & 0, & 25/18\} \\ \{0.6, & 1, & 0, & -25/18\} \\ \{1.5, & 0, & 0, & 25/18\} \end{pmatrix} & \text{if } r < 1.5 \\[3ex] 0 & \text{if } r \geq 1.5 \end{cases} .
$$

Explicit polynomial expressions for ζ_{proton} and ζ_{core} are given in Table 3.2.

	ζ_{proton}		ζ_{core}		
	$r < 2$	$r > 2$	$r < 0.6$	$0.6 < r < 1.5$	$r > 1.5$
c_0	0.500000	1.000000	0.000000	-8.487654	0.000000
c_1	0.550000	0.000000	0.000000	49.897119	0.000000
c_2	0.000000	0.000000	6.944444	-100.222908	0.000000
c_3	-0.208000	0.000000	0.000000	97.165066	0.000000
c_4	0.089600	0.000000	-19.290123	46.677336	0.000000
c_5	-0.011520	0.000000	12.860082	8.890921	0.000000

Table 3.2: Polynomial coefficients for quintic splines, $\zeta = \sum_i c_i r^i$.

Explanation of the energy expressions

What gives an electron p character? Consider the electron configuration of neon, with its ten electrons. Two electrons pair up on top of the neon nucleus to form a helium-like core, while the other eight electrons — four spin up and four spin down — are valence electrons that surround the core. We assume that the core electrons form a high concentration of charge around the nucleus that is unperturbed by the presence of valence electrons. Then in order for valence and core electrons to have zero overlap and satisfy the Pauli principle, the valence electron must change sign over the region of the core electron.

For lithium and beryllium, the valence electrons are centered on top of the core electrons, and change sign over the core via a radial node contained in a $2s$ function. For neon, the eight valence electrons cannot all be centered on top of the core electrons, and they instead pack into a tetrahedral or cubic arrangement. In this case — when the electron is shifted off-center — a planar node is preferred, and is represented by a higher angular momentum $2p$ function with no radial nodes.

Imagine an electron approaching a nucleus with surrounding core electrons. Far from the core, the electron is spherical and has the characteristics of a $1s$ function. Closer to the core, the electron develops a planar node and attains p-character. Once on top of the core, the electron develops a radial node and becomes s-like again. In the eFF energy expressions, this p character dependence is represented as a spline that is zero for r $= 0$, rises to a maximum when $x/s = 0.6$, then falls back to zero when $x/s = 1.5$ (Figure 3.1).
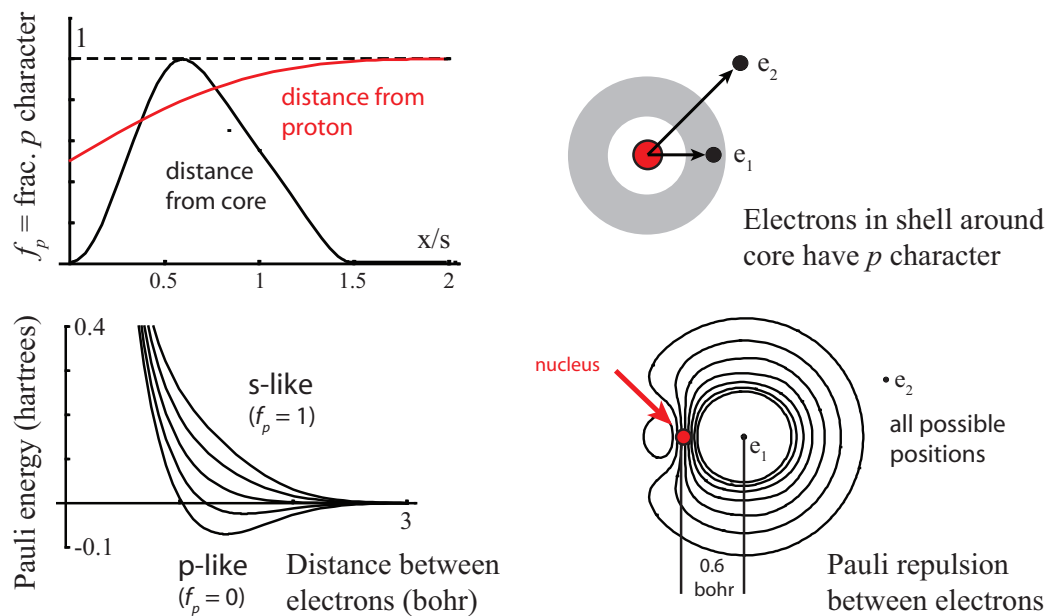
Figure 3.1: Pauli interaction between p-like versus s-like electrons.

The above explains why an electron's shape is modified by the presence of core electrons, which we assume to surround any nuclei with $Z > 2$. We discover that bare nuclei, such as protons and helium nuclei, also affect the shape of nearby

electrons, causing them to become more s-like.

Consider methane. The valence electrons that form the carbon-hydrogen bonds skew toward the proton and away from the nucleus, which make them more s-like than the valence electrons in neon. This is reflected in Pauling's hybridization model [3], which assigns neon valence electrons p hybridization and methane valence electrons sp^3 hybridization. A proton's effect on hybridization is greatest when the proton is near the center of the electron; in the energy expression, this effect is represented by a spline which goes to 0.5 when $x/s=0$, then rises to become 1 when $x/s = 2.5$.

We assume that these two factors — electron proximity to cores, and electron proximity to bare nuclei — are sufficient to determine an electron's hybridization/shape, which we represent with the scalar quantity χ_{ke}; there is an analogous two-body quantity χ_{Pauli} we describe later as well, which includes angle effects. We now discuss how electron shape affects the components in the eFF energy expression.

First, p-like electrons have a higher kinetic energy than similarly sized s-like electrons, due to the presence of the planar node. This effect appears in the eFF energy expression as the factor f_{ke}, which scales between the two extremes c_{s-ke}, the multiplier for a pure s function, and c_{p-ke}, the multiplier for a pure p function. The hybridization variable χ_{ke} varies between one for a pure s function and zero for a pure p function, and is a multiplicative combination of contributions from all nearby protons and cores.

The end result is that the kinetic energy of electrons is raised slightly around cores, which is an effective two-body repulsion between cores and electrons. This interaction has the same character — though the opposite sign — as a conventional force field bond term.

Second, when electrons attain p character, their Pauli repulsion can turn into Pauli attraction. At one extreme is the exchange interaction that stabilizes high-spin configurations of atoms, e.g., Hund's rule; at the other extreme is the repulsion between helium atoms that causes them to repel.

The physical origin of the Pauli attraction between valence electrons on the same atom is as follows. Recall from the last chapter that Pauli repulsion is the consequence of kinetic energy increase upon orbital orthogonalization. However, in an atom like neon, the p electrons are already orthogonal to each other, due to the relative geometry of the planar nodes. Thus the kinetic energy repulsion vanishes, and instead a second-order attractive interaction — two-body exchange energy — becomes dominant. The exchange term arises because the Pauli principle causes same-spin electrons to avoid occupying the same region of space, which causes electron-electron repulsion to decrease. Hence we expect that neon valence electrons are stabilized not only by their attraction to the nucleus, but also by their Pauli attraction to each other.

In the electron force field, E_{Pauli} is modified by two terms, f_{repel}, which ensures that electrons do not coalesce, and f_{switch}, which causes s-like electrons to repel and p-like electrons to attract. They occupy separate ranges: f_{repel} dominates at high overlap, while f_{switch} dominates at lower overlap.

The term f_{switch} is a three-body term that modifies the Pauli interaction between two electrons and depends on the proximity of nearby cores and bare nuclei. It is a function not only of electron-nuclear distances, but also of the electron-core-electron angle; the attractive term reaches a maximum when the electrons are 90º apart from each other. The combined effects of f_{repel} and f_{switch} pushes the electrons apart to an angle larger than 90º in first-row atoms (Figure 3.1).

We consider the f_{switch} modification to the Pauli interaction to be analogous to a conventional force field angle term, since it depends on the electron-core-electron angle. As with the bond term, the effect is limited in range with a strict spline cutoff, so it is not overly expensive to compute.

The f_{repel} term is a two-body electron-electron term, but is new in this eFF; it addresses a problem found in the previous eFF, which is that same size electrons could coalesce under extreme conditions. In the new formulation, we have a singularity at $S = 1$ so that coalescence of same size electrons is no longer possible. We have also added a term that encourages nearby electrons to have the same size.

This helps to stabilize species such as methyl radical, where the radical electron would otherwise be too large. Figure 3.2 shows a comparison between old and new eFF versions of the Pauli repulsion between s-like electrons.
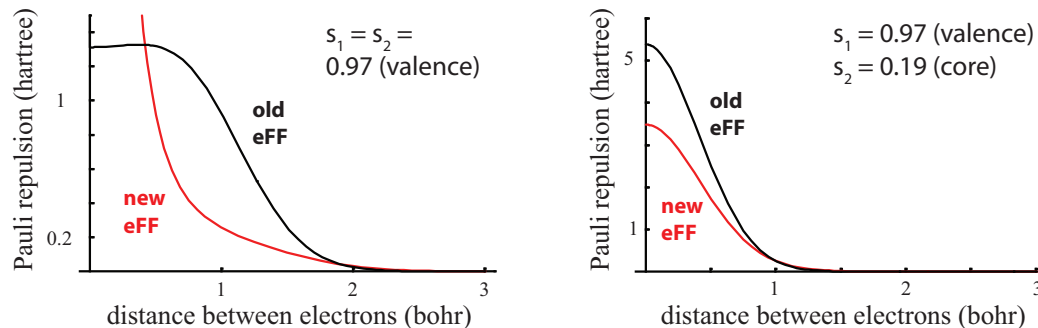
Figure 3.2: Pauli repulsion between s-like electrons is modified to make electron sizes more similar and prevent electron-electron coalescence.

We assume that electrostatics are unchanged between the old and new eFF, and we leave the terms $E_{nuc-nuc}$, $E_{nuc-elec}$, and $E_{elec-elec}$ the same as before. It is possible there could be some benefit to making these terms dependent on electron shape. However the electrostatics in our model are sensitive to small changes, and we have found that most modifications to them cause problems with atom and bond stabilities.

Results and discussion

Atom ionization potentials and polarizabilities

We create atoms with total spins satisfying Hund's rule. When optimized with eFF, hydrogen, helium, lithium, and beryllium all have nucleus-centered electrons, consistent with their electron configurations $1s^1$, $1s^2$, $1s^2 2s^1$, and $1s^2 2s^2$. In boron through neon, the valence electrons arrange themselves according to two rules: (1) same spin electrons form close-packed symmetric shells (i.e., nucleus centered point, line, triangle, or tetrahedron) and (2) shells of up-spin and down-spin electrons rotate relative to each other to minimize electron-electron repulsion. In neon, for example, the up and down spin electrons form two separate tetrahedral shells

which interpenetrate each other to form a cubic lattice (Figure 3.3.
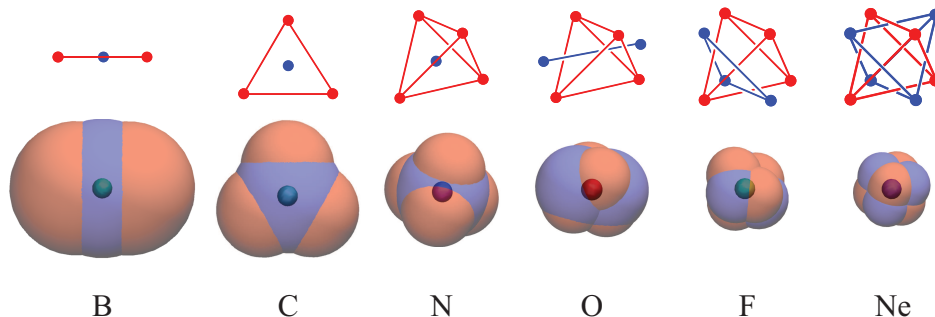
Figure 3.3: Valence electrons of boron through neon arrange themselves into symmetric shells.

The new eFF properly reproduces periodic trends in the adiabatic ionization potential $E(Z) - E(Z+1)$ (Figure 3.4). It is remarkable that with only one set of parameters for the entire set of atoms, and with only spherical Gaussian functions, we are able to properly describe the balance between electron penetration and shielding, and the filling in of $1s$, $2s$, and $2p$ shells, while also reproducing the special stability of half-filled p subshells.
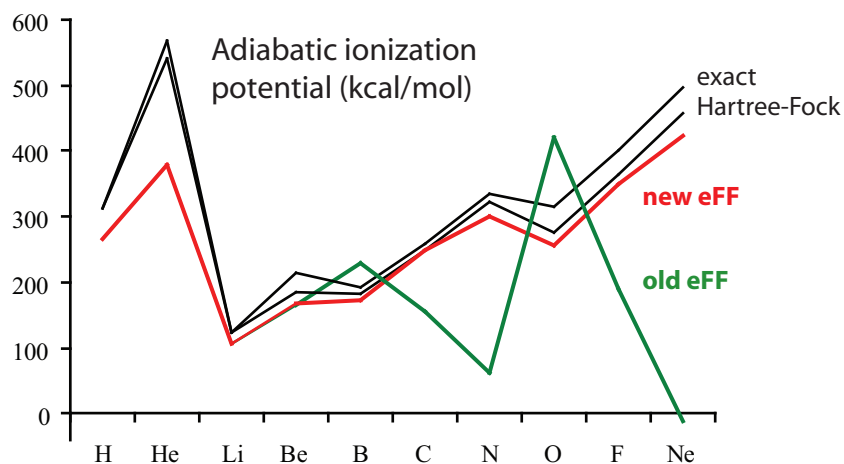
Figure 3.4: The new eFF reproduces the correct periodic trend of ionization potentials for hydrogen through neon, while the old eFF is only suitable for describing hydrogen through carbon.

It is also clear why the old eFF worked well for the atoms hydrogen through carbon, but was not suitable for describing nitrogen, oxygen, fluorine and neon — the ionization potentials starting from boron decreased rather than increased with increasing Z, which was acceptable for boron and carbon, but which led to incorrect IPs for larger Z atoms, culminating in neon being unstable. The old eFF had the incorrect Z dependence for ionization potential because it lacked stabilizing exchange interactions between valence electrons on the same atom.

In addition to ionization potentials, we computed atomic polarizabilities with eFF. This was done using a finite difference approach; the values plotted in Figure 3.5 are the averaged eigenvalues of the atomic polarizability tensor. Polarizabilities have units of volume, and can be taken as a measure of the size of the electrons in a system.
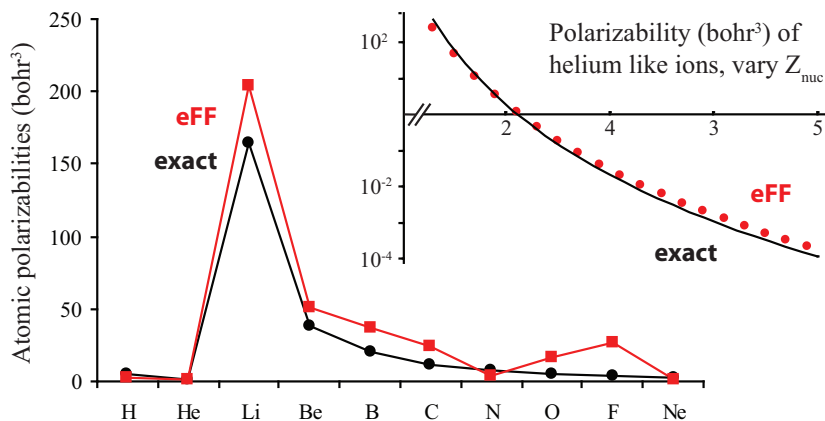
Figure 3.5: The new eFF computes reasonable polarizabilities for first-row atoms. Oxygen and fluorine are exceptional cases, as the eFF gives those two atoms a permanent dipole moment which they should not have.

The simplest cases are the helium-like ions, which contain two nucleus-centered electrons, and a nucleus of variable charge. eFF values were compared to values computed using first-order coupled perturbed Hartree-Fock theory [4]. We found that eFF gave polarizabilities that agreed well with theory over six orders of magnitude. This gave us confidence that eFF could properly describe polarizabilities over a wide range of electron sizes.

We found that first-row atomic polarizabilities were slightly too high ($\sim$15%) for lithium through carbon, and too low ($\sim$30-50%) for nitrogen and neon. Oxygen and fluorine have too-high polarizabilities because eFF gives those atoms a non-spherical charge distribution, which results in a permanent dipole moment that does not exist in the actual atom — the atoms rotate in the presence of an electric field, which produces an artificially high polarizability. All in all though, we find that the general periodic trend is correctly reproduced. eFF may prove to be a useful way to obtain molecular polarizabilities as well, since dipole-dipole, atomic polarizability, and Pauli effects are taken into account in a self-consistent way.

Atom hydrides

We optimize with eFF a series of atom hydrides AH_n, where A = carbon, nitrogen, oxygen, and fluorine, and $n = 1 - 4$ (Figure 3.6). In all cases, we have selected the spin state corresponding to the most stable known ground state geometry. We find very good agreement with known bond lengths and angles (Figure 3.7) and moderately good agreement with known bond dissociation energies $AH_n \rightarrow AH_{n-1} + H$ (Figure 3.8). We reproduce (1) the shrinking of bond lengths with increasing Z, (2) the larger bond angles in CH_2 and CH_3 versus NH_2 and NH_3, and (3) the fact that bonds to nitrogen are weaker due to the special stability of the nitrogen half-filled p shell.

It is encouraging that eFF can describe both radical species and closed-shell species correctly, and at the same level of accuracy. This bodes well for the application of eFF to processes where radical species are present, for example in combustion or oxidation reactions. The closed-shell molecules CH_4, NH_3, OH_2, and FH are isoelectronic with each other, and we find that in these geometries, electrons spin pair with each other. In the open-shell molecules, bond pair electrons are spin paired, but lone pair electrons separate from each other as they do in the free atoms.

Just as CH_4, NH_3, OH_2, and FH are isoelectronic with each other, the molecules CH_3, NH_2, and OH are isoelectronic as well, as are the molecules CH_2 and NH.
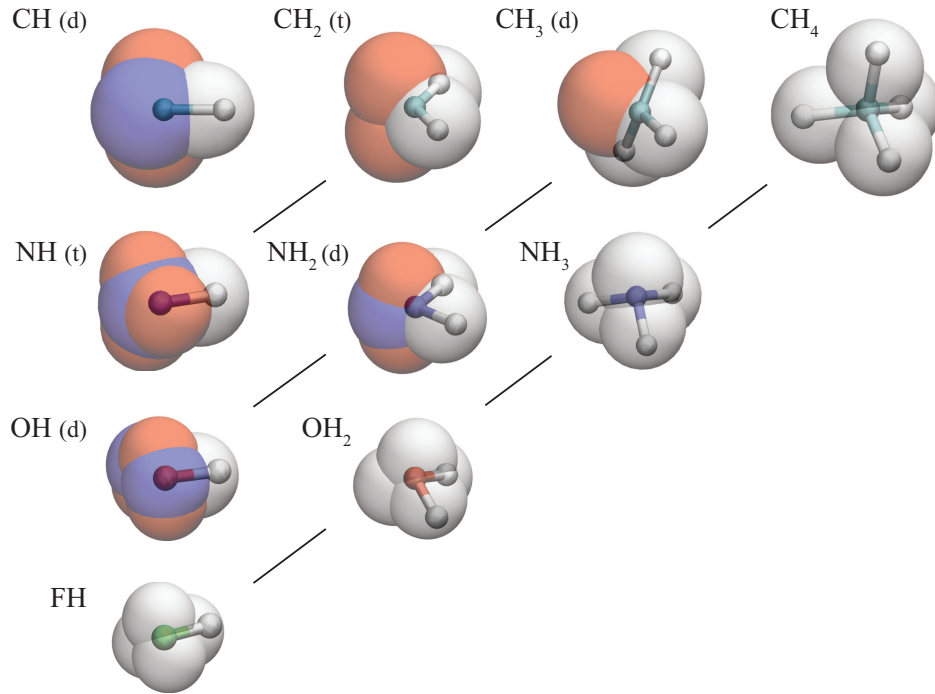
Figure 3.6: eFF describes both open-shell and closed-shell atom hydrides properly.
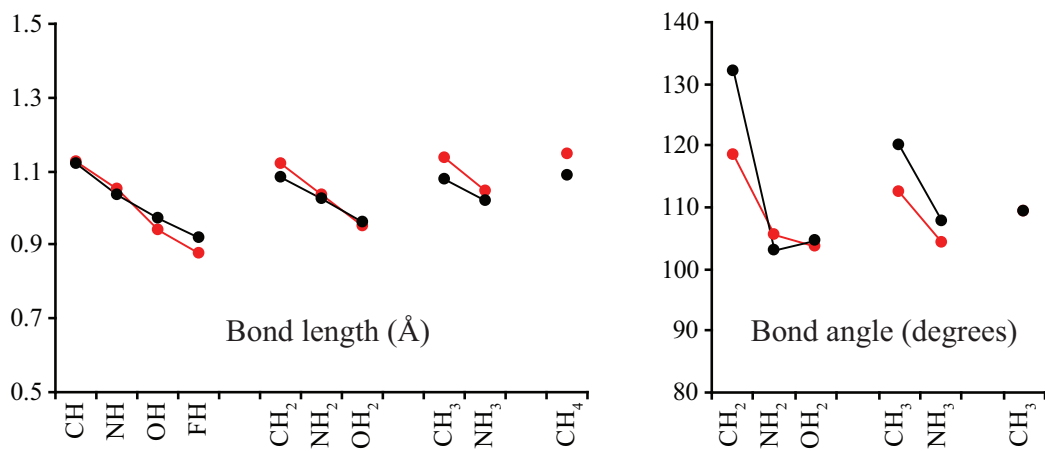
Figure 3.7: Atom hydride bond lengths and angles.
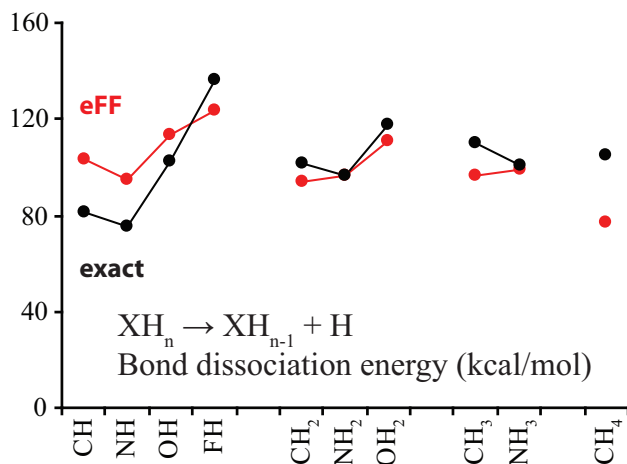
Figure 3.8: Atom hydride bond dissociation energies.

These similarities are reflected in the correspondence of electron arrangements as shown in Figure 3.6. We see, for example, that we can transform $OH(d)$ to $NH_2(d)$ by decreasing the nuclear charge by one and adding a proton, which brings two opposite spin electrons together, and leaves three electrons as lone pair electrons.

It is evident that the nuclei in atom hydrides are in the correct positions, but what about the bond pair and lone pair electrons? Their positions are not directly observable quantities, but we can get some sense of where electrons should be by finding the average position of Boys localized electrons using a density functional theory calculation (B3LYP/6-311g**). For the molecules CH_4, NH_3, OH_2, FH, and Ne, we find that the distance between bond pair electrons and the central nucleus matches those found with DFT, as do the angles between lone pair electrons (Figures 3.9 and 3.10).

However, we find that eFF lone pair electrons are about ∼0.2 bohr further away from the nucleus than they are in DFT. This trend is made further visible if we plot the electron densities of the lone pairs along the electron-center/nuclear-center axis, comparing eFF to DFT (Figure 3.11). In the density functional theory calculation, both the bond pair and the lone pair have a planar node, and are shifted asymmetrically in one direction, with the degree of shift greater in the bond pair than in the lone pair.
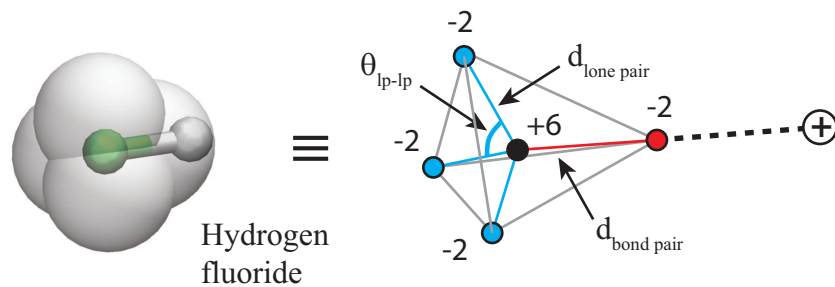
Figure 3.9: Measuring electron-nuclear distances and the angle between lone pairs.
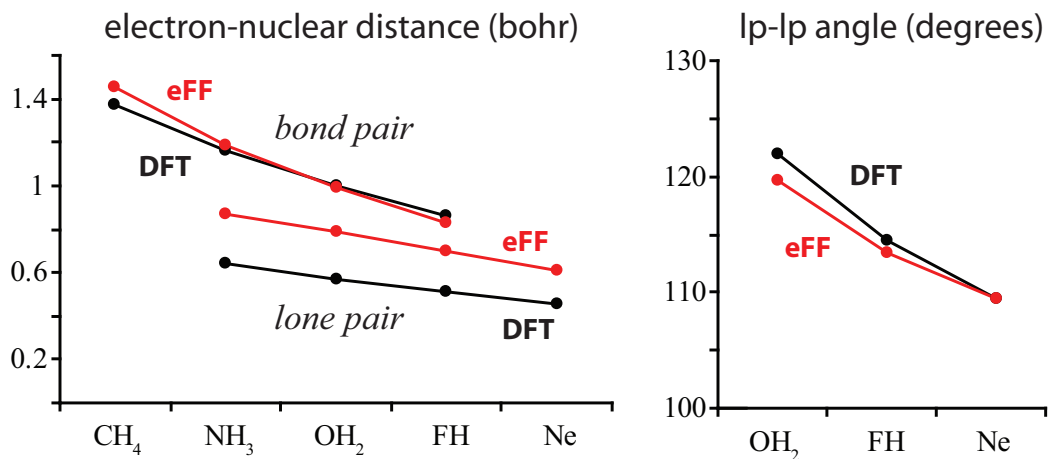
Figure 3.10: Comparison of eFF electron positions versus B3LYP localized orbital positions. There is good agreement, except that eFF lone pairs are further away from the nucleus than B3LYP lone pairs.
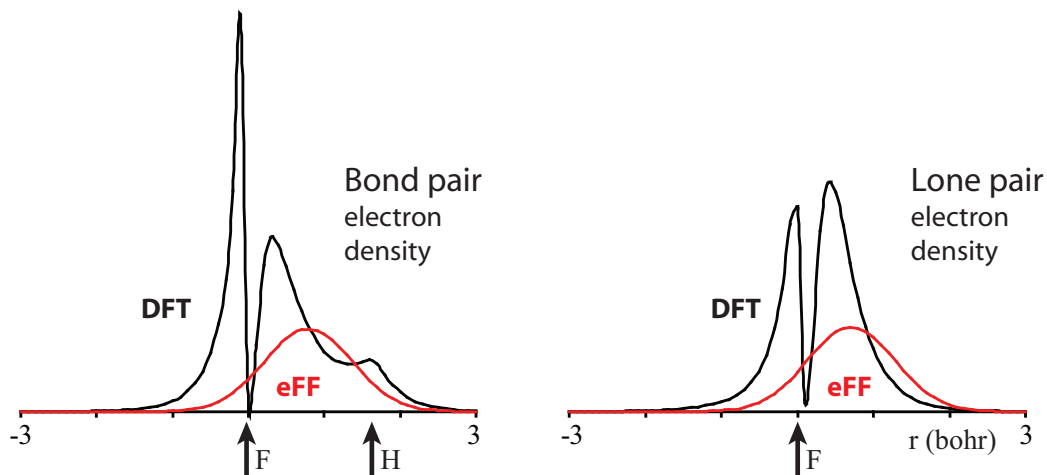
Figure 3.11: Electron densities along lone pairs and bond pairs; a comparison between eFF electron densities and B3LYP localized orbital electron densities.

The eFF wavefunction in contrast has no planar node, but is centered in a way that roughly overlaps the wavefunction on the "bonding side" of the node. This results in good overlap between eFF and DFT wavefunctions in the case of the bond pair, where the "bonding lobe" dominates; but worse overlap in the case of the lone pair, where there is substantial electron density on both sides of the planar node.

In other words, eFF may not describe properly the fact that lone pairs have density on both sides of the nucleus. This does not affect bonding in atom hydrides, but it does make the dipole moment of atom hydrides too high (e.g., FH dipole moment of 2.76 D versus 1.90 D exact; OH_2 dipole moment of 3.27 D versus 1.86 D exact; Figure 3.3), which causes problems in describing intermolecular interactions, as we shall see later. It may also account for the CH_2 singlet-triplet splitting having the wrong sign (singlet found to be 11 kcal/mol more stable than the triplet, when it should be 9.4 kcal/mol less stable [5]).

By optimizing the ionization potentials of high-spin atoms, we have been able to obtain accurate geometries and bond dissociation energies for atom hydrides.

contribution	dipole (debye)	
	eFF	DFT
nuclei	4.20	4.41
$\mathbf{d_{bp \cdot nuc}} - \mathbf{d_{lp \cdot nuc}}$	**-0.68**	**-1.79**
$\theta_{lp \cdot lp} - 109.5^o$	-0.76	-0.72
total	2.76	1.90

Table 3.3: Contributions to the dipole moment of hydrogen fluoride.

We have had the benefit of optimizing the proton-p-character spline to achieve this goal, but it is surprising that optimizing one polynomial creates an agreement that persists over such a range of molecules. By making comparisons to DFT localized orbitals, we find that the bonding electrons are in the locations we would expect, and that the lone pairs, though "lopsided" do make the correct angles with each other. With the caveat that lone range electrostatics is not properly described due to the too-high dipole moments of atom hydrides, we move on to consider other types of bonds.

Carbon-carbon single and multiple bonds

In the new eFF, carbon-carbon single bonds have the bond-centered closed-shell form as in the old eFF; but double and triple bonds now exist as banana bonds instead of sigma-pi bonds (Figure 3.12). Without any particular optimization of parameters, we find that carbon-carbon bond lengths for ethane, and ethylene, and acetylene are within 0.01 Å of the exact values (Figure 3.13). Carbon-hydrogen bond lengths are slightly longer than they should be by ≈ 0.05 Å.

As in the old eFF, carbon-carbon single and double bonds are too strong (for ethane, 140 kcal/mol BDE versus 90 kcal/mol BDE exact; for ethylene, 211 kcal/mol BDE versus 170 kcal/mol BDE exact). Carbon-hydrogen bonds are too weak (for ethane, 76 kcal/mol BDE versus 100 kcal/mol BDE exact; for ethylene, 82 kcal/mol BDE versus 113 kcal/mol BDE exact). The *differences* in CC and CH bond dissociation energies between ethane, and ethylene, and acetylene however are close to the exact values (with the exception of the CC triple bond energy),

107

ethane, staggered
versus eclipsed

ethylene and
twisted form
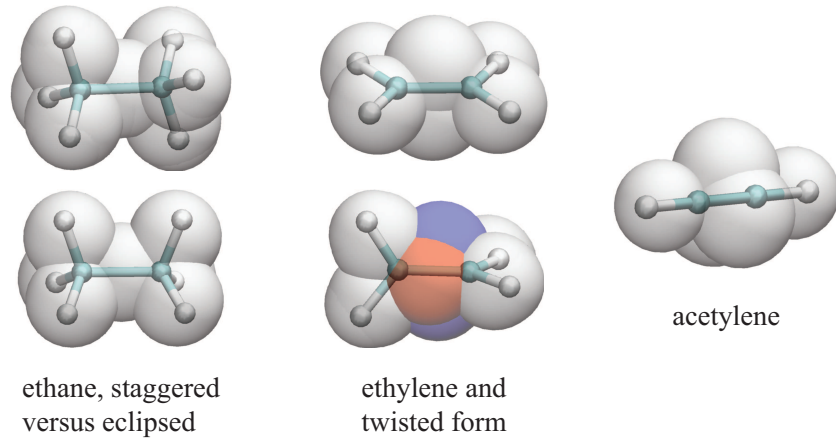
acetylene

Figure 3.12: Electron arrangements in carbon-carbon single, double, and triple bonds.
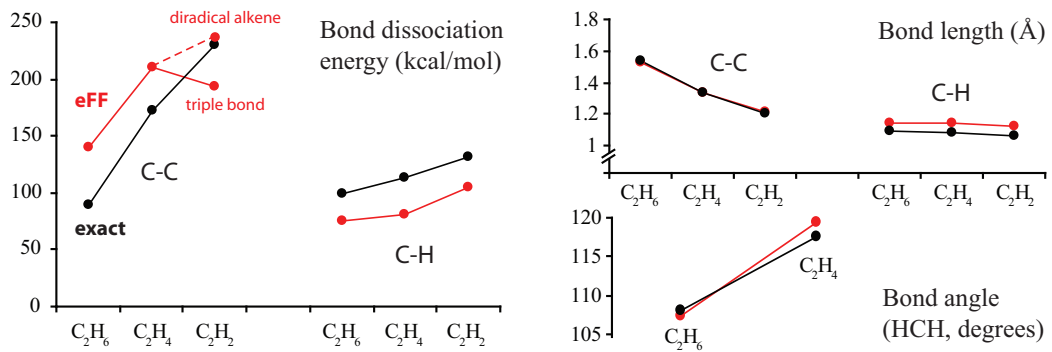
Figure 3.13: Bond dissociation energies and geometry parameters of ethane, ethylene, and acetylene.

suggesting that the energy differences stem from a systematic bias in the energetics of CC versus CH versus radical electrons.

Ethane has a barrier to twisting of 1.6 kcal/mol as it passes from a staggered to an eclipsed form (versus 3.0 kcal/mol exact [6]). As we see later, intermediate range steric repulsions are systematically underestimated in our version of eFF. Twisting ethylene causes the banana bond electrons to separate; at 90º, the up spin electrons align along one axis while the down spin electrons align along a 90º axis. Twisted ethylene is higher in energy than planar ethylene by nearly 15 kcal/mol (versus 65 kcal/mol exact [7]).

Several problem cases that plagued the old eFF are now handled well with the new eFF (Figure 3.14). Previously, it was found that carbon-hydrogen bond lengths for secondary and tertiary carbons were unreasonably high, reaching 1.424 Å in isobutane. With the new eFF, the isobutane CH bond distance is now 1.137 Å, near the exact value of 1.108 Å.
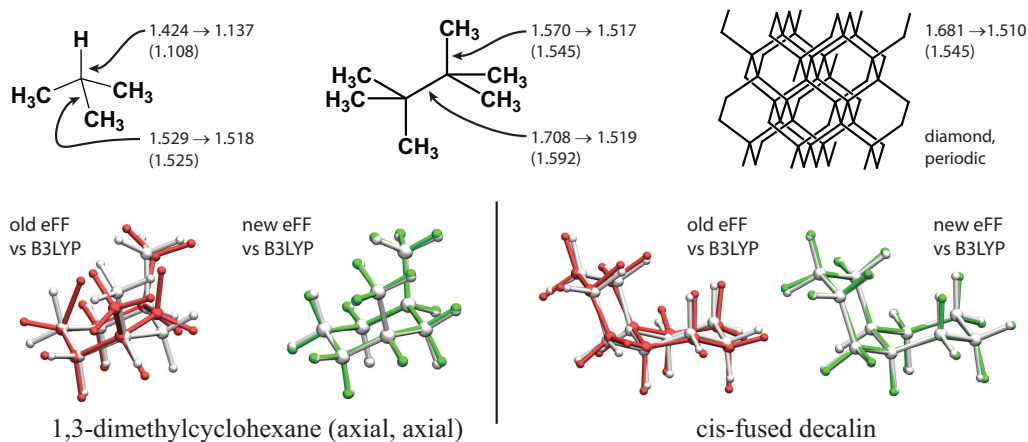
Figure 3.14: Improved geometries for old eFF "problem hydrocarbons".

Carbon-carbon bonds are found to be more rigid as well. Previously, ^{t}Bu $-^{t}$ Bu had a central carbon-carbon bond distance of 1.708 Å; with the new eFF, it is now a more correct 1.519 Å (versus an exact value of 1.592 Å). Diamond now has a CC bond distance of 1.510 Å versus an exact value of 1.545 Å. Geometries such as 1,3-dimethylcyclohexane (axial-axial) and cis-fused decalin no longer display

inappropriate twisting or bending; they in fact superimpose nearly exactly onto B3LYP- optimized structures. It appears as though the attractive three-body potential between valence electrons and nuclei is enforcing more reasonable limits on the range of valence electron motions. We quantify these observations more precisely by measuring the bond lengths and angles of a range of simple substituted alkanes and alkenes (Figures 3.15 and 3.16), and comparing them to exact values.
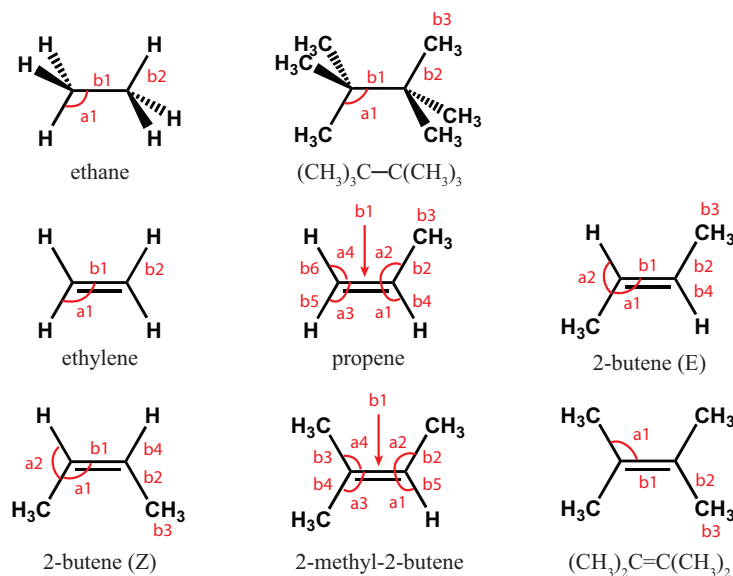
Figure 3.15: Key geometric parameters of substituted alkanes and alkenes.

We find that carbon-hydrogen and carbon-carbon bond lengths are now closer to the correct values. Under the old eFF, carbon-carbon double bonds were nearly the same length as single bonds but under the new eFF are the correct 1.33 Å length. Carbon-hydrogen bonds are no longer overly flexible. We do find some less satisfying consequences, however: carbon-carbon single bonds are too rigid, and carbon-carbon double bonds actually shrink with increasing substitution instead of expanding. Bond angles also show more "scatter" from the exact values. Two possibilities exist: either the bonds themselves are too rigid, or steric effects between adjacent alkyl groups are too small. Our later results tend to support the latter hypothesis, although we have not ruled out the former possibility.

With more complex alkene geometries, eFF-optimized structures superimpose
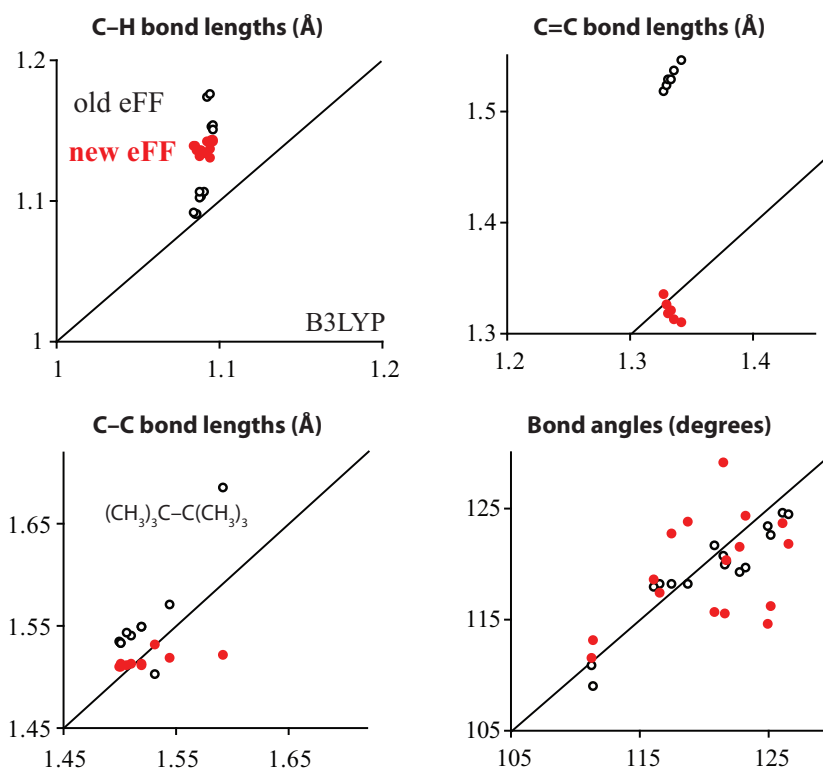
Figure 3.16: Comparison of old versus new eFF geometric parameters for simple substituted alkanes and alkenes.

well onto B3LYP optimized geometries (Figure 3.17). This includes cyclic alkenes with conjugated and non-conjugated double bonds, such as cycloheptene (2.36 Å RMSD), 1,3-cycloheptadiene (0.16 Å RMSD), and even the anti-aromatic cyclooctatetraene (3.29 Å RMSD), where the out-of-plane nature of the molecule is captured. More rigid structures such as dimethylfulvene (1.79 Å RMSD) and dicyclopentadiene (0.22 Å RMSD) match B3LYP structures even more closely.

cycloheptene (2.36)   1,3-cycloheptadiene (0.16)   cyclooctatetraene (3.29)

dimethylfulvene (1.79)   dicyclopentadiene (0.22)
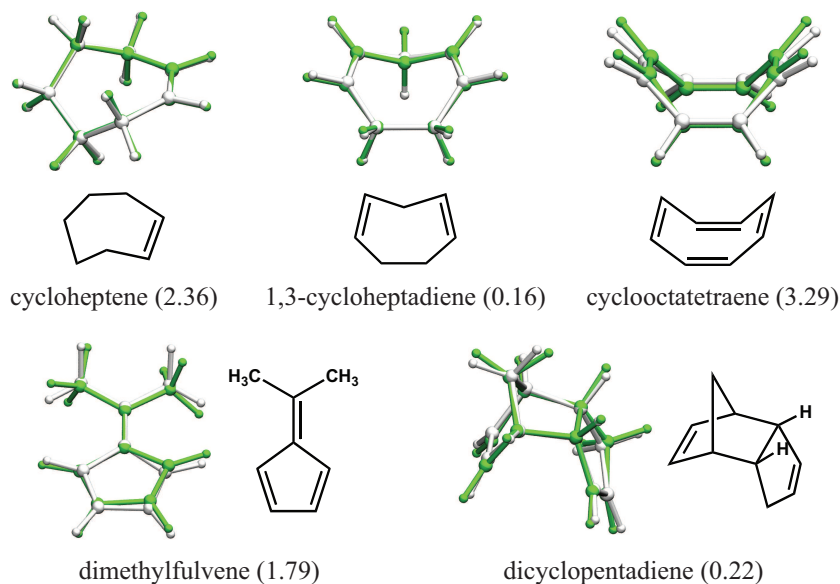
Figure 3.17: Optimized eFF and B3LYP alkenes superimposed, with root-mean-squared deviations (RMSD) given in parenthesis (angstroms).

Work remains to improve the eFF description of multiple bonding. Although bond dissociation energies are reasonable, eFF greatly overestimates the energy gained from turning double bonds into single bonds. As a test case, we consider the [4+2] cycloaddition between 1,3-butadiene and ethylene to produce cyclohexene, whose driving force is the conversion of two double bonds into two single bonds. eFF estimates the reaction energy to be -235 kcal/mol, significantly greater than the B3LYP value of -36 kcal/mol; we see a similar result for the [2+2] addition of two ethylenes to form cyclobutane.

Triple bonds are even more unstable relative to lower-order bonds; they are higher in energy than diradical double bonds by 42 kcal/mol in acetylene and 54

kcal/mol in dimethylacetylene. It appears that adjacent banana bond electrons in eFF repel each other too much. eFF has been parameterized to correctly describe the orthogonality of valence electrons around a single nucleus; perhaps further modifications are needed to transfer those energy expressions to the case of orthogonal electrons within a multiple bond. The too-strong repulsion may also originate from our electron anti-coalescence function, which aggressively keeps electrons of similar size separated.

−235.0 (−35.6)   and   −239.3 (−18.0)

Figure 3.18: eFF overestimates the energy gained from turning double bounds into single bonds; prototype $[2+2]$ and $[4+2]$ cycloadditions are shown, eFF (B3LYP) energy differences in kcal/mol.

$d_{CC} = 1.209$ (1.198), $d_{CH} = 1.120$ (1.063) $d_{CC} = 1.307, d_{CH} = 1.128, \theta_{CCH} = 127.4°$

more stable, 42 kcal/mol

$d_{CC\ triple} = 1.253$ (1.203), $d_{CC\ single} = 1.498$ (1.459) $d_{CC\ triple} = 1.288,\ d_{CC\ single} = 1.486, d_{CH} = 1.128$
$d_{CH} = 1.148$ (1.094)

more stable, 54 kcal/mol

Figure 3.19: eFF alkynes are unstable relative to alkene diradicals. eFF (B3LYP) distances in angstroms.

We have made no efforts to include conjugation or resonance effects in the eFF model, so it is no surprise that benzene exists as 1,3,5-cyclohexatriene in our description, with distinct single and double bonds (with lengths of 1.505 Å and 1.309

Å, respectively). In fact, diradical 1,4-cyclohexadiene — which would be a resonance structure of benzene — exists in eFF as a separate local minimum geometry that is less stable than 1,3,5-cyclohexatriene by 12 kcal/mol. Also, propene and propane have nearly identical CH bond dissociation energies on their alkyl end (75 and 76 kcal/mol respectively), indicating that the allyl radical has no special stability.
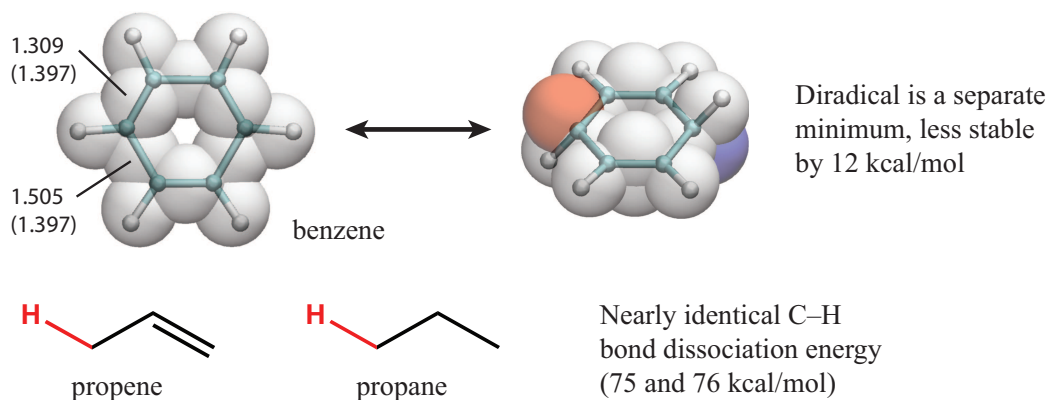
Figure 3.20: eFF shows no resonance stabilization of conjugated double bonds.

All in all, we have made a significant advance over the previous eFF in describing hydrocarbons. Complex structures containing single and double bonds now match closely with B3LYP optimized geometries. Double and triple bonds are now the correct length and size; because double bonds now contain compact banana electrons rather than overly diffuse sigma-pi electrons, structures such as cyclooctatetraene have the correct geometry. Carbon-carbon and carbon-hydrogen bond dissociation energies increase by the correct amount as unsaturation increases (with triple bonds being an exception). It is apparent that the same Pauli function that stabilizes lone pairs on neon also serves to stabilize banana bonds in double and triple bonds; and it is remarkable that without further parameterization that the correct lengths of multiple bonds and the geometries of complex molecules, are reproduced well. Further work remains to obtain better isodemic reaction energies, stabilize triple bonds, and include conjugation effects. Nonetheless, we have validated a basic point — exchange attraction is useful not only for obtaining correct

ionization potentials for high spin atoms, but also for properly describing multiple bonds.

Heteroatoms single and multiple bonds

We now consider molecules isoelectronic to ethane, ethylene, and acetylene containing heteroatoms instead of carbons. As shown in Figure 3.21, the molecules ethane, hydrazine, hydrogen peroxide, and fluorine are isoelectronic to each other; as are ethylene, diimide, and singlet oxygen; and acetylene and dinitrogen.
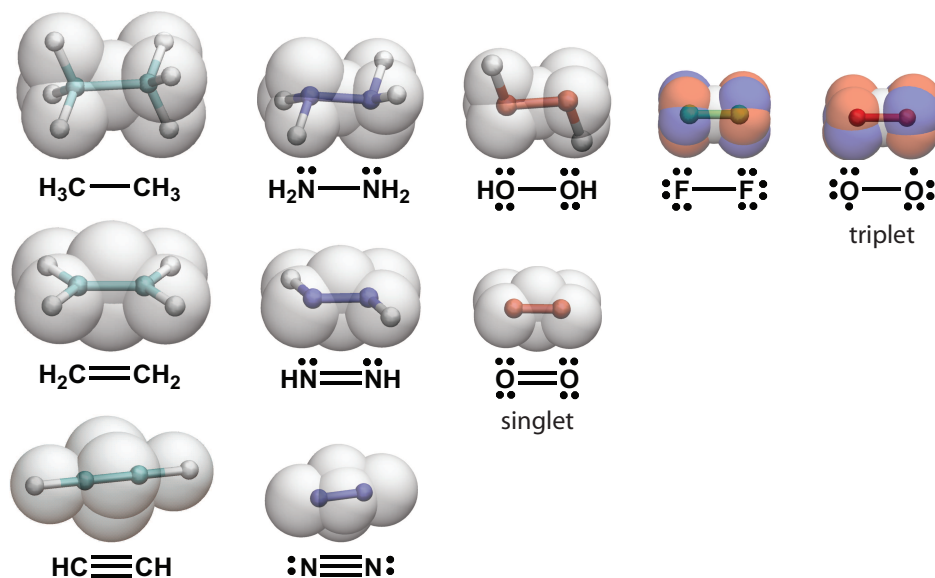
Figure 3.21: Gallery of heteroatom single, double, and triple bonds.

We find that bonds between heteroatoms are too strong and too short (Figure 3.22). For example, while we calculate ethane to have a bond dissociation energy of 140 kcal/mol vs 90 kcal/mol exact, and a bond length of 1.53 Å versus 1.53 Å exact, we calculate F_2 to have a bond dissociation energy of 275 kcal/mol vs 38 kcal/mol exact, and a bond length of 1.05 Å versus 1.35 Å exact. One possibility is that eFF does not have sufficient repulsion between lone pairs. In both the single and double bonds, increasing the nuclear charge causes the bond joining the atoms to become weaker, due in part to the greater repulsion between lone pairs as the bond length shrinks.
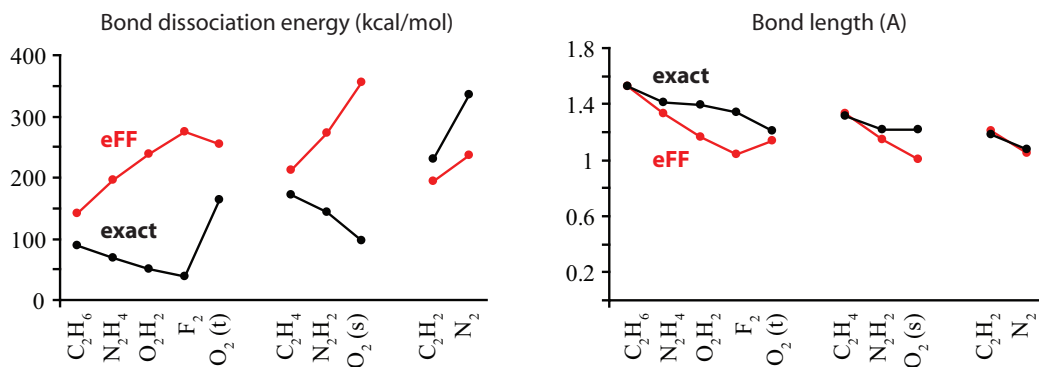
Figure 3.22: Bonds between heteroatoms are too strong and too short, possibly due to insufficient repulsion between lone pairs.

This logic does not extend to N_2, where the lone pairs are directed away from each other — the triple bond in N_2 is more than 100 kcal/mol stronger than the triple bond in acetylene. eFF also predicts that the N_2 bond should be especially strong, but with a bond dissociation energy only 42 kcal/mol stronger than in acetylene.

Triplet oxygen is another unusual case — it is analogous to F_2, but with two fewer lone pair electrons it is able to form two two-center three-electron bonds with a combined strength of 163 kcal/mol, which is 125 kcal/mol stronger than the F_2 bond. It is difficult to tell whether eFF can capture these effects; eFF predicts that the O_2 triplet bond is 20 kcal/mol weaker than the bond in F_2, but it is not clear how this value would change if lone pairs were made to be more repulsive.

To test our hypothesis that lone pairs do not repel strongly enough in eFF, we compute the interaction energy of two neon atoms (Figure 3.23), and compare it to the Hartree-Fock interaction energy, which serves as an accurate estimate of exchange repulsion. We find that eFF significantly underestimates the neon-neon repulsion. In F_2, eFF finds that the lone pairs repel each other with an energy of $\sim$0.25 hartrees. If we assume that the fluorine atoms should repel each other as the neon atoms do, we conclude that the bond length should be larger by $\sim$0.3 Å, which matches the discrepancy between eFF and exact bond lengths. Other contributions, such as the change in electron size upon binding, and the effects of

p versus s character on Pauli repulsion, were found to be minimal.
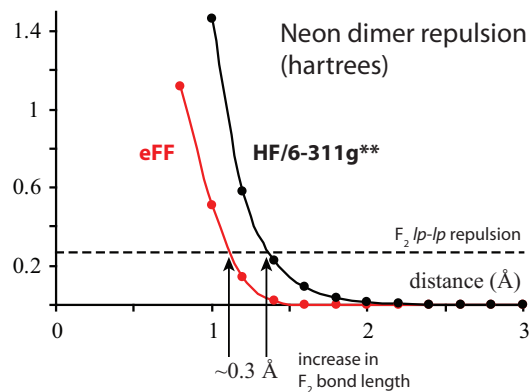
Figure 3.23: Repulsion between neon atoms in eFF is too small.

We conclude that the Pauli repulsion between lone pairs is too small and that it is necessary that this issue be corrected before simulations with heteroatoms can be accurate. Once lone pair-lone pair interactions are properly described, a wide range of organic reactions could be studied using eFF.

Van der Waals dimers and hydrogen bonds

With the electron force field, it should be possible to model interactions between molecules as well as interaction within molecules. We examine as test cases water dimer, hydrogen fluoride dimer, methane-water dimer, and methane-methane dimer (Figure 3.24). The interaction between two methanes is reasonably well-described (ΔE = -0.5 kcal/mol vs -0.3 kcal/mol exact, and R_{CC} = 3.91 Å versus 4.13 Å exact), but in water dimer and HF dimer, the hydrogen bonds are significantly too strong and too short (for water dimer, ΔE = -36 kcal/mol versus -5 kcal/mol exact, with R_{OO} = 2.29 Å versus 2.92 Å exact; for HF dimer, ΔE = -54 kcal/mol versus -5 kcal/mol exact, with R_{FF} = 2.13 Å versus 2.73 exact). The methane-water interaction falls between these two extremes, and has ΔE = -3.9 kcal/mol versus -0.9 kcal/mol exact, and R_{OO} = 3.18 Å versus 3.51 Å exact.

Remarkably, electrostatics and Pauli repulsion are balanced sufficiently in the water and HF dimer cases that the angles they make relative to each other are

$(H_2O)_2$ E = -35.5 (-5.44 kcal/mol)
R_{OO} = 2.29 (2.92 Å),
θ_1 = 4.6° (6°), θ_2 = 112.4° (123°)

$CH_4 \cdot OH_2$ E = -3.9 (-0.9 kcal/mol)
R_{OC} = 3.18 (3.51 Å)

$(HF)_2$ E = -53.7 (-4.56 kcal/mol)
R_{FF} = 2.13 (2.73 Å),
θ_1 = 5.8° (7°), θ_2 = 103.5° (112°)

$(CH_4)_2$ E = -0.5 (-0.3 kcal/mol)
R_{CC} = 3.91 (4.13 Å)
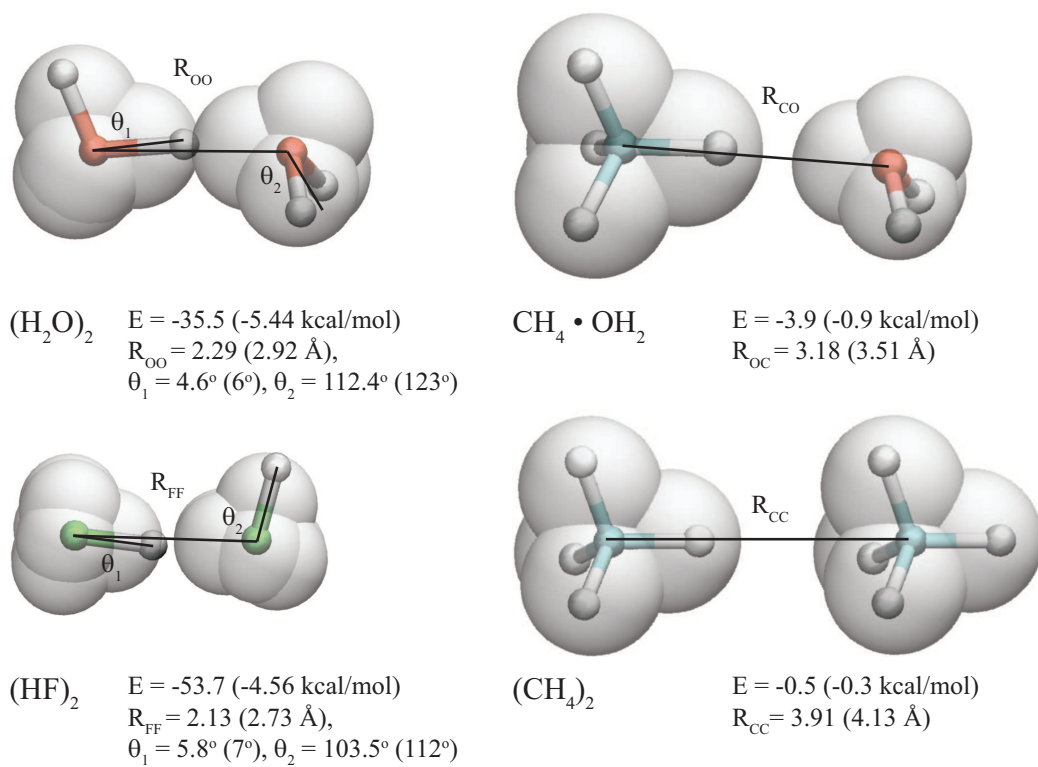
Figure 3.24: Hydrogen bonds in eFF are too strong and too short, probably from a combination of too-small Pauli repulsion and too-large monomer dipoles.

nearly the exact values (water dimer $\theta_1 = 5^o$ versus 6° exact and $\theta_2 = 112^o$ versus 123° exact; HF dimer $\theta_1 = 6^o$ versus 7° exact and $\theta_2 = 104^o$ versus 112° exact).

We propose that eFF hydrogen bonds are too strong and too short because the monomer dipoles are too large and the Pauli repulsion between monomers too small. Taking water dimer as a test case, we attempt to quantify the change in interaction energy and geometry we would expect if the monomer dipoles and Pauli repulsions were correct. We make a dipole moment correction by adding point dipoles onto both water molecules of a magnitude such that the net water dipole goes from 3.27 D to 1.85 D, the exact value. Moving the water molecules apart from each other with bond lengths and angles fixed, we find that the dipole correction makes the water molecules bind by only 18 kcal/mol, with an OO distance of ~2.45 Å. It is clear that although the too-large dipole moment does cause the hydrogen bond to be stronger, it cannot be responsible for all of the too-high eFF hydrogen bond strength of 36 kcal/mol.
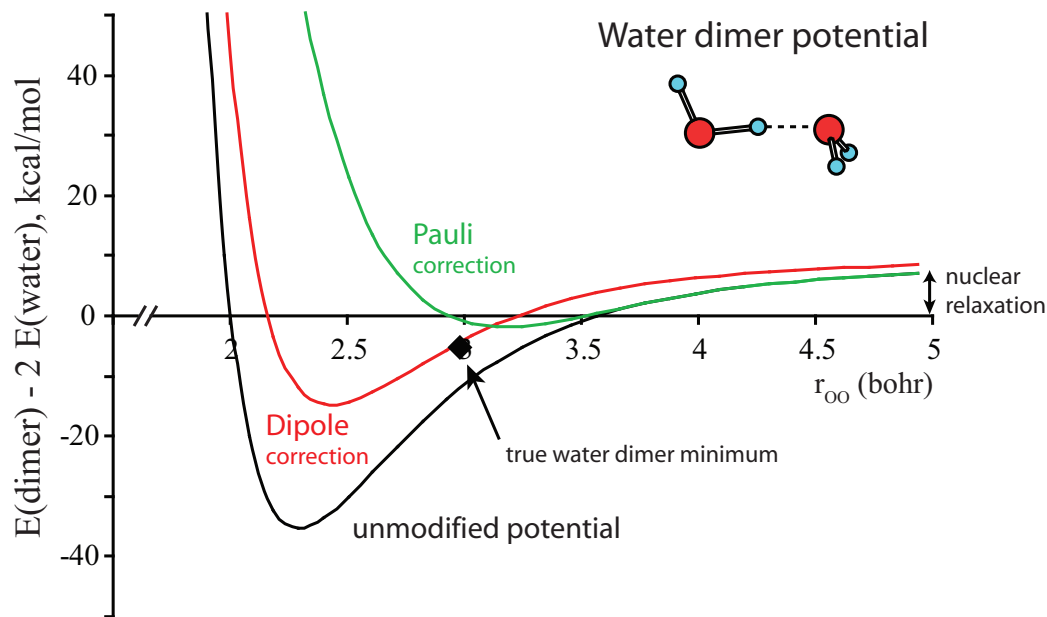
Figure 3.25: Interaction energy of the water dimer, with the estimated effects of changing monomer dipole moments and Pauli repulsions to be the correct values.

We estimate the Pauli correction by taking the difference between eFF and

Hartree-Fock interaction curves for neon dimer and parameterizing it:

$$\log E_{\text{difference}} = 8.55616r - 15.1178r^2 + 8.15818r^3 - 1.65597r^4$$

where r is in bohr and the energy is in hartrees. We correct for the difference in size between a water molecule and a neon atom by scaling the distances by the cube root of the ratio of polarizabilities ($\alpha_{neon} = 2.67$ bohr^3, $\alpha_{water} = 9.92$ bohr^3; $(\alpha_{\text{water}}/\alpha_{\text{neon}})^{1/3} = 1.55$). With the Pauli correction added, the water dimer has a binding energy of $\sim$3 kcal/mol and an OO distance of $\sim$3.2 Å, closer to the expected value. It appears that a combination of correct Pauli repulsion and correct monomer dipole moments is needed to obtain a correct description of hydrogen bonding in eFF.

Unlike with conventional force fields, in eFF hydrogen bonds appear as an emergent consequence of existing electrostatic and Pauli interactions. In attempting to describe inter- and intramolecular bonding with the same set of energy expressions and parameters, we face a more difficult challenge than arises in developing conventional force fields, which usually contain explicit van der Waals and hydrogen bond terms. Advanced water force fields often combine multiple or delocalized charges with polarizable sites and explicit van der Waals and repulsive terms. Such schemes require extensive parameterization against properties of interest and use parameters and functions that are rather system-specific. In contrast, eFF accounts for electrostatic and Pauli effects in a way designed to apply generally over a broad range of molecules, and so may be useful in developing new transferable force fields with accurate descriptions of solvents.

Too-small sterics cause other problems

We found by studying the interaction energy of neon dimer that Pauli repulsions between valence electrons on different atoms were underestimated, which caused bonds between heteroatoms to be too strong, and hydrogen bonds to be too strong as well. We show in this section that this effect causes problems in other systems

as well, including systems that were previously well-described by the old version of eFF.

Cyclic alkanes with more than three carbons are nonplanar, and the old eFF reproduced well the magnitude of key dihedral angles measuring the twist of cycloalkanes out of planarity. The new eFF does slightly worse, making cyclobutane, cyclopentane, and cyclohexane more planar than they should be (Table 3.4). This is likely a consequence of the too-small barrier to ethane rotation discussed previously (1.6 kcal/mol versus 3 kcal/mol exact). We find that other intermediate range steric interactions are underestimated as well (Table 3.5), including the gauche versus trans butane interaction (0.4 versus 0.9 kcal/mol B3LYP), and the 1,3-diaxial interaction (3.3 kcal/mol versus 5.9 kcal/mol B3LYP).

	key dihedral (degrees)		
	old eFF	new eFF	B3LYP
cyclobutane	0.3	0.0	18.0
cyclopentane	-21.5	-18.9	-33.2
cyclohexane (chair)	57.7	50.6	56.6
cyclohexane (twist-boat)	-34.0	-27.1	-32.3

Table 3.4: New eFF makes cyclic alkanes slightly more planar than they should be.

			ΔE (kcal/mol)		
system	energy of	relative to	old eFF	new eFF	B3LYP
ethane	eclipsed	staggered	2.1	1.6	2.7
butane	gauche	trans	1.6*	0.4	0.9
cyclohexane	twist-boat	chair	4.7	4.3	6.3
1,3-dimethyl-cyclohexane	ax-ax	eq-eq	5.8	3.3	5.9
	ax-eq	eq-eq	2.7	0.7	2.1
decalin	cis	trans	12.1	1.1	3.2
2-pentene	major	minor	5.5	5.2	4.6

Table 3.5: New eFF underestimates the magnitude of intermediate range steric repulsions.

The old eFF was used to study the dynamics of hydrogen plasmas, but the new eFF is no longer useful for that purpose, because it improperly stabilizes triangular and tetrahedral clusters of hydrogen atoms (triangular H_3 is 28 kcal/mol more stable than $H_2 + H$, and tetrahedral H_4 is 28 kcal/mol more stable than $H_2 + H_2$). This is a clear consequence of insufficient Pauli repulsion between s-like electrons.

$H_2 + H \longrightarrow$

line

$\Delta E = 42.0 \rightarrow 12.5$
(9 kcal/mol)

triangle

$\Delta E = -28.3$ kcal/mol

$H_2 + H_2 \longrightarrow$

square

$\Delta E = 131.7 \rightarrow 3.6$
(147 kcal/mol)

tetrahedron

$\Delta E = -27.6$ kcal/mol

wrongly stable with new eFF
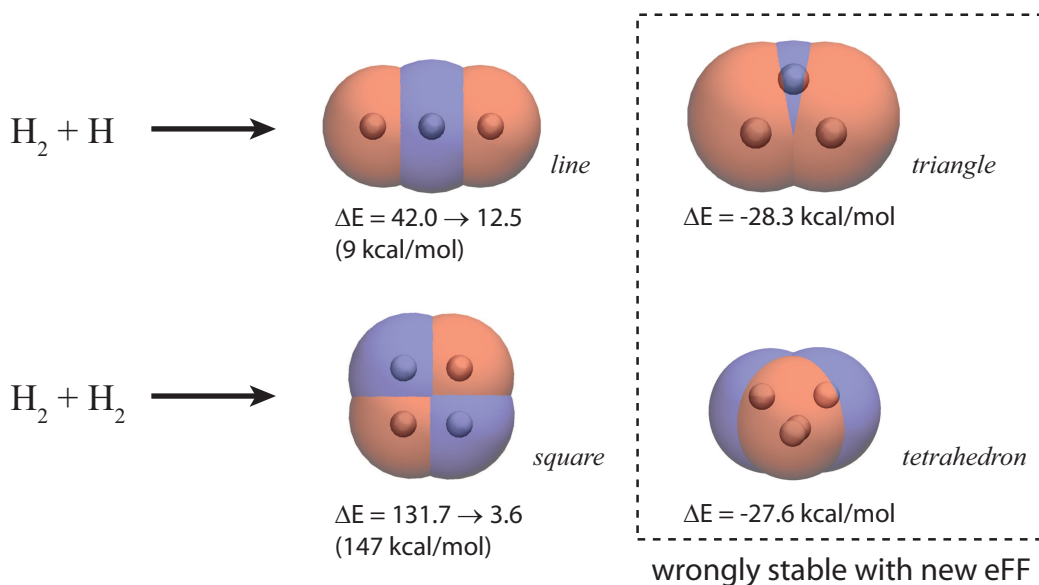
Figure 3.26: The new eFF creates spurious stable minima corresponding to unphysical arrangements of hydrogen atoms.

We have been curious to study bonding in electron-rich solids, and were delighted to find that the new eFF could optimize a cluster of twelve boron atoms in an icosaheral arrangement (Figure 3.27). Such an icosahedral arrangement mirrors the units found in α-boron solid, and it was not possible to obtain such a structure with the old eFF. With the new eFF, the boron-boron distances are nearly identical to those found with B3LYP (1.677 Å versus 1.673 Å B3LYP), and a slight shear distortion is also reproduced.

However, we also discover with the new eFF a boron-centered amorphous jumble of atoms 600 kcal/mol more stable than the icosahedral structure; such a structure does not have any special stability according to B3LYP. It is possible to destabilize this structure by adjusting other parameters in the eFF, and to obtain
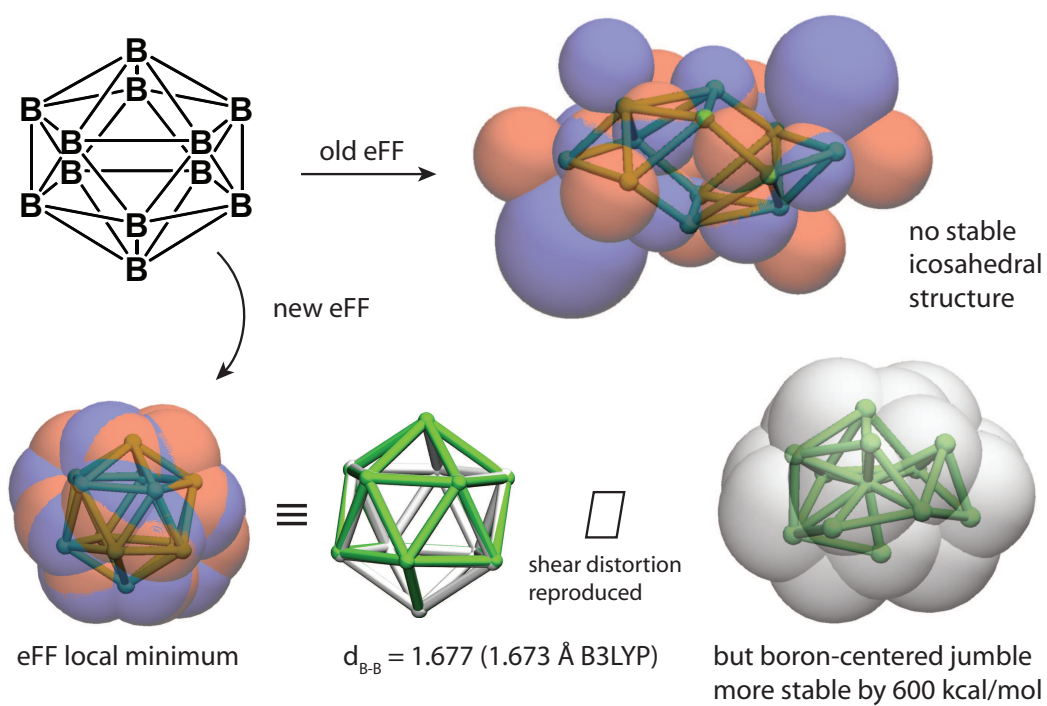
Figure 3.27: Icosahedral boron cluster B_{12} is stable with the new eFF, and matches a B3LYP optimized geometry well; however an amorphous boron-centered structure is found to be even more stable.

stable structures for B_{12}, larger boron hydrides, and carboranes; but we would prefer to stay with a single set of parameters that treated all systems consistently.

Based on the above results, it is not possible to unequivocally recommend the new eFF over the old eFF, even though the new eFF describes with higher accuracy atoms, molecules with lone pairs, atom hydrides, and single and double bonds.

Conclusion

We have outlined a new eFF that accounts for changes in electron shape caused by the influence of nearby nuclei and core electrons. Previously we had assumed that the Pauli principle was manifested solely by electrons repelling each other. In this chapter, we demonstrate an important exception to the rule — when electrons are orthogonal to each other, as they are when they attain p character and are at a 90° angle to each other, the Pauli repulsion is reduced and can become attractive. This is due to the same decrease in electron-electron repulsion between same spin electrons which causes the ground state of atoms to be high spin (Hund's rule).

By including electron shapes, we can with a single set of parameters obtain correct ionization potentials and polarizabilities for atoms from hydrogen through neon. Electrons arrange themselves into s-like and p-like shells naturally, and the special stability of s shells, p shells, and even half-filled p shells emerges naturally from the eFF energy expressions.

Conceptually it should be possible to extend eFF to higher-row atoms by parameterizing interactions between electrons and larger cores, such as neon, argon, and so on.

We obtain good geometries and bond dissociation energies for atom hydrides and hydrocarbons as well, in the process correcting many of the issues afflicting the old eFF, such as carbon-hydrogen bonds that were too variable in length, and double bonds that were too long. In most cases, hydrocarbon geometries containing single and double bonds optimized with eFF match B3LYP geometries well, even for flexible molecules such as cycloheptene and cyclooctatetraene.

The new version of eFF has clear limitations as well. It is too easy to turn dou-

ble bonds into single bonds, and triple bonds are unstable relative to double bond diradicals, suggesting that banana bond electrons repel each other too strongly. We do not account for conjugation, so benzene appears as 1,3,5-cyclohexatriene. We also find that in making it easier for valence electrons to pack together to form atoms, we have degraded the accuracy of part of the old eFF — the Pauli repulsion between s-like electrons is now underestimated in a variety of systems. This underestimation causes heteroatom bonds and hydrogen bonds to be too short and too strong, and causes hydrogen and boron clusters to arrange themselves in unphysical configurations.

To correct this problem, we have attempted to modify the Pauli potential to be more repulsive while still preserving a proper description of first row atoms, but it has not been straightforward to do. We may have overconstrained our energy expression by assuming that exchange attraction could be approximated by a functional form similar to that used to describe exchange repulsion. In the future, it may be useful to investigate separate functional forms for (1) exchange repulsion between s-like electrons, which arises from the increase of kinetic energy upon orbital orthogonalization; and (2) exchange attraction between p-like electrons, which arises from the decrease of electron-electron repulsion as a consequence of the Pauli principle.

Nonetheless, our results suggest strongly that (1) it is possible to describe systems with p-like electrons using only spherical Gaussian functions,(2) electron shape can be specified implicitly, by considering the position of the electron relative to the nuclei of the system, and (3) the dominant effects to consider for interactions of p-like electrons are changes in kinetic energy and Pauli interactions.

These terms take the form of two and three body terms involving nuclei and electrons, analogous to the bond and angle terms found in traditional force fields. It is more than likely that future eFFs will find it advantageous to include such terms in order to account for the diversity of electron shapes present in molecular systems while maintaining the simplicity of propagating spherical Gaussian functions.

Supplemental tables

	new eFF energy (au)		ionization potentials (kcal/mol)			
	E(Z)	E(Z+1)	new eFF	old eFF	HF	exact
H	-0.424413	0	266.3	266.3	313.6	313.6
He	-2.300987	-1.697653	378.6	378.6	540.8	567.0
Li	-6.114980	-5.944908	106.7	105.6	123.1	124.3
Be	-12.144527	-11.878010	167.2	165.8	185.6	215.0
B	-20.634538	-20.359386	172.7	228.4	183.0	191.4
C	-31.949192	-31.554495	247.7	155.3	249.1	259.7
N	-46.398088	-45.919451	300.0	60.9	322.6	335.2
O	-64.141692	-63.732720	257.1	421.1	276.3	314.0
F	-85.639717	-85.082131	350.4	190.2	363.1	401.8
Ne	-111.218594	-110.546393	421.9	-12.8	457.8	497.3

Table 3.6: Ionization potentials of first row atoms; HF = Hartree-Fock/6-311g**

	dipole (debye)	polarizability (bohr^3)				
	eFF	eFF σ_1	eFF σ_2	eFF σ_3	eFF avg σ	exact
H	0.000	3.1	3.1	3.1	3.1	4.5
He	0.000	0.7	0.7	0.7	0.7	1.4
Li	0.000	204.4	204.4	204.4	204.4	164.0
Be	0.000	51.5	51.4	51.4	51.5	37.8
B	0.001	42.7	42.5	**23.9**	36.4	20.4
C	0.001	39.2	**8.7**	**8.2**	18.7	11.9
N	0.000	4.5	4.5	4.4	4.5	7.4
O	**0.071**	37.4	**5.9**	**2.9**	15.4	5.4
F	**0.338**	79.7	**24.6**	**5.0**	36.4	3.8
Ne	0.000	1.1	1.1	1.1	1.1	2.7

Table 3.7: Polarizabilities of first row atoms

	spin	E (hartrees)	BDE (kcal/mol)		bond length (angstroms)		bond angle (degrees)	
			eFF	exact	eFF	exact	eFF	exact
H	d	-0.424413						
C	t	-31.94919						
N	q	-46.39809						
O	t	-64.14169						
F	d	-85.63972						
CH	d	-32.5385	103.5	81.4	1.124	1.120		
NH	t	-46.97412	95.1	75.1	1.051	1.036		
OH	d	-64.74731	113.7	102.3	0.94	0.970		
FH	s	-86.24148	111.3	136.4	0.874	0.917		
CH_2	t	-33.11301	94.2	101.8	1.119	1.08	118.7	135.5
CH_2	s	-33.130497	105.2	92.4	1.137	1.109	125.0	102.0
NH_2	d	-47.55188	96.2	96.6	1.033	1.024	105.5	103.2
OH_2	s	-65.3489	111.2	117.9	0.949	0.958	103.7	104.5
CH_3	d	-33.69142	96.6	109.6	1.133	1.079	112.5	120.0
NH_3	s	-48.13353	98.7	101	1.044	1.017	104.5	107.8
CH_4	s	-34.23913	77.4	104.8	1.144	1.086	109.5	109.5

Table 3.8: Atom hydride bond dissociation energies and geometries.

	spin	dipole (debye)		
		eFF	mp2	expt
H	d	0.000		
C	t	0.001		
N	q	0.000		
O	t	0.071		
F	d	0.338		
CH	d	1.258	1.539	
NH	t	1.567	1.592	
OH	d	2.559	1.702	1.660
FH	s	2.769	1.824	1.820
CH_2	t	1.534	0.612	
CH_2	s	1.381	0.590	
NH_2	d	2.398	1.864	
OH_2	s	3.269	1.936	1.850
CH_3	d	1.256	0.000	0.000
NH_3	s	2.945	1.622	1.470
CH_4	s	0.000	0.000	0.000

Table 3.9: Atom hydride dipole moments; MP2/cc-pvtz dipoles are from the NIST webbook.

	B3LYP/6-311g**			eFF		
	$d_{nuc \cdot bp}$	$d_{nuc \cdot lp}$	$\theta_{lp \cdot lp}$	$d_{nuc \cdot bp}$	$d_{nuc \cdot lp}$	$\theta_{lp \cdot lp}$
CH_4	1.375			1.452		
NH_3	1.161	0.642		1.187	0.871	
OH_2	0.999	0.572	121.9	0.987	0.788	119.7
FH	0.861	0.508	114.5	0.830	0.696	113.4
Ne		0.456	109.5		0.613	109.5

Table 3.10: Atom hydride bond pair and lone pair geometry parameters; distances are in bohr and angles are in degrees.

relative to	energy of	ΔE (kcal/mol)	
		eFF	exact
C_2H_6	2 CH_3 (d)	140.4	89.7
C_2H_4	2 CH_2 (t)	211.1	172.2
C_2H_2	2 CH (d)	194.3	229.8
C_2H_6	C_2H_5 (d) + H (d)	75.9	100.1
C_2H_4	C_2H_3 (d) + H (d)	82.0	113.3
C_2H_2	C_2H (d) + H (d)	105.2	131.8
C_2H_6 (staggered)	C_2H_6 (eclipsed)	1.6	3.0
C_2H_4 (planar)	C_2H_4 (twisted)	15.4	65.0

Table 3.11: Bond dissociation and relative conformer energies of ethane, ethylene, and acetylene.

	spin	E (kcal/mol)
H	d	-0.424413
CH	d	-32.538497
CH_2	t	-33.113010
CH_3	d	-33.691424
C_2H_5	d	-67.061321
C_2H_3	d	-66.007466
C_2H	d	-64.794602
C_2H_6 (staggered)	s	-67.606657
C_2H_6 (eclipsed)	s	-67.604039
C_2H_4 (planar)	s	-66.562498
C_2H_4 (twisted)	s	-66.538012
C_2H_2	s	-65.386616

Table 3.12: Absolute energies of ethane, ethylene, acetylene, and related conformers and fragments.

	spin	d$_{CC}$ (Å)			d$_{CH}$ (Å)		
		eFF	B3LYP	exact	eFF	B3LYP	exact
H	d						
CH	d				1.124	1.128	1.120
CH$_2$	t				1.119	1.080	1.085
CH$_3$	d				1.133	1.080	1.079
C$_2$H$_5$	d	1.512	1.487		1.129	1.083	
C$_2$H$_3$	d	1.319	1.305	1.316	1.141	1.088	1.085
C$_2$H	d	1.196	1.202	1.217	1.110	1.064	1.047
C$_2$H$_6$ (staggered)	s	1.530	1.531	1.536	1.141	1.093	1.091
C$_2$H$_6$ (eclipsed)	s	1.533	1.544		1.140	1.092	
C$_2$H$_4$ (planar)	s	1.335	1.327	1.339	1.138	1.085	1.086
C$_2$H$_4$ (twisted)	s	1.345	1.327		1.137	1.085	
C$_2$H$_2$	s	1.209	1.198	1.203	1.120	1.063	1.063

Table 3.13: Bond lengths of ethane, ethylene, acetylene, and related conformers and fragments.

	spin	a_{HCH} (degrees)			a_{HCH} radical end (degrees)		
		eFF	B3LYP	exact	eFF	B3LYP	exact
H	d						
CH	d						
CH_2	t				118.7	134.7	135.5
CH_3	d				112.5	120.0	120.0
C_2H_5	d	108.1	108.2		110.2	117.5	
C_2H_3	d	124.6	115.9	121.5	127.5	138.5	137.3
C_2H	d						
C_2H_6 (staggered)	s	107.4	107.6	108.0			
C_2H_6 (eclipsed)	s	107.0	107.1				
C_2H_4 (planar)	s	119.5	116.4	117.6			
C_2H_4 (twisted)	s	114.4	116.5				
C_2H_2	s						

Table 3.14: Bond angles of ethane, ethylene, acetylene, and related conformers and fragments.

	spin	E (hartrees)	BDE (kcal/mol)		bond length (Å)	
			eFF	exact	eFF	exact
O	s	-64.102759				
O	t	-64.141692				
N	d	-46.315322				
F	d	-85.620743				
NH	s	-32.538497				
OH	d	-64.747313				
NH	t	-46.974123				
CH_2	t	-33.11301				
NH_2	d	-47.551883				
CH_3	d	-33.691424				
C_2H_6	s	-67.606657	140.4	89.6	1.530	1.528
N_2H_4	s	-95.41651	196.2	68.2	1.329	1.413
O_2H_2	s	-129.873617	237.8	51.2	1.169	1.396
F_2	s	-171.679689	275.0	37.9	1.045	1.345
O_2	t	-128.650873	255.0	163.4	1.137	1.208
C_2H_4	s	-66.562498	211.1	172.2	1.335	1.317
N_2H_2	s	-94.382841	272.7	144.0	1.146	1.216
O_2	s	-128.85089	356.1	96.0	1.003	1.216
C_2H_2	s	-65.386616	194.3	229.7	1.209	1.186
N_2	s	-93.007331	236.4	334.9	1.052	1.078

Table 3.15: Heteroatom single, double, and triple bonded species bond dissociation energies and bond lengths.

132

Bibliography

[1] **Frost, A. A.** 1967. A floating spherical Gaussian orbital model of molecular structure. III. First-row atom hydrides. *J. Phys. Chem.* **72(4)**:1289-1293.

[2] **Pakiari, A. H., Khalesifard, M. F.** 1993. A study of lone pair description in molecules by the floating spherical Gaussian orbital (FSGO) method. Part 2. *Theochem.* **107(1-2)**:29-39.

[3] **Pauling, L.** 1931. The nature of the chemical bond. Application of results obtained from the quantum mechanics and from a theory of paramagnetic susceptibility to the structure of molecules. *J. Am. Chem. Soc.* **53**:1367-1400.

[4] **McDowell, H. K., Porter, R. N.** 1977. Reduced Green's functions and coupled perturbed Hartree-Fock calculations. II. Application to the static dipole polarizability of the helium isoelectronic sequence. *J. Chem. Phys.* **66(11)**:4725-4735.

[5] **Russo, N., Sicilia, E., Toscano, M.** 1992. Geometries, singlet-triplet separations, dipole moments, ionization potentials, and vibrational frequencies in methylene (CH_2) and halocarbenes (CHF, CF_2, CCl_2, CBr_2 and Cl_2). *J. Chem. Phys.* **97(7)**:5031-5036.

[6] **Pitzer, R. M.** 1983. The barrier to internal rotation in ethane. *Acc. Chem. Res.* **16**:207-210.

[7] **Jarowski, P. D., Diederich, F., Houk, K. N.** 2006. Butatrienes as extended alkenes: barriers to internal rotation and substitution effects on the stabilities of the ground states and transition states. *J. Phys. Chem. A* **110**:7237-7246.

Chapter 4

Development of an electron force field. III. Metallic electrons and the uniform electron gas. Creation of a correlation function

Introduction

We presented in the last chapters an electron force field that could describe covalent, ionic, and multicenter bonds between first-row atoms, distinguishing between s-like and p-like electrons. In this chapter, we show that eFF can be modified to describe delocalized or metallic electrons, and we develop a term to account for electron correlation.

Electrons are fermions, and same-spin electrons strive to avoid each other. However, when many electrons are forced into a region with a flat potential, the result can be a lowering of kinetic energy as indistinguishable electrons mix and delocalize over a wider region of space. This effect is responsible for the high conductivity of metals, the stability of benzene and other conjugated pi systems, and the ability of chloroplasts in plants to harvest light energy.

Is it possible for us to model the energetics of delocalized electrons using *localized* spherical Gaussians? Recall that previously we modeled p electrons using spherical Gaussian functions by modifying the effective interactions between electrons; we use a similar procedure here.

We would also like to develop an eFF expression for electron correlation. eFF

uses as its wavefunction a product of three-dimensional orbitals, implicitly assuming that electrons move independently of each other. We know this is not true, and we have already added Pauli terms to the electron force field to account for same spin electrons excluding each other. Additionally all electrons, regardless of spin, repel each other via Coulomb repulsion, which causes electrons to instantaneously avoid each other in space. This instantaneous correlation of electron motions tends to lower the overall energy of the system; the energy difference is termed "electron correlation".

To model the delocalization of electrons in a uniform potential and electron correlation effects, it is useful to study the uniform electron gas, which consists of electrons moving in a uniform background charge that exactly neutralizes the electron charge. The system is characterized by a single density parameter r_s, defined such that the density $\rho = (4/3\pi r_s^3)^{-1}$. In the limit of high density (small r_s), the kinetic energy dominates, and we can take the wavefunction to be the Slater determinant of particle-in-a-box orbitals (Hartree-Fock approximation). The energy per particle in Hartrees is then [1]

$$E = \frac{6}{5}\left(\frac{9\pi}{4}\right)^{2/3}\frac{1}{r_s^2} - \frac{3}{\pi}\left(\frac{9\pi}{4}\right)^{1/3}\frac{1}{r_s}. \tag{4.1}$$

Note that the uniform electron gas at *high* densities behaves like an ideal gas, which we usually consider to be a valid approximation for atomic gases at *low* densities. In an atomic gas, the potential energy dominates at high densities, while in an electron gas, the potential energy dominates at low densities. This results in a "reversal" of phase changes [2] — as the density of a uniform electron gas is decreased, it transitions from a gas to a Fermi liquid, where electrons move freely past each other, but have some affinity for each other. As the density is decreased further, the Fermi liquid becomes a Wigner crystal, where electrons localize and arrange themselves in a crystalline array that minimizes electrostatic potential energy.

The crossover point between electron gas and Fermi liquid occurs roughly when

the kinetic and potential energies are the same, $r_s = 0.74$ bohr. The Wigner crystal was proposed by Wigner [3] in 1934, but only recently with high-accuracy quantum Monte Carlo computations has it been possible to determine the crossover point from a Fermi liquid; it was found by Ceperley and Adler [4] to occur at the very low density $r_s = 100$ bohr.

Metals have an r_s that ranges from 1.87 bohr (Be) to 5.62 bohr (Cs), well within the Fermi liquid range [2]. It has been possible to obtain "exact" energies for the uniform electron gas within this regime using diffusion Monte Carlo, and Ceperley and Alder [4] found that electron correlation effects are significant, with the exact energy greater than the Hartree-Fock energy by as much as 60%. We attempt to use eFF to reproduce both Hartree-Fock and exact uniform electron gas energies as a function of density.

For studying delocalized electrons in metals in molecules, the uniform electron gas serves as model for one extreme — completely delocalized electrons in a uniform potential — that contrasts with the systems containing nuclei we have studied thus far. It will serve as the most severe test of eFF's ability to describe delocalized electrons with localized orbitals, and act as an anchor point for interpolation in developing eFF functions applicable to a wide range of potentials and electron localizations.

In regards to developing an eFF correlation function, there has been a long history in the density functional community of developing functionals with the uniform electron gas (such as the local density approximation [5]) that can be transferred with some modifications to inhomogeneous systems containing nuclei (generalized gradient approximation [6] and hybrid functionals [7]). We hope to replicate the success of this approach in the context of the electron force field.

There have been previous efforts to simulate the uniform electron gas using classical particles. Early approaches used screened Coulomb potentials to model electron-electron interactions, with added interactions to account for Pauli repulsion [8]. More recent efforts have focused on reproducing the proper momentum distribution of electrons in dynamics simulations using momentum-dependent po-

tentials [9, 10]. Our model is more ambitious in two regards. First, it allows electrons to have different sizes depending on the local electrostatic environment, a degree of freedom useful for describing molecules and different electron packings. Second, we estimate electron correlation, which in the Fermi liquid regime constitutes a large portion of the total energy.

This chapter is organized as follows. We begin by discussing the partition of energy into kinetic energy, electrostatic potential energy, and exchange and correlation components, as in density functional theory. We propose two sets of exchange/correlation functions, one suitable for describing the uniform electron gas, and another suitable for describing systems containing nuclei; we leave the work of interpolating between these two cases for a later date. With these energy functions, we compute the energetics, pair distribution functions, heat capacity, and oscillations of a uniform electron gas; and the energies and geometries of a variety of atoms and molecules with s-like electrons, with correlation included.

Energy expressions

As before, the system is composed of point nuclei with coordinates $\mathbf{R}$ and momenta $\mathbf{P}$, and of electrons defined by spherical Gaussian wave packets with positions $\mathbf{x}$, translational momenta $\mathbf{p_x}$, sizes s, and radial momenta p_s:

$$\Psi \propto \prod_j \exp\left[-\left(\frac{1}{s^2} - \frac{2p_s}{s}i\right)(\mathbf{r} - \mathbf{x})^2\right] \cdot \exp[i\mathbf{p_x} \cdot \mathbf{x}]. \tag{4.2}$$

Then the overall energy is a sum of the Hartree product kinetic energy, Hartree product electrostatic energy, and exchange and correlation energies:

$$E = E_{ke} + E_{nuc\cdot nuc} + E_{nuc\cdot elec} + E_{elec\cdot elec} + E_{exch} + E_{corr}.$$

The electrostatic energy and kinetic energy expressions are the same as before:

$$E_{ke} = \sum_i \frac{3}{2} \frac{1}{s_i^2}$$

$$E_{nuc\cdot nuc} = \sum_{i<j} \frac{Z_i Z_j}{R_{ij}}$$

$$E_{nuc\cdot elec} = -\sum_{i,j} \frac{Z_i}{R_{ij}} \, \mathrm{Erf}\left(\frac{\sqrt{2}\, R_{ij}}{s_i}\right)$$

$$E_{elec\cdot elec} = \sum_{i<j} \frac{1}{x_{ij}} \, \mathrm{Erf}\left(\frac{\sqrt{2}\, x_{ij}}{\sqrt{s_i^2 + s_j^2}}\right).$$

We define an exchange energy as a pairwise sum over same-spin electrons, and a correlation energy as a pairwise sum over opposite-spin electrons. For the uniform electron gas, we use exchange and correlation functions defined as:

$$E_{exch} = \sum_{\sigma_i = \sigma_j} \frac{1}{2} \frac{a_{exch} S_{ij}^2}{1 - S_{ij}^2} \cdot (t_{11} + t_{22})$$

$$E_{corr} = \sum_{\sigma_i \neq \sigma_j} \frac{-a_{corr}}{1 + b_{corr} s_{avg}} \cdot S_{ij}^{1/2}$$

where the parameters are $a_{exch} = 1/2$, $a_{corr} = 0.111283$ hartrees, $b_{corr} = 0.110253 \mathrm{bohr}^{-1}$; and the kinetic energy sum $t_{11} + t_{22}$ and average electron size s_{avg} are defined as

$$t_{11} + t_{22} = \frac{3}{2}\left(\frac{1}{s_1^2} + \frac{1}{s_2^2}\right)$$

$$s_{avg} = \sqrt{(s_1^2 + s_2^2)/2}.$$

For systems with nuclei, we use a modified exchange function:

$$E_{exch} = \sum_{\sigma_i = \sigma_j} \frac{1}{2} \frac{S_{ij}^2}{1 - S_{ij}^2}\left((a_{exch} + b_{exch} f_{size} + c_{exch})(t_{11} + t_{22}) - c_{exch}\frac{2t_{12}}{S_{ij}}\right)$$

where $f_{size} = s_1/s_2 + s_2/s_1 - 2$, and we set the parameters to be $a_{exch} = 0.4$, $b_{exch} = 0.15$, and $c_{exch} = 1$. We use as the correlation function the uniform electron gas correlation function multiplied by three.

On the exchange and correlation partitioning of energies

The terms "exchange" and "correlation" are like the terms "nonlinear," "enantioselective," and "structured" in the terms nonlinear dynamics, enantioselective catalysis, and structured programming respectively — they represent quantities made notable by their absence in historically prominent methods.

In *ab initio* methods, exchange refers to the difference in energy between a Slater determinant and a Hartree product wavefunction, while correlation refers to the difference in energy between the exact energy and the Slater determinant energy (Table 4.1). Physically, exchange can be viewed as the effect of adding Pauli repulsion to an independent-electron mean-field model, while correlation can be viewed as the effect of adding instantaneous Coulomb repulsion (as opposed to the Coulomb repulsion that determines the shape of the orbitals) to a mean-field model.

Since exchange and correlation are defined with respect to the levels of approximation within a specific method, we must take care in attempting to compare these quantities across *different* methods.

In density functional theory, we estimate correlation by integrating over a function of the electron density. Because of the way DFT is formulated, it emphasizes corrections to an independent particle model made when electrons are close to each other, so-called *local* or *dynamic* correlations. In contrast, configuration interaction methods most easily correct for longer range *static* correlations made when electrons delocalize over a longer distance, as in resonance stabilization or bond breaking — density functional theory neglects these effects. Although for many chemical problems it is acceptable to neglect long-range electron correlation, it is not so acceptable to neglect long-range electron exchange. Modern *hybrid* density functionals combine a local exchange which is compatible with local correlation functionals with some fraction of longer-range nonlocal Hartree-Fock exchange (exact exchange).

139

Terms	Effects described	Method name
Ab initio (wavefunction based)		
Hartree product	ke + electrostatics + self	
Slater determinant	+ exchange - self	Hartree-Fock
Few Slaters	+ static correlation	Gen. valence bond
Many Slaters	+ dynamic correlation	Config. interaction
Density functional theory (Kohn-Sham)		
Hartree product	ke + electrostatics + self	
f Slater determinant	+ f exact exchange - f self	
$(1 - f)$ exch functional	+ $(1 - f)$ local exchange	
corr functional	+ dynamic correlation	LDA, GGA (f = 0); hybrid (f $\neq$ 0)
Electron force field		
Hartree product	ke + electrostatics	
pairwise exchange	+ exchange	eFF (exch only)
pairwise correlation	+ dynamic correlation	eFF (exch + corr)

Table 4.1: Comparison of terms and physical effects included in *ab initio* versus density functional versus electron force field methods.

Most work to improve *ab initio* methods has focused on finding more efficient ways to add dynamic correlation in a consistent way, whether through perturbation theory, configuration interaction, coupled cluster methods, or other schemes. Most work to improve density functional theory has focused on developing "non-local" correlation functionals, perhaps based on orbitals [11]; and on correcting the so-called "self-interaction error," caused because in orbital schemes where less than the full quantity of exact exchange is used, some residual self-repulsion of individual electrons against themselves remains.

In the electron force field, we approximate exchange energy as a pairwise sum over same-spin electrons, and correlation energy as a pairwise sum over opposite-spin electrons. Since exchange arises as a consequence of Pauli repulsion, it is straightforward to see why it would be computed as an interaction between same-spin electrons. However, why should we restrict correlation to be an interaction between opposite-spin electrons? We reason that same-spin electrons are *already* segregated from each other because of the Pauli principle, so that the effects of adding electron correlation to pairs of same-spin electrons should be small com-

pared to the electron correlation that acts between opposite-spin pairs.

With this scheme, both exchange and correlation are treated at the same level, in a consistent way. It should be possible to account for both long- and short-range exchange and correlation, since we are summing over electrons that may be far away from each other. Also, because we compute electrostatic interactions only between different electrons, there is no self-interaction error. Our method of estimating electron correlation as a pairwise sum over orbitals is reminiscent of the independent electron pair approximation (IEPA) methods developed back in the 1960s [12, 13]. However, since those methods were developed in a configuration interaction framework, there were some issues with size consistency, which occurred because virtual orbitals could mix and lower the correlation energy even when molecules were infinitely separated [14]. Our method should have no such difficulties.

We consider the sum of kinetic energy, electrostatic potential energy, and pairwise exchange to be the equivalent of a Hartree-Fock calculation; and the further addition of pairwise correlation to be the equivalent of an "exact calculation," comparable to a configuration interaction or B3LYP calculation. There are some difficulties with direct comparisons: Hartree-Fock can be computed in the exact basis limit, while we are limited to a subminimal basis of spherical Gaussians; also there are differences in the way static versus dynamic correlations are handled in CI versus DFT methods. With these caveats, we proceed with our comparisons, and find, remarkably, that the agreement is often quite reasonable.

Exchange and correlation functions for the uniform electron gas

In the simplest approximation, we take the eFF exchange energy to be the pairwise sum of kinetic energy changes upon pairwise orbital orthogonalization:

$$E_{exch} = \sum_{\sigma_i = \sigma_j} \frac{S_{ij}^2}{1 - S_{ij}^2} \left(t_{11} + t_{22} - \frac{2t_{12}}{S_{ij}} \right).$$

The formula can be interpreted as quantifying the effect of moving electron density from the region between the two electrons to the electron centers. For systems with nuclei, we found it necessary to modify this function with scaling factors and additional terms to prevent electron-electron coalescence, in order to obtain stable atoms and bonds. For the uniform electron gas, we obtain good agreement with Hartree-Fock energies versus density if we scale the function by $1/4$ and neglect the t_{12} term entirely:

$$E_{exch} = \sum_{\sigma_i = \sigma_j} \frac{1}{4} \frac{S_{ij}^2}{1 - S_{ij}^2} \left(t_{11} + t_{22} \right).$$

In developing the correlation function, we assumed that the function had the form

$$E_{corr} = \sum_{\sigma_i \neq \sigma_j} f(s_{avg}) \cdot g(S_{ij})$$

where $s_{avg} = \sqrt{(s_i^2 + s_j^2)/2}$. We experimented with different functional forms for $g(S)$, then evaluated the energy of an *fcc* lattice of electrons for different electron densities. Since all the electrons were the same size, we could factor out $f(s_{avg})$ and determine what f had to be in order to fit the correlation energy. We found that if $g(S)$ varied too quickly, electrons tended to expand to maximize their overlap with each other in an unphysical way. However, if $g(S)$ varied too slowly, an unphysically high $f(s_{avg})$ was needed to obtain the correct correlation energy. Through trial and error, we found optimal forms for $f(s_{avg})$ and $g(S)$:

$$
\begin{aligned}
f(s_{avg}) &= \frac{-a_{corr}}{1 + b_{corr} s_{avg}} \\
g(S_{ij}) &= S_{ij}^{1/2}
\end{aligned}
$$

where the parameters are listed in the previous section.

Static properties of the uniform electron gas

We model the uniform electron gas as a periodic lattice of same-size electrons, as in a Wigner lattice, but at a density well within the Fermi liquid regime. We consider three structures initially (Figure 4.1): a close packed face-centered cubic structure (*fcc*), where electrons are spin-paired on top of each other; and two open-shell structures (NaCl and sphalerite), which fill interstices in the *fcc* lattice with electrons of opposite spin, and have octahedral and tetrahedral coordinations, respectively.
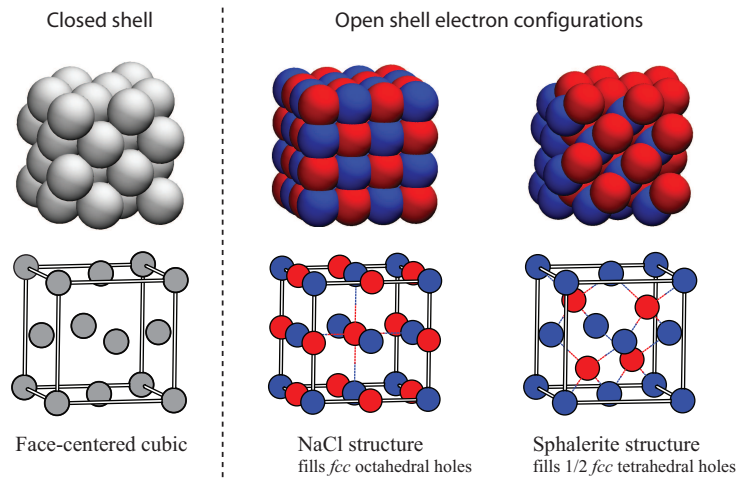
Figure 4.1: Uniform electron gas represented as different packings of localized electrons.

For comparison purposes, we calculate the Hartree-Fock energy per electron using equation 4.1, and the exact energy per electron using an analytic expression due to Perdew and Wang [15], fit to the quantum Monte Carlo calculations of Ceperley and Alder for an unpolarized uniform electron gas [4]. Over the range $r_s = 1$ to 10 bohr, we find that all of the eFF (exchange only) energies agree with the Hartree-Fock energies to within 0.01 hartrees per electron, and all of the eFF (exchange + correlation) energies agree with the exact energies to within 0.005 hartrees per electron (Figure 4.2).

The different lattices are very close in energy to each other, with the eFF
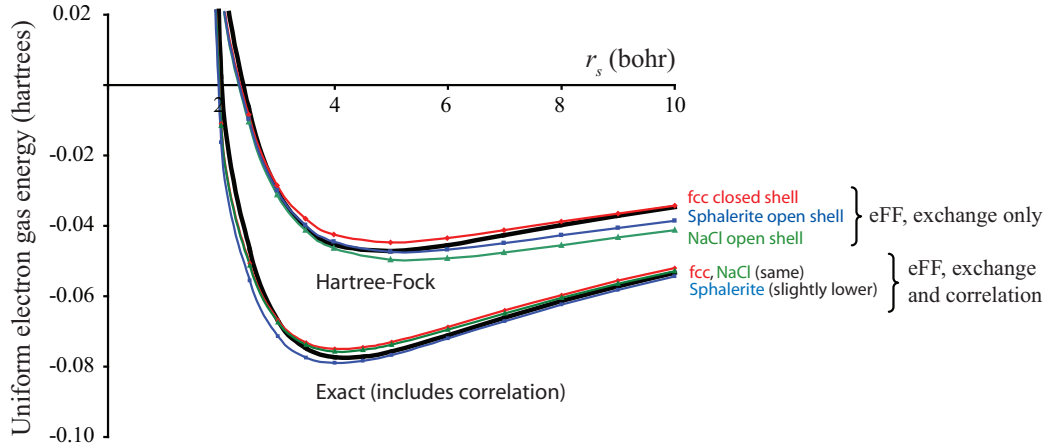
Figure 4.2: Uniform electron gas energy versus density. eFF with exchange matches Hartree-Fock, while eFF with exchange and correlation matches exact quantum Monte Carlo energies.

(exch only) energies within 0.01 hartrees per electron of each other, and the eFF (exchange + correlation) energies within 0.005 hartrees per electron of each other. Hence the uniform electron gas is fluxional, varying easily from one lattice type to another.

The energies are similar because the electrons vary in size to accommodate different packing arrangements (Figure 4.3). In general, lower densities create larger electrons. Open-shell lattices pack the electrons together more tightly, which reduces their size and increases their kinetic energy. Counteracting this increase in kinetic energy is the fact that electrons of opposite spin are no longer placed on top of each other, which reduces the electron-electron repulsion. For eFF (exch only), the electron-electron repulsion lowering dominates, and NaCl is the most stable, followed by sphalerite, and then fcc. The differences in energy are the greatest at low densities (high r_s), where potential energy dominates and differences in electron-electron repulsion are made most apparent.

Adding correlation tends to equalize the energies of the different lattices. Correlation acts as a stabilizing factor that favors the overlap of opposite-spin electrons, which causes the electrons in the uniform electron gas to expand slightly. The
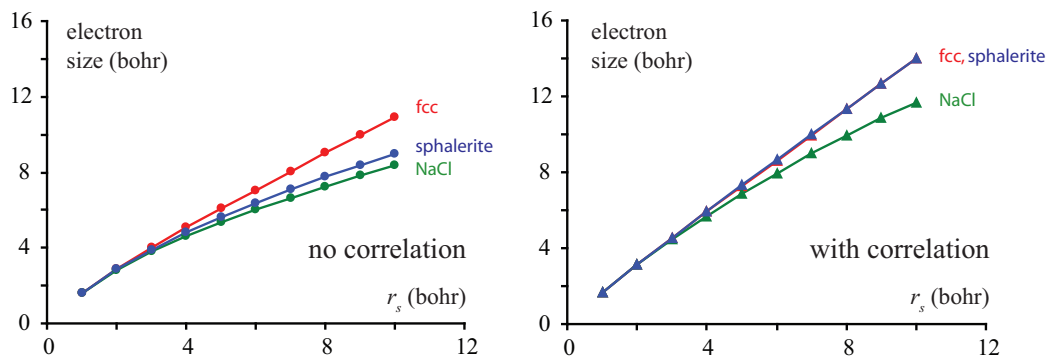
Figure 4.3: Density versus electron size. Adding correlation causes the electrons to grow larger.

closed-shell lattices are preferentially stabilized since their opposite spin electrons have more overlap with each other. Without correlation, open-shell lattices were slightly more stable than closed-shell lattices; adding correlation counteracts this preference and makes open-shell and closed-shell lattices have nearly the same energy, even at low densities.

The electrons in sphalerite have the most room to expand, and as a result, the eFF (exchange + correlation) energy of the sphalerite lattice is slightly below the others. Is it possible that less tightly packed lattices would see even more correlation stabilization? We consider other lattices with a variety of packing fractions and coordinations (Figure 4.4), and compare their energies to Hartree-Fock and exact values (Figure 4.5).

For eFF (exchange only), nearly all the lattices have the same energy (within 0.01 hartrees per electron), with the exception of diamond with its very low packing fraction. For eFF (exchange and correlation), all of the close-packed structures have similar energy (within 0.005 hartrees per electron), but the correlation function lowers the energy of closed-shell non-close-packed structures too much, and raises the energy of open-shell non-close-packed structures too much as well. The last effect is probably an artifact of the electrons expanding too much when correlation is added.

It is worthwhile to investigate the origin of exchange and correlation stabiliza-

	packing fraction	closed-shell configurations		open-shell configurations	coordination
	34%	**diamond** (A4)			
	52%	simple cubic (A$_h$)	$\longrightarrow$	**CsCl** (B2)	
	68%	**body-centered cubic** (*bcc*, A2)			
close packed	74%	**hexagonal close packed** (*hcp*, A3) $\longrightarrow$		**wurtzite** (B4)	
	74%	**face-centered cubic** (*fcc*, A1)		**sphelerite** (B3)	
				NaCl (B1)	

Figure 4.4: Survey of electron packings considered, showing a variety of packing fractions and coordinations.
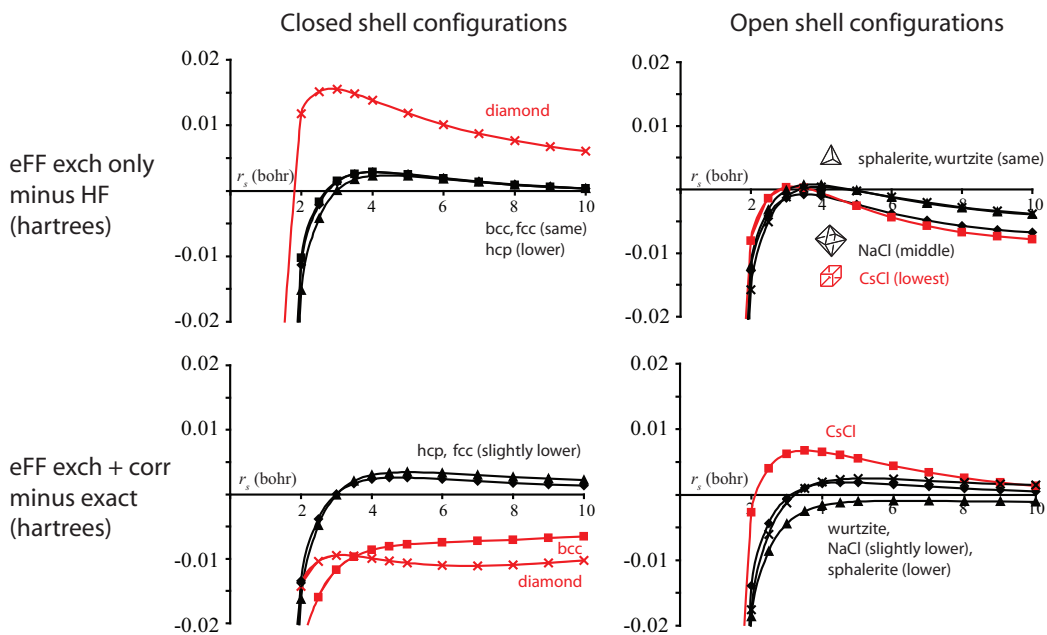
Figure 4.5: Energetics of different electron packings, with non-close-packed configurations marked red, and close-packed configurations marked black. All close-packed arrangements have similar energies which are near the exact values.

tions in eFF. In configuration interaction methods, the exchange and correlation energies arise from the explicit form of the wavefunction. The electron-electron repulsion is lower in a CI wavefunction than in a HF wavefunction, for example, because the CI wavefunction increases the average distance between electrons. In contrast, in density functional theory the exchange and correlation energies arise mostly implicitly, from a functional that is applied to a wavefunction that does not necessarily segregate electrons from each other to the extent they would be separated in an exact description. The term "mostly" is used here because some self-consistent variation of the orbitals that is dependent on the correlation energy is allowed, and so a limited amount of explicit electron segregation may take place.

We suspect that eFF, like DFT, falls into the category of methods that compute exchange and correlation energies implicitly. To check whether this is the case, we compare the electron-electron pair distribution functions in eFF with Hartree-Fock pair distribution functions [16], and exact pair distribution functions [17] fit to quantum Monte Carlo results. Disregarding spin, we would expect electrons to be further apart at lower density (higher r_s), where the average electron size is larger. Looking at the spin-averaged pair distribution function for eFF (exchange + correlation), we find some partial segregation of electrons that becomes larger at higher r_s (Figure 4.6) — the remainder of the difference must be made up implicitly, as discussed above.

In computing pair distribution functions of electrons in Gaussian orbitals, we have used the relation

$$\rho(r_{12}) = \frac{1}{2}\left(\frac{1}{\pi s_{avg}^2}\right)^{3/2} \exp(-(r_c^2 + r_{12}^2)/s_{avg}^2) \cdot \frac{\sinh 2rr_c/s_{avg}^2}{rr_c/s_{avg}^2}$$

where r_{12} is the distance between electrons, and r_c is the midpoint between two Gaussian orbitals.

Looking at the spin-resolved pair distribution functions (Figure 4.7), we find that eFF (exchange only) causes same-spin electrons to avoid each other, but in a way that exaggerates the effects of different electron sizes. Adding correlation
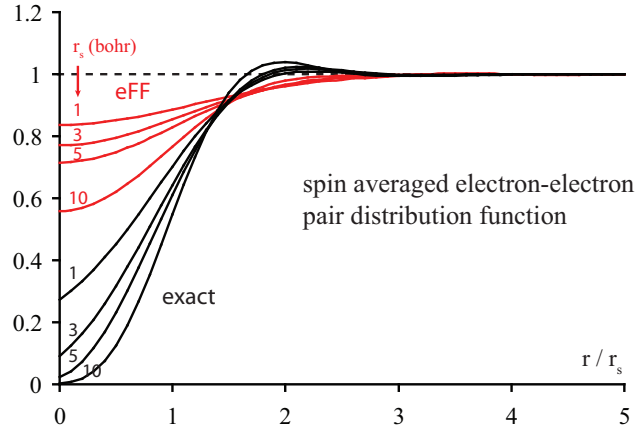
Figure 4.6: Spin-averaged electron-electron pair distribution function, showing partial explicit segregation of electrons in eFF.

damps out some of the oscillations present in the pair distribution functions by increasing the electron sizes, but the exaggerated effect of different electron sizes on same-spin exclusion remains. In contrast, opposite-spin electrons with correlation do not avoid each other as they should. When the spin-average is taken, it looks as if we have the right dependence of segregation on electron size, but it is in reality the result of an error cancellation between same- and opposite-spin pair distributions.

We have shown that using a localized electron model, we obtain good energies for the uniform electron gas over a range of Fermi liquid densities ($r_s = 1$ to 10 bohr). eFF with exchange agrees well with Hartree-Fock energies, while eFF with exchange and correlation agrees well with exact QMC-derived energies. Different close-packed lattices have very similar eFF (exchange + correlation) energies, supporting the view that the uniform electron gas at Fermi liquid densities has a fluxional structure. An analysis of electron-electron pair distribution functions reveals that there is some explicit segregation of electrons that increases with increasing electron size; however, the exchange and correlation stabilizations still come mostly from the exchange and correlation functions rather than any explicit optimization of electron positions or sizes.

Same spin pair distribution   Opposite spin pair distribution
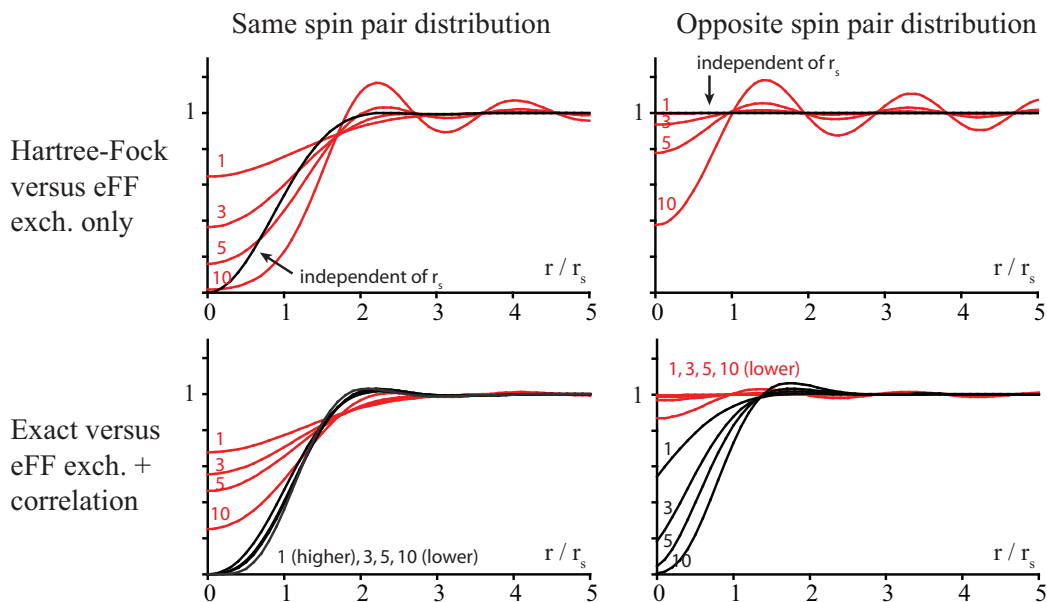
Figure 4.7: Spin-resolved electron-electron pair distribution functions, showing that eFF keeps same-spin electrons apart, but allows opposite-spin electrons to mingle.

Dynamic properties of the uniform electron gas

We study electron excitations at finite temperature by giving the electron positions and sizes initial random velocities, and propagating the resulting dynamics at constant energy and volume. We use as a test case a NaCl lattice of 64 electrons with $r_s = 2$ bohr. At low temperatures, the electrons make small excursions about their equilibrium positions, but at higher temperatures they mix more freely (Figure 4.8).

We can measure the heat capacity of the electron liquid by plotting the total energy as a function of temperature (T = 50 to 500 K, Figure 4.10). In a classical solid, the heat capacity at low temperatures is given by the Dulong and Petit expression $C_v = 3k_B N$, since there is an equipartition of energy among all the degrees of freedom in the solid. In metals, the heat capacity at temperatures below the Fermi temperature ($T_F = 140,000$ K for $r_s = 2$ bohr) scales as $C_v \propto T/T_F$; the heat capacity is much lower than would be expected from a classical solid, because

230 K   1110 K
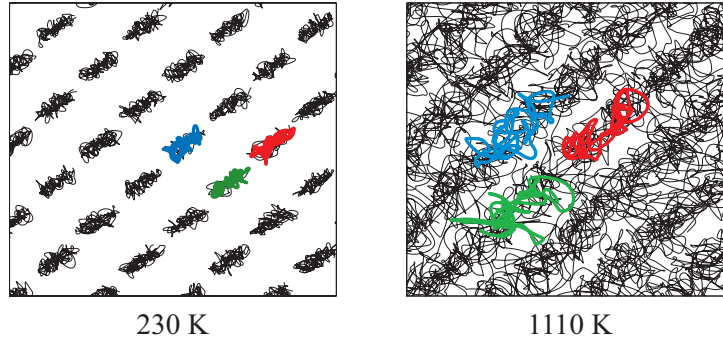
Figure 4.8: Electron trajectories in a uniform electron gas ($r_s = 2$ bohr) at low and high temperature.

only states near the Fermi level can be excited [16] (Figure 4.9).
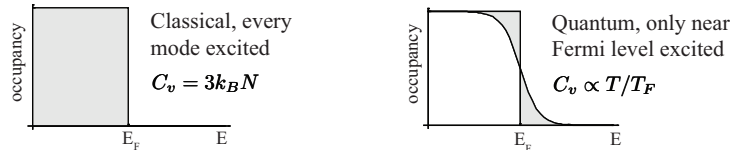
Figure 4.9: At low temperatures, the heat capacity of a metal goes to zero because only electrons near the Fermi level are excited.

The eFF electron gas has a heat capacity that matches classical, not quantum, statistics (Figure 4.10), suggesting that all of the available modes are being excited uniformly, a contention further supported by the spectrum of phonon excitations (Figure 4.11) derived by computing the Fourier transform of the velocity autocorrelation function [18].

Since we are simulating electrons as classical particles interacting via effective potentials, it is not surprising that we reproduce classical and not quantum statistics. Other researchers who have created quasiclassical models of the uniform electron gas have reproduced the correct Fermi-Dirac distribution of momenta using momentum dependent potentials, which spread out the particles in momentum phase space. For example, in 1987, Dorso and Randrup [9] applied a Pauli potential of the form

$$V(p, q) = V_0(\hbar/p_0 q_0)^D \exp(-p_{ij}^2/p_0^2 + q_{ij}^2/q_0^2)$$
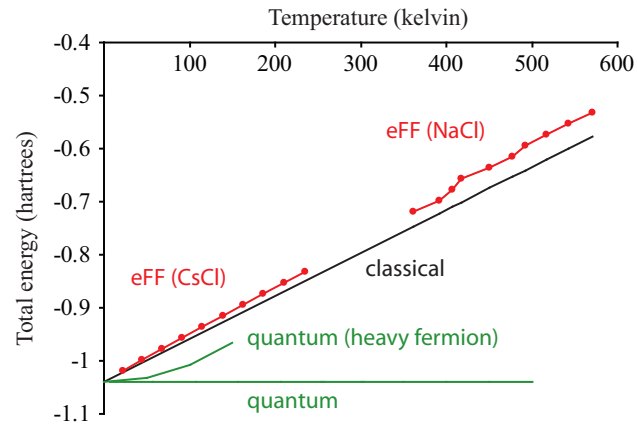
Figure 4.10: eFF uniform electron gas has the heat capacity of a solid crystal, not a metal with Fermi-Dirac statistics. The heat capacity in this figure is given by the slope, since we are plotting total energy versus temperature.
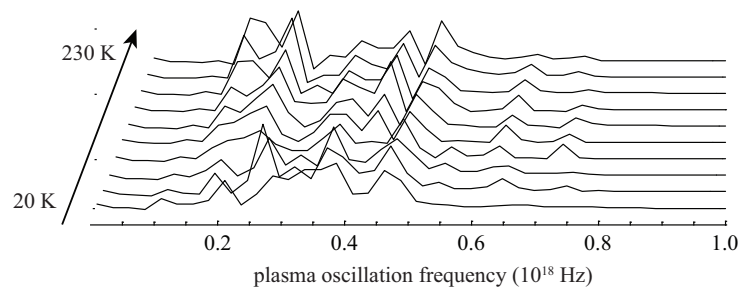
Figure 4.11: Plasma oscillations are excited uniformly over the range of temperatures considered.

to a periodic system of point particles with positions q and momenta p, and found that a Metropolis simulation produced a proper Fermi-Dirac distribution of momenta. In their system, the repulsion is greater when two nearby particles have different momenta; investigation by Cordero and Hernandez [19] has shown that this kind of potential causes nearby particles to "lock momenta" and move collectively. In 1997, Ortner et al. [10] used Dorso's potential to simulate some dynamic properties of the uniform electron gas, including plasma oscillations.

In the future we will try adding a momentum-dependent repulsion function to eFF to reproduce Fermi-Dirac distributions of momenta. However, we will need to proceed carefully to ensure (1) that energy remains conserved, and that there is no energy loss via hysteresis effects and (2) that we still obtain correct dynamics when electrons are associated with nuclei.

Exchange and correlation functions for systems with nuclei

With the uniform electron gas exchange and correlation functions established, we now attempt to describe systems containing nuclei. Ideally, we would be able to apply the uniform electron gas functionals to these systems without modification. As a test case, we examined the Hartree-Fock repulsion between two helium atoms, and between a helium and a hydrogen atom. However, we found that the uniform electron gas exchange function by itself was not repulsive enough to reproduce the interaction (Figure 4.12).
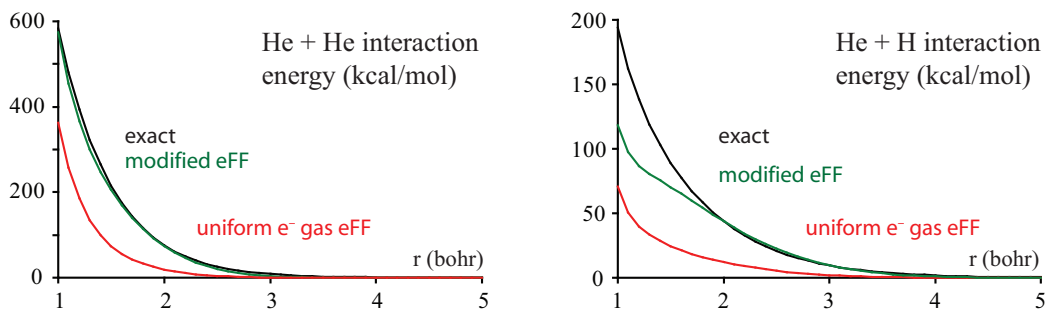
Figure 4.12: We modify the exchange interaction to fit properly the interaction energy of He_2 and HeH.

We saw this as an opportunity to develop a new exchange functional that could draw from some of the insights gained from the uniform electron gas work, as well as from the previous incarnations of eFF, while correcting some past deficiencies. In the work on hydrogen plasma and uniform electron gas, we used a Pauli repulsion function of the form

$$E_{Pauli} = \sum_{\sigma_i = \sigma_j} \left(\frac{S_{ij}^2}{1 - S_{ij}^2} + (1 - \rho) \frac{S_{ij}^2}{1 + S_{ij}^2} \right) \Delta T_{ij}$$

with scaling factors added. It proved to be a capable function, able to correctly determine the relative energies of a wide range of hydrocarbon conformers. However, it was slightly too repulsive, giving an energy barrier for $H_2 + H \rightarrow H + H_2$ as 42 kcal/mol rather than the exact 9 kcal/mol. It was also possible for same-spin electrons of the same size to coalesce.

In the work on p-like electrons, we used a Pauli repulsion function of the form

$$E_{Pauli} = \sum_{\sigma_i = \sigma_j} \frac{1}{2} \frac{S_{ij}}{1 - S_{ij}^2} \cdot \left(\left(a + b \left(\frac{s_j}{s_i} + \frac{s_i}{s_j} - 2 \right) \right) \cdot \frac{S_{ij}}{1 - S_{ij}^2} + c(1 - S_{ij}) \right) \cdot \Delta T_{ij}$$

which had a singularity when $s_i = s_j$ and $S \rightarrow 1$, eliminating the coalescence problem. However it was not repulsive enough, which caused structures like tetrahedral H_4 to be inappropriately stable.

We notice that the uniform electron gas function has a singularity as $S \rightarrow 1$, since it is missing a t_{12} term. This led us to try puting the t_{12} term back into our exchange function, but with a scaling factor different from the one in front of the $t_{11} + t_{22}$ term. We justify this procedure on the grounds that when nuclei are present, the kinetic energy at the electron centers is underestimated, since we are missing the proper nuclear-electron cusp, while the Gaussian description of electrons at the electron midpoint is a relatively better representation. Thus in computing the kinetic energy change upon orthogonalization, which moves electron density from the electron midpoint to the electron centers, we should multiply the t_{ii} terms by a larger factor than the t_{ij} terms. We write the final exchange function

as follows:

$$E_{exch} = \sum_{\sigma_i = \sigma_j} \frac{1}{2} \frac{S_{ij}^2}{1 - S_{ij}^2} \left((a_{exch} + b_{exch} f_{size} + c_{exch})(t_{11} + t_{22}) - c_{exch} \frac{2t_{12}}{S_{ij}} \right)$$

where $f_{size} = s_1/s_2 + s_2/s_1 - 2$. The parameters, adjusted to reproduce the He_2 repulsion and the correct bond length for LiH, are specified in the energy expression section.

The new exchange reproduces the repulsion of He_2 and HeH well, and has the desired anticoalescence singularity. Plotted against the previous Pauli repulsion functions, we see it is more repulsive than the p-like electron function, and slightly less repulsive than the original Pauli function, as desired (Figure 4.13).
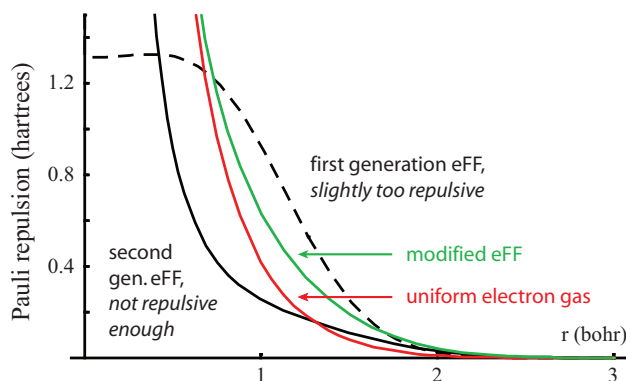
Figure 4.13: Comparison of the new exchange potential to previous Pauli potentials, showing that the new potential has a reasonable amount of repulsion.

In order to obtain correct geometries for LiH and BeH_2, we need to include a relative-size-dependent term f_{size} in the function, as we did in the p-like electron eFF, but we find that the parameter multiplying it is smaller than it was previously (0.15 versus 3).

In developing a correlation function for systems containing nuclei, we use H_2 bond breaking as a test case, which turns out to present some complications, since both unrestricted and restricted Hartree-Fock formalisms have problems describing the correct dissociation of hydrogen molecule. The unrestricted HF wavefunction for H_2 is simply $\phi_1(r_1)\phi_2(r_2)$, where ϕ_1 and ϕ_2 are orbitals localized on

different nuclei. However, since electrons are indistinguishable, the wavefunction $\phi_2(r_1)\phi_1(r_2)$ should be equally valid, and it turns out that the generalized valence bond wavefunction $\phi_1(r_1)\phi_2(r_2) + \phi_2(r_1)\phi_1(r_2)$ has a lower energy than the UHF wavefunction. This difference is termed "static correlation," since it represents the interaction of electrons occupying orbitals that are far apart from each other. The exact energy is even lower than the GVB energy, and we assume that the energy difference arises from "dynamic correlation," the stabilizing interaction of electrons that are near to each other.

We can thus take the difference between exact and GVB energies to be a measure of dynamic correlation, and the difference between exact and UHF energies to be a measure of dynamic *and* static correlation. When we apply the uniform electron gas correlation functional to H_2, we find that it falls off similarly to the exact minus GVB curve, suggesting that we account for dynamic but not static correlation (Figure 4.14). The exact minus UHF curve has a peculiar behavior, reaching a maximum near the point where the wavefunction transitions from a closed- to an open-shell form. Creating a function that reproduces this peak would be challenging, and we sidestep this issue by claiming that, like DFT, our eFF correlation functional reproduces dynamic and not static correlation effects.
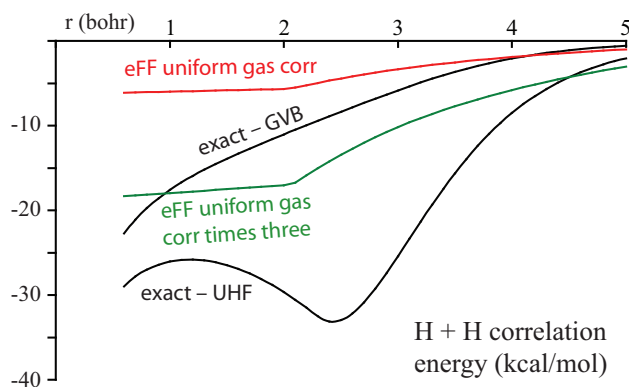
Figure 4.14: We scale the correlation function to match the long range falloff of the GVB correlation energy in H_2.

To better match the falloff of the exact minus GVB curve, we multiply the

uniform gas correlation energy by three. Future functionals would likely interpolate between these two extremes.

To clarify what effects eFF includes and what it does not, we plot the H_2 bond-breaking potential energy surface (Figure 4.15). We see that eFF with exchange is nearly 20 kcal/mol above the UHF curve, due to the deficiency inherent in the eFF single Gaussian basis. The total correlation energy at that point is nearly 27 kcal/mol, but we only account for 18 kcal/mol of it. We also see that both forms of eFF fall off like UHF, not GVB. We conclude that we are accounting for dynamic correlation properly, but not static correlation; and that a further future correction will be needed to account for deficiencies in the single Gaussian basis. We have not attempted to have either the exchange or correlation functional correct for basis set deficiencies, because we would like to keep the terms of the eFF force field as "clean" and focused on single tasks as possible.
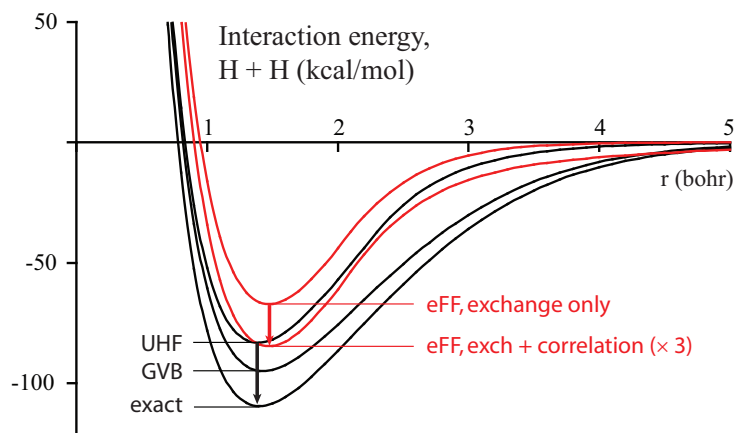
Figure 4.15: Comparison of H_2 potential energy curves; we limit the correlation function to correcting correlation, not deficiencies in the basis.

Performance of new functions on systems with nuclei

We start by testing the new exchange function on simple molecules with nuclei and s-like electrons (Figure 4.16). This includes the hydrides LiH, BeH, BeH_2 used to fit the exchange function, as well as the hydrogen systems H_3 (linear TS), H_4

(square TS), H_3^+, H_4^{2+}, and the lithium systems Li_2, Li_2^+, Li_3^+, and Li_4^{2+}. We find excellent agreement between eFF (exchange only) and unrestricted Hartree-Fock (6-311g** basis) for bond lengths (Figure 4.17), except for the lithium geometries, which are consistently too long by ≈ 0.2Å.
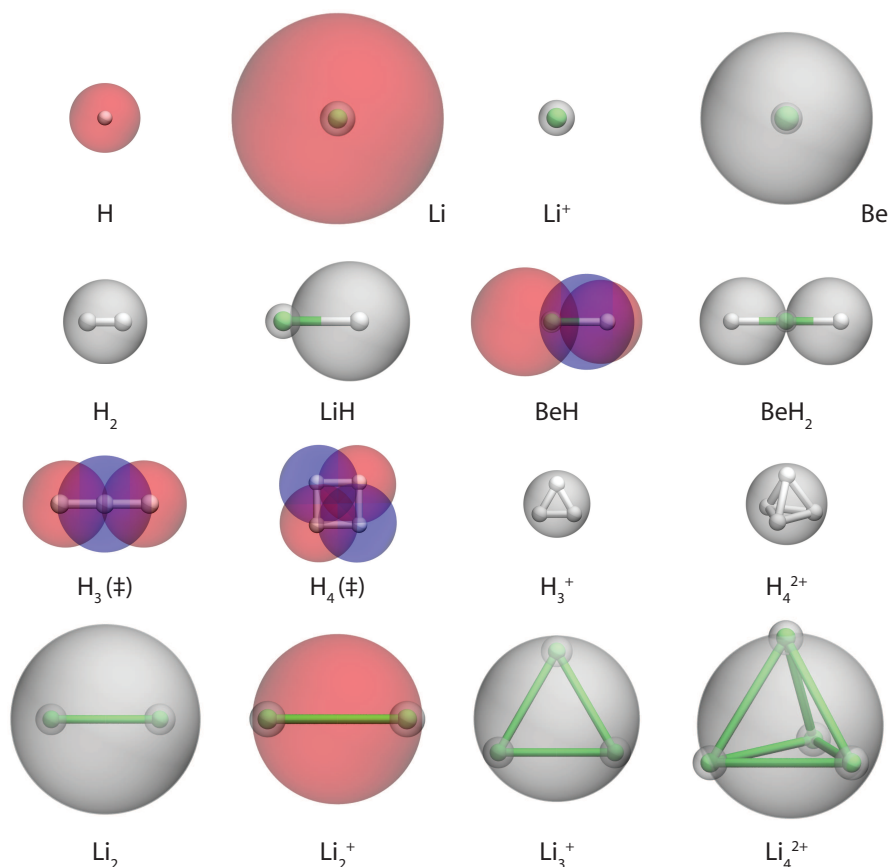
Figure 4.16: Gallery of systems with nuclei and s-like electrons.

There is good agreement on dissociation energies as well (Table 4.2, Figure 4.17, Table 4.7). For the first time, we obtain a reasonable energy for the H_3 linear transition state relative to $H_2 + H$ (20.3 kcal/mol versus 24.3 kcal/mol UHF). We also obtain a reasonable energy for the forbidden H_4 square transition state (101.5 kcal/mol versus 121.4 kcal/mol UHF). Adding a proton to dihydrogen creates the

157

energy of	relative to
H_2	$H + H$
LiH	$Li + H$
BeH	$Be + H$
BeH_2	$BeH + H$
H_3 (linear)	$H_2 + H$
H_4 (square)	$H_2 + H_2$
H_3^+ (triangle)	$2H + H^+$
H_4^{2+} (tetrahedron)	$2H + 2H^+$
Li_2	$2Li$
Li_2^+	$Li + Li^+$
Li_3^+ (triangle)	$2Li + Li^+$
Li_4^{2+} (tetrahedron)	$2Li + 2Li^+$

Table 4.2: Key to tested geometries and dissociation energies.
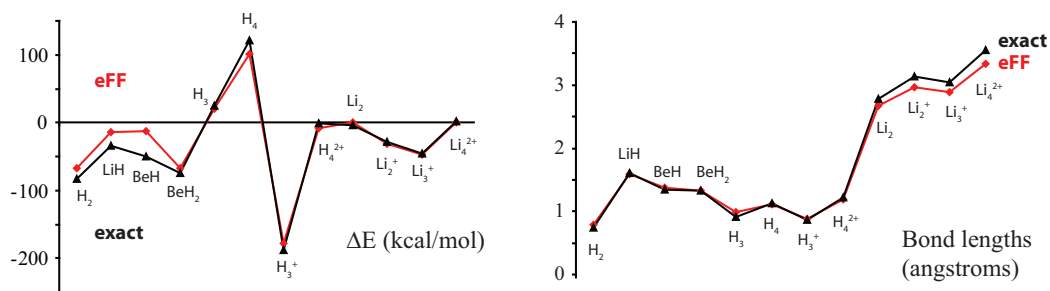
Figure 4.17: eFF with exchange shows good agreement with Hartree-Fock for bond lengths and dissociation energies of s-electron systems.

two-electron triangular ion H_3^+, with a stability of -177.5 kcal/mol versus -187.6 kcal/mol UHF relative to separated atoms; adding another proton results in a tetrahedron that is barely stable relative to separated atoms (-8.3 kcal/mol versus -1.7 kcal/mol UHF).

We obtain correct dissociation energies for a variety of homonuclear lithium complexes, such as the dimer Li_2 (0.9 kcal/mol versus -4.0 kcal/mol UHF), the one-electron ion Li_2^+ which has a stronger bond (-31.4 kcal/mol versus -29.0 kcal/mol UHF), as well as the triangular cation Li_3^+ (-46.6 kcal/mol versus -46.0 kcal/mol UHF), and the tetrahedral cation Li_4^{2+} (0.4 kcal/mol versus 1.2 kcal/mol UHF). That we are able to obtain correct dissociation energies for homonuclear lithium clusters is remarkable in light of the long length and weakness of the bond; it represents an extreme in bonding.

The molecules H_2, LiH, and BeH are underbound by 20-40 kcal/mol. We understand that H_2 is underbound because of deficiencies in the basis, but the weak bond in LiH and BeH is surprising, given that the ionization potentials of Li and Be match the Hartree-Fock values exactly (Li: 123 kcal/mol eFF versus 123 kcal/mol HF, 186 kcal/mol eFF versus 186 kcal/mol eFF). Previously we had believed that localized Gaussian functions were a good basis for representing LiH; we may have to reevaluate this notion. At least there is some consistency now between the dissociation energy of hydrides and the dissociation energy of H_2.

We assess the new eFF correlation function by comparing eFF correlation energies to B3LYP minus UHF in the above series of s-electron containing molecules (Figure 4.18). Adding correlation tends to decrease electron-electron repulsion and shrink bond lengths. For the most part, we obtain the correct change in bond length upon adding correlation, with eFF bond length differences systematically larger than B3LYP minus HF differences by -0.03 to -0.05 Å. The bond length changes are especially large in the lithium clusters.

Where exact energies are available, the correlation energies agree well with exact minus UHF energies, though not as well with B3LYP minus UHF energies (Table 4.8, H_2: -16.5 kcal/mol eFF versus -20.8 kcal/mol exact, LiH: -22.8 kcal/mol
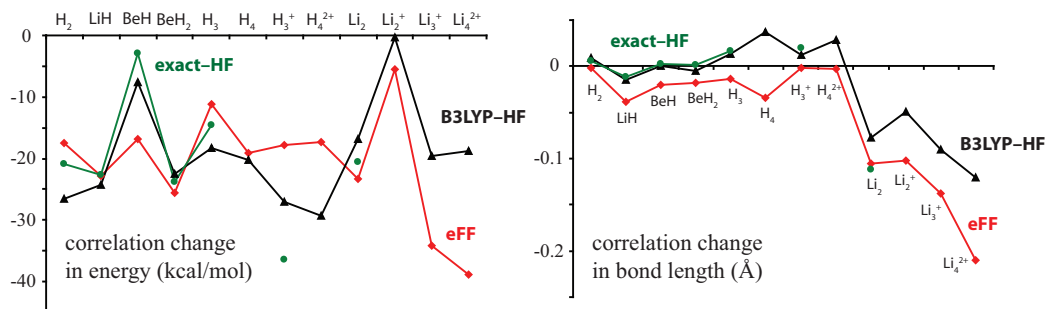
Figure 4.18: eFF reproduces some energy and bond length changes caused by adding correlation.

versus -22.7 kcal/mol exact, BeH_2: -25.6 kcal/mol versus -23.8 kcal/mol exact, H_3 (linear): -11.1 kcal/mol versus -14.6 kcal/mol exact, and Li_2: -23.3 kcal/mol versus -20.5 kcal/mol exact).

We do less well for the geometries BeH (-16.9 kcal/mol versus -2.9 kcal/mol exact) and H_3^+ (-17.8 kcal/mol versus -36.4 kcal/mol exact) — the reasons for these discrepancies are unknown. We tend to overestimate the correlation of lithium two-electron systems and underestimate the correlation of hydrogen two-electron systems, which suggests that there may be some effects of having nuclei nearby we should be including, or that core-valence correlation is not balanced as well as correlation between core-like electrons.

We turn to a simpler problem, finding the correlation energy of core electrons. Consider the effect of increasing the nuclear charge of a helium atom. As Z increases, the electrons are drawn more tightly inward, which causes the electron-electron repulsion to increase. We would expect that the correlation energy would increase as well; however, at the same time, it becomes more difficult to excite the electrons to virtual orbitals, which makes the electrons less mobile. The end result is that the correlation energy of core electrons remains virtually unchanged as Z increases. Density functional methods tend to overestimate the correlation energy of highly charged ions isoelectronic to helium [20]. With the eFF correlation function, we find that the correlation energy of the core-like electrons has the correct trend of remaining virtually unchanged as Z increases (Figure 4.19).
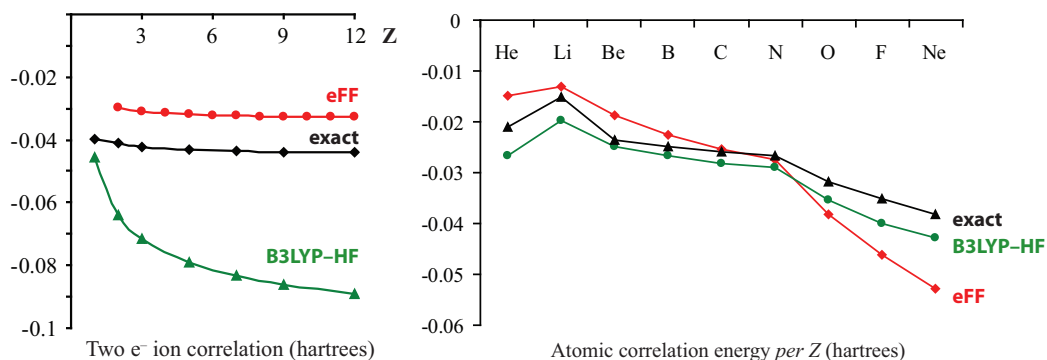
Figure 4.19: Atomic correlation energies, eFF reproduces major trends.

Encouraged by this success, we examined the total atomic correlations of the atoms helium through neon. We evaluated the correlation energy as a single point correction to atoms optimized with the eFF for p-like electrons discussed in the previous chapter. We reproduced the general trend and magnitude of correlation energies correctly (Figure 4.19), but (1) helium correlation energy is too small (2) lithium through carbon correlation energies are too small and increase too quickly; (3) oxygen through neon correlations are too large and increase too quickly. It will be interesting to discover what will happen once the correlation function is applied self-consistently to atoms.

Overall, we have remarkably good agreement between eFF (exchange only) and Hartree-Fock energies and bond lengths, suggesting that the new exchange function is a good candidate for further development. The correlation function slightly exaggerates the change in bond length that occurs when correlation is added, but reproduces overall trends correctly. Where exact energies are available, we observe reasonable agreement between eFF correlation energies and exact minus Hartree-Fock energies. Finally, we have shown some promising results in reproducing atomic correlation energies, but a definitive verdict will have to wait until we develop a system for handling p-like electrons compatible with the new exchange and correlation functions.

Conclusion

The centerpiece of this chapter was the uniform electron gas, a system character-ized by a single density parameter that can exist as a uniform gas, Fermi liquid, or Wigner crystal, depending on density. We saw the uniform electron gas as both a model for electron delocalization, and a starting point for developing new exchange and correlation functions. In developing previous electron force fields, we had focused on reproducing the best known "exact" energy with our Pauli function. In this chapter, we sought to reproduce two energies: the Hartree-Fock energy, based on a combination of eFF kinetic energy, electrostatic potential en-ergy, and exchange energy; and the exact energy, based on the above combination with correlation energy added.

We were successful in describing the uniform electron gas using localized elec-trons. With the appropriate exchange and correlation functions, we found that we could reproduce Hartree-Fock and exact energies of the uniform electron gas as a function of density. As a further surprise, we discovered that the energies of many different lattices were similar, hinting that the uniform electron gas at Fermi liquid densities had a fluxional structure. As a caveat, we noted that our potentials in their current form could only reproduce a classical and not a quantum distribution of momenta.

After extending and modifying the exchange and correlation functions, we were able to describe systems with nuclei and s-like electrons, with good agreement between eFF (with exchange) and Hartree-Fock, and eFF (with exchange and correlation) and exact energies. For example, by fitting parameters to reproduce He_2 repulsion, the bond length of lithium hydride, and the long range decay of H_2 dynamic correlation energy, we obtained exchange/correlation functions that could reproduce the barrier to the reaction $H_2 + H \rightarrow H + H_2$ (20.3 kcal/mol eFF with exchange versus 24.3 kcal/mol unrestricted Hartree-Fock; 9.1 kcal/mol eFF with exchange and correlation versus 9.7 kcal/mol exact).

We still have separate versions of exchange/correlation functions, one for the uniform electron gas, and another for systems with nuclei. Future versions of eFF

should handle both extremes using a single set of functions, interpolating smoothly between uniform and non-uniform electrostatic potentials, just as the eFF in the previous chapter interpolated between s-like and p-like electron shapes. We hope the ideas provided in this chapter serve as a useful first step in that direction.

Supplemental tables

r_s	fcc	bcc	hcp	diamond	HF
1	0.5115	0.5219	0.4903	0.5870	0.6468
2	0.0359	0.0369	0.0320	0.0589	0.0472
2.5	-0.0086	-0.0082	-0.0107	0.0087	-0.0065
3	-0.0286	-0.0285	-0.0299	-0.0145	-0.0299
3.5	-0.0382	-0.0381	-0.0390	-0.0259	-0.0407
4	-0.0426	-0.0427	-0.0432	-0.0317	-0.0455
5	-0.0449	-0.0450	-0.0452	-0.0356	-0.0474
6	-0.0437	-0.0438	-0.0439	-0.0356	-0.0457
7	-0.0415	-0.0416	-0.0416	-0.0342	-0.0429
8	-0.0390	-0.0391	-0.0391	-0.0324	-0.0400
9	-0.0367	-0.0367	-0.0367	-0.0305	-0.0373
10	-0.0344	-0.0345	-0.0345	-0.0287	-0.0348

Table 4.3: Uniform electron gas energy versus density for closed-shell packings, with r_s in bohr and the energy per atom in hartrees. We are comparing eFF with exchange to Hartree-Fock energies.

r_s	NaCl	CsCl	sphalerite	wurtzite	HF
1	0.5109	0.5346	0.5112	0.4901	0.6468
2	0.0344	0.0390	0.0350	0.0314	0.0472
2.5	-0.0106	-0.0079	-0.0097	-0.0116	-0.0065
3	-0.0313	-0.0296	-0.0301	-0.0311	-0.0299
3.5	-0.0415	-0.0404	-0.0400	-0.0405	-0.0407
4	-0.0465	-0.0460	-0.0448	-0.0451	-0.0455
5	-0.0498	-0.0500	-0.0476	-0.0477	-0.0474
6	-0.0494	-0.0501	-0.0469	-0.0469	-0.0457
7	-0.0478	-0.0487	-0.0451	-0.0450	-0.0429
8	-0.0457	-0.0467	-0.0429	-0.0428	-0.0400
9	-0.0436	-0.0447	-0.0408	-0.0406	-0.0373
10	-0.0415	-0.0426	-0.0387	-0.0386	-0.0348

Table 4.4: Uniform electron gas energy versus density for open-shell packings, with r_s in bohr and the energy per atom in hartrees. We are comparing eFF with exchange to Hartree-Fock energies.

r_s	fcc	bcc	hcp	diamond	QMC
1	0.4508	0.4454	0.4305	0.5018	0.5870
2	-0.0110	-0.0233	-0.0139	-0.0119	0.0024
2.5	-0.0507	-0.0628	-0.0517	-0.0572	-0.0468
3	-0.0668	-0.0786	-0.0670	-0.0764	-0.0669
3.5	-0.0732	-0.0846	-0.0729	-0.0844	-0.0749
4	-0.0750	-0.0860	-0.0744	-0.0873	-0.0773
4.5	-0.0746	-0.0853	-0.0738	-0.0875	-0.0772
5	-0.0731	-0.0835	-0.0722	-0.0863	-0.0757
6	-0.0688	-0.0786	-0.0678	-0.0822	-0.0711
7	-0.0641	-0.0734	-0.0631	-0.0772	-0.0661
8	-0.0596	-0.0684	-0.0587	-0.0723	-0.0614
9	-0.0556	-0.0639	-0.0547	-0.0678	-0.0571
10	-0.0520	-0.0599	-0.0511	-0.0636	-0.0533

Table 4.5: Uniform electron gas energy versus density for closed-shell packings, with r_s in bohr and the energy per atom in hartrees. We are comparing eFF with exchange and correlation to quantum Monte Carlo energies.

r_s	NaCl	CsCl	sphalerite	wurtzite	QMC
1	0.4504	0.4836	0.4446	0.4290	0.5870
2	-0.0115	-0.0003	-0.0162	-0.0152	0.0024
2.5	-0.0512	-0.0428	-0.0555	-0.0529	-0.0468
3	-0.0674	-0.0607	-0.0714	-0.0681	-0.0669
3.5	-0.0738	-0.0682	-0.0774	-0.0740	-0.0749
4	-0.0757	-0.0708	-0.0790	-0.0754	-0.0773
4.5	-0.0753	-0.0711	-0.0784	-0.0748	-0.0772
5	-0.0738	-0.0701	-0.0767	-0.0732	-0.0757
6	-0.0695	-0.0667	-0.0720	-0.0687	-0.0711
7	-0.0648	-0.0627	-0.0671	-0.0640	-0.0661
8	-0.0604	-0.0588	-0.0624	-0.0595	-0.0614
9	-0.0564	-0.0552	-0.0582	-0.0555	-0.0571
10	-0.0528	-0.0520	-0.0544	-0.0519	-0.0533

Table 4.6: Uniform electron gas energy versus density for open-shell packings, with r_s in bohr and the energy per atom in hartrees. We are comparing eFF with exchange and correlation to quantum Monte Carlo energies.

		no correlation		with correlation		
energy of	relative to	eFF	HF	eFF	B3LYP	exact
H_2	$H + H$	-67.2	-83.4	-84.7	-110.0	-104.2
LiH	$Li + H$	-13.6	-33.9	-36.4	-58.2	-56.6
BeH	$Be + H$	-12.9	-49.9	-29.8	-57.5	-52.8
BeH_2	$BeH + H$	-66.7	-75.1	-92.3	-97.6	-98.9
H_3 (linear)	$H_2 + H$	20.3	24.3	9.1	6.0	9.7
H_4 (square)	$H_2 + H_2$	101.5	121.4	82.4	101.2	147.0
H_3^+ (triangle)	$2H + H^+$	-177.5	-187.6	-195.3	-214.6	-224.0
H_4^{2+} (tetrahedron)	$2H + 2H^+$	-8.3	-1.7	-25.6	-31.0	
Li_2	$2Li$	0.9	-4.0	-22.4	-20.8	-24.5
Li_2^+	$Li + Li^+$	-31.4	-29.0	-36.9	-29.3	
Li_3^+ (triangle)	$2Li + Li^+$	-46.6	-46.0	-80.7	-65.6	
Li_4^{2+} (tetrahedron)	$2Li + 2Li^+$	0.4	1.2	-38.4	-17.6	

Table 4.7: Comparison of dissociation energies (kcal/mol) of s-like geometries.

energy of	relative to	eFF corr	B3LYP-HF	exact-HF
H_2	$H + H$	-17.5	-26.6	-20.8
LiH	$Li + H$	-22.8	-24.4	-22.7
BeH	$Be + H$	-16.9	-7.6	-2.9
BeH_2	$BeH + H$	-25.6	-22.6	-23.8
H_3 (linear)	$H_2 + H$	-11.1	-18.3	-14.6
H_4 (square)	$H_2 + H_2$	-19.1	-20.2	
H_3^+ (triangle)	$2H + H^+$	-17.8	-27.0	-36.4
H_4^{2+} (tetrahedron)	$2H + 2H^+$	-17.4	-29.2	
Li_2	$2Li$	-23.3	-16.9	-20.5
Li_2^+	$Li + Li^+$	-5.5	-0.3	
Li_3^+ (triangle)	$2Li + Li^+$	-34.1	-19.6	
Li_4^{2+} (tetrahedron)	$2Li + 2Li^+$	-38.9	-18.8	

Table 4.8: Comparison of correlation energies (kcal/mol) of s-like geometries.

	no correlation		with correlation		
	eFF	HF	eFF	B3LYP	exact
H_2	0.780	0.735	0.778	0.744	0.741
LiH	1.594	1.607	1.556	1.593	1.596
BeH	1.377	1.341	1.357	1.341	1.343
BeH_2	1.333	1.332	1.315	1.327	1.334
H_3 (linear)	0.989	0.913	0.975	0.927	0.930
H_4 (square)	1.119	1.131	1.085	1.168	1.220
H_3^+ (triangle)	0.875	0.870	0.873	0.882	0.889
H_4^{2+} (tetrahedron)	1.183	1.225	1.180	1.254	
Li_2	2.675	2.785	2.569	2.707	2.673
Li_2^+	2.971	3.141	2.869	3.092	
Li_3^+ (triangle)	2.892	3.044	2.754	2.953	
Li_4^{2+} (tetrahedron)	3.339	3.547	3.129	3.426	

Table 4.9: Comparison of bond lengths (angstroms) of s-like geometries.

	eFF corr	B3LYP-HF	exact-HF
H_2	-0.002	0.009	0.005
LiH	-0.038	-0.014	-0.011
BeH	-0.020	0.001	0.002
BeH_2	-0.018	-0.005	0.002
H_3 (linear)	-0.014	0.014	0.017
H_4 (square)	-0.034	0.037	
H_3^+ (triangle)	-0.002	0.012	0.019
H_4^{2+} (tetrahedron)	-0.003	0.029	
Li_2	-0.105	-0.077	-0.112
Li_2^+	-0.102	-0.049	
Li_3^+ (triangle)	-0.138	-0.090	
Li_4^{2+} (tetrahedron)	-0.210	-0.121	

Table 4.10: Comparison of bond length differences (angstroms) upon adding correlation for s-like geometries.

	spin	correlation energy (kcal/mol)		
		eFF	B3LYP-HF	exact [21]
He	s	-0.0297	-0.0531	-0.0420
Li	d	-0.0390	-0.0593	-0.0454
Be	s	-0.0745	-0.0993	-0.0940
B	d	-0.1130	-0.1338	-0.1240
C	t	-0.1522	-0.1695	-0.1551
N	q	-0.1928	-0.2023	-0.1861
O	t	-0.3050	-0.2830	-0.2539
F	d	-0.4144	-0.3589	-0.3160
Ne	s	-0.5278	-0.4283	-0.3810

Table 4.11: Comparison of atomic correlation energies.

Bibliography

[1] **Gell-Mann, M., Brueckner, K. A.** 1957. Correlation energy of an electron gas at high density. *Phys. Rev.* **106(2)**:364-368.

[2] **Giuliani, G., Vignale, G.** 2005. *Quantum theory of the electron liquid.* Cambridge University Press, Cambridge (ISBN-13 978-0-521-82112-6).

[3] **Wigner, E.** 1934. On the interaction of electrons in metals. *Phys. Rev.* **46**:1002-1011.

[4] **Ceperley, D. M., Alder, B. J.** 1980. Ground state of the electron gas by a stochastic method. *Phys. Rev. Lett.* **45(7)**:566-569.

[5] **Kohn, W., Sham, L. J.** 1965. Self-consistent equations including exchange and correlation effects. *Phys. Rev.* **140(4A)**:A1133-A1138.

[6] **Langreth, D. C., Mehl, M. J.** 1983. Beyond the local-density approximation in calculations of ground-state electronic properties. *Phys. Rev. B.* **28(4)**:1809-1834.

[7] **Becke, A. D.** 1993. Density-functional thermochemistry. III. The role of exact exchange. *J. Chem. Phys.* **98(7)**:5648-5652.

[8] **Norman, G. E., Valuev, A. A.** 1978. Electrical conductivity of nonideal plasma. *Plas. Phys.* **21**:531-544.

[9] **Dorso, C., Duarte, S., Randrup, J.** 1987. Classical simulation of the fermi gas. *Phys. Lett B.* **188(3)**:287-294.

[10] **Ortner, J., Schautz, F., Ebeling, W.** 1997. Quasiclassical molecular-dynamics simulations of the electron gas: Dynamic properties. *Phys Rev. E.* **56(4)**:4665-4670.

[11] **Mattsson, A. E.** 2002. Density functional theory: in pursuit of the "divine" functional. *Science.* **298**:759-760.

[12] **Sinanoglu, O.** 1964. Many-electron theory of atoms, molecules, and their interactions. *Adv. Chem. Phys.* **6**:315.

[13] **Nesbet, R. K.** 1965. Electronic correlation in atoms and molecules. *Adv. Chem. Phys.* **9**:321.

[14] **Szabo, A., Ostlund, N. S.** 1989. *Modern quantum chemistry: introduction to advanced electronic structure theory.* McGraw-Hill, New York. (ISBN 0-486-691186-1).

[15] **Perdew, J. P., Wang, Y.** 1992. Accurate and simple analytic representation of the electron-gas correlation energy. *Phys. Rev. B.* **45**:13244-13249.

[16] **Kittel, C.** 1991. *Introduction to solid state physics.* Sixth edition. John Wiley and Sons.

[17] **Perdew, J. P., Wang, Y.** 1992. Pair-distribution function and its coupling-constant average for the spin-polarized electron gas. *Phys. Rev. B.* **46(20)**:12947-12954.

[18] **Berens, P. H., Mackay, D. H., White, G. M., Wilson, K. R.** 1983. Thermodynamics and quantum corrections from molecular dynamics for liquid water. *J. Chem. Phys.* **79(5)**:2375-2389.

[19] **Cordero, P., Hernandez, E. S.** 1995. Momentum-dependent potentials: towards the molecular dynamics of fermionlike classical particles. *Phys. Rev. E.* **51(3)**:2573-2579.

[20] **Perdew, J. P., McMullen, E. R., Zunger, A.** 1981. Density-functional theory of the correlation energy in atoms and ions: a simple analytic model and a challenge. *Phys. Rev. A.* **23(6)**:2785-2789.

[21] **Veillard, A., Clementi, E.** 1968. Correlation energy in atomic systems. V. Degeneracy effects for the second-row atoms. *J. Chem. Phys.* **49(5)**:2415-2421.

[12] **Sinanoglu, O.** 1964. Many-electron theory of atoms, molecules, and their interactions. Adv. Chem. Phys. **6**:315.

[13] **Nesbet, R. K.** 1965. Electronic correlation in atoms and molecules. Adv. Chem. Phys. **9**:321.

[14] **Szabo, A., Ostlund, N. S.** 1989. Modern quantum chemistry: introduction to advanced electronic structure theory. McGraw-Hill, New York. ISBN 0-486-691186-1.

[15] **Perdew, J. P., Wang, Y.** 1992. Accurate and simple analytic representation of the electron-gas correlation energy. Phys. Rev. B. **45**:13244-13249.

[16] **Kittel, C.** 1991. Introduction to solid state physics. Sixth edition. John Wiley and Sons.

[17] **Perdew, J. P., Wang, Y.** 1992. Pair-distribution function and its coupling-constant average for the spin-polarized electron gas. Phys. Rev. B. **46(20)**:12947-12954.

[18] **Berens, P. H., Mackay, D. H., White, G. M., Wilson, K. R.** 1983. Thermodynamics and quantum corrections from molecular dynamics for liquid water. J. Chem. Phys. **79(5)**:2375-2389.

[19] **Cordero, P., Hernandez, E. S.** 1995. Momentum-dependent potentials: towards the molecular dynamics of fermionlike classical particles. Phys. Rev. E. **51(3)**:2573-2579.

[20] **Perdew, J. P., McMullen, E. R., Zunger, A.** 1981. Density-functional theory of the correlation energy in atoms and ions: a simple analytic model and a challenge. Phys. Rev. A. **23(6)**:2785-2789.

[21] **Veillard, A., Clementi, E.** 1968. Correlation energy in atomic systems. V. Degeneracy effects for the second-row atoms. J. Chem. Phys. **49(5)**:2415-2421.

Published papers

Wolff/Cope reaction

Sarpong, R.; **Su, J.T.**; Stoltz, B.M. "The Development of a Facile Tandem Wolff/Cope Rearrangement for the Synthesis of Fused Carbocyclic Skeletons." *JACS* **2003** 125(45), 13624-13625.

Su, J.T.; Sarpong, R.; Stoltz, B.M.; Goddard, W.A. "Substituent Effects and Nearly Degenerate Transition States: Rational Design of Substrates for the Tandem Wolff-Cope Reaction." *JACS* **2004** 126(1), 24-25.

Density functional theory on water clusters

Su, J.T.; Xu, X.; Goddard, W. A., III; "Accurate Energies and Structures for Large Water Clusters Using the X3LYP Hybrid Density Functional." *JPC A* **2004** 108(47), 10518-10526.

Origin of hypervalent reactivity in IBX

Su, J.T.; Goddard, W. A., III; "Enhancing 2-Iodoxybenzoic Acid Reactivity by Exploiting a Hypervalent Twist." *JACS* **2005** 127(41), 14146-7.

The Development of a Facile Tandem Wolff/Cope Rearrangement for the Synthesis of Fused Carbocyclic Skeletons

Richmond Sarpong, Julius T. Su, and Brian M. Stoltz*

Division of Chemistry and Chemical Engineering, California Institute of Technology, Pasadena, California 91125

Received July 29, 2003; E-mail: stoltz@caltech.edu

The synthesis of medium-sized rings possessing functionality poised for further manipulation is a considerable challenge in synthetic chemistry.[1] In particular, seven-membered rings are increasingly common in many natural products of interest to the academic and pharmaceutical communities.[2] Our interest in the synthesis of fused [n − 7] bicyclic compounds (n = 5 or 6) was piqued by the natural products guanacastepene (1)[3] and inelega-nolide (2),[4] which have been identified as important synthetic targets due to their biological relevance and interesting structural architecture (Scheme 1). We envisioned either compound as arising from a core fused cycloheptadienone such as 3, a motif not directly available using existing methodologies. Diene 3 was recognized to be the product of a ketene-Cope rearrangement with concomitant opening of a strained cyclopropane ring. In turn, ketene 4 could be produced by a Wolff rearrangement of diazo ketone 5, readily available from known β-keto esters such as 6.[5] Herein, we report the development of a new tandem Wolff/Cope rearrangement that allows mild, facile, and conceptually novel access to a range of [n − 7] bicycles.[6] We also describe the fortuitous observation that cycloheptadienones such as 3 can photolytically rearrange to the corresponding [n − 5] fused bicycles via a 1,3-acyl migration.

We initiated our efforts by preparing the parent fused [5 − 3] bicyclic diazo ketone 5a and subjecting it to a battery of conditions known to promote Wolff rearrangements (Scheme 2). Since its discovery in 1902,[7,8] the Wolff rearrangement has been the subject of intense study, which has resulted in a variety of conditions known to promote the transformation.[9] Many of these standard protocols such as Ag₂O, AgOBz, CuI, and Cu(0) produced a complex mixture of products that included the homologated acid 7.[10] Although production of 7 pointed toward the generation of the desired ketene intermediate (4a), it was clear that the strain release Cope rearrangement was not readily occurring. With this in mind, extensive literature searching and experimentation led to the use of modified sonochemical conditions, originally reported by Montero for simple Wolff rearrangements.[11] To our delight, treatment of diazo ketone 5a under our modified Montero conditions employing AgOBz (0.1 equiv) and Et₃N (1.0 equiv) at 45 °C in THF with sonication for 30 min led exclusively to the desired Wolff/ Cope product (3a) in 95% isolated yield.

Using these optimized conditions, we investigated the substrate scope of this rearrangement for the synthesis of cycloheptadienones fused to five- or six-membered rings. As shown in Table 1, a variety of substitution on the diazo ketones is tolerated in the tandem rearrangement. The mild conditions support the rearrangement of substrates carrying a host of hydroxyl protection groups (entries 1−3) and even an enol ether (entry 4). Substitution on the olefin is also possible at both the terminal (entries 1−4 and 7) and internal positions (entry 5). Although olefin substitution is not a requirement for the tandem process, high yields of the cycloheptadienone products could be realized only under photolytic conditions in these cases (entries 6 and 8). Additionally, a bis-quaternary substituted

Scheme 1

Guanacastepene A (1)

Ineleganolide (2)
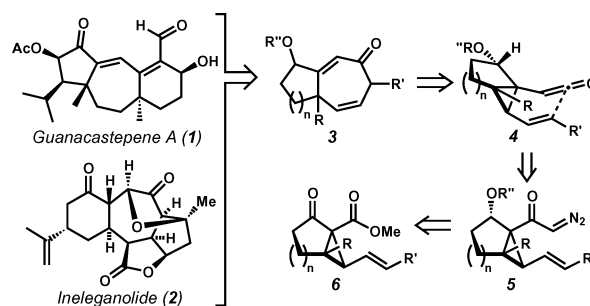
Scheme 2
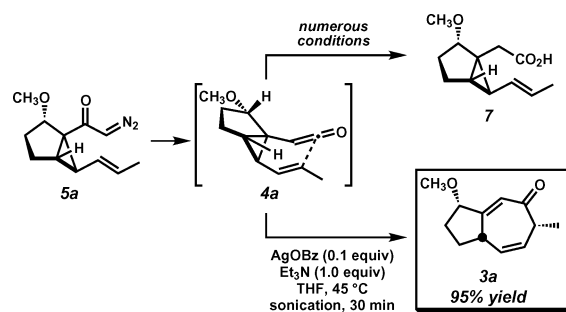
cyclopropane readily participates in the rearrangement and, in the case shown, produces a tricyclic dienone either under silver(I) or photochemical promotion (entry 7).[12] Finally, both [5−7] (entries 1−7) and [6−7] (entry 8) fused bicyclic dienones can be prepared by this methodology.

Although certain substrates produced high yields of the Wolff/ Cope rearrangement products under both the sono- and photo-chemical conditions, others did not. For instance, while photolysis of 5a did produce varying amounts of cycloheptadienone 3a, prolonged exposure to light led to a new product, which was identified as the vinyl cyclopentenone 8a (Scheme 3). This unexpected product likely arises by a Norrish Type I fragmentation followed by a recombination with the transient allyl radical, resulting in a net 1,3-acyl migration.[13,14] This mechanism and the intermediacy of 3a were confirmed by independent photolysis of pure 3a, which leads to the production of cyclopentenone 8a. Of particular note is the complete diastereoselective nature of the rearrangement, which produces the fused bicyclo[3.3.0]octane (8a) as a single isomer. Interestingly, this cascade process constitutes a formal tandem Wolff/vinyl cyclopropane rearrangement.[15]

The application of this novel rearrangement trio (Wolff/Cope/ 1,3-acyl shift) to a variety of substrates is outlined in Table 2. Again, numerous protection groups as well as olefin substitution patterns are tolerated in the cascade. The diastereoselectivity of the process is maintained even for the production of an α-quaternary substituted enone (entry 4). Furthermore, both [5 − 5] and [6 − 5] fused cyclopentenones are available in good yields. Finally, it is interesting

Table 1. Tandem Wolff/Cope Rearrangement

entry	substrate	product	conditions[a]	% yield
1.			R = CH₃ A	95
2.			R = MOM A	88
3.			R = PMB A	92
4.			A	98
5.			A	98
6.			B	80
7.			A	76
			B	94[b]
8.			B	88

[a] Condition A: AgOBz (0.1 equiv), Et₃N (1.0 equiv), THF, 45 °C, sonication for 30 min. Condition B: *hν* (310 nm), THF, 23 °C, 1 h. [b] Experiment performed in PhH for 2 h.

Scheme 3

5a → 3a → 8a
hν, THF, 23 °C, 12 h, **72% yield**
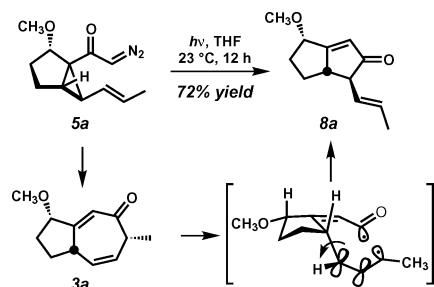
Table 2. Wolff/Cope/[1,3]-Acyl Shift Rearrangement

entry	substrate	product	conditions[a]	time	% yield
1.			R = CH₃ B	12 h	72
2.			R = MOM B	6 h	69
3.			R = PMB B	6 h	75
4.			B[b]	2 h	80
5.			A	0.5 h	57
6.			B[c]	6 h	55
			A	0.5 h	72

[a] Condition A: AgOBz (0.1 equiv), Et₃N (1.0 equiv), THF, 45 °C, sonication. Condition B: *hν* (254 nm), THF, 23 °C. [b] Performed with a 450 W medium-pressure Hg lamp in THF at 40 °C. [c] *hν* (310 nm).

to note that in the cases of entries 5 and 6 (Table 2), better yields of the [6−5] fused bicycles were obtained using silver(I)/sonochemical activation than with photolytic initiation. Since we

have never observed the cycloheptadienone products from these substrates under nonphotolytic conditions (entries 5 and 6), we cannot exclude the possibility of a direct Wolff/vinyl cyclopropane rearrangement as a mechanism in these cases.

In summary, we have developed a set of mild processes for the conversion of vinyl cyclopropyl diazo ketones to highly functionalized cycloheptadienones (i.e., **5**→**3**) and vinyl cyclopentenones (i.e., **5**→**8**) by use of a target-inspired tandem Wolff/Cope rearrangement sequence. This facile methodology allows rapid access to a variety of structurally diverse, complex polycyclic enones. The utility of these new cascade sequences in complex synthetic problems is currently under investigation.

Supporting Information Available: Experimental details and characterization data for all new compounds (PDF). This material is available free of charge via the Internet at http://pubs.acs.org.

References

(1) Molander, G. A. *Acc. Chem. Res.* **1998**, *31*, 603−609.

(2) For reviews on seven-membered ring natural products, see: (a) Fraga, B. M. *Nat. Prod. Rep.* **1996**, *13*, 307−326. (b) Wender, P. A.; Love, J. A. In *Advances in Cycloaddition*; Harmata, M., Ed.; JAI Press: Greenwich, CT, 1999; Vol. 5, pp 1−45. (c) Lautens, M.; Klute, W.; Tam, W. *Chem. Rev.* **1996**, *96*, 49−92.

(3) (a) Brady, S. F.; Singh, M. P.; Janso, J. E.; Clardy, J. *J. Am. Chem. Soc.* **2000**, *122*, 2116−2117. (b) Recently, the total synthesis of guanacastepene was completed, see: Lin, S.; Dudley, G. B.; Tan, D. S.; Danishefsky, S. J. *Angew. Chem., Int. Ed.* **2002**, *41*, 2188−2191. (c) For a complete list of approaches to the guanacastepene core, see Supporting Information.

(4) Duh, C.-Y.; Wang, S.-K.; Chia, M.-C.; Chiang, M. Y. *Tetrahedron Lett.* **1999**, *40*, 6033−6035.

(5) For details, see Supporting Information.

(6) A single example of a Wolff/Cope rearrangement has been reported, see: Freeman, P. K.; Kuper, D. G. *Chem. Ind. (London)* **1965**, 424−425.

(7) Wolff, L. *Ann.* **1902**, *325*, 129−195.

(8) (a) For a review on the Wolff rearrangement, see: Doyle, M. P.; McKervey, M. A.; Ye, T. *Modern Catalytic Methods for Organic Synthesis with Diazocompounds*; Wiley: New York, 1998. (b) For a recent study of the Wolff rearrangement, see: Julian, R. R.; May, J. A.; Stoltz, B. M. Beauchamp, J. L. *J. Am. Chem. Soc.* **2003**, *125*, 4478−4486.

(9) (a) Horner, L.; Spietschka, E. *Chem. Ber.* **1952**, *85*, 225−229. (b) Arndt, F.; Eistert, B. *Chem. Ber.* **1935**, *68*, 200−208. (c) Newman, M. S.; Beal, P. F. *J. Am. Chem. Soc.* **1950**, *72*, 5163−5165. (d) Yates, P.; Crawford, J. *J. Am. Chem. Soc.* **1966**, *88*, 1562−1563. (e) Yates, P.; Fugger, J. *Chem. Ind. (London)* **1957**, 1511−1511.

(10) Analysis of the crude reaction mixtures suggested products resulting from reduction of the diazo group, C−H insertion, and cyclopropanation.

(11) (a) Winum, J.-Y.; Kamal, M.; Leydet, A.; Roque, J.-P.; Montero, J.-L. *Tetrahedron Lett.* **1996**, *37*, 1781−1782. (b) Müller, A.; Vogt, C.; Sewald, N. *Synthesis* **1998**, 837−841.

(12) The substrate in Table 1, entry 7 was designed using theoretical/computational insights. Su, J. T.; Sarpong, R.; Stoltz, B. M.; Goddard, W. A. California Institute of Technology, Pasadena, CA, 2003. Unpublished work.

(13) For general reviews of Norrish Type I fragmentations, see: (a) Coyle, J. D.; Carless, H. A. J. *Chem. Soc. Rev.* **1972**, *1*, 465−480. (b) Chapman, O. L.; Weiss, D. S. *Org. Photochem.* **1973**, *3*, 197−277. (c) Horspool, W. M. *Photochemistry* **1994**, *25*, 67−100.

(14) For a specific example which details a Norrish fragmentation with 1,3-acyl migration, see: Paquette, L. A.; Eizember, R. F. *J. Am. Chem. Soc.* **1967**, *89*, 6205−6208.

(15) Recently, a dienyl Pauson−Khand reaction of enynes to access related vinyl cyclopentenones has been reported, see: Wender, P. A.; Deschamps, N. M.; Gamber, G. G. *Angew. Chem., Int. Ed.* **2003**, *42*, 1853−1857.

JA037587C

Substituent Effects and Nearly Degenerate Transition States: Rational Design of Substrates for the Tandem Wolff−Cope Reaction

Julius T. Su, Richmond Sarpong, Brian M. Stoltz,* and William A. Goddard III*

Division of Chemistry and Chemical Engineering, California Institute of Technology, Pasadena, California 91125

Received August 1, 2003; E-mail: stoltz@caltech.edu; wag@wag.caltech.edu

The Cope reaction is a degenerate transformation whose synthetic utility lies in its versatility as a *stereospecific relay of functionality*.[1] Expanding the reaction's functional scope while preserving its specificity allows for more direct formation of desired products. Recently, Stoltz et al. have discovered[2] a novel tandem Wolff−Cope reaction involving the rearrangement of vinylcyclopropyl ketene intermediates (e.g., **2** and **7**) to [n − 7] bicyclic structures (e.g., **3** and **9**) that serve as a motif for a number of natural product syntheses (Scheme 1). The reaction produces products cleanly and in high yield with a variety of substrates, but interestingly is thwarted by substitution at certain positions (4 and 5, see Table 2). First-principles quantum mechanics (B3LYP flavor of unrestricted density functional theory, 6-31G** basis functions)[3] indicate this substituent limitation to be a direct consequence of a competing low-barrier pathway that leads to an unstable and undesired *trans*-olefin product via a boatlike transition state. *The lowered barrier of the competing pathway is a direct result of the appended ketene functionality.* Understanding how methyl substituents influence our *specific* Wolff−Cope transition state leads us to the design of new 4,5-substituted substrates predicted to rearrange successfully. Understanding how ketene and related functionalities influence the *general* Cope transition state leads us to insights into transition-state mutability which may be exploited in other reaction designs.

Divinylcyclopropane analogues of **4** have been observed[4] to rearrange into fused cycloheptadienes (e.g., **6**) in high yield. The relative instability of the *trans*-olefin product **5** drives its corresponding activation energy upward to a safely inaccessible level.[5] We now consider the reaction of ketene vinylcyclopropane substrate **7**. Products **8** and **9** are conjugated to the newly formed carbonyl, and are equally stabilized relative to **5** and **6**, but transition state **11** is more stabilized relative to **10** than **13** is relative to **12** (Figure 1). The energies of transition states **11** and **13** (Figure 2) are thus similar, and the reaction outcome becomes highly sensitive to substituent effects that can change the relative ordering of the two energies.

Geometries **10** and **12** are nearly intermediate between the starting structures and products, and are termed synchronous; in contrast, geometries **11** and **13** display a higher degree of asynchronicity, so that the new carbon−carbon bond is more fully formed when the cyclopropane bond begins to break.[6] The additional radicaloid character of transition state **11** is stabilized by conjugation through the forming carbonyl.[7] A comparison with allene substrates (not shown) indicates that the relative stabilization is due in equal parts to an allylic radical effect and to the increased electronegativity of the oxygen center.

To explain why the ketene group stabilizes **11** and **13** to nearly equal energies, we first note that Cope transition states can be viewed as a resonance hybrid of aromatic and diradical forms.[8] Comparing the relative energies of generalized valence bond (GVB) pairs (Table 1) in model transition states **14−16**, we see that a diradical form contributes significantly to **16**-chair but not **16**-boat,

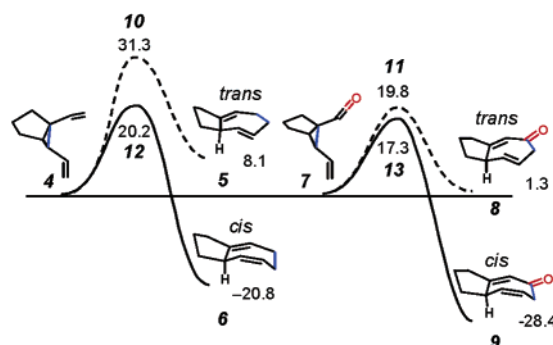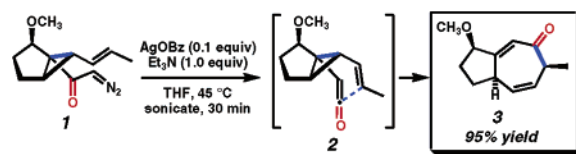**Scheme 1.** Tandem Wolff−Cope Rearrangement

Figure 1. (a) Cope reaction pathways available to a divinylcyclopropane substrate lead to either the desired *cis*-olefin product or a less stable undesired *trans*-olefin product. (b) Analogous pathways for a ketene-substituted substrate show a smaller activation energy difference (ΔG in kcal/mol, T = 298 K). All structures are drawn from actual coordinates.
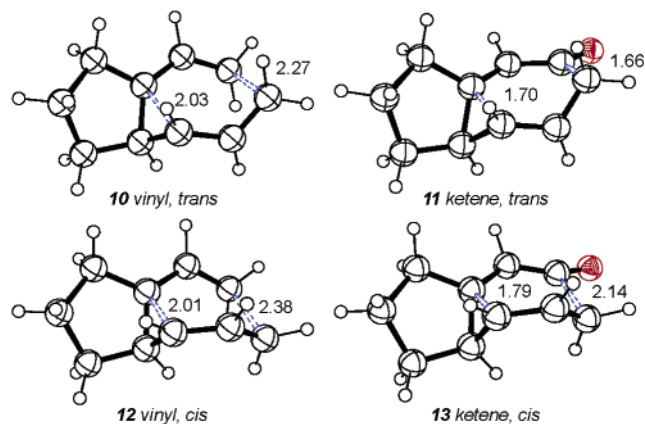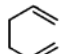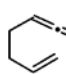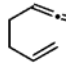

Figure 2. Transition states leading to the trans (**10**, **11**) and cis (**12**, **13**) products from vinyl-substituted (**10**, **12**) and ketene-substituted (**11**, **13**) substrates. Transition state **11** differs from the others in its radicaloid character and extreme degree of asynchronous bond formation (distances in angstroms).

a difference consistent with divergent radical-chair vs. aromatic-boat pathways in the ketene Cope reaction. In the full system, we find that **13** is predominantly aromatic ($\Delta E_{\text{singlet}-\text{triplet}}^{\text{vertical}}$ = 51.0 kcal/mol) while **11** has some radical character ($\Delta E_{\text{singlet}-\text{triplet}}^{\text{vertical}}$ = 31.6 kcal/mol) and is thus more susceptible to the influence of the radical-stabilizing carbonyl.[9]

The addition of methyl substituents (Table 2) leaves the geometries of the cis (boat) and trans (chair) transition states largely

Table 1. Single Point Energies (kcal/mol) of Alternate GVB Pairings in Model Transition-State Structures[a]

#	Reactant	TS			
14		boat	9.1	14.0	9.1
		chair	0.0	16.5	0.0
15		boat	18.7	40.8	41.4
		chair	0.0	33.6	42.6
16		boat	0.0	20.6	23.9
		chair	1.9	2.0	13.6

[a] The diradical pair (shaded) makes a significant resonance contribution (lower energy) to the ketene chair structure but not the ketene boat structure, a difference present to a lesser extent in model allene **15** as well.

Table 2. Effect of Single Methyl Substituents on the Relative Activation Energies of Cis/Trans Pathways[a]

#	subst pos.	$\Delta G_{cis}^{\ddagger}$	$\Delta G_{trans}^{\ddagger}$	$\Delta G_{cis\text{-}trans}^{\ddagger}$
7	none	15.8	18.3	−2.5
17a	1	15.0	17.4	−2.4
17b	2	14.6	19.2	−4.6
17c	3	16.6	20.0	−3.4
17d	4	22.4	19.7	2.7
17e	5	18.3	17.3	1.0

[a] Shading indicates reactions predicted to fail ($\Delta G_{cis\text{-}trans} > 0$). Of twelve substrates (similar to **17a−e**) tried experimentally, seven were predicted to rearrange and did so, and five were predicted to fail and did so.[10]
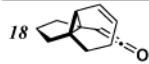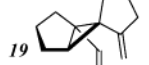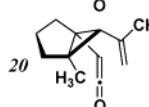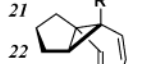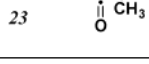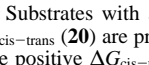
unperturbed. Positions 4 and 5 are separated by only 2.13 Å in **13**, so substitution at either position causes a large (6.6 and 2.5 kcal/mol, respectively) destabilization. The substituents in **11** are spaced farther apart; the largest substituent effect (1.7 kcal/mol) arises from a near-eclipsing interaction between position 3 and the carbonyl oxygen. The end result is consistent with experimental observation: substitution at positions 4 or 5 causes destabilization of the desired cis transition state relative to the undesired trans transition state and causes the reaction to fail.[10]

To design substrates that will successfully undergo the Wolff−Cope rearrangement, we may either stabilize **13** or destabilize **11**. Cyclic substrates **18** and **19** (Table 3) enforce the cis transition state while making it impossible for the substrate to attain a trans transition-state configuration. Such a strategy has been employed successfully to achieve rearrangement of a bis-quaternary substrate (e.g., **18**).[2]

Although substrate **17e** with substitution at position 5 alone does not rearrange, we expect that substrate **20** with substitution at *both* positions 5 and 2 will rearrange, due to destabilization of **11** from a 1,3-diaxial interaction. Preliminary experimental efforts suggest that this strategy may promote an alternate cis pathway that leaves the cyclopropane ring intact. Finally, substitution at position 4 (**17d**) is still problematic and, as shown with substrates **21−23**, cannot be reversed by Me, tBu, or Si(CH$_3$)$_3$ (TMS) substitution at position 1.

In conclusion, in the tandem Wolff−Cope reaction the ketene group preferentially stabilizes radical over aromatic pathways, causing two normally energy-separated transition states to become nearly degenerate. We can use small changes in transition-state stabilities ($\Delta G^{\ddagger} \approx 2$ kcal/mol) to select between two highly disparate products (trans vs cis cycloheptenes, $\Delta G \approx 29$ kcal/mol) in a controlled fashion. For pericyclic reactions in general, this reaction highlights the need to consider high-lying transition states that may

Table 3. Designed Substrates and Their Calculated Activation Energies[a]

#	Geometry (cis vs. trans)	(R =)	$\Delta G_{cis}^{\ddagger}$	$\Delta G_{trans}^{\ddagger}$	$\Delta G_{cis\text{-}trans}^{\ddagger}$
18		-		16.0	-	-
19		-		13.1	-	-
20			15.5	19.5	−4.0
21		TMS	20.7	17.9	2.8
22		CH$_3$	21.9	20.4	1.6
23		tBu	23.6	22.9	0.7

[a] Substrates with an enforced cis transition state (**18**, **19**) or negative $\Delta G_{cis\text{-}trans}$ (**20**) are predicted to rearrange successfully; the others (**21−23**) have positive $\Delta G_{cis\text{-}trans}$ and are predicted to fail.

become accessible with newly added functionality. The study also suggests new opportunities for reaction control via the deliberate construction of polymorphic transition states.

Supporting Information Available: Energies, ball-and-stick figures, Cartesian coordinates, and vibrational frequencies for **4−23** (PDF). This material is available free of charge via the Internet at http://pubs.acs.org.

References

(1) Reviews: (a) *Comprehensive Organic Synthesis*; Trost, B. M., Ed.; Pergamon Press: New York, 1992; Vol. 5, Chapter 7.1, pp 785−826. (b) Houk, K. *Angew Chem., Int. Ed.* **1992**, *31*, 682−708. (c) Staroverov, V. N.; Davidson, E. R. *J. Mol. Struct. (THEOCHEM)* **2001**, *573*, 81−89.

(2) Our theory was developed concurrently with the experiments described in Sarpong, R.; Su, J. T.; Stoltz, B. M. *J. Am. Chem. Soc.* **2003**, *125*, 13624−13625. The theoretical and experimental communications were submitted simultaneously.

(3) Run with Jaguar 5.0, Schrodinger, L.L.C. Portland, OR, 1991−2003.

(4) (a) Marino, J. P.; Kaneko, T. *J. Org. Chem.* **1974**, *39*, 3175−3176. (b) Piers, E.; Ruediger, E. H. *Can. J. Chem* **1983**, *61*, 1239−1247. (c) Davies, H. M. L.; Doan, B. D. *J. Org. Chem.* **1999**, *64*, 8501−8508. (d) Harvey, D. F.; Grenzer, E. M.; Gantzel, P. K. *J. Am. Chem. Soc.* **1994**, *116*, 6719−6732.

(5) Reversal from boat/chair 1,5-hexadiene: $\Delta G^{\ddagger}_{chair-boat} \approx 11$ kcal/mol. Goldstein, M. J.; Benzon, M. S. *J. Am. Chem. Soc.* **1972**, *94*, 7147−7149.

(6) Stable dipolar and radical intermediates were also considered, but only true transition states ($\lambda_1 < 0$, $\lambda_n > 0$) were found.

(7) Radical stabilizing Cope transition state: (a) Staroverov, V. N.; Davidson, E. R. *J. Am. Chem. Soc.* **2000**, *122*, 7377−7385. (b) Hrovat, D. A.; Chen, J.; Houk, K. N.; Borden, W. T. *J. Am. Chem. Soc.* **2000**, *122*, 7456−7460. (c) Black, K. A.; Wilsey, S.; Houk, K. N. *J. Am. Chem. Soc.* **1998**, *120*, 5622−5627. (d) Doering, W. v. E.; Wang, Y. *J. Am. Chem. Soc.* **1999**, *121*, 10112−10118. (e) Sakai, S. *J. Mol. Struct (THEOCHEM)* **2002**, *583*, 181−188.

(8) Boat vs chair pathways. (a) Experiment supports same mechanism: Shea, K. J.; Stoddard, G. J.; England, W. P.; Haffner, C. D. *J. Am. Chem. Soc.* **1992**, *114*, 2635−2643. (b) Octafluoro- and decafluorohexadienes show radicaloid chair and aromatic boat: Black, K. A.; Wilsey, S.; Houk, K. N. *J. Am. Chem. Soc.* **2003**, *125*, 6715−6724. (c) Staroverov, V. N.; Davidson, E. R. *J. Am. Chem. Soc.* **2000**, *122*, 186−187.

(9) We have found that **13** is geometrically similar to a boatlike *diradical* transition structure ($\Delta G^{\ddagger} = 44.3$ kcal/mol, $\Delta E_{triplet-singlet} = 17.3$ kcal/mol); the separate transition structure suggests that geometric constraints may prevent **13** from effectively resonating with a diradical form.

(10) Products were observed consistent with further reaction of a *trans*-cycloheptene intermediate: at low temperatures only homologated acid was recovered, and at higher temperatures a complex mixture of undesired products was recovered. No starting material was recovered.

JA037716P

Accurate Energies and Structures for Large Water Clusters Using the X3LYP Hybrid Density Functional

Julius T. Su, Xin Xu, and William A. Goddard III*

Materials and Process Simulation Center (139-74), Division of Chemistry and Chemical Engineering, California Institute of Technology, Pasadena, California 91125

We predict structures and energies of water clusters containing up to 19 waters with X3LYP, an extended hybrid density functional designed to describe noncovalently bound systems as accurately as covalent systems. Our work establishes X3LYP as the most practical ab initio method today for calculating accurate water cluster structures and energies. We compare X3LYP/aug-cc-pVTZ energies to the most accurate theoretical values available ($n = 2-6, 8$), MP2 with basis set superposition error (BSSE) corrections extrapolated to the complete basis set limit. Our energies match these reference energies remarkably well, with a root-mean-square difference of 0.1 kcal/mol/water. X3LYP also has *ten times less BSSE* than MP2 with similar basis sets, allowing one to neglect BSSE at moderate basis sizes. The net result is that X3LYP is ~*100 times faster* than canonical MP2 for moderately sized water clusters.

1. Introduction

We predict structures and energies of water clusters containing up to 19 waters with X3LYP,[1,2] an extended hybrid density functional designed to describe noncovalently bound systems well. Our work establishes X3LYP as the most practical ab initio method today for calculating accurate water cluster structures and energies.

We compare our X3LYP results to the most accurate theory available[3-8] for modest-sized water clusters, MP2 calculations using triple-ζ-plus basis sets with basis set superposition error corrections extrapolated to the complete basis set limit. Our energies match these reference energies to a root-mean-square (rms) deviation of 0.1 kcal/mol of water.

This agreement is remarkable, especially since the noncovalent bonding in water clusters (polar, hydrogen bonded) differs greatly from the bonding in the rare neutral gas dimers used to train X3LYP. In contrast, the popular hybrid functional B3LYP[9-11] provides acceptable geometries and thermochemistry for covalent molecules, but its poor description of London dispersion (van der Waals attraction) leads to poor binding energies[4,12-15] (Table 1) for water clusters.

Two consequences follow:

First, the result establishes the generality of the X3LYP functional, supporting its application to more diverse van der Waals and hydrogen bonded complexes. This validation sets the stage for first principles predictions of noncovalent interactions of ligands to proteins and DNA, with implications for the emerging field of genome-wide structure based drug design.

Second, X3LYP now represents the state of the art for practical ab initio calculations on water clusters, since

(1) *We can use smaller basis sets while preserving accuracy.* Post-Hartree–Fock methods such as MP2 require higher angular momentum basis functions to properly describe the correlation cusp[16] and suffer from slow and unsystematic convergence to the complete basis set limit.[17]

We expect the basis set requirements for DFT methods to be greatly reduced, and our results bear this out: X3LYP/aug-cc-pVTZ agrees with MP2/aug-cc-pV5Z extrapolated to the complete basis set limit to within 0.1 kcal/mol/water, a difference well within the uncertainty of both methods.

(2) *We can neglect BSSE at moderate basis sizes.* Basis set superposition error has long plagued canonical MP2 calculations, with a correction of ~1.1 kcal/mol for water hexamer even with the aug-cc-pV5Z basis set.[3] This is larger than the energy difference between water hexamer isomers (<0.5 kcal/mol). X3LYP has *ten times less* basis set superposition error than MP2 with comparable basis sets, allowing smaller basis sets to be used. Non-BSSE and BSSE energies converge quickly to the same value with increasing basis set size, so that for moderate sized bases (aug-cc-pVTZ), we can neglect BSSE.

Not including BSSE in X3LYP calculations speeds up our calculations significantly, since a BSSE calculation requires N single point energies with the full system basis, where N is the number of water monomers in the complex.

(3) *Density functional methods are faster than MP2.* For larger clusters, X3LYP is at least 100 times faster than canonical MP2 at the same basis set level, where BSSE is neglected for both calculations. The speed advantage becomes even bigger for larger clusters, since density functional methods scale as a factor of N better than canonical MP2 (formally N^4 vs N^5, with improvements possible for both).

With this superior combination of speed and accuracy, we expect X3LYP to displace MP2-corrected Hartree–Fock (HF) as the preferred method for performing ab initio calculations on water clusters.

2 Computational Details

2.1. X3LYP Functional. The details of the X3LYP hybrid density functional are described elsewhere.[1,2] The X3LYP hybrid functional was developed to describe accurately the thermochemistry of molecules while reproducing the properties (equilibrium distance, binding energy, and Pauli repulsion) of helium

---

* To whom correspondence should be addressed. E-mail: wag@wag.caltech.edu.

TABLE 1: Binding Energies of Presumed Global Minimum $(H_2O)_n$ Clusters $(-\Delta E$, kcal/mol$)^a$

		6-31g**			6-311g**++			aug-cc-pVDZ		aug-cc-pVTZ(-f)			MP2/CBS[3]	MP2/TZ2P++[5]
n	structure	LMP2	B3LYP	X3LYP	LMP2	B3LYP	X3LYP	B3LYP	X3LYP	LMP2	B3LYP	X3LYP	Xantheas	Lee
2	linear	6.55	7.56	7.96	5.06	5.82	6.23	4.71	5.11	4.43	4.61	5.00	4.97	4.88
3	cyclic	20.94	25.03	26.24	14.64	17.30	18.45	14.76	15.91	12.31	14.42	15.52	15.82	15.11
4	cyclic	34.94	41.73	43.57	24.48	30.73	32.49	26.79	28.55	17.12	26.03	27.73	27.63	26.72
5	cyclic	44.68	53.34	55.71	32.33	40.78	43.05	35.53	37.83	28.65	34.37	36.57	36.28	35.17
6	cage	58.34	70.73	74.27	39.86	48.83	52.06	42.91	46.14	34.75	41.70	44.78	45.79	44.04
7	prism′	73.04	87.02	91.41	49.12	60.12	64.07	52.74	56.67	42.71	51.45	55.27		54.81
8	D2d	92.61	110.73	116.14	64.14	77.01	81.88	68.35	73.27	59.69	66.60	71.35	72.57	70.06
9	D2dDD	99.37	123.08	129.03	71.38	87.94	93.41	77.36	82.93		75.07	80.36		79.14
10	prism	117.03	139.83	146.80	82.40	99.75	106.00	87.84	93.98		85.81	91.82		90.07
11	Pr443											97.79		96.69
12	Pr444											112.14		112.59
13	Pr454											122.41		
14	Pr2444											133.82		
15	Pr555											142.34		
16	Pr4444											153.08		
17	Pr454(4)											163.20		
18	Pr44244											175.65		
19	globular											184.13		

^{a} The LMP2, B3LYP, and X3LYP results have not been corrected for BSSE; the MP2/CBS results have been extrapolated to a complete basis set; and the MP2/TZ2P++ results include 50% of the BSSE correction. The binding energy is given relative to fully separated and relaxed water monomers. Geometry labeling follows the convention of Lee et al.[5-7]

and neon dimers, whose binding is wholly due to dispersion. For these rare gas dimers, the repulsive energy component of X3LYP (total energy minus correlation) is fit to match Hartree−Fock energies. Thus, near equilibrium distances, X3LYP is expected to give correct contributions of dispersion to bonding.

X3LYP extends B3LYP[18] by writing the nonlocal gradient correction in terms of the F^X extended exchange functional, which is written as a linear combination of B88 and PW91 exchange functionals:

$$E_{XC}^{X3LYP} = a_0 E_x^{exact} + (1-a_0)E_x^{Slater} + a_x \Delta E_x^X + a_c E_c^{VWN} + (1-a_c)E_c^{LYP} \quad (1)$$

$$\Delta E_x^X = E_X^{LDA} - \int F^X(s)\rho^{4/3}\mathrm{d}r \quad (2)$$

$$s = \frac{|\nabla\rho|}{(24\pi^2)^{1/3}\rho^{4/3}} \quad (3)$$

$$F^X(s) = 1 + a_{x1}(F^{B88}(s)-1) + (1-a_{x1})(F^{PW91}(s)-1) \quad (4)$$

$$\{a_0, a_x, a_{x1}, a_c\} = \{0.218, 0.709, 0.765, 0.129\} \quad (5)$$

The four mixing parameters were determined through a least-squares fit to the total energies of 10 atoms, the ionization potentials of 16 atoms, the electron affinities of 10 atoms, and the atomization energies for 33 diatomic and five triatomic molecules selected to represent the important chemistry of first- and second-row elements (including open- and closed-shell molecules; molecules with single, double, and triple bonds; ionic systems; and systems requiring multiple determinants for proper descriptions). Helium and neon rare gas dimers were included as representative van der Waals systems, but no data on water dimer or higher clusters were included.

The accuracy of X3LYP for the thermochemistry (cohesive energies, ionization potentials, electron affinities, proton affinities) of the G2 set of 148 molecules is better than all other DFT methods considered (seven GGA methods and seven hybrid methods) as is the s→d excitation energies for transition-metal atoms. An earlier test for water dimer[2] led to a binding energy (D_e) within 0.05 kcal/mol of the exact value and a O−O distance (R_e) within 0.004 Å of the exact value.

2.2. Quantum Mechanics Calculations. All calculations were performed using the Jaguar 5.0[19] software package, with default options unless indicated otherwise.

In the LMP2 method,[20,21] occupied orbitals are only allowed to correlate with virtual orbitals localized on the atoms of the local occupied Hartree−Fock orbital, with an initial wave function obtained from Pipek−Mezey localization[22] of the HF reference wave function. Only valence electrons were included in the LMP2 correlation. In all cases, SCF convergence under the DIIS scheme was achieved to 50 μhartree.

For LMP2, B3LYP, and X3LYP, the default pseudospectral implementation of Jaguar was used to accelerate evaluation of two-electron integrals. In previous X3LYP calculations,[12,13] the pseudospectral capabilities were turned off to simplify comparison with previous results obtained using other methods.

All geometries were converged to a maximum gradient of 4.5×10^{-4} hartree/bohr, an rms gradient of 3.0×10^{-4} hartree/bohr, a maximum nuclear displacement of 1.8×10^{-3} bohr, and an rms nuclear displacement of 1.2×10^{-3} bohr.

We used the following basis sets: 6-31g**[23] (25 basis functions/water), 6-311++g** (36 basis functions/water), aug-cc-pVDZ[24] (41 basis functions/water), and aug-cc-VTZ(-f)[24] (58 basis functions/water, without f functions). BSSE corrections were carried out where stated explicitly, using the function counterpoise method[25] and taking into account fragment relaxation energy terms[26,27]

$$\Delta E(BSSE) = E^{full}(full) - \sum_{fragments} E^{full}(fragment) + \sum_{fragments} \Delta E_{relax}^{fragment}(fragment) \quad (6)$$

where E^{full} and $E^{fragment}$ indicate the energy calculated with the full- and fragment-only basis sets, respectively.

2.3. Multibody Decomposition. A multibody decomposition of total binding energy for water hexamers was computed by taking into account $2^6 - 1 = 63$ possible present/absent combinations of water fragments and computing their energies using both a fragment-only basis and a full-system basis (to estimate the magnitude of BSSE). Although the complex is symmetric, symmetry was not used. The final multibody contributions Δ^n can be written in terms of linear combinations
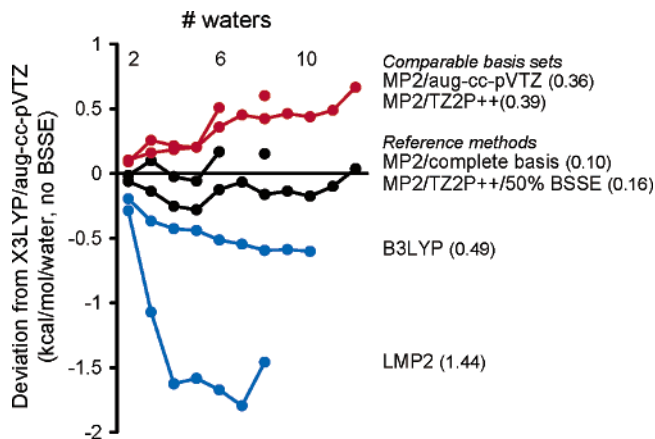
Figure 1. Deviation of global minimum water cluster energies for different levels of theory. Here the reference is X3LYP/aug-cc-pVTZ. We compare MP2 energies from Xantheas[3] and Lee[7] with comparable basis sets; MP2 reference energies obtained from extrapolation to a complete basis[3] (BSSE and no BSSE converge to same energies) and from inclusion of 50% BSSE;[7] and B3LYP and LMP2 energies using the aug-cc-pVTZ(-f) basis set (no BSSE). The total root-mean-squared errors (kcal/mol/water) are indicated in parentheses.

of Σ^n; the sum of energies of all species with n fragments included

$$\begin{pmatrix} \Delta^6 \\ \Delta^5 \\ \Delta^4 \\ \Delta^3 \\ \Delta^2 \end{pmatrix} = \begin{pmatrix} 1 & -1 & 1 & -1 & 1 & -1 \\ & 1 & -2 & 3 & -4 & 5 \\ & & 1 & -3 & 6 & -10 \\ & & & 1 & -4 & 10 \\ & & & & 1 & -5 \end{pmatrix} \begin{pmatrix} \Sigma^6 \\ \Sigma^5 \\ \Sigma^4 \\ \Sigma^3 \\ \Sigma^2 \\ \Sigma^1 \end{pmatrix} \quad (7)$$

and $\Delta^1 = \Sigma^1 - 6 \, E(\text{ref water})$. The sum of all Δ^n gives the total binding energy.

3. Results and Discussion

3.1. Water Cluster Global Minima. To compare the overall energetics of clusters up to 19 waters, we started with globally minimized water clusters from Wales et al.[28] (optimized with the TIP4P force field) and carried out a full optimization for each level of theory and basis set presented in Table 1. Figure 1 shows that even *without* using BSSE corrections, the X3LYP/aug-cc-pVTZ(-f) energies are in excellent agreement with the best theoretical estimates available, deviating by an rms of 0.10 kcal/mol/water from the results of Xantheas et al.[3,8] (MP2/CBS extrapolation with a polynomial function from an aug-cc-V5Z basis), who considered up to eight waters. Lee et al.[7] carried out a less complete MP2 than Xantheas (MP2 using the triple-ζ TZ2P[2+] basis with 50% BSSE correction) but considered up to 12 waters; their cluster binding energies are systematically higher than Xantheas' energies (presumed to be more accurate) by ~0.2−0.3 kcal/mol/water, differing from our energies by an RMS of 0.16 kcal/mol/water. Our results agree well with Xantheas, with little evidence of systematic error (Figure 1).

Figure 1 and Table 1 compare non-BSSE-corrected energies calculated at different levels of theory. Like X3LYP, B3LYP converges quickly to a limiting energy with increasing basis set size, and B3LYP-optimized geometries are similar to X3LYP-optimized geometries (six-cage $C_{rms} = 0.02$ Å, 8-D_{2d} $C_{rms} = 0.01$ Å). However, B3LYP systematically underestimates water cluster binding energies (rms of 0.51 kcal/mol/water vs MP2/CBS).
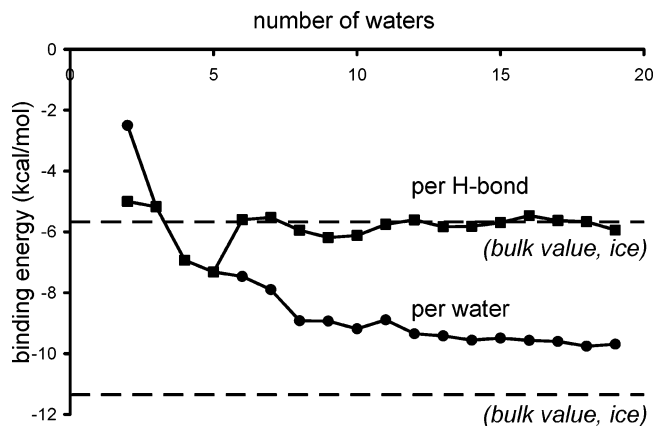

Figure 2. Binding energy (kcal/mol) per hydrogen bond and per water molecule for global minimum water clusters at the level of X3LYP/aug-cc-pVTZ(-f). The energy per hydrogen bond converges quickly to the experimental binding energy of ice at 0 K, $\Delta H/2 = -5.68$ kcal/mol, but the energy per water does not due to the five to seven "dangling" hydrogen bonds present in the larger clusters ($n = 6-19$).

LMP2 performs even more poorly than B3LYP, converging more slowly to a limiting energy with increasing basis set size and more significantly underestimating water cluster binding energies (rms of 1.43 kcal/mol/water vs MP2/CBS). LMP2-optimized geometries are distorted relative to X3LYP-optimized geometries (six-cage $C_{rms} = 0.70$ Å, 8-D_{2d} $C_{rms} = 0.33$ Å) and are characterized by longer hydrogen bonds and larger out of plane distortions for the "cyclic" complexes. Thus, our results suggest LMP2 is unsuitable for describing water clusters, contrary to the conclusion of previous studies,[29] which considered single-point LMP2 energies at MP2-optimized geometries.

Canonical MP2 (non-BSSE corrected) calculations with aug-cc-pVTZ and TZ2P++ basis sets[3,7] perform better, slightly overestimating water cluster binding energies (rms of 0.28 and 0.20 kcal/mol/water, respectively, vs MP2/CBS). Addition of full BSSE tends to overcorrect this overbinding by a factor of ~2−adding 50% BSSE to provide a better estimate of the true binding[30] leads to an rms of 0.04 and 0.24 kcal/mol/water, respectively, vs MP2/CBS.

We emphasize that BSSE calculations are expensive, requiring the calculation of N single-point energies with the full system basis, where N is the number of water monomers in the complex. For canonical MP2 with large basis sets, BSSE is still a large fraction of the total binding energy (9% for aug-cc-pVTZ, 8-D_{2d} geometry). In contrast, with X3LYP we find that BSSE is only 0.9% of the total binding energy (aug-cc-pVTZ(-f), 8-D_{2d} geometry), and we observe good correspondence with MP2/CBS energies despite neglecting BSSE.

We could not find any published MP2 calculations on $(H_2O)_n$ clusters with $n = 13-19$ and, hence, cannot compare our fully optimized X3LYP binding energies for these systems. However, Figure 2 shows that the X3LYP binding energy *per hydrogen bond* for the "three-dimensional" ($n > 5$) water clusters oscillates near the experimentally determined binding energy of ice at 0 K ($\Delta E/2 = -5.68$ kcal/mol).[24] On the other hand, the binding energy *per water* is lower than the bulk value by the five to seven "dangling" hydrogen bonds present in the three-dimensional clusters.

In developing X3LYP, a criterion was that turning off correlation for noble gas dimers should lead to a repulsive curve much like in HF theory. Thus, the correlation functional in X3LYP represents the dispersive contributions to binding. This allows us to separate the correlation component of the binding energy from the electrostatic and hydrogen bonding terms. We

TABLE 2: Theoretical and Experimental Results for the Structure of Water Hexamer

	group	year	method	most stable structure (theory) or obsd (expt)
theory	Tsai and Jordan[31]	1993	MP2/aug-cc-pVDZ'	prism
	Laasonen et al.[14]	1993	GGA/plane wave	cyclic
	Kim et al.[32]	1994	MP2/6-31+G(2d,p) vib freq	cage
	Lee et al.[15]	1994	BLYP/TZVP	cyclic
	Estrin et al.[12]	1996	GGA(PW/P)/"moderate" basis	prism
	Liu et al.[33]	1996	model potential/DQMC(nuclei)	cage
	Kim and Kim[34]	1998	MP2/9s6p4d2f1g/6s4p2d + diffuse	cage
	Kryachko[35]	1999	MP2/aug-cc-pVDZ	prism
	Lee et al.[7]	2000	MP2/TZ2P++	book
	Xantheas et al.[3]	2002	MP2/CBS extrapolation	prism
	Losada and Leutwyler[36]	2003	MP2/aug-cc-pVTZ	cyclic
	Present work	2004	X3LYP/aug-cc-pVTZ(-f)	cyclic
expt	Liu et al.[33,37]	1996	terahertz laser vib−rot. tunnel spec	cage
	Nauta and Miller[38]	2000	IR/liquid He droplets	cyclic + book
	Fajardo and Tam[39]	2001	IR/para-hydrogen matrix	cyclic + cage/book

TABLE 3: Comparison of $(H_2O)_n$ Water Cluster Minima (kcal/mol)[a]

		X3LYP/aug-cc-pVTZ(-f)				ΔE (others)		
n	structure	$-\Delta E$	$-\Delta E_{BSSE}$	$-\Delta E_0$	$-\Delta G_{50}$	Xantheas (MP2)[3]	Lee (MP2)[7]	B3LYP
6	prism	44.69	44.24	30.66	7.78	**45.86**	43.97	41.49
	cage	44.78	44.35	30.87	8.02	**45.79**	**44.04**	41.68
	book	**45.17**	**44.88**	**31.68**	9.34	45.61	**44.06**	42.26
	bag	44.39	44.08	31.05	8.61		43.37	41.44
	cyclic	**45.04**	**45.02**	**32.23**	**10.35**	44.86	43.48	**42.35**
	cyclic'	44.10	43.99	**31.64**	**10.00**			41.40
8	D_{2d}	71.05	70.43	50.32	16.94	72.57	70.06	66.31
	S_4	71.35	70.58	50.56	17.20	72.56	70.03	66.53
10	prism	91.17	90.26	65.35	22.08		90.07	85.01
	prism'	91.82	91.06	65.91	22.64		89.98	85.84
	butterfly	84.12	83.43	59.68	16.86		87.93	78.29

[a] ΔE and ΔE_{BSSE} correspond to the non-BSSE and BSSE-corrected binding energies, respectively. ΔE_0 is the non-BSSE binding energy with zero-point energy added; ΔG_{50} is evaluated from $\Delta H + T\Delta S$, $T = 50$ K, based on the non-BSSE binding energy and with zero-point energy added. The most stable hexamer structures are indicated in boldface type.

find that the correlation fraction is remarkably consistent, 45−54% of the total binding energy for all water clusters studied (see the Supporting Information for more details).

3.2. Water Cluster Local Minima. *3.2.1. General Discussion.* It is well-established that water trimers through pentamers have cyclic structures, while water clusters larger than hexamer have three-dimensional structures.[40] Among these three-dimensional structures there is some disagreement on the detailed structure of the decamer but not for the octamer, which has a cubic structure.[41,42] As expected, water octamer isomers (D_{2d} and S_4) have similar energies in both X3LYP and MP2 calculations[42,43] (Table 3). Water decamers appear in both X3LYP and MP2 calculations to prefer a pentagonal prism structure over a less symmetric "butterfly" form derived from the cubic octamer. This contrasts with the interpretation of experimental studies that suggest the butterfly form to be the more stable structure.[43]

However, as indicated in Table 2, the structure of water hexamer, intermediate between the two regimes, has been a subject of active debate. We discuss this case in more detail below.

3.2.2. Water Hexamer. The most commonly considered structures are shown in Figure 3, differing in the balance of ring strain against number of hydrogen bonds. Recent theoretical predictions have been ambiguous, with the energy ordering of isomers highly sensitive to basis set size[32] and BSSE inclusion.[31] In addition, methods using a nuclear QMC scheme to calculate zero-point effects have used different model potentials.[44,45]

Experiments have also been ambiguous, with cage structures observed in water clusters formed from supersonic jets[33] and
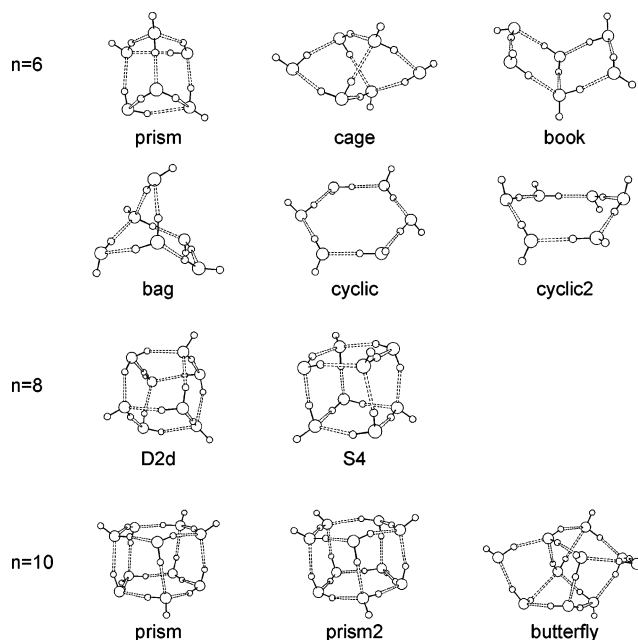
Figure 3. Optimized water cluster minima $(H_2O)_n$; $n = 6, 8, 10$ (X3LYP/aug-cc-VTZ(-f)).

cyclic structures observed in clusters formed in liquid helium droplets[38,46] or solid para-hydrogen matrices.[39]

Our results using X3LYP/aug-cc-pVTZ(-f) indicate that the book and cyclic (chair) structures are the most stable (Table 3, Figure 4). The structures are nearly degenerate (−45.17 and −45.04 kcal/mol, respectively), with an energy ordering that
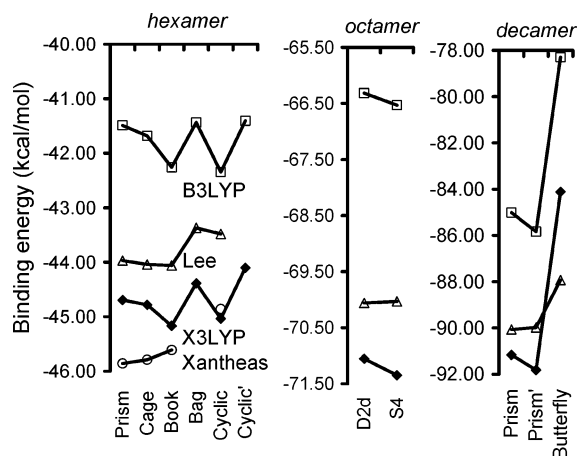
Figure 4. Comparison[3,7] of water cluster minima binding energies (kcal/mol) without BSSE. Negative binding energies are plotted so that the energies of more strongly bound clusters lie at the bottom of the graph.

reverses when BSSE (cyclic now 0.14 kcal/mol more stable), zero-point energy effects (cyclic now 0.55 kcal/mol more stable), or entropic effects (cyclic now 1.01 kcal/mol more stable) are included. We should caution that these zero-point energies and entropic effects are derived using a harmonic normal-mode analysis which may not account for certain "flipping" vibrations in the water hexamer.[36] We find that the cage structure is always less stable and is generally close in energy to the prism.

Our most stable structures (book/cyclic) are different from the most stable structure (prism) predicted with MP2/CBS but are consistent with those observed in the most recent IR/para-hydrogen matrix experiments (book/cyclic). In rationalizing the difference between these experiments and the MP2/CBS results, it has been suggested that the hexamers isolated in para-H2 matrices may represent kinetic and not thermodynamically

favored structures.[39,46] We do not find such an interpretation to be necessary since X3LYP predicts that the book/cyclic structures are the thermodynamically favored structures.

Figure 5 compares the X3LYP results with recent MP2 calculations. With aug-cc-pVTZ(-f), the BSSE error for X3LYP is more than *ten times smaller* than for MP2 methods. X3LYP energies converge quickly to a limiting value with increasing basis set size (Figure 5 and Table 1). For the cyclic and book structures, the X3LYP energies also converge to the MP2 energies in the complete basis set limit; however, for the cage and prism structures, the two methods appear to converge to different energies.

This systematic difference may arise from the fundamental difference in the treatment of electron correlation in MP2 vs X3LYP. Nonetheless, we observe (1) that for the practical triple-ζ basis set the X3LYP energies are well within the uncertainties of similar MP2 calculations and (2) that the B3LYP energies clearly disagree with the MP2 energies, although they follow the same trend as the X3LYP energies.

In the finite basis set description of the hexamer isomers, the X3LYP description of electron correlation is *as consistently valid* as the MP2 perturbative description of electron correlation. Thus the X3LYP cyclic/book geometries are as much "reference" hexamer structures as the MP2 cage geometry currently is considered to be.

3.3. Decomposition of the Total Binding Energy into Multibody Components. It has been estimated that pairwise interactions contribute ~70% to the total binding energy of water clusters.[47,48] These pairwise interactions are expected to be the ones most sensitive to electron correlation and basis set effects.[47−50] This suggests that one could minimize the computational effort required for high accuracy by using a smaller basis set and lower level of theory to calculate three-body and higher terms and focusing the computation on the two-body terms.[29] To test this idea, Table 4 partitions the binding energy
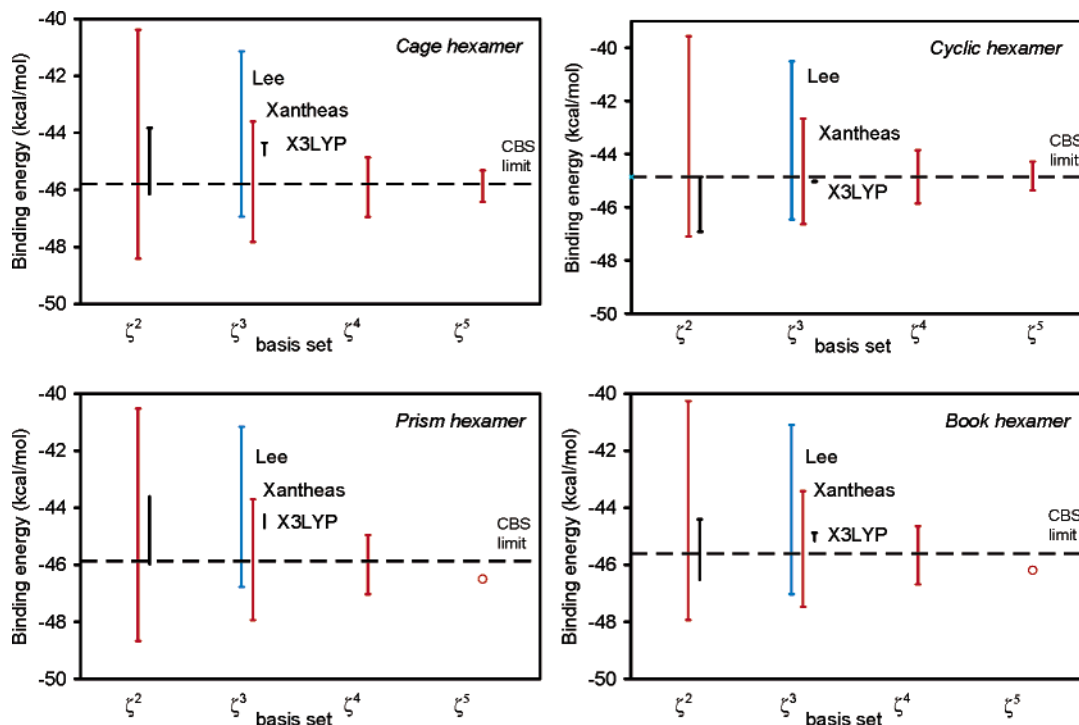

Figure 5. Negative total binding energy as a function of basis set for selected hexamer geometries, with comparison results from Lee[7] and Xantheas.[3] Here the largest basis set on the right and the estimate of the complete basis set (CBS) limit for MP2 is shown with dashes. Lower limits represent non-BSSE energies; upper limits represent BSSE energies. Generally, this lies midway between the BSSE and non-BSSE limits for the finite basis sets. The impact of BSSE for X3LYP is ~1/10th that for MP2.

TABLE 4: Decomposition of Interaction Energies (kcal/mol) for the Cyclic (S_6) Water Hexamer into Multibody Components[a]

interaction	LMP2			B3LYP			X3LYP			MP2		
	no BSSE	BSSE	50% BSSE	no BSSE	BSSE	50% BSSE	no BSSE	BSSE	50% BSSE	no BSSE	BSSE	50% BSSE
1-body	2.89	4.12	**3.51**	1.89	1.89	**1.89**	1.98	1.96	**1.97**	2.59	1.97	**2.28**
2-body	−30.98	−31.63	**−31.31**	−30.01	−29.98	**−29.99**	−32.79	−32.74	**−32.76**	−34.4	−29.46	**−31.93**
3-body	−6.98	−5.76	**−6.37**	−12.27	−12.08	**−12.17**	−12.19	−12.02	**−12.11**	−11.33	−11.61	**−11.47**
4-body	−0.80	−4.18	**−2.49**	−1.52	−2.01	**−1.76**	−1.60	−2.06	**−1.83**	−1.62	−1.51	**−1.57**
5-body	−0.60	1.35	**0.38**	−0.41	−0.13	**−0.27**	−0.40	−0.13	**−0.27**	−0.62		
6-body	0.11	−0.27	**−0.08**	−0.01	−0.03	**−0.02**	−0.01	−0.03	**−0.02**			
total	−36.36	−36.36	**−36.36**	−42.33	−42.33	**−42.33**	−45.01	−45.01	**−45.01**	−45.38	−40.61	

[a] All geometries were optimized at the level of theory indicated. For LMP2, B3LYP, and X3LYP, aug-cc-pVTZ(-f) single-point energies were calculated from an aug-cc-pVTZ(-f) optimized geometry. For MP2 (results taken from Jordan et al.[29]), aug-cc-pVTZ(-f) energies were calculated from a 6-31+G[2d,p]-optimized geometry. The average (boldfaced) of non-BSSE and BSSE energies is taken to estimate the CBS limit.

into multibody terms, allowing a comparison of the MP2 energy components directly with X3LYP energy components (here we average the non-BSSE and BSSE energies to estimate the CBS limit).

The one-body "monomer relaxation" terms in B3LYP and X3LYP deviate from MP2 by similar amounts (0.39 vs 0.31 kcal/mol, respectively) as do the three-body terms (0.71 vs 0.64 kcal/mol, respectively) and higher. However, B3LYP and X3LYP differ significantly from each other in their two-body terms (1.93 kcal/mol vs 0.83 kcal/mol difference) with X3LYP much closer to MP2. This better description of two-body interactions by X3LYP over B3LYP is expected, since X3LYP also describes water dimer and rare gas dimers much more accurately.

We find that LMP2 has the best description of two-body energies (difference of 0.62 kcal/mol from MP2), but that it fails to reproduce the higher body terms (the three body term is only half the correct value). This probably arises from assumptions in LMP2 about localization of electron correlation that are most valid for pairwise interactions. Hydrogen bonds in the LMP2-optimized cyclic water hexamer are also longer than in the corresponding B3LYP and X3LYP-optimized geometries (1.826 Å vs 1.749 and 1.739 Å, respectively). Thus, LMP2 fails to properly describe water clusters.

It has been reported that B3LYP energies approach MP2/CBS values[29] by a "fortuitous cancellation of terms". However, we find no evidence of this trend. Indeed our results suggest that B3LYP is deficient only in its treatment of two-body interactions. Once this is corrected, as in X3LYP, B3LYP leads to a proper description of larger water clusters.

3.4. Vibrational Frequencies: Theory and Experiment. Vibrational frequencies from theory correspond to force constants at the geometric minimum, while vibrational frequencies from experiment correspond to force constants averaged over the zero-point motions, which are quite large in water clusters. With sufficient experimental data on the vibrational overtones, one can correct for anharmonicity to obtain the harmonic normal-mode vibrational frequencies. However this has been determined only for water monomer[51,52] and water dimer.[53−56] To compare theory and experiment we used the corrections for the monomer and dimer to derive the empirical relation between anharmonic and harmonic vibrational frequencies shown in Figure 6. With this relation, we extrapolated the experimentally determined OH stretching vibrations of larger water clusters to corresponding *harmonic* frequencies. Figure 7 shows a comparison of these harmonic frequencies with our theoretical vibrational frequencies, left unscaled.

For cyclic complexes (dimer to pentamer), the waters are arranged symmetrically leading to a clear distinction between bonded and nonbonded O−H stretches. As the number of waters increases, the bonded OH stretch becomes lower in frequency
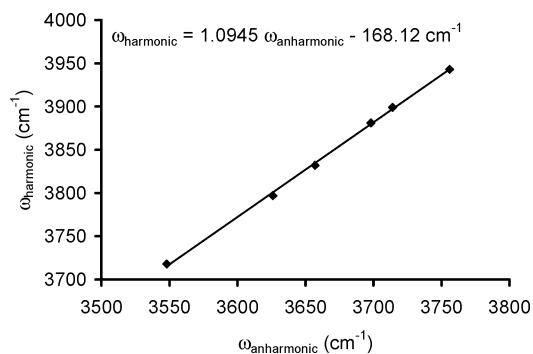

Figure 6. Comparison of experimental harmonic (derived) and anharmonic (measured) O−H stretching frequencies for water monomer and dimer (cm⁻¹). This is used to derive an empirical correction factor to experimental (anharmonic) frequencies for comparison with theoretical (harmonic) frequencies.
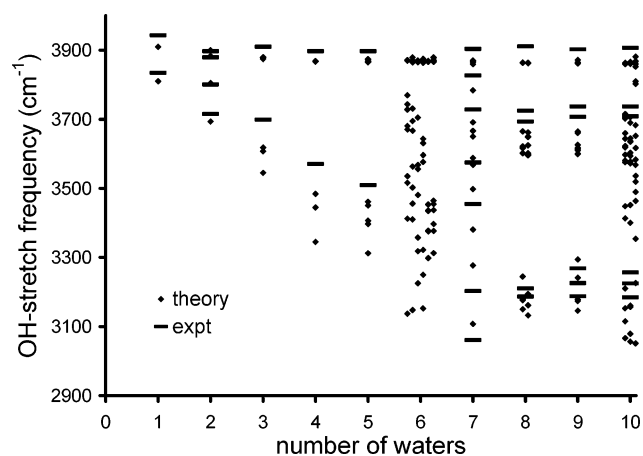

Figure 7. Comparison of O−H stretching frequencies (cm⁻¹), theory (unscaled), and experiment (scaled to obtain the harmonic frequencies). Stretching frequencies for multiple configurations are shown where available: for $n = 6$, prism, cage, book, bag, cyclic, and cyclic′; for $n = 8$, D_{2d} and S_4; and for $n = 10$, prism, prism′, and butterfly.

while the nonbonded OH stretching frequency remains nearly constant. X3LYP clearly reproduces this trend although the overall frequencies are systematically underestimated.

The agreement between theory and experiment for the dimer is good but the monomer agreement is not as close as previously reported.[13] Complexes larger than hexamers are three-dimensional, leading to IR spectra that show a characteristic band structure with a gap between bonded and nonbonded O−H stretches. This band structure and the gap between bands are reproduced well by X3LYP. The OH vibrations from theory and experiment are comparable for all clusters except $n = 6$, consistent with the assignment of cyclic structures to $n \leq 5$ and three-dimensional structures for $n \geq 7$. For $n = 6$ it would
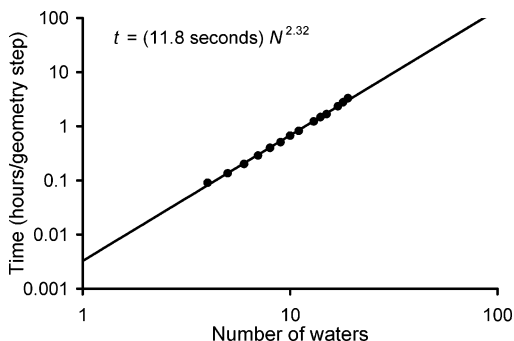
Figure 8. Comparison of computation times (seconds/geometry optimization step) for optimizing the geometry of global minimum water clusters ($n = 4-19$) using Jaguar 5.0 running on one processor of a Pentium 4 Xeon machine (512 K cache), 2.2 GHz, 2 GB memory. The overall computation time scales as $\sim N^{2.3}$.

TABLE 5: Comparison of Computation Times for Optimizing the Geometry of Water Octamer[a]

basis set (basis functions/water)	geometry iteration/s		
	LMP2	B3LYP	X3LYP
6-31g** (25)	1020	154	146
6-311g**++ (36)	4028	475	461
aug-cc-pVTZ(-f) (58)	16035	1572	1380

[a] Computations carried out with Jaguar using one processor of a Pentium 4 Xeon machine (512 K cache), 2.2 GHz, 2 GB memory. These computations all used Jaguar 5.0, which implements pseudospectral acceleration.

be valuable to obtain additional vibrational frequencies to check the assignments.

3.5. Benchmark Results and Timing. The cost of carrying out X3LYP calculations is essentially the same as for B3LYP and other hybrid DFT methods, making it quite practical for systems with hundreds of atoms. Figure 8 shows the timings for water cluster calculations for up to 19 waters indicating that the scaling is as $N^{2.3}$. For larger clusters, the scaling may slow to N^3, as initially faster matrix diagonalization and multiply steps become slower and dominate the computation time. Even with this conservative assumption, using 16 processors with a well parallelized DFT code it should be possible to do comparable calculations on clusters up to 50 waters, at an estimated cost of 30−60 h per geometry step/processor.

In contrast, MP2 calculations are $\sim$100 times slower for the octamer and scale conventionally as $\sim$N.[5] This severe scaling makes canonical MP2 calculations impractical above 8−12 waters even at national computer centers. Local orbital approximations can accelerate MP2 but as mentioned in section 3.3 may be inaccurate for our application.

Table 5 shows that with the aug-cc-pVTZ(-f) basis set geometry optimization of water octamer with X3LYP/B3LYP is 10 times faster than with LMP2. Canonical MP2 is not implemented in Jaguar, but previous benchmarking studies[57] on systems with a similar number of basis functions indicate that LMP2 (using Jaguar software) is more than 10 times faster than canonical MP2 (using Gaussian software). Thus, X3LYP is expected to be more than 100 times faster than canonical MP2 for geometry optimizations with our given basis set for moderately sized water clusters ($n > 8$).

4. Conclusions

The X3LYP hybrid density functional was designed from first principles to accurately account for the dispersion interactions

of bound clusters while maintaining or improving the accuracy of B3LYP for thermochemistry and other properties. Although water dimer and other water cluster systems were not used in determining the parameters of X3LYP, we find that X3LYP leads to binding energies for water clusters up to 12 waters in excellent agreement (average error in binding energy per water of $\sim$0.1 kcal/mol) with the best theoretical results currently available (MP2/CBS, MP2/TZ2P++).

The accuracy of X3LYP indicates that the DFT description is capable of describing the binding of weakly bound complexes for which dispersion plays an important role.

For the same basis set X3LYP is $\sim$100 times faster than MP2, and these costs scale much more slowly with system size. In addition, the BSSE corrections for X3LYP are $\sim$1/10 that of MP2, allowing BSSE corrections to be neglected even for modest basis sets. This leads to an additional saving in computational cost for high accuracy studies. We tested X3LYP for water clusters here because of the widespread interest in their optimum structures and the availability of high accuracy MP2 calculations for comparison. With X3LYP, we can now extract accurate interaction energies from hydrocarbon clusters and other weakly bound systems, and use those data to create purely ab initio based force fields capable of describing protein−ligand binding, DNA−ligand binding, and macromolecule self-assembly.

The one water cluster for which there remains considerable uncertainty is the water hexamer, which is at the crossover point between small clusters which are cyclic and large clusters which have a cage-like three-dimensional structure. With X3LYP we find that the cyclic (chair) and book forms are particularly stable, which agrees with some recent theoretical and experimental studies, but not with others. We have predicted the vibrational spectrum which may provide a target for experiments to test the predicted structure.

Supporting Information Available: Tables of absolute energies, zero point energies, enthalpies, entropies, and dispersion energies of water clusters; ball-and-stick drawings and coordinates of all water clusters considered; anharmonic and harmonic vibrational frequencies of water monomer and dimer; calculated normal-mode frequencies corresponding to water cluster O−H stretching modes; and experimentally determined vibrational frequencies of water clusters and corresponding harmonic vibrational frequencies estimated through an empirical scaling relation. This material is available free of charge via the Internet at http://pubs.acs.org.

References and Notes

(1) Xu, X.; Goddard, W. A., III. The X3LYP extended density functional for accurate descriptions of nonbond interactions, spin states, and thermochemical properties. *Proc. Natl. Acad. Sci. U.S.A.* **2004**, *101* (9), 2673−2677.

(2) Xu, X.; Goddard, W. A., III. Bonding Properties of the Water Dimer: A Comparative Study of Density Functional Theories. *J. Phys. Chem. A* **2004**, *108* (12), 2305−2313.

(3) Xantheas, S. S.; Burnham, C. J.; Harrison, R. J. Development of transferable interaction models for water. II. Accurate energetics of the first few water clusters from first principles. *J. Chem. Phys.* **2002**, *116* (4), 1493−1499.

(4) Maheshwary, S.; Patel, N.; Sathyamurthy, N.; Kulkarni, A. D.; Gadre, S. R. Structure and Stability of Water Clusters $(H_2O)_n$, $n = 8-20$: An Ab Initio Investigation. *J. Phys. Chem. A* **2001**, *105* (46), 10525−10537.

(5) Lee, H. M.; Suh, S. B.; Kim, K. S. Structures, energies, and vibrational spectra of water undecamer and dodecamer: An ab initio study. *J. Chem. Phys.* **2001**, *114* (24), 10749−10756.

(6) Lee, H. M.; Suh, S. B.; Lee, J. Y.; Tarakeshwar, P.; Kim, K. S. Structures, energies, vibrational spectra, and electronic properties of water monomer to decamer. *J. Chem. Phys.* **2000**, *112*, 9759. Erratum: *J. Chem. Phys.* **2001**, *114* (7), 3343.

(7) Lee, H. M.; Suh, S. B.; Lee, J. Y.; Tarakeshwar, P.; Kim, K. S. Structures, energies, vibrational spectra, and electronic properties of water monomer to decamer. *J. Chem. Phys.* **2000**, *112* (22), 9759−9772.

(8) Xantheas, S. S.; Apra, E. The binding energies of the D_{2d} and S_4 water octamer isomers: High-level electronic structure and empirical potential results. *J. Chem. Phys.* **2004**, *120* (2), 823−828.

(9) Lee, C.; Yang, W.; Parr, R. G. Development of the Colle-Salvetti correlation-energy formula into a functional of the electron density. *Phys. Rev. B: Condens. Matter Mater. Phys.* **1988**, *37* (2), 785−9.

(10) Vosko, S. H.; Wilk, L.; Nusair, M. Accurate spin-dependent electron liquid correlation energies for local spin density calculations: a critical analysis. *Can. J. Phys.* **1980**, *58* (8), 1200−11.

(11) Stephens, P. J.; Devlin, F. J.; Chabalowski, C. F.; Frisch, M. J. Ab Initio Calculation of Vibrational Absorption and Circular Dichroism Spectra Using Density Functional Force Fields. *J. Phys. Chem.* **1994**, *98* (45), 11623−7.

(12) Estrin, D. A.; Paglieri, L.; Corongiu, G.; Clementi, E. Small Clusters of Water Molecules Using Density Functional Theory. *J. Phys. Chem.* **1996**, *100* (21), 8701−11.

(13) Kim, K.; Jordan, K. D. Comparison of Density Functional and MP2 Calculations on the Water Monomer and Dimer. *J. Phys. Chem.* **1994**, *98* (40), 10089−94.

(14) Laasonen, K.; Parrinello, M.; Car, R.; Lee, C.; Vanderbilt, D. Structures of small water clusters using gradient-corrected density functional theory. *Chem. Phys. Lett.* **1993**, *207* (2−3), 208−13.

(15) Lee, C.; Chen, H.; Fitzgerald, G. Structures of the water hexamer using density functional methods. *J. Chem. Phys.* **1994**, *101* (5), 4472−3.

(16) Kutzelnigg, W.; Klopper, W. Wave functions with terms linear in the interelectronic coordinates to take care of the correlation cusp. I. General theory. *J. Chem. Phys.* **1991**, *94* (3), 1985−2001.

(17) Halkier, A.; Klopper, W.; Helgaker, T.; Jorgensen, P.; Taylor, P. R. Basis set convergence of the interaction energy of hydrogen-bonded complexes. *J. Chem. Phys.* **1999**, *111* (20), 9157−9167.

(18) Becke, A. D. Density-functional thermochemistry. III. The role of exact exchange. *J. Chem. Phys.* **1993**, *98* (7), 5648−52.

(19) *Jaguar 5.0*; Schrodinger, L.L.C: Portland, OR, 1991−2003.

(20) Saebo, S.; Tong, W.; Pulay, P. Efficient elimination of basis-set-superposition errors by the local correlation method: accurate ab initio studies of the water dimer. *J. Chem. Phys.* **1993**, *98* (3), 2170−5.

(21) Saebo, S.; Pulay, P. Local treatment of electron correlation. *Ann. Rev. Phys. Chem.* **1993**, *44*, 213−36.

(22) Pipek, J.; Mezey, P. G. A fast intrinsic localization procedure applicable for ab initio and semiempirical linear combination of atomic orbital wave functions. *J. Chem. Phys.* **1989**, *90* (9), 4916−26.

(23) Hariharan, P. C.; Pople, J. A. Effect of d-functions on molecular orbital energies for hydrocarbons. *Chem. Phys. Lett.* **1972**, *16* (2), 217−19.

(24) Kendall, R. A.; Dunning, T. H., Jr.; Harrison, R. J. Electron affinities of the first-row atoms revisited. Systematic basis sets and wave functions. *J. Chem. Phys.* **1992**, *96* (9), 6796−806.

(25) Boys, S. F.; Bernardi, F. The calculation of small molecular interactions by the differences of separate total energies. Some procedures with reduced errors. *Mol. Phys.* **1970**, *19* (4), 553−566.

(26) Xantheas, S. S. On the importance of the fragment relaxation energy terms in the estimation of the basis set superposition error correction to the intermolecular interaction energy. *J. Chem. Phys.* **1996**, *104* (21), 8821−8824.

(27) Szalewicz, K.; Jeziorski, B. Comment on "On the importance of the fragment relaxation energy terms in the estimation of the basis set superposition error correction to the intermolecular interaction energy" [*J. Chem. Phys.* **1996**, *104*, 8821.]. *J. Chem. Phys.* **1998**, *109* (3), 1198−1200.

(28) Wales, D. J.; Hodges, M. P. Global minima of water clusters $(H_2O)_n$, n<21, described by an empirical potential. *Chem. Phys. Lett.* **1998**, *286* (1, 2), 65−72.

(29) Pedulla, J. M.; Vila, F.; Jordan, K. D., Binding energy of the ring form of $(H_2O)_6$: comparison of the predictions of conventional and localized-orbital MP2 calculations. *J. Chem. Phys.* **1996**, *105* (24), 11091−11099.

(30) Kim, K. S.; Tarakeshwar, P.; Lee, J. Y. Molecular Clusters of Pi-Systems: Theoretical Studies of Structures, Spectra, and Origin of Interaction Energies. *Chem. Rev.* **2000**, *100* (11), 4145−4185.

(31) Tsai, C. J.; Jordan, K. D., Theoretical study of the $(H2O)_6$ water cluster. *Chem. Phys. Lett.* **1993**, *213* (1−2), 181−8.

(32) Kim, K.; Jordan, K. D.; Zwier, T. S., Low-Energy Structures and Vibrational Frequencies of the Water Hexamer: Comparison with Benzene-$(H_2O)_6$. *J. Am. Chem. Soc.* **1994**, *116* (25), 11568−9.

(33) Liu, K.; Brown, M. G.; Carter, C.; Saykally, R. J.; Gregory, J. K.; Clary, D. C. Characterization of a cage form of the water hexamer. *Nature (London)* **1996**, *381* (6582), 501−503.

(34) Kim, J.; Kim, K. S. Structures, binding energies, and spectra of isoenergetic water hexamer clusters: Extensive ab initio studies. *J. Chem. Phys.* **1998**, *109* (14), 5886−5895.

(35) Kryachko, E. S. Ab initio studies of the conformations of water hexamer: modeling the pentacoordinated hydrogen-bonded pattern in liquid water. *Chem. Phys. Lett.* **1999**, *314* (3, 4), 353−363.

(36) Losada, M.; Leutwyler, S. Water hexamer clusters: Structures, energies, and predicted mid-infrared spectra. *J. Chem. Phys.* **2002**, *117* (5), 2003−2016.

(37) Liu, K.; Brown, M. G.; Saykally, R. J. Terahertz Laser Vibration−Rotation Tunneling Spectroscopy and Dipole Moment of a Cage Form of the Water Hexamer. *J. Phys. Chem. A* **1997**, *101* (48), 8995−9010.

(38) Nauta, K.; Miller, R. E. Formation of cyclic water hexamer in liquid helium: the smallest piece of ice. *Science (Washington, D.C.)* **2000**, *287* (5451), 293−295.

(39) Fajardo, M. E.; Tam, S. Observation of the cyclic water hexamer in solid parahydrogen. *J. Chem. Phys.* **2001**, *115* (15), 6807−6810.

(40) Keutsch, F. N.; Saykally, R. J. Water clusters: untangling the mysteries of the liquid, one molecule at a time. *Proc. Natl. Acad. Sci. U.S.A.* **2001**, *98*, (19), 10533−10540.

(41) Sadlej, J.; Buch, V.; Kazimirski, J. K.; Buck, U. Theoretical study of structure and spectra of cage clusters $(H_2O)_n$, $n = 7-10$. *J. Phys. Chem. A* **1999**, *103* (25), 4933−4947.

(42) Gruenloh, C. J.; Carney, J. R.; Arrington, C. A.; Zwier, T. S.; Fredericks, S. Y.; Jordan, K. D. Infrared spectrum of a molecular ice cube: the S_4 and D_{2d} water octamers in benzene-(water)8. *Science (Washington, D.C.)* **1997**, *276* (5319), 1678−1681.

(43) Buck, U.; Ettischer, I.; Melzer, M.; Buch, V.; Sadlej, J. Structure and spectra of three-dimensional $(H_2O)_n$ clusters, n=8, 9, 10. *Phys. Rev. Lett.* **1998**, *80*, (12), 2578−2581.

(44) Gregory, J. K.; Clary, D. C. A Theoretical Study of the Cage Water Hexamer Structure. *J. Phys. Chem. A* **1997**, *101* (36), 6813−6819.

(45) Severson, M. W.; Buch, V. Quantum Monte Carlo simulation of intermolecular excited vibrational states in the cage water hexamer. *J. Chem. Phys.* **1999**, *111* (24), 10866−10875.

(46) Burnham, C. J.; Xantheas, S. S.; Miller, M. A.; Applegate, B. E.; Miller, R. E. The formation of cyclic water complexes by sequential ring insertion: Experiment and theory. *J. Chem. Phys.* **2002**, *117* (3), 1109−1122.

(47) Masella, M.; Flament, J. P. A pairwise and two many-body models for water: influence of nonpairwise effects upon the stability and geometry of $(H_2O)_n$ cyclic ($n = 3-6$) and cagelike ($n = 6-20$) clusters. *J. Chem. Phys.* **1997**, *107* (21), 9105−9116.

(48) Hodges, M. P.; Stone, A. J.; Xantheas, S. S. Contribution of Many-Body Terms to the Energy for Small Water Clusters: A Comparison of ab Initio Calculations and Accurate Model Potentials. *J. Phys. Chem. A* **1997**, *101* (48), 9163−9168.

(49) Pedulla, J. M.; Kim, K.; Jordan, K. D. Theoretical study of the n-body interaction energies of the ring, cage and prism forms of $(H_2O)_6$. *Chem. Phys. Lett.* **1998**, *291* (1, 2), 78−84.

(50) Xantheas, S. S. Ab initio studies of cyclic water clusters $(H_2O)_n$, n=1−6. II. Analysis of many-body interactions. *J. Chem. Phys.* **1994**, *100* (10), 7523−34.

(51) Benedict, W. S.; Gailar, N.; Plyler, E. K. Rotation−vibration spectra of deuterated water vapor. *J. Chem. Phys.* **1956**, *24*, 1139−65.

(52) Kuchitsu, K.; Morino, Y. Estimation of anharmonic potential constants. II. Bent XY2 molecules. *Bull. Chem. Soc. Jpn.* **1965**, *38* (5), 814−24.

(53) Fredin, L.; Nelander, B.; Ribbegard, G. Infrared spectrum of the water dimer in solid nitrogen. I. Assignment and force constant calculations. *J. Chem. Phys.* **1977**, *66* (9), 4065−72.

(54) Nelander, B. Infrared spectrum of the water-hydrogen sulfide complex. *J. Chem. Phys.* **1978**, *69*, (8), 3670−1.

(55) Bentwood, R. M.; Barnes, A. J.; Orville-Thomas, W. J. Studies of intermolecular interactions by matrix isolation vibrational spectroscopy. Self-association of water. *J. Mol. Spectrosc.* **1980**, *84* (2), 391−404.

(56) Tursi, A. J.; Nixon, E. R. Matrix-isolation study of the water dimer in solid nitrogen. *J. Chem. Phys.* **1970**, *52* (3), 1521−8.

(57) Murphy, R. B.; Beachy, M. D.; Friesner, R. A.; Ringnalda, M. N. Pseudospectral localized Moeller−Plesset methods: theory and calculation of conformational energies. *J. Chem. Phys.* **1995**, *103* (4), 1481−90.

Enhancing 2-Iodoxybenzoic Acid Reactivity by Exploiting a Hypervalent Twist

Julius T. Su and William A. Goddard III*

Division of Chemistry and Chemical Engineering, California Institute of Technology, Pasadena, California 91125

Received July 5, 2005; E-mail: wag@wag.caltech.edu

Among oxidizing agents, 2-iodoxybenzoic acid (IBX) stands out for being mild, selective, and environmentally friendly, as it contains no toxic or expensive heavy metals, and variants exist that operate in aqueous solution.[1] IBX effects oxidations of functionality beyond simple alcohols,[2,3] making it an ideal reagent for carrying out a wide range of oxidative transformations were it possible to tame and enhance its reactive capabilities.

We propose a modification of IBX predicted to increase its oxidizing power while preserving its selectivity, based on a new mechanism in which the rate-limiting step is *hypervalent twisting*. Our mechanism, derived from density functional quantum mechanics (QM) calculations,[4] also explains the native alcohol size-selectivity of unmodified IBX.

Hypervalent twisting is a coordinated motion of ligands driven by the necessity of generating a stable, planar form of the byproduct IBA **4** from an IBX−alcohol intermediate **3** (Figure 1). The proposed modification, substitution of IBX at the *ortho* position, lowers the barrier of this step. Since the rate-accelerating *ortho* position is near the site of substrate binding, it offers a possible route to an oxidant capable of chiral discrimination.[5]

We find that alcohols exchange with the hydroxyl ligand of IBX **1** via a low-barrier (∼9 kcal/mol) acid-catalyzed pathway, producing an IBX−alcohol complex **2** blocked from eliminating IBA (Figure 1). To form the oxidation products, **2** must twist, moving the *oxo* group into the plane and the alcohol out of the plane to form complex **3** (rate-limiting barrier of ∼12 kcal/mol). Only after the twisting barrier has passed can the complex between ‡$_{twist}$ and **3** eliminate IBA **4** to produce the oxidation product **5** (∼5 kcal/mol barrier). Intermediates **1**, **2**, **4**, and **5** consistent with our calculations have been observed by NMR.[6]

This hypervalent twist mechanism explains the propensity of IBX to oxidize large alcohols faster than small ones. Larger alcohols have a lower twisting barrier since the twisting is driven forward by a repulsion between the alkoxy ligand and the *ortho* hydrogen that is relieved as the motion is completed (Figure 3). Figure 2 shows that lower twisting barriers correlate well with higher measured oxidation rates over the alcohols examined.

To accelerate the overall reaction, we propose placing a bulky substituent in the *ortho* position to encourage IBX twisting. As a simple test, an *ortho* methyl substituent lowers ΔG_{twist} by >2.4 kcal/mol over a test set of seven alcohols, with a typical rate acceleration of ∼100 times (Figure 2). The rate acceleration is especially pronounced for the secondary alcohols 2-propanol and 2,4-dimethyl-3-pentanol, consistent with increased steric repulsion between the *ortho* methyl and the alcohol.

The optimum size for the *ortho* group is a compromise between being large enough to favor the twisted form and being small enough to allow a favorable equilibrium between **1** and **2** (Ph and *t*-Bu are too large). Medium-sized nonpolar aliphatics, such as methyl, ethyl and isopropyl, provide the best balance of good twisting and ligand exchange thermodynamics.[8]
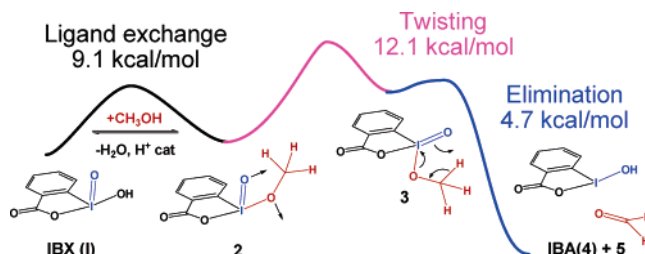

Figure 1. Hypervalent twist (HT) mechanism showing the reaction path and associated barriers for oxidation of alcohols by IBX (barriers relative to reactants at each step). The coordinated motion that converts intermediate **2** to **3** is the rate-limiting step of the reaction.
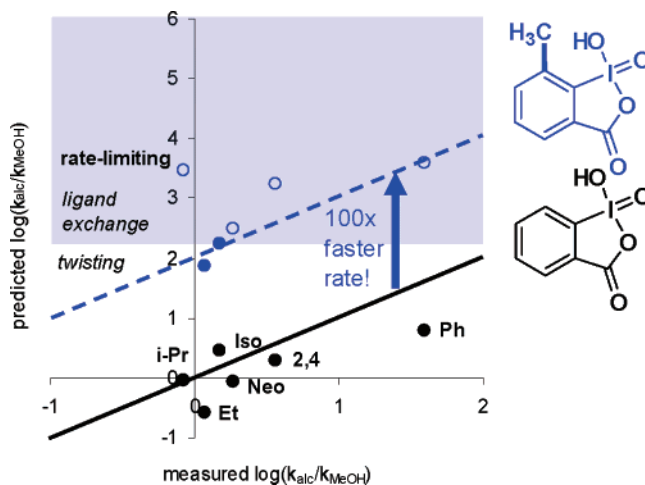

Figure 2. Alcohol oxidation rates estimated from hypervalent twisting barriers show good correlation with experimentally measured rates. We predict that *ortho*-methyl IBX multiplies the twisting rate by a factor of 100, up until ligand exchange becomes the rate-limiting step of the overall oxidation.
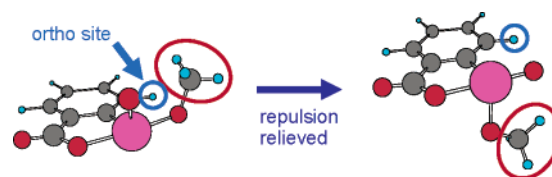

Figure 3. Explanation of IBX−alcohol size-selectivity: large alcohols twist IBX more easily, which makes them oxidize more quickly. The proposed *ortho*-substituted IBX enhances this effect and should be more active.

We now consider the nature of the hypervalent twist. IBX and its alcohol derivatives can exist favorably in untwisted and twisted conformations. In contrast, the byproduct IBA is only stable in a planar form−the form of IBA with hydroxyl and carboxylic acid ligands 90° from each other is destabilized by ∼48 kcal/mol relative to planar IBA.

Figure 4 shows that this stability difference affects the barriers to IBA elimination and product formation: the transition state is
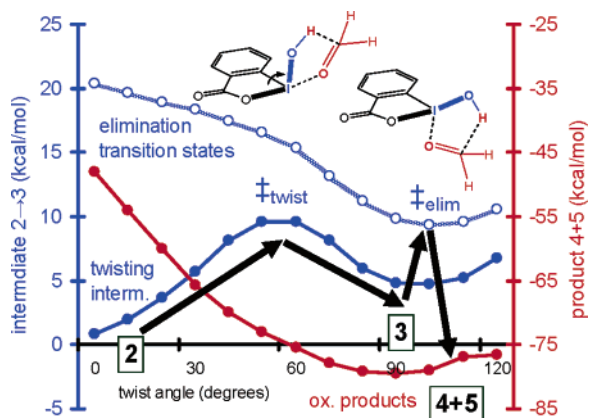
Figure 4. The alcohol−IBX intermediate **2** (blue curve, solid circles) can pass through elimination transition states (blue curve, open circles) to form oxidation products (red curve). The black arrows show the most favorable reaction pathway, where **2** twists past ‡twist to form **3**, access ‡elim, and form oxidation products **4** and **5**.
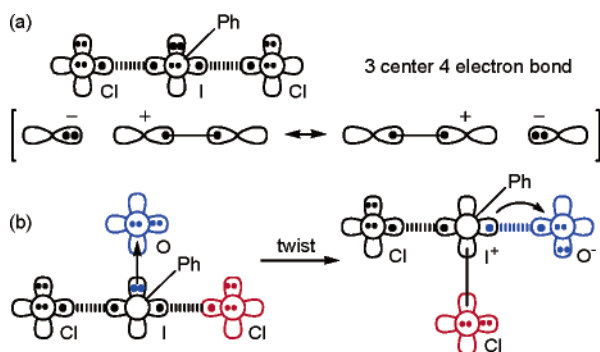

Figure 5. Hypervalent bonding in analogues to IBA **4**, IBX **2**, and twisted IBX. (a) Resonance structures responsible for the half-ionic half-covalent three-center four-electron bond in PhICl$_2$, similar to IBA; (b) structures of PhIOCl$_2$, similar to those of IBX and twisted IBX.

product-like. Intermediate **2** prefers to twist first (12 kcal/mol), then eliminate IBA (5 kcal/mol), rather than eliminate IBA directly without twisting (20 kcal/mol).

To understand why IBX twists readily while IBA prefers so strongly to be planar, consider the bonding of iodine in IBA (Figure 5). Iodine makes a normal covalent bond to the phenyl carbon, leaving two doubly occupied 5p orbitals perpendicular to this bond. In IBA, one doubly occupied orbital is flanked by hydroxyl and carboxylic acid ligands opposite each other, bound by a three-center four-electron bond that is half-ionic and half-covalent. The two anionic ligands must be opposite to each other to gain full stability from resonance.

In IBX and its alcohol derivatives, the other doubly occupied orbital is used to make a dative donor−acceptor bond to the oxo group. Upon twisting, as with IBA, the methoxy ligand loses resonance with the acid ligand, making it less strongly bound, but unlike in IBA, the *oxo* group picks up the resonance with that ligand to compensate. In addition, the *oxo* bond becomes more covalent in character, as the iodine transfers an electron to the oxygen to avoid placing three electrons into one p orbital. These balanced effects make the twisted complex a true intermediate only ∼3 kcal/mol less stable than the untwisted complex.

Our work has focused on accelerating the overall oxidation rate by lowering the twisting barrier, but beyond a certain point, ligand exchange becomes the rate-limiting step. For methanol oxidation, this point is reached when the barrier to hypervalent twisting of ∼12 kcal/mol is lowered to the ligand exchange barrier of ∼9 kcal/mol, a rate acceleration of ∼270 times.

Scheme 1. Acid-Catalyzed Water/Alcohol Exchange on IBX, Showing Proton Transfer (6.0 kcal/mol barrier) Followed by Coordinated Ligand Motion (9.1 kcal/mol barrier)
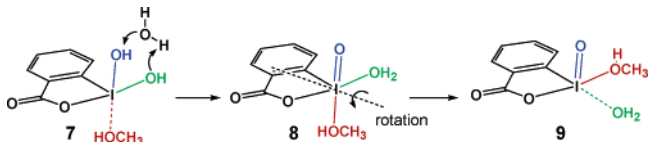
Alcohol/water exchange occurs via two steps: a fast proton transfer and a slower coordinated ligand motion (Scheme 1). The proton transfer starts with protonated IBX complex **7** and preferentially goes in one direction to produce **8** with an out-of-plane *oxo* ligand. Lacking an anionic ligand to twist with, the dative *oxo* ligand (I$^+$−O$^-$) stays out of plane to maximize charge transfer. Once the alcohol ligand has been deprotonated, IBX−alcohol **9** proceeds to twist and oxidize as described previously.

Our studies show that IBX twisting—the coordinated motion of an *oxo* group and an anionic ligand—acts as a gatekeeper to oxidation. Hypervalent bonding concepts explain why the twisting must occur, how it can occur, and when it occurs. By controlling the twisting through *ortho* group substitution, we control the oxidation pathway and unlock IBX's reactive potential.

Note Added after ASAP Publication. The title compound was named incorrectly in the version published ASAP September 15, 2005. The corrected version was published September 20, 2005.

Supporting Information Available: Coordinates, energies, and frequency data for compounds referenced (PDF), and crystal structure and NMR shift comparisons. This material is available free of charge via the Internet at http://pubs.acs.org.

References

(1) Aqueous IBX reactions: (a) Surendra, K.; Srilakshmi, K. N.; Arjun, R. M.; Nageswar, Y. V. D.; Rama, R. K. *J. Org. Chem.* **2003**, *68*, 2048−2049. (b) Thottumkara, A. P.; Thottumkara, K. V. *Tetrahedron Lett.* **2002**, *43*, 569−572.

(2) IBX applications: (a) Frigerio, M.; Santagostino, M. *Tetrahedron Lett.* **1994**, *35*, 3485. (b) Nicolaou, K. C.; Mathison, C. J. N.; Montagnon, T. *J. Am. Chem. Soc.* **2004**, *126*, 5192−5201. (c) Nicolaou, K. C.; Baran, P. S.; Zhong, Y.-L. *J. Am. Chem. Soc.* **2001**, *123*, 3183−3185. (d) Nicolaou, K. C.; Baran, P. S.; Kranich, R.; Zhong, Y.-L. *Angew. Chem., Int. Ed.* **2001**, *40*, 202−206.

(3) Review articles: (a) Stang, P. J. *J. Org. Chem.* **2003**, *68*, 2997−3008. (b) Zhdankin, V. V.; Stang, P. J. *Chem. Rev.* **2002**, *102*, 2523−2584. (c) Tohma, H.; Kita, Y. *Adv. Synth. Catal.* **2004**, *346*, 111−124. (d) Moriarty, R. M. *J. Org. Chem.* **2005**, *70*, 2893−2903.

(4) Method validated by comparing theoretical geometries to a variety of known hypervalent iodine crystal structures; see Supporting Information. Restricted MPW1K/LACV3P**, with single point solvation from Poisson−Boltzmann continuum theory ($\epsilon = 47.2$, $r_{probe} = 2.41$ Å) using Jaguar 6.0 (Schrödinger Inc). Thermochemical corrections (ΔG, ZPE) used calculated vibrational frequencies. Intermediates and transition states were stationary points with the correct number of positive eigenvalues; reactants and products were optimized from transition structures perturbed along a negative eigenvalue path.

(5) Enantioselective hypervalent iodine reagents: (a) Hirt, U. H.; Schuster, M. F. H.; French, A. N.; Wiest, O. G.; Wirth, T. *Eur. J. Org. Chem.* **2001**, 1569−1579. (b) Tohma, H.; Takizawa, S.; Watanabe, H.; Fukuoka, Y.; Maegawa, T.; Kita, Y. *J. Org. Chem.* **1999**, *64*, 3519−3523.

(6) Computed NMR shielding constants correlate well with experimental chemical shifts; see Supporting Information. All comparisons to experiment are to Frigerio, M.; Santagostino, M.; Sputore, S.; Palmisano, G. *J. Org. Chem.* **1995**, *60*, 7272−7276.

(7) $\Delta G_{elim}^{\ddagger} < \Delta G_{twist}^{\ddagger}$ for all alcohols studied; see Supporting Information.

(8) Electronic effects exist but are less significant. Electronegative *ortho* groups, such as fluorine, repel the *oxo* group in intermediate **3**, inhibiting twisting and deactivating the reagent, while electropositive groups, such as B(OMe)$_2$, activate the reagent, but to a lesser extent than even *o*-methyl IBX.

JA054446X